July 2019

Rheological Investigations of Self-Assembled Block Copolymer Nanocomposites with Complex Architectures

Benjamin Yavitt

RHEOLOGICAL INVESTIGATIONS OF SELF-ASSMEBLED BLOCK COPOLYMER NANOCOMPOSITES WITH COMPLEX ARCHITECTURES

A Dissertation Presented

by

BENJAMIN M. YAVITT

Submitted to the Graduate School of the
University of Massachusetts Amherst in partial fulfillment
of the requirements for the degree of

DOCTOR OF PHILOSOPHY

May 2019

Polymer Science and Engineering

RHEOLOGICAL INVESTIGATIONS OF SELF-ASSMEBLED BLOCK COPOLYMER NANOCOMPOSITES WITH COMPLEX ARCHITECTURES

A Dissertation Presented

by

BENJAMIN M. YAVITT

Approved as to style and content by:

_____
James J. Watkins, Co-Chair

_____
H. Henning Winter, Co-Chair

_____
Jonathan P. Rothstein, Member

_____
E. Bryan Coughlin, Department Head
Polymer Science and Engineering

DEDICATION

To the pursuit of knowledge & scientific discovery.

ACKNOWLEDGEMENTS

I am thankful for the funding that has supported the work in this thesis. The NSF Center for Hierarchical Manufacturing (CHM) (NSF CMMI-1025020) at UMass Amherst allowed me to pursue a range of interesting research topics, fueled by general curiosity. Facilities at University of Massachusetts Polymer Science and Engineering Department and the Materials Research Science and Engineering Center (MRSEC DMR 0820506) were used in this thesis. Additional measurements were performed at Brookhaven National Laboratory, NSLS II Beamline 11-BM (Complex Material Scattering, CMS) under user proposal DE-SC0012704.

The PhD is inherently a personal journey that requires perseverance, self-motivation, and dedication to your craft. However, there are many people that influence and define the ultimate path. I would like to acknowledge the support from my committee, Prof. Jim Watkins, Prof. H. Henning Winter and Prof. Jonathan Rothstein. Following your mantra “It’s your PhD” helped me become a more independent scientist and a stronger teacher. I also accepted your advice to stay grounded in the fundamentals of polymer science, chemical engineering, and material science. The scientific landscape is always evolving, yet these tools remain handy to tackle any problem that comes along. I learned to stay curious and follow the interesting problems, and to respect what nature reveals. Always appreciate the complexity and excitement of what you may find.

I have been fortunate to call Conte my home during my studies. I want to express my thanks to “The People of Conte”; the faculty, staff, students and postdocs who keep the wheels turning each and every day. It is important to have a positive workplace environment and I found that at UMass. I believe the strongest aspect of our program is the

close-knit class of peers. We are fortunate to receive a strong network of colleagues and friends on the first day. I learned so much from everyone and I hope I was able to teach others in the process.

Many thanks to all Watkins and Winter group members, past and present. I appreciated being part of a diverse group composed of many different backgrounds and technical expertise. Special thanks go out to Yue, Dong-Po, Huafeng and Gayathri who were heavily involved in the bottlebrush work. I sincerely appreciate the comradery with Vijesh and Olli-Ville over the past 5 years. We dove into the field of rheology head first and traveled through the thick of it together.

I was fortunate to have the opportunity to collaborate and work with many brilliant scientists during my PhD. We shared ideas, resources and materials and I forged many lasting friendships in the process. “Danke” to the crew at Bayreuth University in Germany (Andreas, Paul, Martin and Tobias) for hosting my several times and for coming to visit Amherst. I gained a fresh perspective on research from the international exchange. Many thanks to Chun-Wei for his visit to our group and helping us tackle exciting research in bottlebrush assembly. I also enjoyed the company of our Chinese visitors & officemates (David, Varick, Huagao and Xing). Special appreciation goes to Masa and Ruipeng at NSLS-II for reaching out to our group, encouraging us to apply for beamtime, introducing me to the synchrotron, and helping me establish a future in the field.

My time outside of Conte was enjoyed with friends and roommates in the Yellow House. To Vijesh, Josh, Nick and Cristiam, I was so fortunate to spend four awesome years with you guys. I also cannot forget my friends from undergrad at CWRU who have kept up with me over the past years. I was nervous about leaving CWRU and starting a PhD, so

I appreciate that we were able to get together every year to catch up. Our trips allowed me to take a break and re-center myself as I made my voyage through grad school.

My path into polymer science started almost a decade ago and I would have never made it to UMass without the benefit of several chance encounters. Dr. John Blackwell, Professor of Macromolecular Science and Engineering at CWRU, was my randomly-assigned first year advisor. Dr. Blackwell introduced me to the field of polymer science (which I did not even know existed at the time) and helped me declare my major freshman year. Around the same time, I met Dr. Brian Cromer (PSE class of 2010) who was a senior at CWRU and a teammate of mine on the cross-country team. Cromer showed me the ins-and-outs of polymer coursework, research, and potential career paths after graduation. I did not know about UMass PSE until he decided to go for graduate school. During my junior year, Cromer convinced me to do a summer REU at UMass, working in Prof. Al Crosby's lab. I appreciate the opportunity that Al gave me to see PSE first hand and experience all the fascinating research. The REU was a three-month recruitment visit, and I knew instantly that I wanted to come to back for graduate school. The rest, as they say, is history.

My family is my biggest influence and I appreciate their support. When I was a little kid, whenever someone asked me what I wanted to do when I grew up, I would always answer "go into the family business." Basically, I knew I wanted to get a PhD from the first day of kindergarten. Growing up in an academic household has shaped me into the scientist I am today. My family has shown me that learning is a lifelong journey, and it is something special to share with others in the lab and in the classroom. I want to continue this tradition as I set out on my own career.

ABSTRACT

RHEOLOGICAL INVESTIGATIONS OF SELF-ASSEMBLED BLOCK COPOLYMER NANOCOMPOSITES WITH COMPLEX ARCHITECTURES

MAY 2019

BENJAMIN M. YAVITT, B.S., CASE WESTERN RESERVE UNIVERSITY

M.S., UNIVERSITY OF MASSACHUSETTS AMHERST

Ph.D., UNIVERSITY OF MASSACHUSETTS AMHERST

Directed by: Professors James J. Watkins and H. Henning Winter

The self-assembly of block copolymers (BCP) into microphase separated structures is an attractive route to template and assemble functional nanoparticles (NP) into highly ordered nanocomposites and is central to the "bottom up" fabrication of future materials with tunable electronic, optical, magnetic, and mechanical properties. The optimization of the co-assembly requires an understanding of the fundamentals of phase behavior, intermolecular interactions and dynamics of the polymeric structure. Rheology is a novel characterization tool to investigate these processes in such systems that are not accessible by other means. With the combination of X-ray scattering techniques, structure-property relationships are determined as a function of NP loading in self-assembled hybrid composites. This thesis examines two classes of BCP templates used for nanocomposite assembly. First, low molecular weight, disordered (low χN) BCP surfactants are considered. The addition of NPs with enthalpically favored interactions between the NP and one of the BCP domains boosts the phase segregation strength and drives self-assembly, resulting in highly filled nanocomposites (φ_{NP} ~ 30 vol.%) with small domain spacing (d_0 ~ 10 nm) due to the low N. The effect of NPs on the self-assembly dynamics,

material properties, and temperature dependent phase transitions are considered in the high loading regime. Oscillatory shear rheology reveals a transition from liquid-like to solid-like behavior with increasing NP content. The addition of stiff NPs to a soft polymer matrix, along with favorable intermolecular interactions, produces a x10^3 increase in the magnitude of G^*. Phase transitions are investigated by correlating time-resolved rheology and time-resolved SAXS. Structure development and viscoelasticity scale with the NP content, and a general master curve describing behavior across all NP loadings is constructed. The access to new material properties and transitional phenomenon provides further insight into the complex structure-property relationships of this class of nanocomposites.

The second BCP template is microphase separated bottlebrush block copolymers (BBCP), macromolecules with discrete blocks of densely grafted side chains tethered to a molecular backbone. Highly extended backbone conformations and significant repulsion between grafted side chains are believed to suppress chain entanglements, resulting in rapid self-assembly (order of minutes) into large nanostructures (d_0 > 100 nm) advantageous for optically active materials. A systematic study of model poly(styrene)-*block*-poly(ethylene oxide) (PS-*b*-PEO) BBCPs with short side chains below entanglement molecular weight is conducted. We measure dynamic moduli $G'(\omega)$ and $G''(\omega)$ over a wide range of timescales. The scaling relationships in dynamic data show distinct power law behavior analogous to critical gels. The relaxation mechanisms are a consequence of the reduced entanglements and mobile microstructure. This interplay of high molecular mobility and rapid self-assembly contrasts the viscoelasticity of linear BCP materials with comparable microstructure.

The role that applied shear plays on the directed alignment of microphase separated lamellae in bulk BBCP samples is considered. The periodic structures are found to align at exceptionally low strain amplitudes and mild processing temperatures as confirmed by SAXS. Alignment over several mm^3 is realized by high throughput synchrotron experiments and we hypothesize that this method can be applied as a means of fabricating and processing BCP-based hybrid materials with exceptional long-range order.

Building on the understanding from the highly loaded NP/BCP composites, similar considerations are taken towards the investigation of phase behavior, morphology, and rheological response in NP/BBCP hybrids. The goal is to understand how NPs and intermolecular interactions impacts the unique relaxation processes inherent to BBCP melts. From oscillatory shear rheology measurements, systematic transitions in the long-time relaxations towards solid-like behavior is observed with increasing NP loading, suggesting the NP inhibits the highly mobile microstructure and rapid side chain relaxations. The structure-property relationships realized by both rheology and SAXS lay the groundwork as we explore future manipulation and processing of these diverse structures for both well-established and emergent applications.

TABLE OF CONTENTS

Page

LIST OF TABLES

Table Page

LIST OF FIGURES

Figure Page

CHAPTER 1

SELF-ASSEMBLED NANOPARTICLE/BLOCK COPOLYMER COMPOSITES: DESIGN AND UTILITY

1.1 Block Copolymer Templated Assembly of Inorganic Nanoparticles

Block copolymers (BCP) are an integral component of polymer science.[1,2] When two chemically dissimilar polymer chains are tethered together with a covalent bond, the segments microphase separate into discrete domains, typically on the nanometer length scale. BCPs self-assemble into a range of ordered morphologies; periodic lamellae, hexagonally packed cylinders, and co-continuous gyroid structures.[1,3] The phases are accessed by tuning structural parameters of the block segments, such as the chemical contrast between the two blocks (Flory Huggins interaction parameter (χ)), block length (N), and volume fraction (f). Countless Ph.D. theses have been dedicated to understanding synthetic approaches, physical properties, and practical utility of these diverse materials. While the fundamental phase behavior and synthesis of BCPs is rich, BCPs have found effective use in the development of future materials with tunable electronic, optical, magnetic, and mechanical properties by incorporating functional additives into the nanostructure.[4] For example, inorganic nanoparticles (NP) such as metal oxides, semiconducting, and noble metal NPs with sub-100 nm size and high surface area per volume ratios are introduced into the polymer matrix to form a nanocomposite. NPs retain the attractive physical properties of their bulk counterparts, as well as adopt tunable size dependent properties.[5] For example, localized surface plasmonic resonance in gold (Au) NPs is a function of NP diameter and the plasmonic properties are enhanced when the NPs

are organized and assembled into an ordered nanoscale structure.[6–8] The inherent nanoscale dimensions associated with the BCP structure makes them attractive templates to direct the assembly of NPs. By definition, NP/BCP composites are a class of hybrid materials that take advantage of the natural self-assembly of BCP to build up ordered arrays of NPs.[4,8–12] The "bottom up" approach has garnered considerable interest for a wide range of nanotechnology applications, such as energy storage, photonics, and communications.[13] For example, confinement of NPs within a microphase segregated domain form well-ordered nanoreactors used for the synthesis of cobalt nanowires for high performance thermoelectric applications.[14] Spatial distribution is essential in data storage devices that utilize magnetic nanoparticles (iron oxide, cobalt ferrite) so BCPs are used to control assembly and improve storage density.[15,16] Palladium NPs used in catalysis require clear dispersion and high interfacial area, which is also achieved by self-assembly with BCPs.[17]

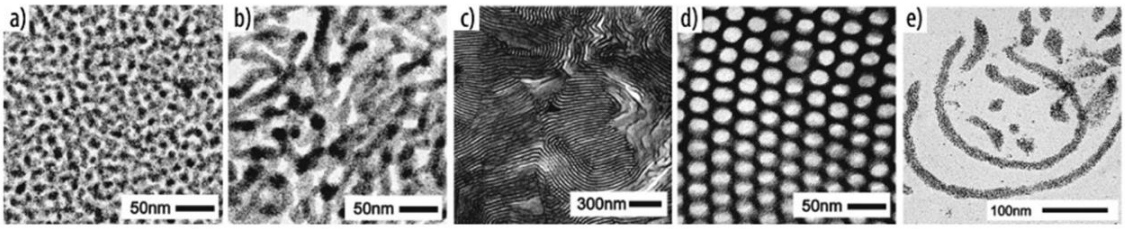

Figure 1.1 TEM micrographs of metal-block copolymer hybrid films with different morphologies. **(a)** Spherical micellar morphology, **(b)** worm-like micellar morphology, **(c)** lamellar morphology, **(d)** inverse hexagonal morphology. **(e)** Isolated nanocylinders obtained by dissolving hybrid films with worm-like micellar morphology. (Modified from Ref. 4)[4]

The overall performance of the device depends on the efficient organization and spatial distribution of the functional NP directed by the BCP template.[8] Therefore, recent work has focused on understanding the physics of controlled co-assembly of the NP and BCP. The parameter space is very large. There is a seemingly endless combination of BCPs that can be prepared through various synthetic approaches.[2] The same can be said for the

preparation of inorganic NPs with tunable size, composition, surface functionality, etc.[12] The thermodynamics and kinetics of the cooperative interactions between the NP and BCP are key for successfully assembling each component into a well-ordered structure. While many elegant examples have been produced and demonstrated in the literature, progression toward scaled up fabrication has remained a challenge.[13]

Lab scale preparation techniques of controlled NP assembly with BCP templates are described in several review articles.[4,8,9,12] One common method of fabrication is in-situ NP formation within a microphase separated BCP template by the reduction of NP precursors selectively incorporated into one domain of the BCP.[8] While in-situ methods are easy to implement, the control over particle size and inter-particle ordering in not precise. The lack of control severely impacts the desired properties contributed from the NP, which are inherently size dependent. Another fabrication strategy is the co-assembly of pre-synthesized NPs within the BCP matrix during solvent or thermal annealing.[9] This method takes full advantage of the precise control over particle size, overcoming some of the disadvantages of the in-situ method. As previously mentioned, careful synthetic approaches are used to fabricate well defined NPs of tunable size and shape with a variety of surface modification, which is essential for optimizing the intermolecular interactions that dictate the co-assembly. The bottom up fabrication approach is promising as both a cost-effective solution processable and scalable method for fabricating NP based nanocomposites.[18]

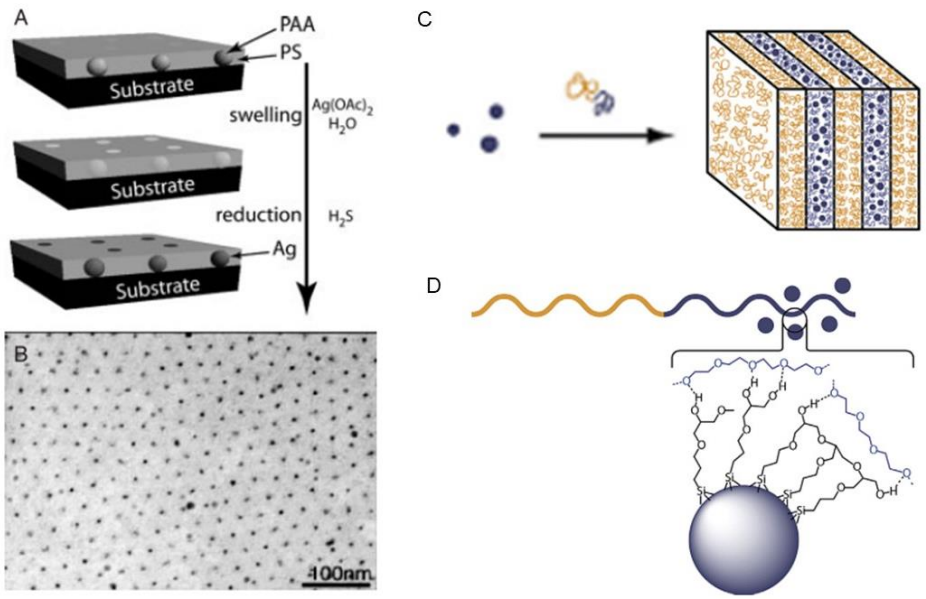

Figure 1.2 (a) Schematic of the nanoreactor scheme approach. Top: thin film of solvent-cast spherical PS-*b*-PAA. Middle: selective swelling of PAA spheres with metal precursor. Bottom: formation of metal nanocrystals by reduction of metal precursor. **(b)** Transmission electron micrograph of thin film, demonstrating the hexagonal array of Ag nanodots within the PS matrix. **(c)** An ensemble of particles in which the diameter of all the particles is smaller than the root-mean-square-end-to-end distance of the block to which they are attracted results in a regular, in this case, lamellar morphology. **(d)** Representation of the favorable interaction of the aluminosilicate nanoparticles with the PEO block of a block copolymer. (Modified from Ref. 4 & 8)[4,8]

The successful assembly of NPs into the polymer matrix is governed by a delicate balance between enthalpy and entropy.[4,19] The addition of NPs imparts significant polymer chain stretching, which leads to an overall decrease in the entropic contribution to the free energy of the system. Thermodynamically, this penalty is offset by favorable intermolecular interactions between the polymer and the NP which result in an enthalpic contribution. Modifying the surface of the inorganic nanoparticles with organic ligands is a straight forward approach to introducing said intermolecular interactions (van der Waals or hydrogen bonding). Aside from the enthalpic contributions, these interactions are used to control dispersion and selective placement of the NP within a specific BCP domain.[12] Understanding the nature of the surface ligand interaction and the resulting distribution of

NPs into the domain is essential. Pioneering work by Kramer and coworkers showed that Au NPs capped with poly(styrene) (PS) ligands preferentially assembled into the PS domain of a lamellar forming poly(styrene)-*block*-poly(2-vinyl pyridine) (PS-*b*-P2VP) BCP.[20,21] However, Au particles capped with a blend of PS and P2VP chains were found to localize at the interface of the BCP domains. Additional studies showed that the overall dispersion of Au within the PS matrix was controlled by the areal density of ligands on the NP surface.[22] NPs were either dispersed uniformly throughout the domain, or concentrated at the edges and center of the domain.

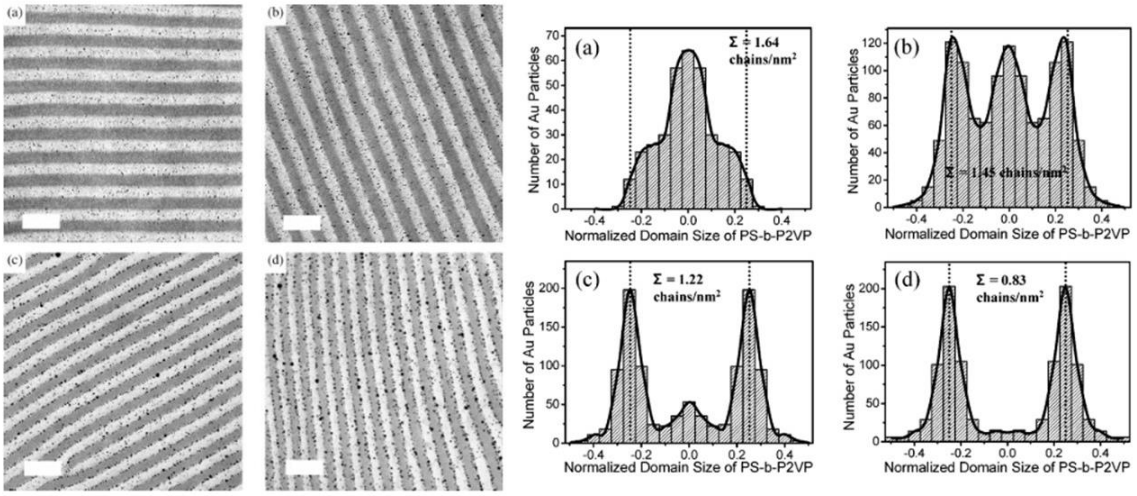

Figure 1.3 Cross-sectional TEM images of PS-*b*-P2VP block copolymer containing PS-coated gold nanoparticles whose surfaces are covered with various chain areal densities of PS chains (M_n = 3.4 kg/mol): **(a)** 1.64, **(b)** 1.45, **(c)** 1.22, and **(d)** 0.83 chains/nm^2. Scale bar is 100 nm. Histograms of particle positions from the TEM micrographs in: **(a)** 1.64, **(b)** 1.45, **(c)** 1.22, and **(d)** 0.83 chains/nm^2. Interfaces of the PS domain are at -0.25 and +0.25, and data are averaged at a given position relative to zero, i.e., number of particles at -0.2) (number of particles at -0.2 + number of particles at +0.2)/2. (Modified from Ref. 22)[22]

The thermodynamic balance constrains the NP size relative to the BCP domain size and polymer chain length.[8] Bockstaller et al. demonstrated the size selective assembly of two different types of NPs in a symmetric PS-*block*-poly(ethylene propylene) (PS-*b*-PEP) BCP.[23] Au NPs with a diameter of d_{NP} = 3.5 nm assembled at the BCP interface, while

silicon dioxide (SiO_2) NPs with a diameter of d_{NP} = 21.5 nm localized in the center of the PEP domain. Here, the entropic effects dominated and drove the NPs to regions of the polymer matrix that incurred the least penalty. Besides demonstrating interesting polymer physics correlations, the potential utility of a multicomponent ternary composite was intriguing. Understanding the thermodynamic balance and the rich interactions between the NP and BCP is essential for truly precise control over the spatial organization and structure during device fabrication.

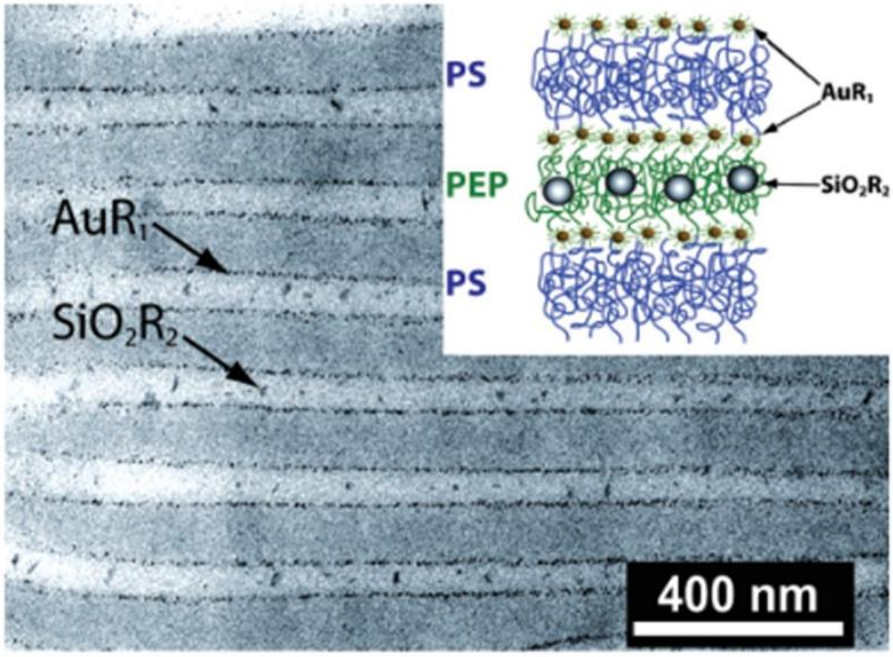

Figure 1.4 Bright field electron micrograph of a ternary blend of PS-PEP + AuR_1 + SiO_2R_2 with inorganic filling fraction (φ = 0.02, respectively, after microsectioning normal to the layer direction (no stain). Gold nanocrystals appear as dark spots along the IMDS; silica nanocrystals reside in the center of the PEP domain. Inset: Schematic of the particle distribution (size proportions are changed for clarity). (Modified from Ref. 23) [23]

Hydrogen bonding is an effective intermolecular interaction to utilize. Hydrogen bonding is highly directional, and the strength/lifetime of the interaction is dependent on the type of hydrogen bond donator and acceptor.[24] A single hydrogen bond is a relatively weak intermolecular interaction (~ 10 kJ/mol), but multiple coordinated interactions

increase the macroscale strength of the association.[25] The selective coordination between a hydrogen bond donating and hydrogen bond accepting group introduces a level of specificity in tailoring coordinated interactions. Hydrogen bonding has been implemented extensively between surface coated Au NPs with PS-*b*-P2VP or PS-*b*-P4VP.[26–29] The nitrogen in P2VP or P4VP hydrogen bonds exceptionally well to pendant -OH or -COOH groups from surface functionalized ligands, resulting in a robust, directed association.

1.2 Physics of Block Copolymer Self Assembly

The bottom up fabrication of NP/BCP composites is driven by the rich field of BCP phase behavior. The morphology of a di-block BCP is governed by the Flory Huggins parameter χ, block length N, and volume fraction f.[1] Plotting the product χN versus f defines the classical phase diagram and maps out the equilibrium structures that form.[30,31] Significant theoretical and experimental work has been conducted to predict states of segregation and types of morphologies.[3,31–33] The microphase segregation of symmetric linear BCPs (f = 0.5) is considered within the strong segregation limit (SSL) when the product χN is above a critical limit ($\chi N > 10.5$), meaning the two domains are well-ordered and density distribution across the interface is high.[34] The equilibrium structure is driven by the minimization of interfacial area and reduction of chain stretching.[3] Therefore, symmetric systems with $f = 0.5$ tend to form lamellar morphologies, where the interface is flat. Pushing the volume fraction towards the asymmetric limits leads to a morphology transition from lamellar to cylindrical domains, and eventually to spherical domains, where the interfacial curvature is very high. The bi-continuous/gyroid morphology is accessed in a small band of volume fraction along the order-order transition (OOT).

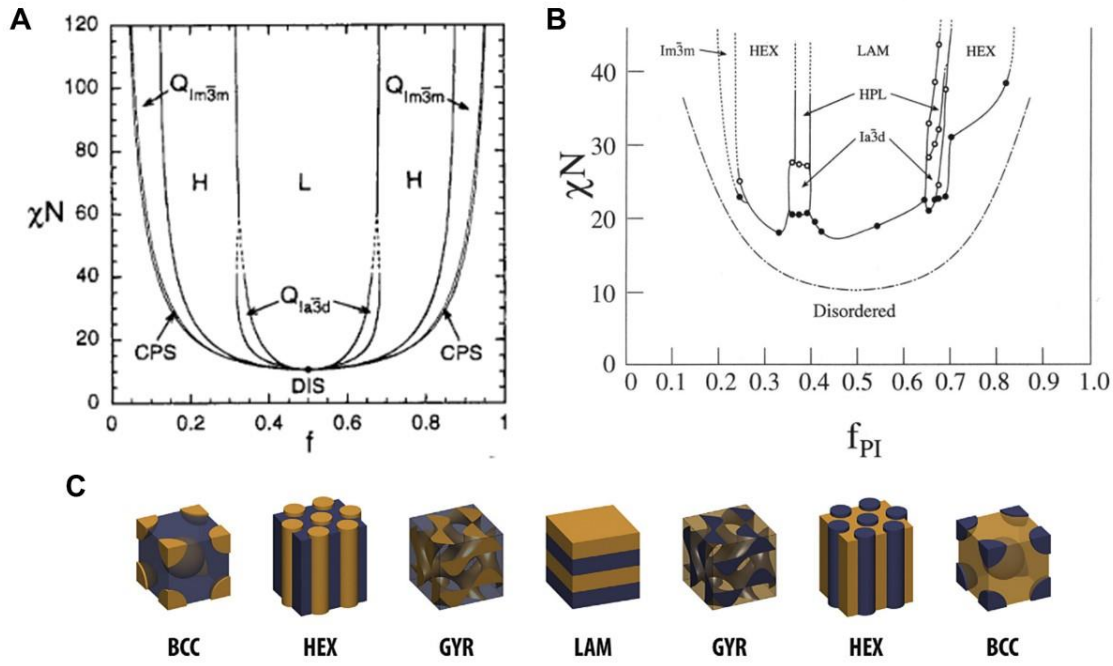

Figure 1.5. **(a)** Mean-field phase diagram for conformationally symmetric diblock melts. **(b)** χN versus *f* diagram for PI-PS diblock copolymers. Open and filled circles represent the order-order (OOT) and order-disorder (ODT) transitions. The dash-dot curve is the mean field prediction for the ODT. Solid curves have been drawn to delineate the different phases observed but might not correspond to precise phase boundaries. **(c)** Order-order transitions as a function of block volume fraction. (Modified from Ref 4,31, & 33)[4,31,33]

The volume fraction between each domain is important to consider especially once NPs are introduced to the system. NPs contribute additional volume as they are added to their respective domain. Therefore, NPs can be used to tune the overall volume fraction, pushing the system across the phase diagram while keeping the BCP template constant. Intermolecular interactions influence the vertical axis of the phase diagram through the overall χ of the system. Strong enthalpic interactions increase the effective χ (χ_{eff}) resulting in stronger segregation strength.[13]

The most commonly studied BCP template is the classic linear A-B di-block architecture. However, powerful synthetic approaches have been developed to build a suite of complex architectures and arrangement of the blocks.[2] Discrete block segments are

attached in many configurations, for example A-B-A or A-B-C linear tri-blocks, cyclic structures, or more recently branched, comb and star architectures.[2] The constraint and confinement from the covalent attachment is advantageously used to frustrate assembly and achieve highly curved interfaces and nontraditional morphologies. The customization and wide parameter space provides endless opportunities to design materials with characteristic lattice spacings from below 10 nm to over several hundreds of nanometers.

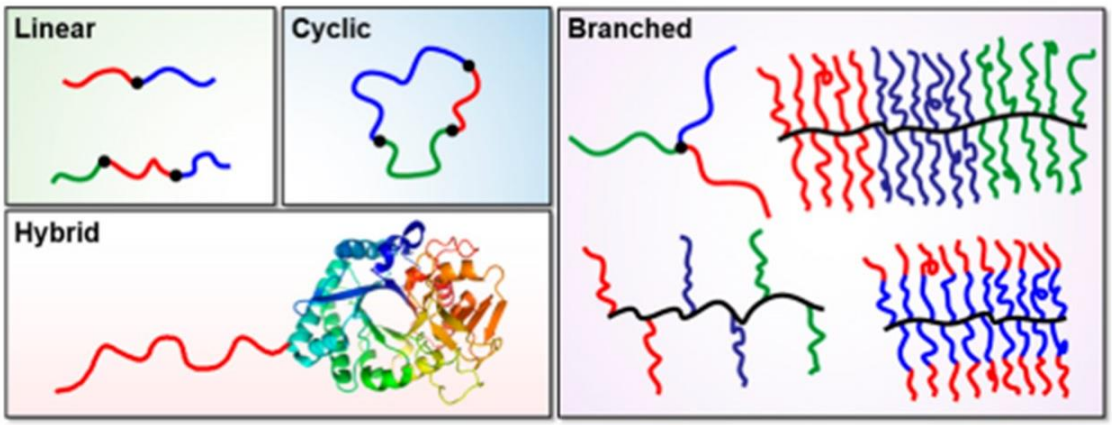

Figure 1.6. Illustration highlighting select examples of currently accessible molecular designs (Modified from Ref. 2)[2]

1.3 Structural Characterization Techniques

Specialized characterization techniques are required to determine the self-assembled structure (which is inherently heterogeneous) over a range of length scales. As previously described, the NP dispersion and assembly is of interest on the nanometer length scale. The ordering and assembly of the BCP template is typically on the order of 10 nm, while the long-range repetition of the pattern can persist up to one hundred nanometers or even micron scale. Certain lithography applications require assemblies with grain sizes of ordered structure on the order of several millimeters.[35]

Electron microscopy is used to obtain a real space view of the NP assembly. Thin slices of a nanocomposite are prepared for transmission electron microscopy (TEM) by

microtoming.[4] Contrast in the image arises from the difference in nuclear mass between the inorganic particles and the organic polymer matrix. Scanning electron microscopy (SEM) is primarily used to look at thin film surfaces or fractured bulk composites. TEM and SEM resolve structure from d_0 = 1 - 100 nm, but the data is not necessarily representative of the bulk, large volume assembly.

Scattering is another a powerful tool for determining the structure over a wide range of length scales. Scattering contrast arises from differences in scattering length density/electron density distribution, which is desirable for a NP embedded in a polymer matrix.[36,37] Understanding the structure of BCP morphology from scattering is well understood and established.[3,38,39] The structure is resolved from constructive scattering of the ordered morphology, which produces defined Bragg peaks. The relative position of the Bragg peaks (peak ratio) is used to resolve the morphology. However, the scattering signal from nanocomposites becomes convoluted from the multiple hierarchical features in the assembly and their independent long-range organization.

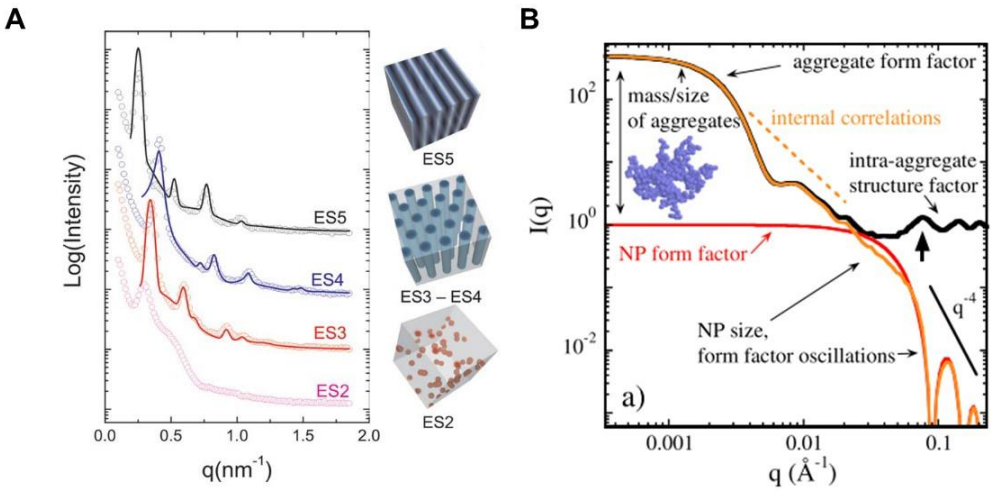

Figure 1.7 (a) Left: SAXS scattering profiles from the microphase separated samples at room temperature. Solid lines correspond to the fits of the experimental data to the theoretical scattering functions proposed by Forster et al. Right: schematic representation

of the different equilibrium structures observed here. **(b)** Illustration of scattering typical of NP aggregates. (Modified from Ref. 37 & 40)[37,40]

1.4 Rheological Characterization Techniques

While characterization techniques such as X-ray scattering, or electron microscopy are useful for direct structure determination, these tools resolve behavior under primarily static conditions, leaving out the dynamic description of the material. Rheology is utilized to determine such dynamic properties that are not accessible by other means. Rheology is the study of materials under flow and external deformation and is widely applied to polymeric materials within polymer science.[41,42] Rheology provides insight into the underlying interactions and relaxation processes between the NPs and BCP chain segments. The application of cooperative rheological and morphological characterization is desired to establishing meaningful structure-property relationships directed towards defining effective assembly and processing guidelines for these important nanomaterials.

Polymeric materials inherently exhibit a combination of both viscous and elastic behavior in response to applied stress and strain. The ability to both store and dissipate energy is such a manner is known as viscoelasticity.[42] Viscoelastic behavior is time dependent, meaning a material's response to stress and strain changes as a function of time. The relaxation modulus *G(t)* represents the relationship between stress and strain as a function of time.[42] However, this relationship assumes that small changes in stress correspond to small changes in strain (multiplied by the modulus), and that the small deformations do not perturb the structure of the material.[43] Therefore, the viscoelastic response is unaffected by the applied stress. With this assumption, *G(t)* becomes a very powerful parameter and can be used to describe all linear viscoelastic functions.[44] The nanostructure of NP/BCP composites may be fragile and susceptible to significant stress

deformations. Therefore, it is important to operate within the "linear viscoelastic regime" (LVR) to determine reliable structure-property relationships through *G(t)*.

Rheological measurements are performed in a rheometer, an instrument that applies precise stress (σ) and/or strain (γ) to the sample. This thesis focuses on rotational rheology in the shear deformation mode. Due to the inherent time dependence of the viscoelastic behavior, relaxation processes are characterized over a range of time scales by applying oscillatory shear deformations. The frequency of the oscillations is inversely proportional to the characteristic relaxation time being probed in the experiment.[42] Such measurements are referred to as small amplitude oscillatory shear (SAOS) when operated in the small deformation limit (or LVR). In an oscillatory experiment, the applied deformation (either stress or strain) is a time dependent sine function. The resulting material response is also a sine function with equivalent frequency. The phase shift (δ) between the input and output waveform is used to describe the intermediate between the elastic ($\delta = 0$) and viscous ($\delta = \pi/2$) limit, i.e. the viscoelasticity. The relationship between σ and γ (shear modulus G) is deconvoluted into two components; an in-phase contribution known as the storage modulus (G') and an out of phase contribution known as the loss modulus (G''). G' and G'' are represented as functions of frequency ($G'(\omega)$ and $G''(\omega)$) to incorporate the time dependence. A rheometer typically operates over a frequency range of three decades (ω = 0.1 – 100 rad/s), which is limiting and rarely covers the entire dynamic profile of a material. To obtain the full dynamic response over a wider frequency range, the time and temperature dependence of the viscoelasticity are correlated together (assuming the various relaxations in the material have similar temperature dependence).[45,46] This correlation is known as the Time-Temperature Superposition (tTS) principle. Materials that obey tTS are referred to

as “thermorheologically simple”. In 1955, Williams, Landel, and Ferry proposed an empirical method to describe the temperature dependence of the relaxations with respect to a reference temperature (T_0) through the shift factor a_T, resulting in the WLF equation.[47] WLF is the standard model used to determine shift factors at temperatures in the vicinity of the glass transition temperature (T_g). Unfortunately, the temperature dependence of shift factors $a_T(T)$ cannot be definitively predicted from molecular models (such as Rouse or Rouse-Bueche), so shifting of viscoelastic data must be carried out manually or objectively and fit to the WLF model.[45]

The linear viscoelasticity of linear BCPs is a rich field of research.[48–53] Considerable work has been presented establishing the rheological properties of many microphase-separated BCP systems, as well as assessing the impact of structural design parameters such as molecular weight, volume fraction, and morphology.[51,52] Microstructure and microphase segregation significantly impact the linear viscoelastic properties and the relaxation of structure across all accessible timescales.[52] In particular, the long range order of the morphology contributes to a low frequency plateau in $G'(\omega)$. Viscoelasticity persists to times scales much longer than that of the relaxations of individual chains. Therefore, there is no terminal relaxation pattern described by liquid like flow ($G'(\omega) \sim \omega^2$, $G''(\omega) \sim \omega^1$), which is characteristic of other entangled polymer melts or disordered systems. This plateau behavior is roughly dependent on the specific BCP morphology, which can be identified by the power law scaling of $G'(\omega)$ at the low frequency limit.[52] Phase transitions (such as order-to-disorder transitions (ODT)) are also sensitive to rheological characterization.[50,54] BCPs have fundamentally different viscoelastic responses above and below the microphase separation transition (MST).

Microphase segregated systems are highly viscoelastic, while disordered systems behave like viscous liquids in the terminal limit. Evidence of the ODT using dynamic mechanical analysis was presented in separate works by Bates and Han.[49,53–55] For example, poly(ethylene propylene)-*b*-poly(ethyl ethylene) (PEP-*b*-PEE) di-block copolymers exhibit a drastic drop in G^* upon heating through the MST.[49,53] Complementary frequency sweeps of $G'(\omega)$ and $G''(\omega)$ above and below the MST confirmed the low frequency scaling behaviors of the ordered and disordered states. The microstructure was identified with scattering techniques to confirm the ordering. Here, rheological characterization was coupled with conventional scattering experiments to resolve quintessential structure-property relationships.

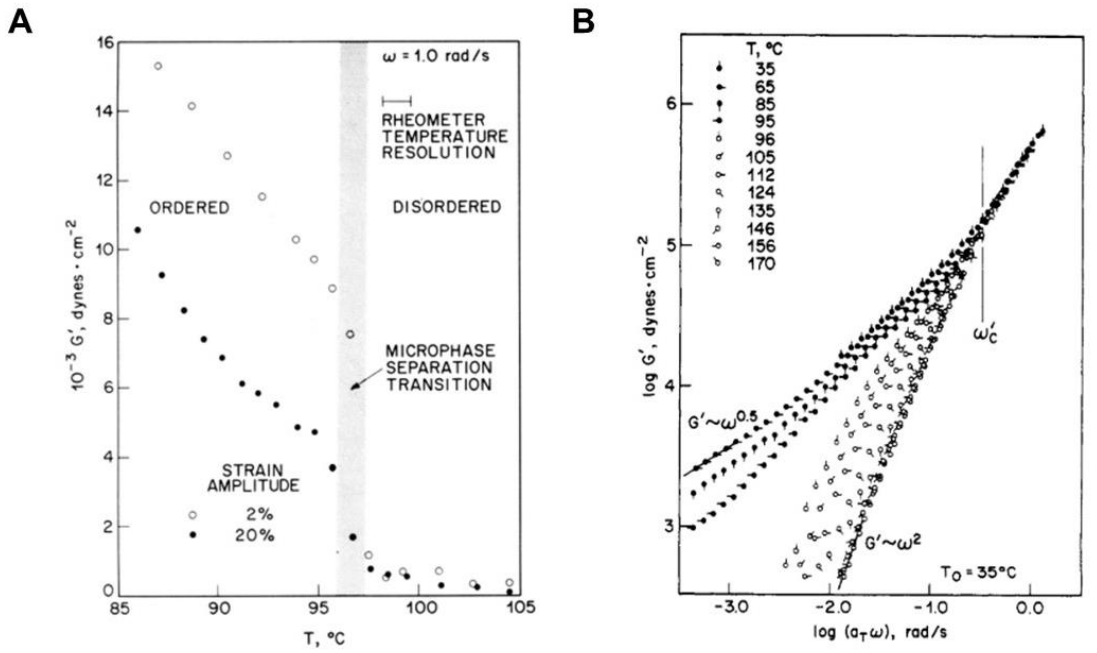

Figure 1.8 (**a)** Temperature dependence of G' obtained at two strain amplitudes and a single frequency (ω = 1.0 rad/s) while heating sample PEP-PEE. The discontinuity in G' at 96 °C results from the microphase separation transition. **(b)** Reduced frequency plot for representative dynamic elastic data obtained from sample PEP-PEE. Shift factors were determined by concurrently superimposing G' and G'' data for $\omega > \omega_{IC}$ and $\omega > \omega$" respectively. The filled and open symbols correspond to the ordered and disordered

states. Failure of time-temperature superposition for T = 196 °C derives from fluctuation effects. (Modified from Ref. 53)[53]

Naturally, nanocomposites also occupy a large thrust of the field of rheology. Rheology has been effectively used to establish mechanical enhancement in polymeric materials with the addition of NPs.[56–59] From a physical standpoint, NPs constrain native polymer chain relaxations through entropic effects. Previously discussed energetic constraints from intermolecular bonding can also impact the relaxation mechanism and timescales. A series of papers from Mendoza et al. illustrates the approach of using rheology to resolve dynamic behavior in PS-*b*-P4VP BCPs with Au NPs assembled in the P4VP domain.[60–63] Their approach utilized in-situ NP assembly from inorganic precursors. Structure-property relationships were established as a function of NP loading. Concentrations were relatively low (φ_{NP} < 10 vol.%) due to limitations of the fabrication approach. The NPs significantly impacted the segmental mobility of the PS and P4VP chains in the form of T_g shifts up to ΔT_g = 25 °C. The transition from the glassy plateau was also shifted to lower ω in dynamic measurements due to artificial filling of the P4VP domain. At exceptionally high-volume fractions of P4VP block (f ~ 0.24), the entanglement regime extends to the lowest accessible ω, suggesting the material did not relax because of the various topological constraints (entanglement, NPs, and enthalpic effects). The researchers were also able to align the nanostructures using oscillatory shear alignment, producing Au nanorods in a well ordered cylindrical array.[62]

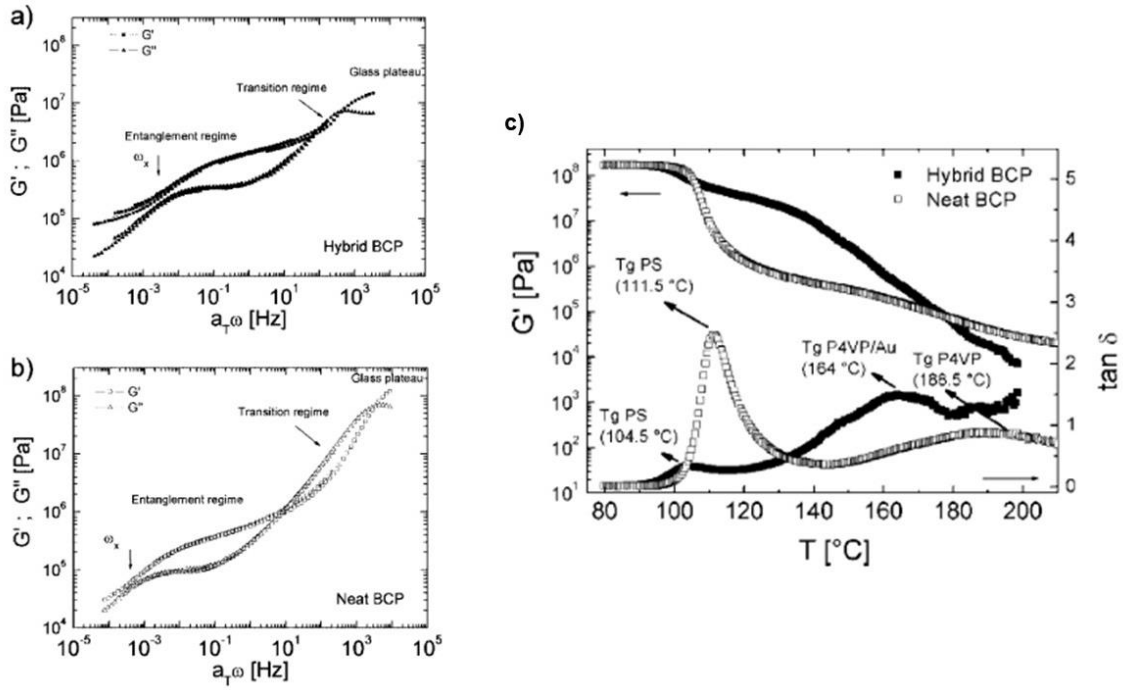

Figure 1.9 Master curves for storage (*G′*) and viscous moduli (*G″*) for **(a)** hybrid BCP PS-b-(P4VP/HAuCl4)$_{1.0}$ (filled symbols) and **(b)** neat material PS-b-P4VP (open symbols). Data were built using time-temperature superposition from frequency sweep tests at temperatures from 110 °C to 170 °C, with intervals of 10 °C each test. Reference temperature T_0 = 130 °C. **(c)** Isochronal temperature ramp in the linear viscoelastic regime. The elastic modulus (*G′*) and the loss tangent (*tan δ*) are shown for the hybrid PS-b-(P4VP/HAuCl4)$_{1.0}$ and neat block copolymers. Test conditions are as follows: strain amplitude of 0.5%, frequency of 1 Hz, and heating rate of 0.5 K/min. Note the shift in *Tg* for the hybrid system. (Modified from Ref. 60) [60]

1.5 Thesis Outline

The incorporation of high NP content into microphase separated BCPs with small domain spacing has remained a significant challenge. On the other end of the spectrum, achieving exceptionally large domain spacing is highly desired but also difficult due to kinetic frustrations from chain entanglements that arise at large MW. At such extreme limits, “unconventional” or “complex” BCP architectures are necessary. This thesis explores structure-property relationships in such materials through a cooperative approach of rheology and scattering characterization. Rheology is used to determine relaxation processes, viscoelastic behavior and mechanical properties, such as shear modulus (*G).*

Scattering is a powerful tool to observe temperature dependent phase behavior and phase transitions in the hierarchically assembled nanomaterials. The interplay between dynamics and structure will be evaluated, and structural/physical mechanisms will be proposed and discussed.

Chapter 2 describes the structural and rheological characterization of a NP/BCP system directed toward high loading of NPs (φ ~ 30 vol.%) and small domain spacing (d_0 ~ 10 nm) for applications in lithography and high energy density storage.[15,64] We utilize an additive driven assembly approach of low molecular weight BCP surfactants with small diameter surface functionalized zirconium dioxide (ZrO_2) NPs to satisfy strict design requirements. Our focus is on the impact of NPs on self-assembly dynamics and linear viscoelasticity in the highly loaded regime. In-situ SAXS and time resolved rheology are utilized to define the dynamics and mechanisms of structure development during thermal annealing. After self-assembly, temperature dependent morphology and linear viscoelastic behavior is characterized and discussed regarding the NP loading and extent of intermolecular interactions.

Chapters 3 – 5 considers a separate architecture of BCP focused on large domain spacings (d_0 ~ 100 nm) and rapid self-assembly (t ~ minutes) for applications in materials with enhanced and tunable optical and plasmonic properties. Here, the interplay between structure and dynamics is investigated in microphase separated bottlebrush block copolymer (BBCPs) and their NP composite counterparts. BBCPs are macromolecules with discrete blocks of densely grafted side chains tethered to a molecular backbone. Highly extended backbone conformations and significant repulsion between grafted side chains suppress chain entanglements in the melt. Chapter 3 details a systematic

investigation of the viscoelastic behavior in poly(styrene)-*block*-poly(ethylene oxide) PS-*b*-PEO BBCPs. The phase behavior is characterized as a function of block composition and overall backbone degree of polymerization. The BBCPs are compared to complementary linear BCPs (LBCP) to understand the impact of the brush architecture on the dynamics of self-assembly and mechanical properties. Finally, the relaxation processes of the BBCPs are described by a new model for the relaxation time spectrum $H(\tau)$.

The brush architecture lends itself to displaying interesting behavior under controlled shear processing. Chapter 4 explores the impact of applied shear on the directed alignment and orientation of lamellae in microphase separated BBCPs through a combination of parallel plate oscillatory shear and ex-situ transmission SAXS. Strong alignment of the lamellar domains is achieved along the shear direction with varying degrees of global orientation and grain quality under controlled shearing conditions. Alignment over several mm^3 is realized by high throughput synchrotron experiments. Here, we take our understanding of polymer processing and combine it with the structure-property relationships developed in Chapter 3 to develop an industrially relevant processing protocol.

Chapter 5 returns the focus to NP composites, specifically NP/BBCP composites fabricated through co-assembly approaches developed in our group. The objective is to understand how the addition of NPs, hydrogen bonding interactions, and the phase behavior effects the unique relaxation dynamics in BBCPs. Temperature controlled SAXS is used to determine phase transitions in the melt state, and rheology is used to define systematic transitions in the relaxation features and characteristic timescales as a function of NP loading. The NPs potentially inhibit the highly mobile structure and chain relaxations

inherent to the brush architecture. The consequences on future material processing and optimization of mechanical properties are discussed.

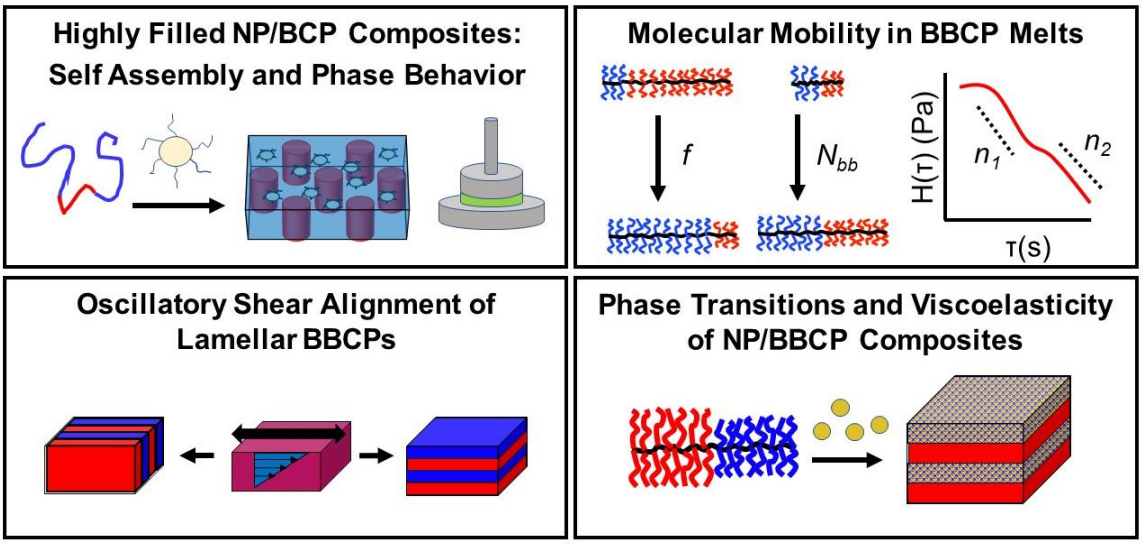

Figure 1.10 Thesis overview

1.6 References

(1) Bates, F. S.; Fredrickson, G. H. Block Copolymers—Designer Soft Materials. *Phys. Today* **1999**, *52* (2), 32.

(2) Bates, C. M.; Bates, F. S. 50th Anniversary Perspective : Block Polymers—Pure Potential. *Macromolecules* **2017**, *50* (1), 3–22.

(3) Bates, F. S.; Fredrickson, G. H. Block Copolymer Thermodynamics: Theory and Experiment. *Annu. Rev. Phys. Chem.* **1990**, *41* (1), 525–557.

(4) Hoheisel, T. N.; Hur, K.; Wiesner, U. B. Block Copolymer-Nanoparticle Hybrid Self-Assembly. *Prog. Polym. Sci.* **2015**, *40*, 3–32.

(5) Yoo, M.; Kim, S.; Bang, J. Design and Fabrication of Thermally Stable Nanoparticles for Well-Defined Nanocomposites. *J. Polym. Sci. Part B Polym. Phys.* **2013**, *51* (7), 494–507.

(6) Jones, M. R.; Osberg, K. D.; MacFarlane, R. J.; Langille, M. R.; Mirkin, C. A. Templated Techniques for the Synthesis and Assembly of Plasmonic Nanostructures. *Chem. Rev.* **2011**, *111* (6), 3736–3827.

(7) Pletsch, H.; Tebbe, M.; Dulle, M.; Forster, B.; Fery, A.; Forster, S.; Greiner, A.; Agarwal, S. Reversible Gold Nanorod Alignment in Mechano-Responsive Elastomers. *Polymer (Guildf).* **2015**, *66*, 167–172.

(8) Bockstaller, M. R.; Mickiewicz, R. A.; Thomas, E. L. Block Copolymer Nanocomposites: Perspectives for Tailored Functional Materials. *Adv. Mater.* **2005**, *17* (11), 1331–1349.

(9) Sarkar, B.; Alexandridis, P. Block Copolymer–nanoparticle Composites: Structure, Functional Properties, and Processing. *Prog. Polym. Sci.* **2015**, *40*, 33–62.

(10) Ciebien, J. F.; Clay, R. T.; Sohn, B. H.; Cohen, R. E. Brief Review of Metal Nanoclusters in Block Copolymer Ðlms S. *New J. Chem.* **1998**, 685–691.

(11) Lin, Y.; Boker, A.; He, J.; Sill, K.; Xiang, H.; Abetz, C.; Li, X.; Wang, J.; Emrick, T.; Long, S.; et al. Self-Directed Self-Assembly of Nanoparticle / Copolymer Mixtures. *Nature* **2005**, *404*, 55–59.

(12) Kao, J.; Thorkelsson, K.; Bai, P.; Rancatore, B. J.; Xu, T. Toward Functional Nanocomposites: Taking the Best of Nanoparticles, Polymers, and Small Molecules. *Chem. Soc. Rev.* **2013**, *42* (7), 2654–2678.

(13) Lin, Y.; Daga, V. K.; Anderson, E. R.; Gido, S. P.; Watkins, J. J. Nanoparticle-Driven Assembly of Block Copolymers: A Simple Route to Ordered Hybrid Materials. *J. Am. Chem. Soc.* **2011**, *133*, 6513–6516.

(14) Rajan, G. S.; Mauritz, K. A.; Stromeyer, S. L.; Kwee, T.; Mani, P.; Weston, J. L.; Nikles, D. E.; Shamsuzzoha, M. Poly(Styrene-b-Ethylene/Butylene-b-Styrene)/Cobalt Ferrite Magnetic Nanocomposites. *J. Polym. Sci. Part B Polym. Phys.* **2005**, *43* (12), 1475–1485.

(15) Garcia, C. B. W.; Zhang, Y.; Mahajan, S.; DiSalvo, F.; Wiesner, U. B. Self-Assembly Approach toward Magnetic Silica-Type Nanoparticles of Different Shapes from Reverse Block Copolymer Mesophases. *J. Am. Chem. Soc.* **2003**, *125* (44), 13310–13311.

(16) Warren, S. C.; Messina, L. C.; Slaughter, L. S.; Kamperman, M.; Zhou, Q.; Gruner, S. M.; DiSalvo, F. J.; Wiesner, U. B. Ordered Mesoporous Materials from Metal Nanoparticle-Block Copolymer Self-Assembly. *Science* **2008**, *320* (5884), 1748–1752.

(17) Yin, D.; Horiuchi, S.; Masuoka, T. Lateral Assembly of Metal Nanoparticles Directed by Nanodomain Control in Block Copolymer Thin Films. *Chem. Mater.* **2005**, *17* (3), 463–469.

(18) Song, D.-P.; Li, C.; Li, W.; Watkins, J. J. Block Copolymer Nanocomposites with High Refractive Index Contrast for One-Step Photonics. *ACS Nano* **2016**, *10* (1), 1216–1223.

(19) Gai, Y.; Lin, Y.; Song, D.-P.; Yavitt, B. M.; Watkins, J. J. Strong Ligand–Block Copolymer Interactions for Incorporation of Relatively Large Nanoparticles in Ordered Composites. *Macromolecules* **2016**, *49* (9), 3352–3360.

(20) Chiu, J. J.; Kim, B. J.; Kramer, E. J.; Pine, D. J. Control of Nanoparticle Location in Block Copolymers. *J. Am. Chem. Soc.* **2005**, *127* (14), 5036–5037.

(21) Chiu, J. J.; Kim, B. J.; Yi, G. R.; Bang, J.; Kramer, E. J.; Pine, D. J. Distribution of Nanoparticles in Lamellar Domains of Block Copolymers. *Macromolecules* **2007**, *40* (9), 3361–3365.

(22) Kim, B. J.; Bang, J.; Hawker, C. J.; Kramer, E. J. Effect of Areal Chain Density on the Location of Polymer-Modified Gold Nanoparticles in a Block Copolymer Template. *Macromolecules* **2006**, *39* (12), 4108–4114.

(23) Bockstaller, M. R.; Lapetnikov, Y.; Margel, S.; Thomas, E. L. Size-Selective Organization of Enthalpic Compatibilized Nanocrystals in Ternary Block Copolymer/Particle Mixtures. *J. Am. Chem. Soc.* **2003**, *125* (18), 5276–5277.

(24) Mendes, A. C.; Baran, E. T.; Reis, R. L.; Azevedo, H. S. Self-Assembly in Nature: Using the Principles of Nature to Create Complex Nanobiomaterials. *Wiley Interdiscip. Rev. Nanomedicine Nanobiotechnology* **2013**, *5* (6), 582–612.

(25) Van Ruymbeke, E. Preface: Special Issue on Associating Polymers. *J. Rheol. (N. Y. N. Y).* **2017**, *61* (6), 1099–1102.

(26) Jang, S. G.; Khan, A.; Hawker, C. J.; Kramer, E. J. Morphology Evolution of PS- b -P2VP Diblock Copolymers via Supramolecular Assembly of Hydroxylated Gold Nanoparticles. *Macromolecules* **2012**, *45*, 1553–1561.

(27) Jang, S. G.; Kramer, E. J.; Hawker, C. J. Controlled Supramolecular Assembly of Micelle-Like Gold Nanoparticles in PS- b -P2VP Diblock Copolymers via Hydrogen Bonding. *J. Am. Chem. Soc.* **2011**, *133*, 16986–16996.

(28) Song, D.-P.; Lin, Y.; Gai, Y.; Colella, N. S.; Li, C.; Liu, X.-H.; Gido, S. P.; Watkins, J. J. Controlled Supramolecular Self-Assembly of Large Nanoparticles in Amphiphilic Brush Block Copolymers. *J. Am. Chem. Soc.* **2015**, *137* (11), 3771–3774.

(29) Di Mauro, A. E.; Villone, V.; Ingrosso, C.; Corricelli, M.; Oria, L.; Pérez-Murano, F.; Agostiano, A.; Striccoli, M.; Curri, M. L. H-Bonding Driven Assembly of Colloidal Au Nanoparticles on Nanostructured Poly(Styrene-b-Ethylene Oxide) Block Copolymer Templates. *J. Mater. Sci.* **2014**, *49* (15), 5246–5255.

(30) Bates, F. S.; Schulz, M. F.; Khandpur, A. K.; Förster, S.; Rosedale, J. H.; Almdal, K.; Mortensen, K. Fluctuations, Conformational Asymmetry and Block Copolymer Phase Behaviour. *Faraday Discuss.* **1994**, *98*, 7–18.

(31) Khandpur, A. K.; Förster, S.; Bates, F. S.; Hamley, I. W.; Ryan, A. J.; Bras, W.; Almdal, K.; Mortensen, K. Polyisoprene-Polystyrene Diblock Copolymer Phase Diagram near the Order-Disorder Transition. *Macromolecules* **1995**, *28* (26), 8796–8806.

(32) Leibler, L. Theory of Microphase Separation in Block Copolymers. *Macromolecules* **1980**, *13* (6), 1602–1617.

(33) Matsen, M. W.; Bates, F. S. Unifying Weak- and Strong-Segregation Block Copolymer Theories. *Macromolecules* **1996**, *29* (4), 1091–1098.

(34) Semenov, A. N. Contribution to the Theory of Microphase Layering in Block-Copolymer Melts. *Zh. Eksp. Teor. Fiz* **1985**, *88* (4), 1242–1256.

(35) Song, D.-P.; Li, C.; Colella, N. S.; Xie, W.; Li, S.; Lu, X.; Gido, S. P.; Lee, J.-H.; Watkins, J. J. Large-Volume Self-Organization of Polymer/Nanoparticle Hybrids with Millimeter-Scale Grain Sizes Using Brush Block Copolymers. *J. Am. Chem. Soc.* **2015**, *137*, 12510–12513.

(36) Genix, A.-C.; Oberdisse, J. Nanoparticle Self-Assembly: From Interactions in Suspension to Polymer Nanocomposites. *Soft Matter* **2018**, *14*, 5161–5179.

(37) Genix, A.-C.; Oberdisse, J. Structure and Dynamics of Polymer Nanocomposites Studied by X-Ray and Neutron Scattering Techniques. *Curr. Opin. Colloid Interface Sci.* **2015**, *20* (4), 293–303.

(38) Shibayama, M.; Hashimoto, T.; Kawai, H. Ordered Structure in Block Polymer Solutions. 1. Selective Solvents. *Macromolecules* **1983**, *16*, 16–28.

(39) Okamoto, S.; Saijo, K.; Hashimoto, T. Real-Time SAXS Observations of Lamella-Forming Block Copolymers under Large Oscillatory Shear Deformation. *Macromolecules* **1994**, *27* (20), 5547–5555.

(40) Ninago, M. D.; Satti, A. J.; Ciolino, A. E.; Valles, E. M.; Villar, M. A.; Vega, D. A.; Sanz, A.; Nogales, A.; Rueda, D. R. Synthesis and Morphology of Model PS-b-PDMS Copolymers. *J. Polym. Sci. Part A Polym. Chem.* **2010**, *48*, 3119–3127.

(41) Tadmor, Z.; Gogos, C. G. *Principles of Polymer Processing - 2nd Ed.*; 2006.

(42) Macosko, C. W. *Rheology: Principles, Measurements, and Applications*; Wiley VCH: New York, 1994.

(43) Winter, H. H.; Mours, M. Rheology of Polymers near Liquid-Solid Transitions. *Adv. Polym. Sci.* **1997**, *134*, 165–234.

(44) Winter, H. H. Glass Transition as the Rheological Inverse of Gelation. *Macromolecules* **2013**, *46* (6), 2425–2432.

(45) Dealy, J. M.; Plazek, D. Time-Temperature Superposition—a Users Guide. *Rheol. Bull* **2009**, *78* (2), 16–21.

(46) van Gurp, M.; Palmen, J. Time-Temperature Superposition for Polymeric Blends. *J Rheol Bull* **1998**, *65*, 5–8.

(47) Williams, M. L.; Landel, R. F.; Ferry, J. D. The Temperature Dependence of Relaxation Mechanisms in Amorphous Polymers and Other Glass-Forming Liquids1. *J. Am. Chem. Soc.* **1955**, *679* (12), 3701–3707.

(48) Mortensen, K.; Almdal, K.; Bates, F. S.; Koppi, K. A.; Tirrell, M. V.; Nordén, B. Shear Devices for in Situ Structural Studies of Block-Copolymer Melts and Solutions. *Phys. B Phys. Condens. Matter* **1995**, *213–214* (C), 682–684.

(49) Bates, F. S. Block Copolymers near the Microphase Separation Transition. 2. Linear Dynamic Mechanical Properties. *Macromolecules* **1984**, *17* (12), 2607–2613.

(50) Fredrickson, G. H.; Bates, F. S. Dynamics of Block Copolymers: Theory and Experiment. *Annu. Rev. Mater. Sci.* **1996**, *26* (1), 501–550.

(51) Colby, R. H. Block Copolymer Dynamics. *Curr. Opin. Colloid Interface Sci.* **1996**, *1*, 454–465.

(52) Colby, R. H. Melt Rheology of Block Copolymers. In *Encyclopedia of Materials: Science and Technology*; 2001; pp 727–730.

(53) Rosedale, J. H.; Bates, F. S. Rheology of Ordered and Disordered Symmetric Poly(Ethylenepropylene)-Poly(Ethylethylene) Diblock Copolymers. *Macromolecules* **1990**, *23* (8), 2329–2338.

(54) Han, C. D.; Kim, J. Rheological Technique for Determining the Order-Disorder Transition of Block Copolymers. *J. Polym. Sci. Part B Polym. Phys.* **1987**, *25* (8), 1741–1764.

(55) Han, C. D.; Kim, J.; Kim, J. K. Determination of the Order-Disorder Transition Temperature of Block Copolymers. *Macromolecules* **1989**, 383–394.

(56) Srivastava, S.; Shin, J. H.; Archer, L. A. Structure and Rheology of Nanoparticle–polymer Suspensions. *Soft Matter* **2012**, *8* (15), 4097.

(57) Kim, D.; Srivastava, S.; Narayanan, S.; Archer, L. A. Polymer Nanocomposites: Polymer and Particle Dynamics. *Soft Matter* **2012**, *8* (42), 10813.

(58) Kumar, S. K.; Krishnamoorti, R. Nanocomposites: Structure, Phase Behavior, and Properties. *Annu. Rev. Chem. Biomol. Eng.* **2010**, *1*, 37–58.

(59) Akcora, P.; Kumar, S. K.; Moll, J. F.; Lewis, S.; Schadler, L. S.; Li, Y.; Benicewicz, B. C.; Sandy, A.; Narayanan, S.; Ilavsky, J.; et al. "Gel-like" Mechanical Reinforcement in Polymer Nanocomposite Melts. *Macromolecules* **2010**, *43* (2), 1003–1010.

(60) Mendoza, C.; Pietsch, T.; Gutmann, J. S.; Jehnichen, D.; Gindy, N.; Fahmi, A. Block Copolymers with Gold Nanoparticles: Correlation between Structural Characteristics and Mechanical Properties. *Macromolecules* **2009**, *42* (4), 1203–

1211.

(61) Mendoza, C.; Gindy, N.; Wilhelm, M.; Fahmi, A. Linear and Non-Linear Viscoelastic Rheology of Hybrid Nanostructured Materials from Block Copolymers with Gold Nanoparticles. *Rheol. Acta* **2011**, *50* (3), 257–275.

(62) Mendoza, C.; Pietsch, T.; Gindy, N.; Fahmi, A. Fabrication of 3D-Periodic Ordered Metallic Nanoparticles in a Block Copolymer Bulk Matrix via Oscillating Shear Flow. *Adv. Mater.* **2008**, *20* (6), 1179–1184.

(63) Mendoza, C.; Gindy, N.; Gutmann, J. S.; Frömsdorf, A.; Förster, S.; Fahmi, A. In Situ Synthesis and Alignment of Au Nanoparticles within Hexagonally Packed Cylindrical Domains of Diblock Copolymers in Bulk. *Langmuir* **2009**, *25* (16), 9571–9578.

(64) Cushen, J. D.; Otsuka, I.; Bates, C. M.; Halila, S.; Fort, S.; Rochas, C.; Easley, J. A.; Rausch, E. L.; Thio, A.; Borsali, R.; et al. Oligosaccharide/Silicon-Containing Block Copolymers with 5 Nm Features for Lithographic Applications. *ACS Nano* **2012**, *6* (4), 3424–3433.

CHAPTER 2

HIGHLY LOADED NP/BCP COMPOSITES via. ADDITIVE DRIVEN ASSEMBLY: SELF-ASSEMBLY DYNAMICS, MATERIAL PROPERTIES, AND PHASE TRANSITIONS

2.1 Introduction & Project Motivation

Precise control over the organization and assembly of NPs within BCP templates has been demonstrated but the desire for high concentrations of nanoparticles in a specific domain has remained a challenge. In some systems, the high loading of NPs is achieved by enthalpically favored interactions between the NPs and the BCP chain segments that offset the entropic penalty of the chain stretching, leading to increased sequestration of NP into the desired BCP domain up to 30 vol. %.[1,2] The high loading of NPs, as well as the introduction of additional intermolecular interactions, places extra constraints (topologically and energetically) on the mobility and relaxation behavior of the polymer chain segments. Such affects will have a significant impact on the melt flow and rheological properties of the material and should be taken into consideration when discussing the mechanical properties, proccessability, and fabrication of these materials.[3,4] Attention to the drastic difference in modulus between the components of the composite is also important as polymeric materials are much softer than inorganic materials by several orders of magnitude in modulus.[5] The addition of hard NPs to a soft polymer matrix leads to a large increase in the magnitude of overall modulus and viscosity, which can be advantageous for tuning mechanical properties or disadvantageous to processing of the materials. The properties are optimized by controlled the NP concentration and understanding the underlying physics of the polymer-particle interactions.

Multiple material systems utilizing hydrogen bond driven co-assembly were discussed and referenced in Chapter 1. Here, we focus on this intermolecular approach to develop composites with small domain spacings (d_0 ~ 10 nm) and large volume fraction of NP fillers (φ_{NP} ~ 30 vol. %). Densely filled, well-ordered materials are desirable for applications requiring small feature sizes, such as lithography or high density energy and memory storage.[6,7] We focus on the combination of low molecular weight (MW) BCP matrices with multifunctional surface functionalized NP such that segment specific interactions between the NP and one block of the BCP yield a highly filled and well-ordered material. As previously described, the ordering and morphology is governed by relative volume fractions of the BCP, as well as the product χN. χ_{eff} is increased through hydrogen bonding interactions with a specific BCP, leading to enhanced phase segregation in the BCP system while still maintaining small domain sizes due to small N.[2] The phase behavior is rich, and the morphologies of the phase diagram are traversed by changing the volume fraction of the NP filled domain. The intermolecular interaction strength and surface density of functional groups influence the phase behavior and material properties of these systems.[2,8–10] The unique ability to control the ordering in these materials makes them ideal templates for many nanotechnology applications.

Our approach is referred to as *additive driven assembly*. One of the first demonstrations of additive driven assembly of low χN materials was through induced ordering of commercial poly(ethylene oxide)-*block*-poly(propylene oxide)-*block*-poly(ethylene oxide) (PEO-*b*-PPO-*b*-PEO) surfactants (Trade name "Pluronic") by the addition of short chain homopolymer poly(acrylic acid) (PAA).[11–13] The favorable hydrogen bond interactions between pennant carboxylic acids on PAA and the ether

oxygen in the PEO backbone resulted in an increased χ_{eff} which produced microphase segregation between the BCP domains of various ordered morphologies with d_0 as low as 5 nm.[12] The morphology was directly impacted by the BCP volume fraction and PAA MW. Small molecule (SM) acids will also induce assembly in Pluronic materials through a similar mechanism. Additives with hydrogen bond donating pennant groups, such as benzene hexacarboxylic acid (BHCA) and benzene hexol (HHB) were shown to drive Pluronic F108 into an ordered cylindrical hexagonal packed morphology at loadings of additive up to 30 wt.%.[10] Upon further loading, an order-to-order transition (OOT) to spherical morphology was observed. Eventually, inorganic based additives, such as surface functionalized NPs, were shown to drive assembly in low *N* poly(stryrene)-*block*-poly(ethylene oxide) (PS-*b*-PEO), Pluronic F108, and F127.[2,7] Functionalized Polyhedral Oligomeric Silsesquioxane (POSS) with hydrogen bonding capability have also been used.[14] The inorganic fillers are of particular interest and provides an opportunity to develop functional materials with a wide array of enhanced properties dependent on the intrinsic property of the additive.

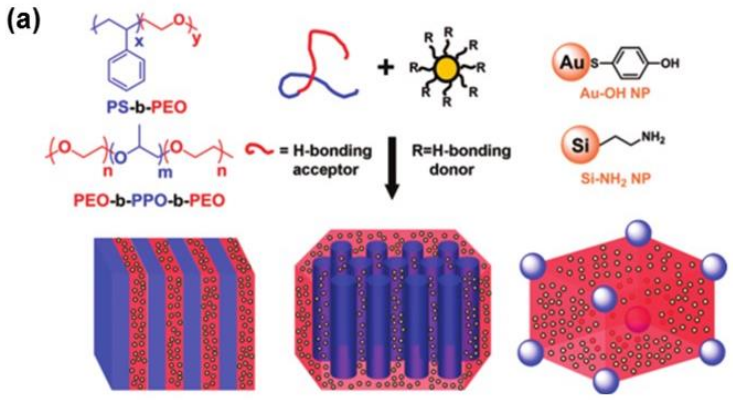

Figure 2.1 Schematic representation of NP-driven Assembly of BCPs via H-bonding. (Modified from Ref. 2)[2]

More recently, SAOS measurements were used to investigate OOT and ODT in the SM/Pluronic composite systems.[15] Multiple carboxylic acid and hydroxyl functionalized benzoic derivatives were blended with Pluronic F108 to induce microphase separation between the PEO and PPO domains. The number of functional groups per SM was varied from one group (benzoic acid) to six groups (BHCA). ODTs were detected by significant decreases in $G'(\omega)$ during heating at 5 °C intervals from T = 70 °C to above T = 160 °C. The T_{ODT} increased with increased loading of small molecules, and saturated at loadings up to 30 wt. % (T_{ODT} = 140 °C). Overall, the T_{ODT} was found to vary widely with the type of additive but scaled systematically with number, position, and variety of functional groups. BHCA was shown to increase T_{ODT} the most. The increase in T_{ODT} is directly related to an increase in microphase segregation strength, or the effective increase in χ due to the introduction of the additive. Through this study, protocols for investigating rheological properties and phase transitions in additive driven assembly materials using SAOS were established.

In this chapter, we will use rheological characterization to investigate the material properties and phase transitions of such model NP/BCP composites with high volume fraction of NP. We are interested in drawing connections between the macroscale properties and microscale structure. Rheology can be used to determine phase transitions (such as the ODT), chain relaxation dynamics, liquid-solid transitions, and mechanical properties in these systems not accessible by scattering or microscopy. X-ray scattering will be used to determine the internal structure of the NP distribution and BCP morphology, which will be correlated to the macroscale mechanical response. Our aim is to observe the dynamics of self-assembly using time-resolved SAXS and rheology techniques. We

hypothesize an ODT will occur at high temperatures due to the inverse temperature dependence of both the intermolecular interactions strength and χ. SAOS will be used to determine the impact of NP loading on the viscoelasticity in the ordered and disordered state. We hope to develop a better understanding of the nature of interactions between the NP and the coordinating block of the BCP. Additionally, understanding the temperature dependent behavior of the composites is critical to developing guidelines for practical use. The knowledge gained from this investigation will be required for future design and development of novel hybrid nanocomposites based on BCP/NP materials.

2.2 Experimental

2.2.1 Material Selection

A model additive driven assembly system is essential for this investigation. It is important to adhere to strict material design criteria, especially when considering the rheological experiments, which require large amounts of bulk material for characterization. Consequently, it is necessary to obtain large sample quantities (hundreds of milligrams) of the BCP matrix. Low χ, low N is necessary so that the neat BCP is initially disordered and below the critical microphase segregation limit. Finally, one of the blocks of the BCP must exhibit hydrogen bond accepting capability. Pluronic F108 and F127 fit all design criteria and were extensively used in previous studies as BCP templates.[2,10,14]

The selection criteria for the inorganic NP are much stricter. The diameter of the NP (d_{NP}) is the most important. The NPs are primarily confined within the major domain of the BCP template, which is on the order of $d_0 \sim 10$ nm for such low N materials. If the particles are too large ($d_{NP} > d_0$), the entropic penalty of chain stretching will be too high and the NPs will not disperse in the domain.[16] Rather, they will aggregate together,

preventing the self-assembly of the BCP structure. The radius of gyration (R_g) of the polymer chain must be commensurate to the size of the particle.[17–19] For Pluronic F108 and F127, R_g is approximately ~ 5 nm.[2] Therefore, to maximize NP loading, d_{NP} must be less than 5 nm. The next criterion is the presence of surface ligands on the NP. The assembly of the composite is driven by the enthalpic contribution of favorable hydrogen bonding between the NP and the hydrogen bond accepting block of the polymer. The ideal NP must have adequate surface coverage of organic ligands with polar groups for hydrogen bond donation (-OH, -COOH, -NH_2). Finally, due to the high loadings of filler, hundreds of milligram scale quantities are necessary. The best candidates for additive filler materials are batch-synthesized surface functionalized metal oxide NP, as well as functionalized POSS additives. Both systems are commercially available and could be utilized for this study.

We use the following material system suggested by the material design parameters: poly(ethylene oxide)-*block*-poly(propylene oxide)-*block*-poly(ethylene oxide) (PEO-*b*-PPO-*b*-PEO) triblock copolymer (Pluronic F127, M_n ~ 12 kg/mol, f_{PEO} = 0.7) was supplied by BASF and used as received. Zirconium Oxide (ZrO_2) Nanocrystals (sPCNI-15-PMA) were purchased from Pixelligent, Inc. ZrO_2 NP were received as a 15 wt. % dispersion in propylene glycol monomethyl ether acetate (PGMEA). In certain cases, PEO homopolymer (M_n = 10 kg/mol) was bought from Sigma Aldrich and used as received.

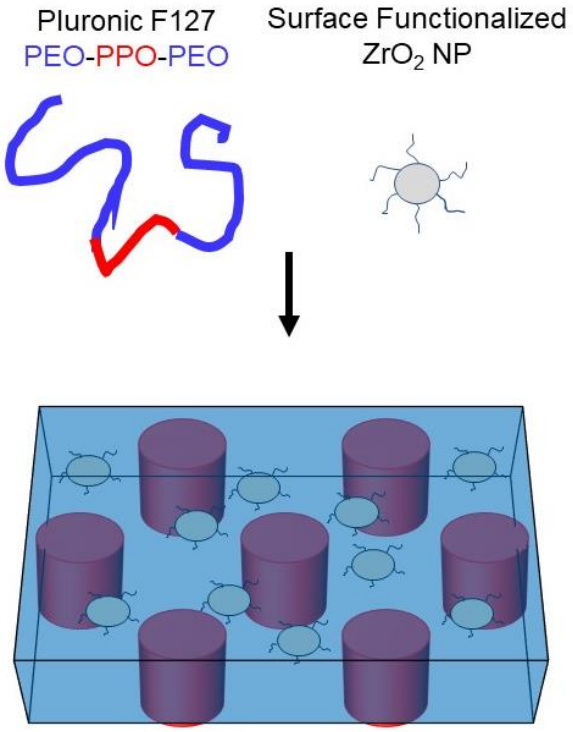

Figure 2.2 Schematic of proposed additive driven self-assembly of low χN Pluronic F127 with surface functionalized ZrO_2 NPs. NPs assemble in the major domain (PEO) in blue and microphase segregate from the minor PPO domain in red

2.2.2 Sample Preparation

Stock ZrO_2 NPs are solvent exchanged to a 5 wt.% solution in tetrahydrofuran (THF) by fully evaporating PGMEA under nitrogen environment and re-dispersing in THF (assisted by ultrasonication). NP/BCP composites are fabricated by mixing appropriate amounts of ZrO_2 in THF solution with a 5 wt.% solution of F127 in THF at separate nanoparticle loadings of 0, 10, 20, 30, and 40 wt.%. Here, wt.% is defined as total mass of NP with respect to the total composite solids mass. Relative mass and volume compositions with respect to all F127 or PEO content are calculated and reported in Table 2.1. The total solid mass per sample is approximately 300 mg. The solutions are stirred with magnetic stir bar and assisted heat until they became homogenous. Solutions are drop cast by syringe through a 0.45 um PTFE syringe filter into a 60 mm glass petri dish. Films are dried at

room temperature over several days, followed by additional drying with nitrogen purge. Once all the solvent has evaporated, the bulk films are removed by razor blade.

Samples are further prepared for various characterizations techniques. Bulk material is used to form 20 mm diameter circular samples for rheological characterization. Sections of film are placed in a mold on hot plate (T = 70 °C) and melt pressed to shape. Samples for small angle X-ray scattering (SAXS) measurement are prepared with similar protocol by pressing bulk material into a 0.5 mm thick metal washer and sealed with Kapton tape.

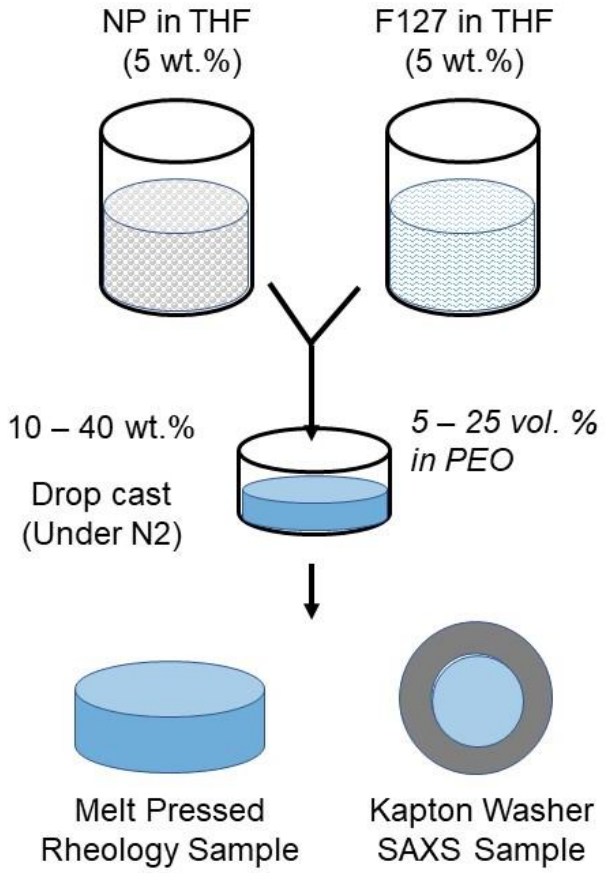

Figure 2.3 NP/BCP composite samples preparation by drop-casting well dispersed solutions of variable NP contents, followed by melt pressing into two sample geometries for rheology and SAXS characterization.

Table 2.1 Various compositions of NP loading in BCP composite

Weight %	Volume %	Weight % in PEO domain	Volume % in PEO domain
10	3.9	13.7	5.4
20	8.3	26.3	11.4
30	13.4	34	18.1
40	19.4	48.8	25.6

2.2.3 Characterizations

The size and dispersion of ZrO_2 NPs are characterized by *Transmission Electron Microscopy* (TEM, JEOL 2000FX, 200 kV) by drop casting a dilute NP solution (0.5 mg/ml) onto a thin carbon film supported by a copper grid. Size distributions are analyzed with Image J software. *Fourier Transform Infrared Spectroscopy* (FTIR, Perkin Elmer 2000) is performed over a range of wavenumber from υ = 4000 cm^{-1} to 650 cm^{-1} to identify functional groups within the organic ligands on surface coated NP. A NP solution of 3 mg/ml is drop cast onto sample stage while nitrogen is used to dry off excess solvent. *Thermogravimetric Analysis* (TGA, TA Instrument Q50) is used to measure the mass fraction of inorganic core by heating from T = 25 °C to 700 °C at 10 °C/min under nitrogen flow. *Differential Scanning Calorimetry* (DSC, TA Instruments Q200) heating-cooling-heating cycles from T = -60 to 160 °C at 10 °C/min are used to determine thermal transitions such as crystallization and melting.

Morphology, domain spacing (d_0), and NP dispersion & structure are characterized by small angle X-ray scattering (SAXS) and wide angle X-ray scattering (WAXS) on a Ganesha SAXS-Lab with Cu Kα 0.154 nm line. Domain spacings $d_0 = 2\pi/q^*$ are determined from q^* = primary peak position in nm^{-1}. A Linkam Heating stage (HFS600E-P) was used for temperature controlled SAXS measurements. Samples were heated to T = 70 °C and

held isothermally for 4 h, during which continuous SAXS measurements were performed (~ 10 minutes/scan). After in-situ annealing, the temperature was increased from T = 70 °C to 140 °C at 10 °C intervals. Single exposure measurements were 10 minutes long with approximately 5 min. equilibration time in between each temperature. Scattering intensity ($I(q)$) is normalized with respect to incident beam intensity (I_0) and the thickness of the sample (0.5 mm).

Dynamic moduli were measured by small amplitude oscillatory shear (SAOS) using a Malvern Kinexus Rotational Rheometer and a 20 mm parallel plate geometry. Measurements were conducted in the low strain limit at strain amplitudes of γ = 0.1 %. Samples were heated to T = 70 °C, and time resolved mechanical spectroscopy (TRMS) was performed in the form of continuous frequency sweeps over 4 hr. at T = 70 °C.[20] Following TRMS, SAOS isothermal frequency sweeps from ω = 1 - 100 rad/s were conducted from T = 70 °C - 140 °C at 10 °C intervals. Various superposition principles (Time-time superposition, concentration superposition, and time-temperature superposition (tTS)) are utilized when applicable. Rheological data is analyzed using IRIS Rheo-Hub 2018 software.[21]

2.3 Results

2.3.1 Nanoparticle Characterization

ZrO_2 NPs were solvent exchanged from PGMEA to THF. The TEM image in Figure 2.4a implies excellent dispersion of the particles after drop casting from dilute solution. The average particle diameter is measured as d_{NP} = 2.5 nm (std. dev. ± 0.3 nm) according to Image J analysis. TGA in Figure 2.4b shows an inorganic core content of 77 wt.%, indicating significant coverage of organic ligand groups. FTIR spectrum in Figure

2.4c reveals strong peak in the range of ν = 3300 cm^{-1} associated with -OH stretching as well as evidence of –COOH group stretching at around ν = 1700 cm^{-1}, indicating presence of strong polar functional groups to facilitate dispersion in various polar solvents, as well as capacity to coordinate with hydrogen bond accepting moiety, such as the ether oxygen in PEO.

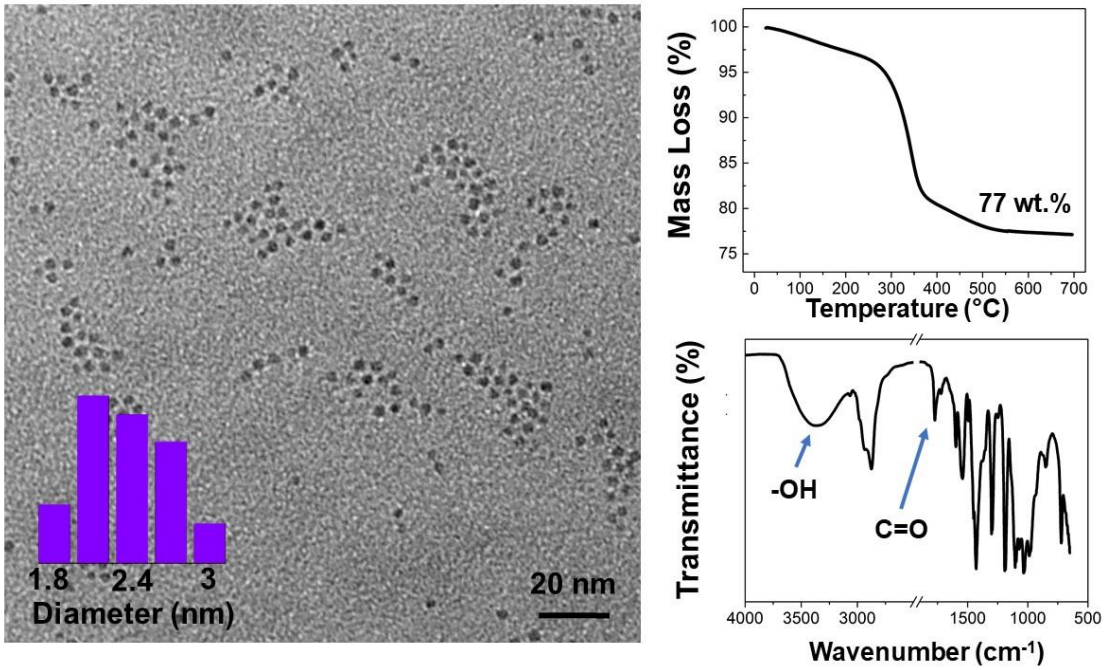

Figure 2.4 (a) TEM image of ZrO_2 NP drop-cast from THF solution. Particles are well dispersed with narrow size distribution of d_{NP} = 2.5 ± 0.3 nm. **(b)** TGA of dried ZrO_2 NP heating to T = 700 °C. 23 wt.% is lost, corresponding to the organic ligand shell around the purely inorganic nanocrystal. Corresponding volume fractions are calculated accordingly. **(c)** FTIR Spectra of ZrO_2 particles. Broad peak at 3300 cm^{-1} characteristics of alcohol or phenol hydroxyl (–OH) stretch. Peak at 1700 cm^{-1} characteristic of carboxylic acid (C=O) stretch. Spectrum remarkably like ZrO_2 NP used by Song et al. for hydrogen bonding in PEO based block copolymer templates.[22]

2.3.2 Structure and Morphology after Drop-casting

NPs and F127 were mixed in THF solution at loadings from 0 wt.% to 40 wt.%. After drop casting and solvent removal, films appeared opaque and brittle. Room temperature SAXS/WAXS measurements (Figure 2.5) and DSC heating scans (Figure 2.6) suggest significant PEO crystallization in the neat F127. Bragg scattering peaks are

observed across a wide q range in SAXS resulting from crystalline lamellae and the PEO crystal unit cell in the WAXS regime. The crystalline peak at q = 0.3 nm^{-1} decreases in intensity with the addition of NP loading from 10 to 40 wt.%. Significant scattering emerges at higher q due to the form factor of embedded NP (q = 2 nm^{-1} and q = 3.5 nm^{-1}). As NP loading increases, the peaks corresponding to the particle spacing at q = 2 nm^{-1} increases in intensity due to the increased volume content as well as the significant electron density contrast between the NP and the surrounding polymer matrix. A peak in the WAXS regime at q = 11 nm^{-1} corresponding the crystal lattice of the ZrO_2 NP also grows in intensity up to 40 wt.%. Unfortunately, Bragg peaks resulting from the BCP microphase segregation are not observed. It appears that the NPs prevent co-assembly at room temperature. DSC traces in Figure 2.6 further describe the nature of PEO crystallization during the second heating cycle from T = 0 - 100 °C. An endotherm at a melting temperature of T_m = 56 °C reveals the melting of PEO crystallites in the neat F127. T_m decreases with the addition of NPs and the overall area of the endotherm shrinks as well, suggesting the NPs are reducing the amount of crystallinity in the PEO domain. The enthalpy of melting (ΔH_m) is calculated by integrating the area within the endotherm.[15] A normalized percent crystallinity per gram of PEO (X, in units of g^{-1} PEO) is calculated from ΔH_m, where X is normalized with respect to neat F127 ($X_{0\%}$ = 1). The DSC shows that PEO crystallinity is partially suppressed with the addition of NPs to $X \approx 0.75$. Surprisingly, the crystallization suppression appears to be independent of the NP loading, contradictory to other systems where strong hydrogen bonding reduces PEO crystallization linearly with the addition of NPs and SM additives.[2,15]

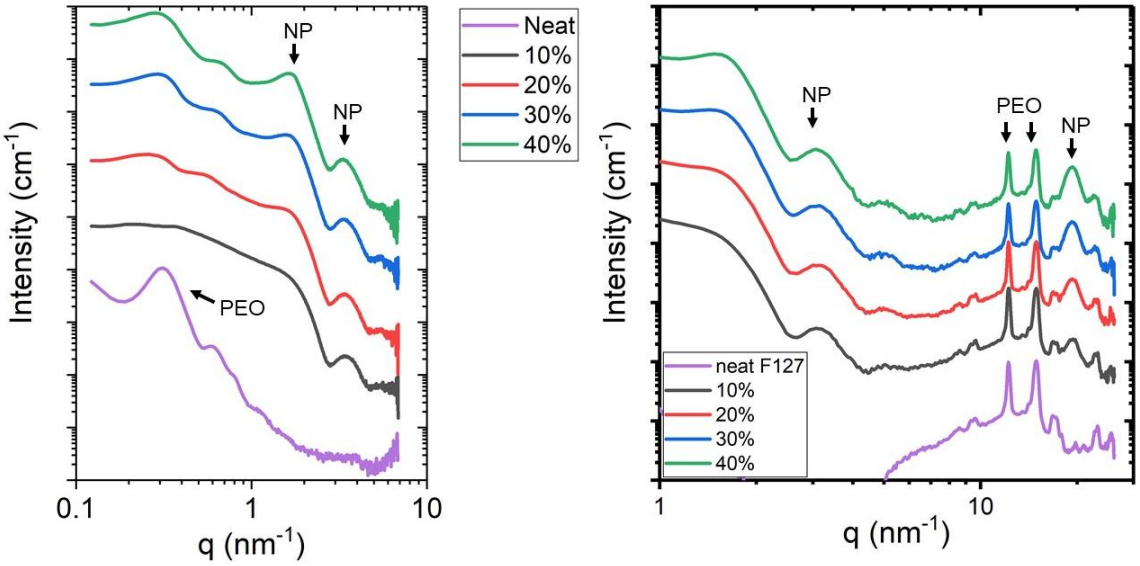

Figure 2.5 Room temperature **(a)** SAXS (on left) and **(b)** WAXS (on right) of neat F127 (pink) and NP loaded composites. NP scattering at high *q* increases significantly with increased loading up to 40 wt.% (green).

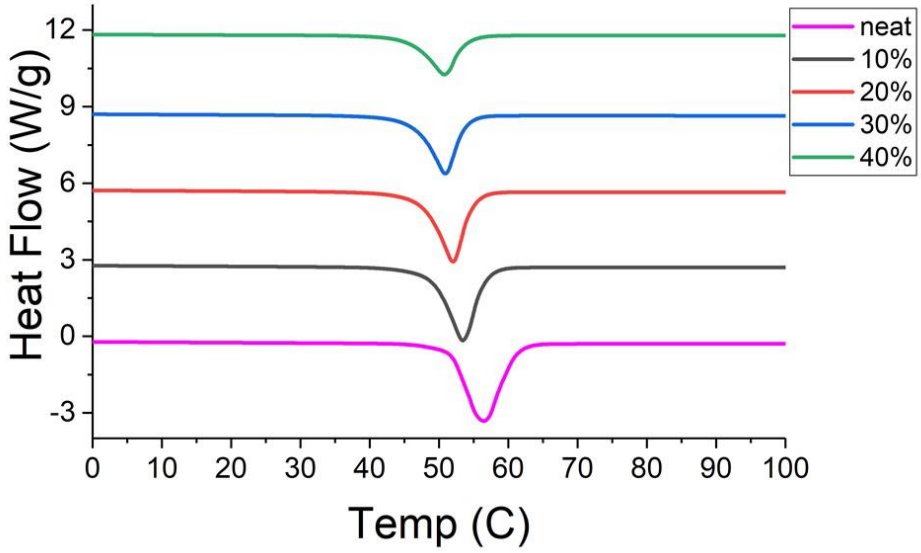

Figure 2.6 DSC curves of 2nd heating from T = 0 °C to 100 °C. Peaks show endotherm of PEO crystal melting. Curves are vertically shifted for clarity. Normalized percent crystallinity X calculated from peak integrations: $X_{0\%}$ = 1, $X_{10\%}$ = 0.78, $X_{20\%}$ = 0.77, $X_{30\%}$ = 0.75, $X_{40\%}$ = 0.77.

2.3.3 Self-Assembly Dynamics: In-situ SAXS & Rheology

It is apparent from room temperature SAXS/WAXS and DSC that the PEO is semi-crystalline and that the NPs do not significantly induce microphase separation between

PEO and PPO blocks. Therefore, to accelerate the microphase separation and encourage intermolecular interactions, the composites were heated above T_m. Upon heating, the cooperative assembly of the NPs within the BCP matrix was investigated by in-situ SAXS. Each bulk composite was heated to T = 70 °C (well above T_m of PEO crystal domain) in the Linkam heat stage. Continuous SAXS spectra were measured for 4 h. at the elevated temperature. Individual spectra at 10 min. time intervals are presented in Figure 2.7. Immediately after reaching a thermal equilibrium at T = 70 °C, a weak scattering feature at q = 0.6 nm^{-1} appears in the neat F127, depicted in Figure 2.7a. The melt microstructure of F127 does not change over the 4 h. annealing time as all spectra at all time steps are imposed on each other. In Figure 2.7b-e, sharp primary scattering peaks (q^*) emerges at q = 0.5 nm^{-1} (d_0 = 12.6 nm) across all loadings of NP. In the case of 20, 30, and 40 wt.%, a second Bragg peak at a ratio of q^*: $\sqrt{3}q^*$ evolves, suggesting the assembly of the BCP into a cylindrical morphology. Spherical morphology is also possible, but unlikely as the spherical morphology arises at extreme volume fraction asymmetry. Our observations are consistent with previous reports according to the overall volume fraction of the NP/BCP domain.[10] While the high order reflection becomes more pronounced at higher NP loading, the peak becomes convoluted in the high q scattering range and overlaps with the form factor of the NP. Throughout the 70 °C anneal, the q^* peak position does not shift, but becomes sharper and narrower, along with a decrease in the power law scaling at low q. The decrease is most significant in the first hour of heating and begins to reach a steady state after 4 h. of thermal equilibrium at T = 70 °C. Evolution of the spectra in the high q range ($1 < q < 3$ nm^{-1}) is relatively constant throughout the entire isothermal process. The Guinier regime ($q \sim 1$ nm^{-1}) corresponds to the characteristic size of the NP.[23] Scattering

in this regime is mostly static, suggesting the NP size is independent of annealing time and does not coarsen. Oscillations in the spectra typical of a spherical particle are observed at q = 3.5 nm^{-1}, consistent with the spherical shape resolved in TEM. Overall, the shape and size of the NP are independent of the time resolved development of microphase separation and morphology. We attempt to isolate different structural features in the SAXS spectra. The convolution of multiple scattering sites and contrasts makes it difficult to quantitatively extract information from the spectra without a model. Currently, we are not aware of a model appropriate for the hierarchical assembly and the appropriate length scales in this system.

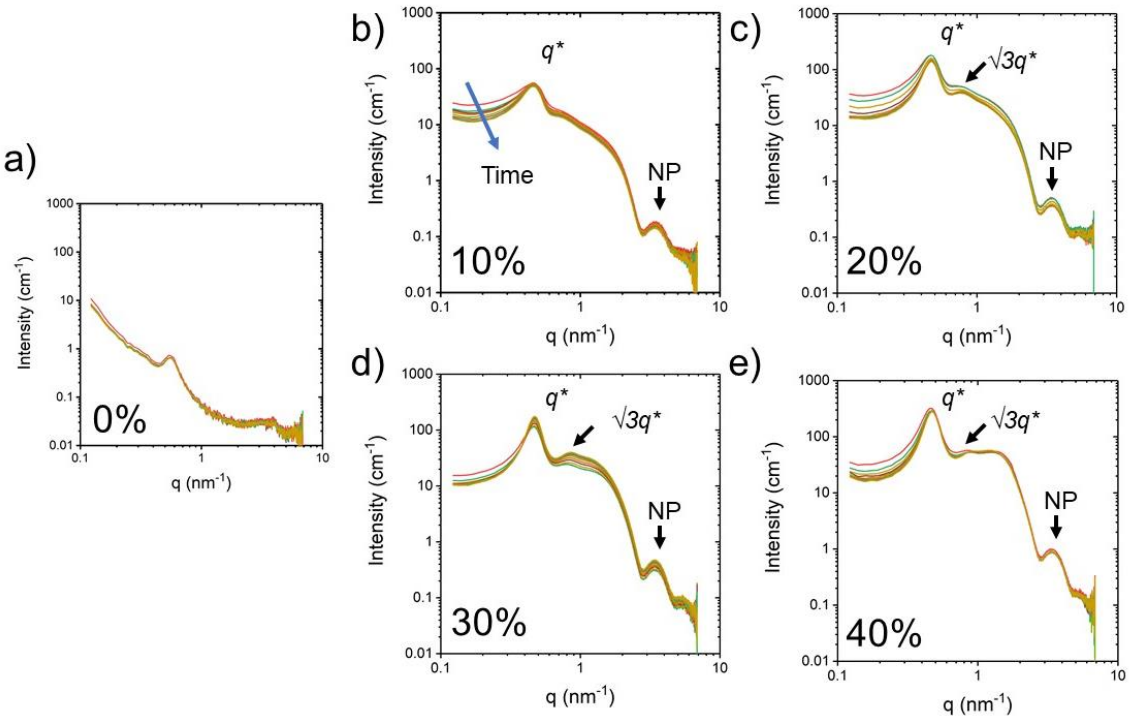

Figure 2.7 Temperature controlled SAXS spectra of **(a)** neat F127, **(b)** 10 wt.%, **(c)** 20 wt.%, **(d)** 30 wt.%, and **(e)** 40 wt.% during isothermal annealing at T = 70 °C. Morphological evolution observed in the 1-D spectra, highlighted by a sharpening of the primary peak and decrease in low q scattering.

In-situ SAXS reveals the time dependent self-assembly of an ordered nanocomposite upon heating above T_m of PEO. With the assistance of the ZrO_2 NP, F127

assembles into cylindrical morphology and the NPs are well-dispersed into the matrix. The particle size and shape do not change. The evolution of the SAXS spectra suggests additional structural development after the melting transition, where a steady state structure is achieved after 4 hr. of thermal annealing. The dynamics of the structural evolution was further investigated by time resolved small amplitude oscillatory shear (SAOS) rheology, also known as time resolved mechanical specreoscopy (TRMS). Storage ($G'(\omega)$) and loss modulus ($G''(\omega)$) are measured as a function of frequency by continuous frequency sweeps across a range of ω = 1-100 rad/s while holding the temperature constant at T = 70 °C for 4 h. The structure changes during the measurements according to SAXS. Therefore, each data point in the frequency sweep represents a different material state. Interpolation is necessary to obtain dynamic data as a function of frequency at discrete material states. The cyclic frequency sweeps are sorted and smoothed according to procedures established by Mours and Winter.[20] Individual curves of $G'(\omega_i,t)$ and $G''(\omega_i,t)$ represent the evolving moduli (where i = 1, 2, …, N, where N is the number of discrete frequency sweeps). Figure 2.8 shows the evolution of G' (open symbols) and G'' (closed symbols) at a constant frequency of ω = 10 rad/s for the samples. At this frequency, the dynamic moduli of neat F127 (0 wt.%) represented by the pink circles is low and viscously dominated ($G'' > G'$). The dynamic moduli do not evolve during isothermal treatment, mirroring the observations in time-resolved SAXS. However, G' and G'' appear to increase significantly for all NP loaded composites. The 10 wt.% sample (grey curve) begins in a viscously dominated state, but G' becomes much larger and crosses over G'' at t = 1.5 h. While both G' and G'' increase for the 20 wt.% sample (red curve), a crossover is quickly detected at $t \approx 0.5$ h. Interestingly, 30 and 40 wt.% (blue and green curves respectively) are initially elastically

dominated, so no crossover in *G'* and *G"* is observed during the annealing. However, both moduli do increase, with *G'* increasing much more significantly. Overall, the magnitude of the modulus scales with NP loadings. The fast growth of the modulus at short time is qualitatively consistent with the rapid drop in the low *q* scattering intensity and sharpening of *q** observed in the SAXS, suggesting that the growth of *G'* may be correlated to the structural evolution.

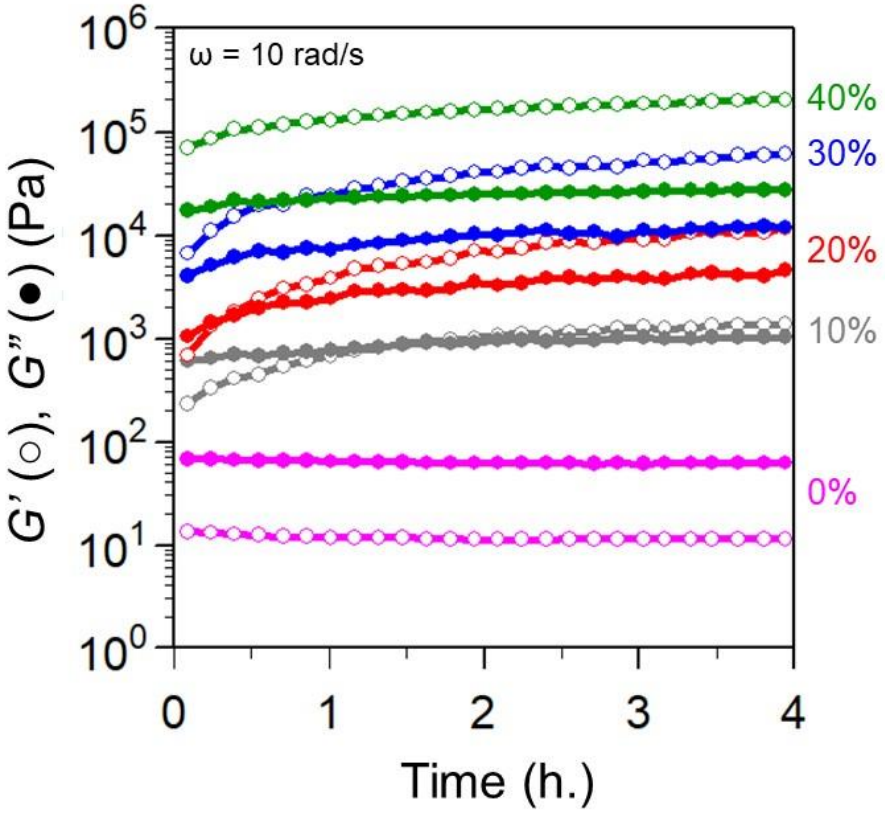

Figure 2.8 Evolution of *G'* (open symbols) and *G"* (closed symbols) at ω = 10 rad/s during isothermal annealing at *T* = 70 C. F127 (pink), 10 wt.% (grey), 20 wt.% (red), 30 wt.% (blue), and 40 wt.% (green). Neat F127 shows no increase in *G'* or *G"*. Composites modulus grows and begins to plateau out after 4 h.

The evolution of *G'* and *G"* is modeled by an exponential growth function (Eq. 2.1) to define characteristic time of structural growth.

$$G'(t) = G'_i + (G'_\infty - G'_i)\left(1 - exp\left[-\left(\frac{t}{\tau'}\right)\right]\right) \quad \text{Eq. 2.1}$$

In Eq. 2.1, G_i and G_∞ are the initial and final modulus, and τ' is the characteristic time. Fits to the growth function are presented in Table 2.2. We see that the final modulus trends with the loading as expected. The growth time of 20 wt.% is the slowest, however the increase in modulus is the largest. The trend is qualitatively consistent with the SAXS in Figure 2.7c, where the spectra for 20 wt.% appears to take the longest time to reach a steady state in comparison to the other composites. Overall, the change in G'' is independent of loading while G' is much more drastic.

Table 2.2 Fit parameters for Eq. 2.1 representing exponential growth of G' and G'' at ω = 10 rad/s during isothermal heating of T = 70 °C

Loading (wt. %)	G'_i (Pa)	G'_∞ (Pa)	τ' (h.)	G''_i (Pa)	G''_∞ (Pa)	τ''(h.)
0	--	--	--	--	--	--
10	1.6×10^2	1.7×10^3	2.2	5.6×10^2	1.1×10^3	1.9
20	3.8×10^2	2.1×10^4	5.5	9.8×10^2	4.8×10^3	2.0
30	6.3×10^3	8.8×10^4	3.8	4.0×10^3	1.3×10^4	1.9
40	7.1×10^4	1.6×10^5	2.2	1.7×10^4	2.8×10^4	1.7

We consider the exponential growth analysis in Table 2.2 at an arbitrary frequency of ω = 10 rad/s, which inherently neglects the full dynamic behavior during structure development. The initial viscoelastic character is highly frequency dependent. The trends in structural development may not be universal across all experimental timescale. To describe the entire viscoelastic response during structural evolution, we apply time-time superposition (ttS) to the same dynamic data sets.[20,24] After sorting each frequency sweep into individual frequencies and smoothing the growth curves, the dynamic data is further processed by an interpolation procedure, where the curves are converted from $G(\omega_i,t)$ to

$G(\omega,t_i)$ to construct data sets of frequency sweeps at discrete times t_i. The interpolated frequency sweeps are manually shifted to superimpose into a single master curve (Figure 2.9a). Shift factors a_2 (time shift) and b_2 (modulus shift) are generated for an arbitrary reference time of t = 600 sec (or 10 min. the first measurable frequency sweep). a_2 and b_2 are presented in Figure 2.9b and Figure 2.9c respectively. Here, the validity of ttS is empirically demonstrated. Neat F127 does not exhibit any material change. Therefore, no shifting is required so $a_2 \approx 1$ and $b_2 \approx 1$ across all times. All composites displayed structural evolution, so significant shifting is necessary on both axis to generate master curves. The 10 wt.% sample has the strongest dependence of both $a_2(t)$ and $b_2(t)$. The time dependence follows a negative power law, which decreases with increasing NP loading. Additionally, we calculate the shifting slope (a_2/b_2), which relates the relative time and modulus shift for each composite. A slope of $a_2/b_2 \approx 1.3$ is calculated for all composites and is greater than 1, indicating the necessary time shift is larger than the modulus shift at each time. The universality of a_2/b_2 suggests that the extent of modulus development is coupled to the timescale of growth despite the different power law dependence of $a_2(t)$ and $b_2(t)$.

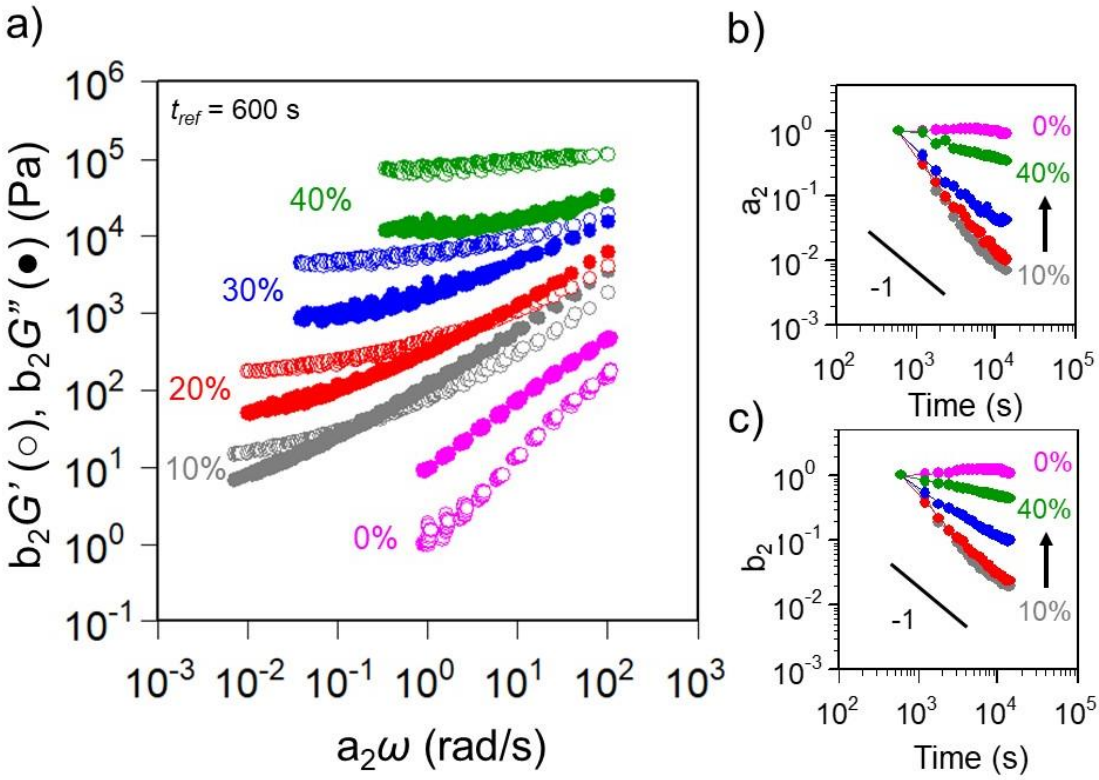

Figure 2.9 (a) Master curves generated by time-time superposition of the viscoelastic data from time resolved rheology (interpolation of frequency sweeps followed by shifting with shift factors a_2 and b_2). Time-time shift factors **(b)** a_2 and **(c)** b_2 for all composites.

Surprisingly, we found that the master curves from ttS could be superimposed and shifted a second time by using NP loading as a shift parameter. Figure 2.10a shows a single master curve taking the data in Figure 2.9a and manually shifting both vertically and horizontally according to the NP concentration (wt.%) with a reference dataset of 10 wt.%. Shift factors a_{NP} and b_{NP} are presented in Figure 2.10b. The scaling of the shift factors is no longer power law. Both the horizontal and the vertical shift factor could possibly exhibit polynomial type scaling. The near linear relationship between a_{NP} and b_{NP} is intriguing. The deviation at high NP loading is likely due to the manual shifting and experimental error compounded from the ttS. The observed time-concentration superposition was unexpected, and is very different from the classically understood time-concentration superposition observed in coacervate or nanofilled polymer systems.[25,26] In such cases,

time-concentration superposition is used to correlate the dynamics of a material to a composition or loading of some additive. However here, time dependent structural development and concentration are correlated. The significance of ttS and loading superposition will be elaborated on in the discussion (Section 2.4).

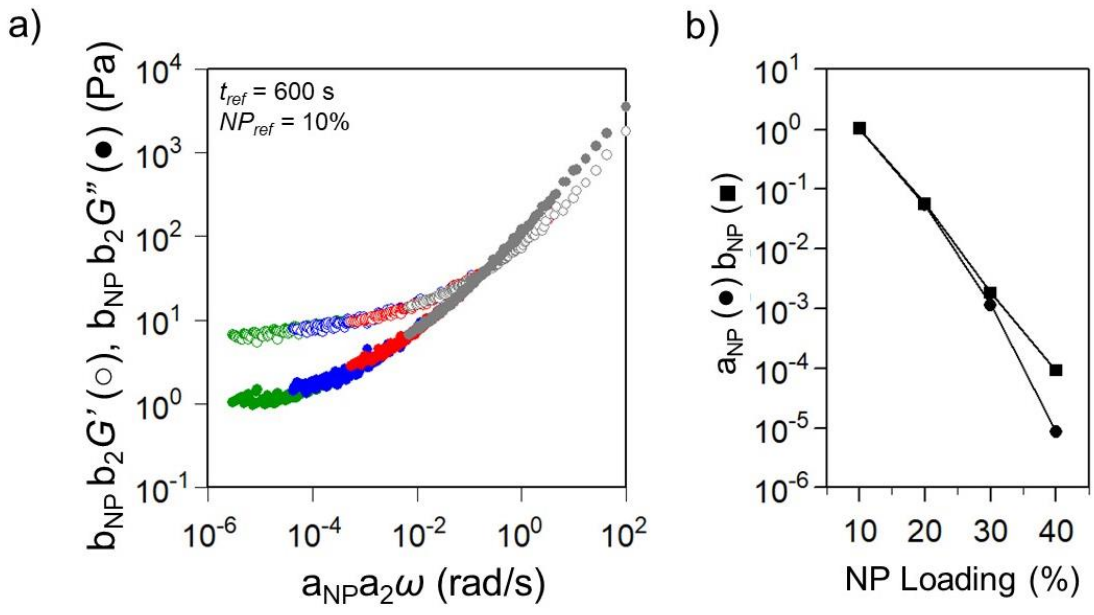

Figure 2.10 (a) Concentration superposition of time-time master curves from Figure 2.9 at a reference loading of 10 wt.%. 10 wt.% (grey), 20 wt.% (red), 30 wt.% (blue) and 40 wt.% (green) can be shifted with empirically determined shift factors. **(b)** a_{NP} (horizontal) and b_{NP} (vertical).

2.3.4 Trends in Structure and Linear Viscoelasticity with NP Loading

The morphology and rheological properties of all composites were evaluated after isothermal annealing was completed and a steady state structure was achieved. Figure 2.11a shows SAXS spectra at T = 70 °C for all materials after the 4 h. annealing. Again, the neat F127 is disordered in the melt and does not exhibit any strong scattering features. At 10 wt.% loading, a strong primary scattering peak appears at a q corresponding to d_0 = 13.5 nm of the microphase separation between the major phase (PEO + NP) and the minor phase (PPO). Upon additional loading up to 20 and 30 wt.%, high order scattering peaks

arise at a peak ratio of q^*:$\sqrt{3}q^*$ corresponding to the proposed cylindrical morphology as previously identified during the isothermal structure development. At the higher loading of 20, 30, and 40 wt.%, d_0 = 13.3 nm which is remarkably close to 10 wt.% loading. Therefore, the characteristic spacing of the microphase separation is independent of NP loading within the confined length scale. The NP scattering at high q is well defined and become more intense with higher NP loading. The flat baseline at low q and broad form factor implies significant dispersion of the NPs throughout the major domain.[27] The hierarchical assembly of multiple components across a wide range of nanoscale dimensions is quite impressive.

We also observed that the NP loading significantly impacts the rheological properties in the melt state (at T = 70 °C). The frequency dependent viscoelasticity is presented in a plot η^* vs. G^* (Figure 2.11b) where the slope of the curve qualitatively describes the liquid/solid-like behavior of the material (horizontal curve corresponds to a viscous liquid, while a vertical curve depicts and elastic solid).[28] The neat F127 behaves primarily like a viscous liquid over the probed frequency range (ω = 1-100 rad/s). Upon loading of 10 wt.%, the viscoelastic changes drastically, indicated by the upturn in the slope. The overall modulus is also significantly increased by an order of magnitude from $G^* \sim 10^1$ Pa to $G^* \sim 10^3$ Pa. At 30 and 40 wt.%, the composite transitions to a soft solid with a plateau in G^* forming at low ω ($\eta^* \rightarrow \infty$). The overall modulus scales with NP loading up to a maximum stiffness of $G^* \sim 10^5$ Pa at 40 wt.%.

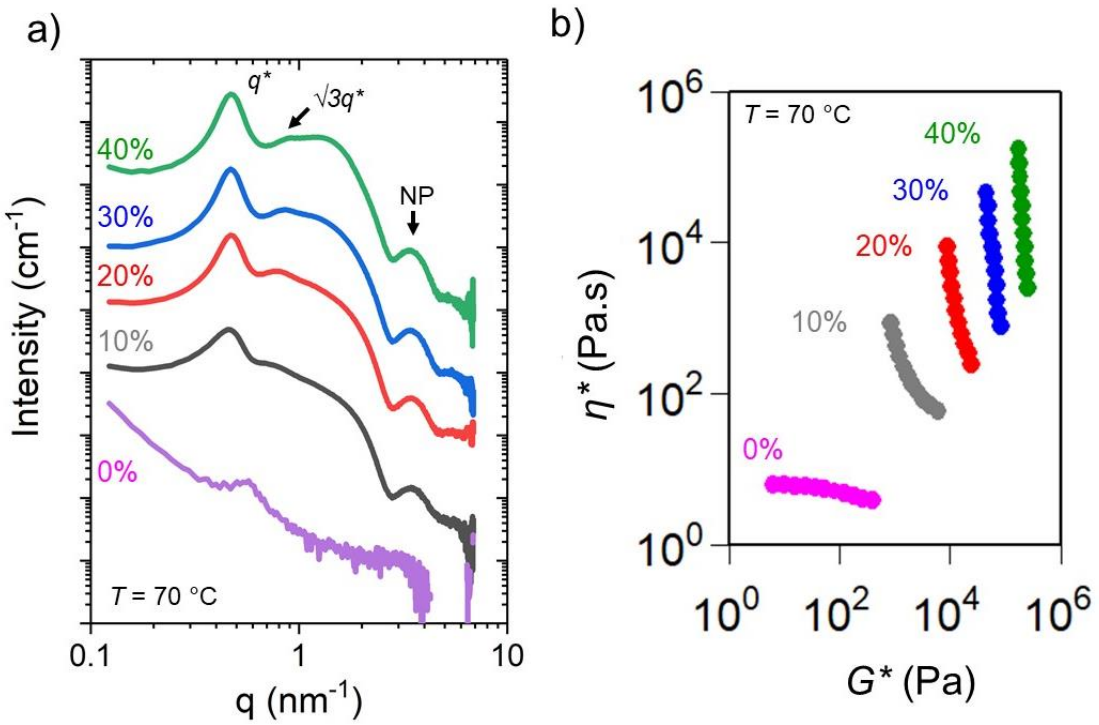

Figure 2.11 (a) SAXS spectra of F127 composites with 0,10, 20, 30, and 40 wt.% nanoparticle loading at T = 70 °C after thermal annealing. Upon additional loading, phase segregation strength increases, as well as prevalence of second order peak at peak ratio q*: q*√3, indicating cylindrical morphology. Additional scattering from NP structure factor can be detected at high q. **(b)** Frequency sweep data represented in plot of η* vs G* for all composites at T = 70 °C. Increase in G*, as well as increase in solid-like behavior upon increased NP loading is clearly represented.

2.3.5 Temperature-dependent Structure-property Relationships

Temperature dependent phase behavior and rheological properties of the steady state structures were determined by SAXS and SAOS by heating the samples through 10 °C steps over a temperature range of T = 70 - 140 °C. SAXS spectra of $I(q)$ at increasing temperature during heating are presented in Figure 2.12. The weak scattering feature in neat F127 at q = 0.5 nm^{-1} quickly disappear upon heating up through T = 100 °C. The low χN of F127 at T = 70 °C is below the critical segregation limit, so a traditional first order ODT is not observed. Instead, a transition to a homogeneous state with no spatial density correlation is resolved. Additionally, $I(q)$ is very weak above T = 100 °C, further suggesting

there is no resolvable structure. The temperature dependent response at 10 wt.% is different than the neat sample. q^* quickly broadens out, suggesting a decrease in the microphase segregation strength. Such a transition was hypothesized as χ_{eff} is driven by the introduced enthalpic interactions between the NP and the PEO. The interactions are assumed to be primarily hydrogen bonding, in which the strength/lifetime is inversely proportional to temperature.[29] The apparent disordering is consistent with rheological investigations by Kothari et al. for the hydrogen bonding SM/F108 composites which disordered in the range of T_{ODT} = 100 - 140 °C.[15] However, the phase transition is much different above 10 wt.%. While q^* decreases in intensity for 20, 30, and 40 wt.% with increasing temperature, a shift to higher q suggests a decrease in the domain spacing of the BCP morphology. The primary peak broadening also indicates a decrease in phase segregation strength, much like that observed at 10 wt.%. However, no first order transitions were observed in $I(q^*)$ or full width at half maximum (FWHM) of q^*. Figure 2.13 shows the trends in d_0 and FWHM of q^* as a function of temperature. Aside from 10 wt.%, d_0 decreases linearly from 13.5 nm at 70 °C to 11.5 nm at 140 °C. q^* broadens in a similar manner according to Figure 2.13b. Despite the presence of a primary scattering peak, the temperature dependent data suggest that at 10 wt.%, the microstructure is weakly segregated and has not transitioned to well-ordered cylindrical morphology. It is important to note that the scattering intensity of both q^* and the high order peaks become convoluted with the high q scattering from the NP form factor. The Guinier ($q \sim 1$ nm^{-1}) and Porod ($q \sim 3$ nm^{-1}) regimes are static across the measured temperature range, suggesting that the size and shape of the NP is not a function of temperature.

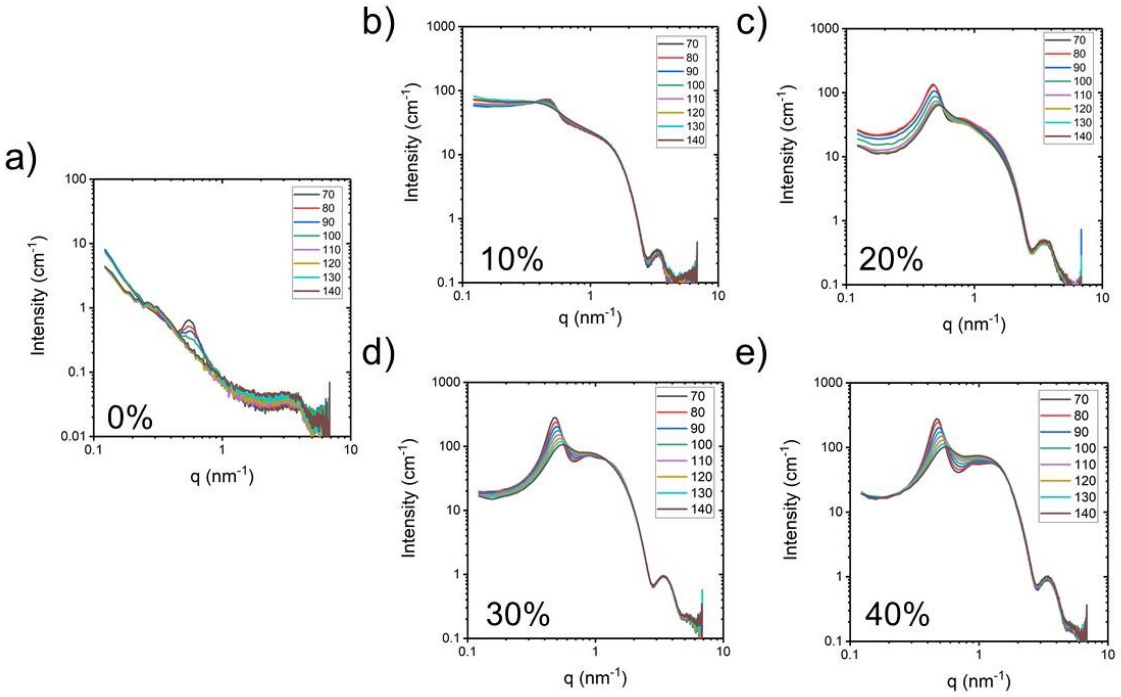

Figure 2.12 SAXS spectra of **(a)** neat F127, **(b)** 10 wt.%, **(c)** 20 wt.%, **(d)** 30 wt.%, and **(e)** 40 wt.% during temperature sweep from T = 70 °C to 140 °C. Each curve in the spectra corresponds to a different measurement temperature.

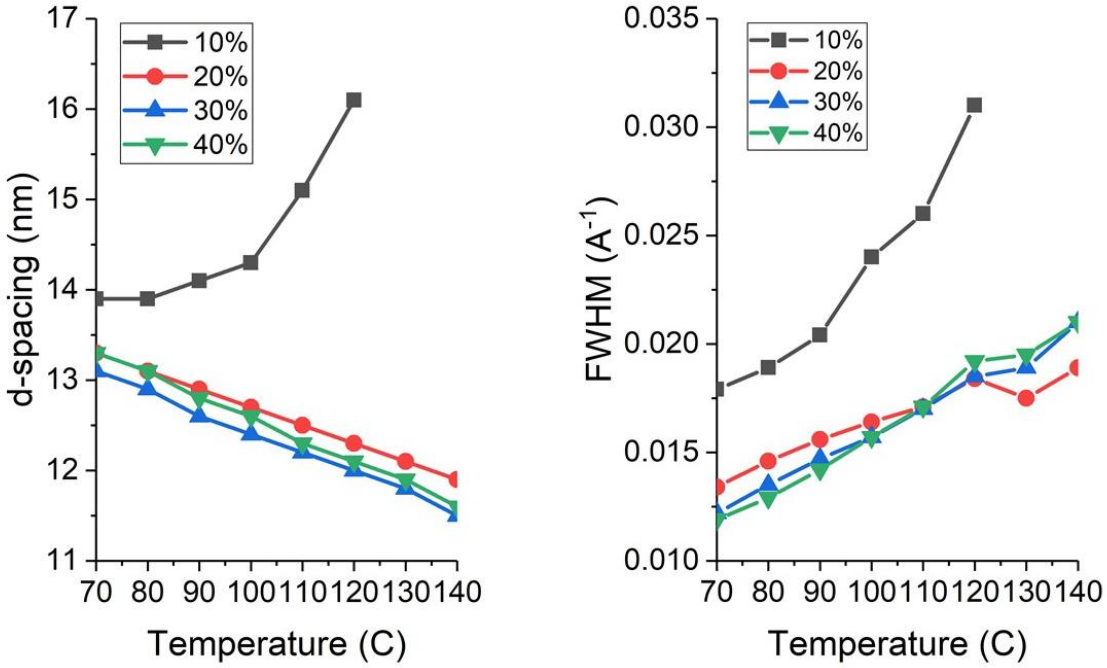

Figure 2.13 Trends in **(a)** domain spacing (on left) calculated from q^* and **(b)** full width at half maximum (FWHM) (on right) of primary peak q^* as a function of increasing temperature.

Equivalent thermorheological properties were determined with SAOS through frequency sweeps collected over the same temperature range as SAXS measurements (T = 70 - 140 °C). Master curves of $G'(\omega)$ and $G''(\omega)$ are constructed with the application of time-temperature superposition (tTS) (Figure 2.14a). It is remarkable that tTS works despite the heterogeneous structure (which appears temperature dependent itself) and the hierarchical structure driven by the NP addition. Shift factors a_T and b_T are determined from tTS shifting and are highly temperature dependent. Figure 2.14b shows shift factors at an arbitrary T_{ref} = 70 °C. a_T is accurately represented by either the WLF equation or an Arrhenius relation. The WLF correlation is not universal across the various NP loadings. More significant shifting along the frequency axis is necessary at higher loading (40 wt.%), indicating the relaxation processes are heavily dependent on NP loading. Therefore, it is difficult to directly compare the various relaxation times of each relaxation process, so we choose to arbitrarily compare from the initial material state measured at T_{ref} = 70 °C. Modulus shift factor b_T was found to be close to 1 for all temperatures however they are necessary to perform the shifting. The overall modulus of the composite increases significantly with increasing NP loading, as suggested by Figure 2.10b. The dynamic response may be described over a much wider range of timescales through the master curves. The neat F127 behaves like a viscous liquid across the entire frequency range, as is expected from all previous characterizations. The composite response is described as a soft solid with increasing degrees of elasticity especially in the high ω regime. While the shape of the $G'(\omega)$ and $G''(\omega)$ curves are different at each NP loading, a significant plateau in G' is observed in the intermediate ω regime ($10^{-1} < a_T\omega < 10^{1}$ rad/s) for all loadings. A downturn in both $G'(\omega)$ and $G''(\omega)$ is detected at the lowest ω, which is inconsistent with

the formation of a solid with a sample spanning, percolating network, where *G'(ω)* would plateau at the longest timescales.[30] Therefore, additional relaxation processes may be dictating the viscoelastic response other than a traditional crosslinked percolation model.

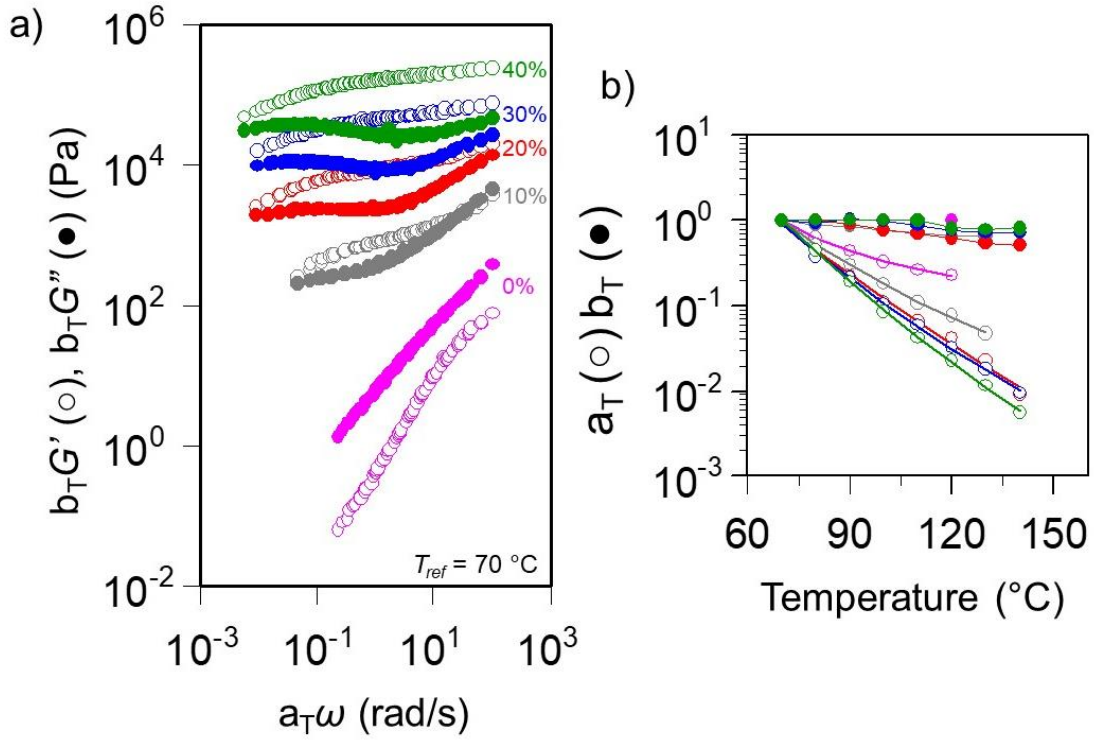

Figure 2.14 (a) Master curves of *G'*(open symbols) and *G"*(closed symbols) generated by time-temperature superposition of temperature dependent frequency sweeps. **(b)** Time-temperature shift factors a_T and b_T. Solid lines show fit to WLF relation

We further describe the impact of high NP loading in terms of the spectrum of relaxation processes which is derived from the definition of the relaxation modulus *G(t)* in Eq. 2.2. The relaxation modulus *G(t)* is a powerful parameter when describing the viscoelastic response of a material under all flow conditions, as it expresses the structural rearrangements of a material in time.[30] *G(t)* is a monotonically decaying function which is defined as the integral over relaxation modes from $0 < \tau_i < \tau_{max}$ of the relaxation time spectrum *H(τ)*.[30]

$$G(t) = \int_0^{\tau_{max}} \frac{d\tau}{\tau} H(\tau) e^{-t/\tau} \qquad \text{(Eq. 2.2)}$$

$H(\tau)$ is a continuous function which can be directly calculated from dynamic data, for example through techniques established by Baumgaertel et al.[31] Figure 2.15 shows the calculated spectra of each composite using the dynamic data in Figure 2.14a at a reference temperature of T_{ref} = 70 °C. The relaxation times cannot be directly compared due to the variable temperature dependence of a_T. However, the shape and scaling of each spectra is of interest. Power law scaling in $H(\tau)$ signifies "self-similar relaxation" behavior where the structure relaxes similarly across a wide range of time scales.[30] The neat F127 scales with power law of $H(\tau) \sim \tau^{-1}$ over most accessible time scales, close to that of a viscoelastic liquid. A distinct increase in the power law scaling is observed for the 10% and begins to plateau at long times. A plateau where $H(\tau) \sim \tau^0$ is characteristic of a purely elastic solid material.[32] The plateau is more significant for the 20, 30 and 40 wt.% samples, which begin to show a positive power law exponent at intermediate timescales ($\tau = 10^{-1} – 10^{1}$ s). The diversity of power law scaling further supports the hypothesis that the NPs are introducing additional relaxation processes not described by a simple percolation model of the critical gel state, particularly at the highest loadings.[30]

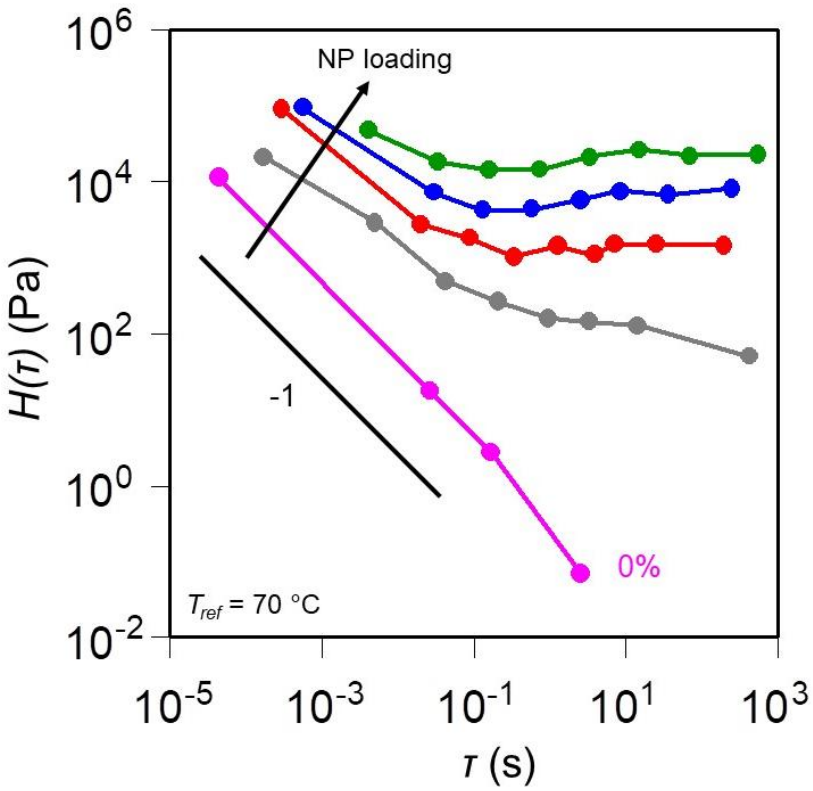

Figure 2.15 Relaxation Time Spectrum $H(\tau)$ calculated from dynamic master curve data in Figure 2.14 at T_{ref} = 70 °C. Neat F127 (pink) is typical for a viscoelastic liquid. Transition to solid behavior observed with increasing nanoparticle loading.

2.3.6 Comparison to Homopolymer Analogs

The role of microphase segregation is important for the utility of the composite material. However, the viscoelastic properties and relaxation processes may more closely related to the intermolecular NP-PEO interactions as opposed to the presence of microphase separation. For comparison, a composite was fabricated using a PEO homopolymer (Mw = 10 kg/mol) according to identical sample preparation and characterization protocols in Section 2.2. The PEO homopolymer interacts with the NP additive and mimics the environment within the major phase of the NP/BCP composite. A NP loading of 26 wt.% was used, which is equivalent to the loading of NP within the PEO domain of the 20 wt.% composite. Figure 2.16 shows all SAXS measurements as

previously described. Isothermal measurements during annealing for 4 h. at T = 70 °C is qualitatively like the F127 composites, where low q scattering decreases in time and the high q scattering is static. However, there is no primary scattering peak q^* which results from microphase separation. The broad peak feature at q = 0.7 nm^{-1} is due to the high concentration of NPs in the polymer matrix, which contribute some measurable structure factor (particle-particle scattering).[33] We experimentally determine the form factor of the NP in dilute conditions by preparing a PEO composite with 1 vol.% NP, followed by subtracting the scattering signal from a pure PEO melt (Figure 2.16c). The high q resolution is very weak and does not follow the expected power law scaling ($I \sim q^{-4}$) due to detector limitations.[27] The flat baseline scattering at low q emphasizes the impact of the structure factor observed in Figure 2.16a.

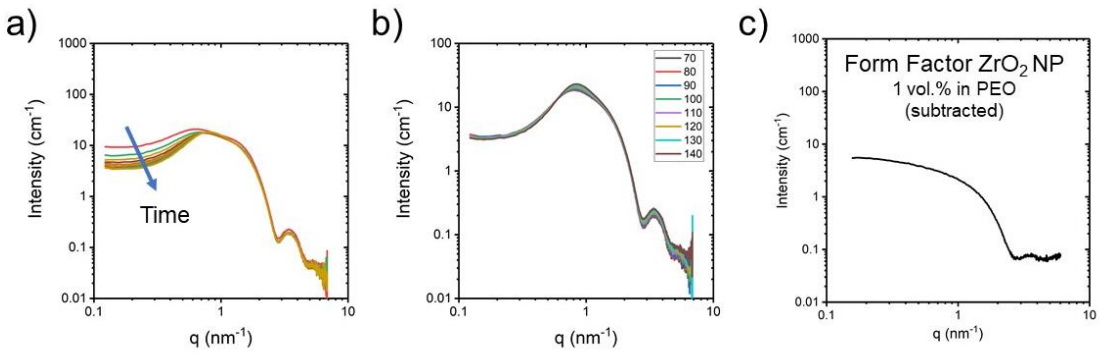

Figure 2.16 (a) Temperature controlled SAXS spectra of PEO composite during 4 h. isothermal annealing at T = 70 °C. **(b)** SAXS spectra of PEO composite during temperature sweep from T = 70 °C to 140 °C. Structure is independent of temperature **(c)** Form factor of ZrO_2 NP measured from dilute conditions in PEO matrix**.**

After the 4 h. annealing, the PEO composite was heated up to T = 140 °C. Figure 2.16b shows the series of temperature dependent SAXS Spectra. We expect the NP size and shape to be constant across the temperature sweep according to previous measurements. *I(q)* does not change substantially. These results suggest the phase transitions observed in Figure 2.12 are a direct consequence of the microphase separation,

or more specifically, the symbiotic relationship between the NP-PEO interactions and the microstructure of the major and minor phases.

The viscoelasticity is presented in Figure 2.17. Figure 2.17a shows the time resolved structure development, plotted as $G'(\omega = 10$ rad/s) and $G''(\omega = 10$ rad/s) in comparison to the 20 wt.% F127 composite. The evolution in both G' and G'' are strikingly distinct between each composite. The PEO composite is initially highly elastic ($G' > G''$) and G' continues to increase, which is expected from the evolution of the SAXS spectra. The overall magnitude of the modulus is an order of magnitude higher in the PEO homopolymer composite compared to the F127 composite. Interestingly, ttS of the time resolved data fails miserably for the PEO composite (Figure 2.17b). An attempt was made to apply both vertical and horizontal shifts to the data, yet it is impossible to superimpose the curves into a single master curve. Therefore, we must conclude that the structure development is closely linked to microphase segregation as well as NP structure.

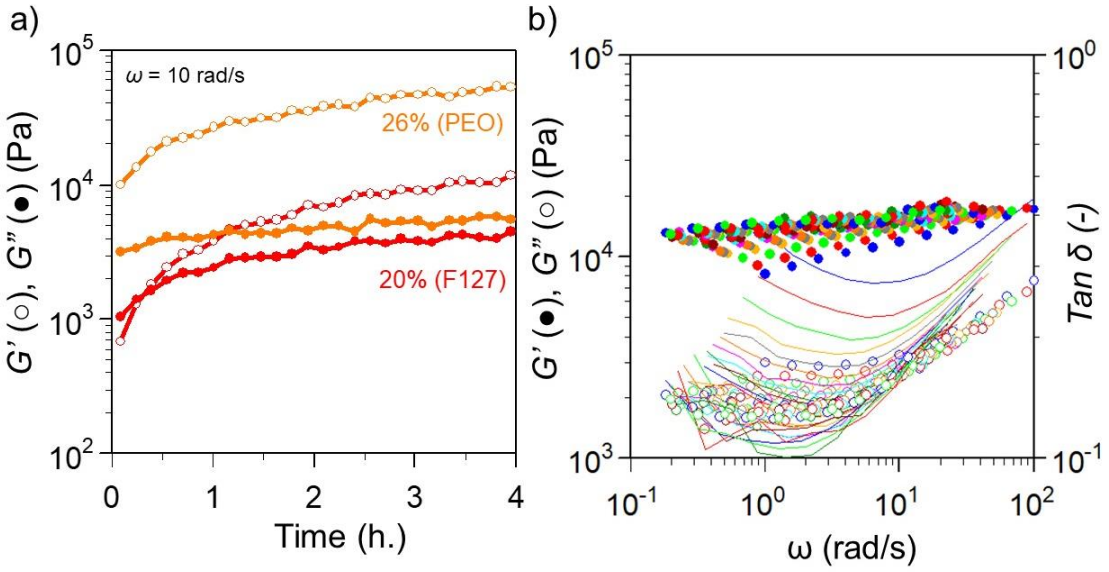

Figure 2.17 (a) Evolution of G' (open symbols) and G'' (closed symbols) at $\omega = 10$ rad/s during isothermal annealing at $T = 70$ °C. 20 wt.% F127 composite (red) shown in comparison to the 26 wt.% PEO composite (orange). **(b)** Interpolated frequency sweeps of G' (closed symbols) and G'' (open symbols) and *tan* δ (lines) at various times throughout TRMS shifted manually. Attempt to superimpose curves with ttS failed.

A dynamic master curve of *G'(ω)* and *G''(ω)* is constructed from the temperature dependent frequency sweeps and presented in Figure 2.18 along with the 20 wt.% composite data in Figure 2.14a. The shape of the PEO composite is strikingly different from the F127 equivalent. The plateau in *G'(ω)* is much more prevalent, distinct, and almost an order of magnitude larger across all accessible frequencies. The PEO composite is much more elastic, as *tan δ* is lower across all frequencies. The increase in elasticity suggests the PPO domains suppress and soften the overall response in the F127. A drop off in *G'(ω)* and *G''(ω)* is observed at the low *ω* limit in both composites, suggesting the longtime dynamics may be similarly directed. Surprisingly, shift factors a_T and b_T are identical, indicating the temperature dependence of the relaxation times is independent of microphase separation. The continuity in the shift factors is strong evidence that the NP-PEO interactions and NP structure directs the temperature dependent viscoelasticity.

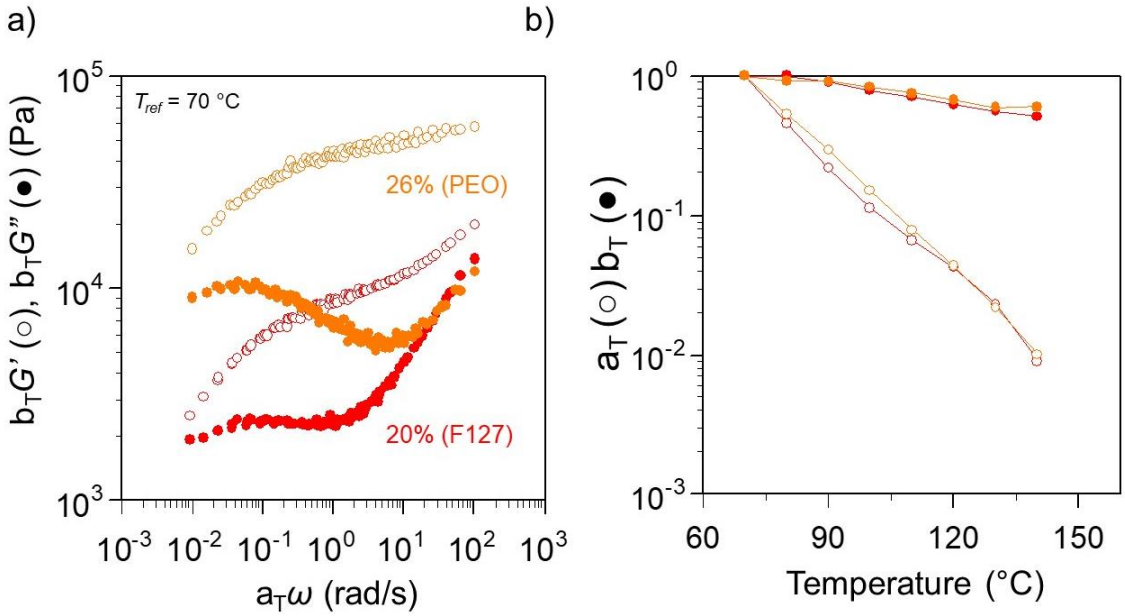

Figure 2.18 (a) Master curves of *G'*(open symbols) and *G''*(closed symbols) generated by time-temperature superposition of temperature dependent frequency sweeps. 20 wt.% F127 composite (red) shown in comparison to the 26 wt.% PEO composite (orange). **(b)** Time-temperature shift factors a_T and b_T.

Overall, the behavior of the PEO analog suggests the use of a BCP template is not required to form a viscoelastic solid composite. However, microphase segregations is important for structure development in the time resolved rheology. The temperature dependent rheology is governed by NP loading as opposed to the microphase segregation. The decrease in modulus and elasticity in the F127 domain suggests that the minor PPO domain suppresses the overall mechanical response.

2.4 Discussion

The additive driven assembly approach affords hierarchical nanostructures of proposed microphase separated PPO domains within a continuous matrix of PEO and NPs. Strong microphase separation and structured assembly of the F127 template only occurs with the addition of NPs at 20 wt.% or above. Below 10 wt.%, the system is weakly microphase segregated and disorders upon heating up to T = 140 °C. Proposed hydrogen bond interactions are primarily used to selectively disperse NPs into the hydrophilic PEO domain and increase the microphase segregation strength, embodied by χ_{eff}. We believe enthalpically strong NP-PEO interactions are necessary for selective self-assembly. Previous work has shown that suppressed PEO crystallinity is evidence of strong hydrogen bonding interactions.[2,10,34] A strong intermolecular interaction can be more energetically favorable than PEO chains crystallizing onto themselves or neighboring chains. In the ZrO_2/F127 system examined in this study, crystallinity is indeed suppressed by the addition of NPs, but not eliminated as described by DSC measurements (Figure 2.6). Therefore, the energetics associated with the enthalpic coordination are not ultimately stronger than the thermodynamic driving force to crystallize. The remaining PEO crystallization inhibits microphase segregation at room temperature and contributes to significant NP aggregation

as the NP mobility is the polymer matrix decreases and access to the PEO chains becomes restricted. We demonstrate that melting the PEO crystals promotes self-assembly into the microphase separated morphology. The mobility of polymer chains increases in the melt state as the energetic barrier is eliminated, facilitating NP dispersion within the PEO domain. It is likely that a combination of hydrogen bonding interactions and steric dispersion forces between NPs contribute to the self-assembly. The NPs are designed to be dispersible in a variety of polar solvents (THF, DMF, PGMEA, etc.) The dispersion of surface coated inorganic NPs is achieved through steric stabilization in the form of repulsive forces between the ligands.[35] FTIR spectra suggest that there are multiple unique functionalities on the NP surface. Therefore, hydrogen bonding through carboxyl or hydroxyl functionality cannot be isolated as the exclusive intermolecular interaction between the NPs and the PEO chains.

Despite the complex surface chemistry on the periphery of the NPs, the evolution of structure is consistent within our understanding of the additive driven assembly motif. The SAXS data highlights the formation of microphase separated BCP domains as evidenced by the evolution of a primary scattering peaks q^*. We focus on the evolution in the low q scattering limit ($q < q^*$), which corresponds to structures larger than the microphase separation and the NP size. The intensity within this regime is proportional to the volume of the scattering object.[33] The low q scattering intensity for a perfectly dispersed single particle should be low and constant with q, consistent with the NP form factor in Figure 2.16c. Here, the structure is homogenous across such large length scales. The form factor of a larger aggregate of NPs will have higher scattering intensity and exhibit power law scaling in q associated with the fractal structure of the aggregate.[27,36] In aggregated NP

suspensions, two Guinier regimes emerge at low and high q corresponding to the size of the aggregate and the size of a single NP. We observe such behavior in the PEO composite analog (Figure 2.16a) were the power law scaling at low q decreases with annealing time and an additional peak emerges at $q \sim 0.7$ nm^{-1}, suggesting a stable aggregate forms with size around 9 nm. In both the PEO composite and the F127 composites, the overall decrease in the intensity in the low q regime towards a constant intensity plateau suggests the concentration of larger aggregates decreases over time and the dispersion becomes homogeneous during thermal annealing. A similar response is observed in NP solutions where aggregation is controlled through tailored electrostatic or steric repulsion.[36] Well-dispersed, stabilized particles exhibit the low q plateau. The scaling becomes power law as the attraction forces between particles are modified to form larger fractal assemblies. The structural transition is also comparable to colloidal suspensions that coalesce during drying as observed by in-situ SAXS.[37,38] We rationalize the NP dispersion in the melt state because the polymer matrix mobility increases, allowing the NPs to access more bonding interactions with the PEO chains. The transition is independent of the NP loading, suggesting the NPs are not "too crowded" even up to 40 wt.%. As previously discussed, the NP shape and size do not change during the time resolved SAXS. We cannot conclude at this point if the NPs distribute randomly within the major domain, or if they pack into ordered lattice structure. It is important to consider that $I(q)$ is a convolution of many structures and electron density contrasts, such as difference between major and minor domains (q^*), the NP-NP dispersion (Guinier regime) and the NP size and shape (Porod regime at high q). Therefore, it is difficult to decouple the contribution from the individual components. The individual contribution of any one isolated feature must be extracted

assuming a model, which to our knowledge has not been developed for our material system with such length scales.

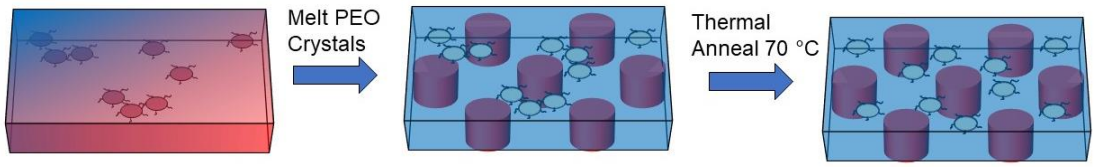

Figure 2.19 Schematic of proposed de-aggregation and re-dispersion of NPs after melting of PEO crystals within F127 template and during extended thermal annealing. NP assembly coincides with the formation of microphase separated domains.

We aim for high NP loadings within the nanoscale assembly. Therefore, the NP packing is quite constrained. Surprisingly, the domain spacing is independent of the NP loading above 20 wt.%. We expect the spacing to increase as NPs occupy additional volume in the major domain and induce chain stretching in the PEO block. In the strong segregation limit, d_0 is proportional to both R_g (proportional to block length N), and χ.[39] We assume χ increases with NP loading due to the enthalpic interaction (increase in χ_{eff}), which should contribute to an increase in d_0. However, there are additional contributions to balance between extra chain stretching, enthalpic interactions, and NP space filling that limits the confinement of the NPs in the small domain. For example, the PPO midblock is also penalized entropically under microphase segregation confinement. We propose that the PPO block reaches a maximum extension upon addition of 20 wt.% NP. One may expect the NPs to impinge and overlap at high NP loading, The interparticle spacing (δ) of spherical particles with uniform diameter is theoretically determined from the limit of maximum packing volume fractions (φ_m = 0.64) according the Eq. 2.3:[40]

$$\delta = d_{NP}\left[\left(1+\frac{1}{\varphi}+\frac{1}{\varphi_m}\right)^{1/3}-1\right] \qquad \text{Eq. 2.3}$$

Where δ is interparticle distance, d_{NP} is NP diameter, and φ is the particle volume fraction. We estimate that δ ranges from 4.4 to 2.2 nm for 10 to 40 wt.% loading respectively. The NP packing becomes congested at highest loading considering d_{NP} = 2.5 nm, but there is adequate space to disperse. The particles do not impinge on one another even at 40 wt.% allowing the PEO chains to sacrifice additional entropy and accommodate the decrease in δ up to 40 wt.%.

It is difficult to quantitatively analyze the SAXS data due to the previously discussed convolution of *I(q)*. The resolution of the measurement timescale (~ 10 minutes) is also much slower than SAOS. We cannot directly comment on comparing characteristic time scales of structure development between the two techniques. We further describe the dynamics of structure development through the application of various superposition principles to the time resolved rheological data. The application of ttS has been discussed in the literature in the form of time-cure superposition, which is used to describe the dynamics and characteristic relaxation times of a polymer network undergoing a crosslinking reaction.[24] Adolf et al. investigated the superposition of dynamic data collected before and after the critical gel point. A material at the gel point exhibits self-similar structure. Moving towards smaller or larger clusters of structure redefines the characteristic relaxation time of that cluster. Therefore, dynamic data can be shifted according the relationship between the extent of a reaction and the characteristic time. Adolf showed excellent superposition both above and below the gel point of a crosslinking epoxy and confirmed the scaling behavior with a previously reported dynamic theory.[24] The analysis served as an inspiration for understanding the validity and significance of ttS in the F127 composites. However, it is immediately apparent from the experimental data

that composites reside exclusively beyond the gel point. Typical power law scaling in $G' \sim G'' \sim \omega^{0.8}$ is observed at the high ω limit in the 10 wt.% sample. At all other loadings, the scaling of G' & G'' shows a structure well beyond the critical gel point.[41] Therefore, we only observe a liquid-to-solid transition from 0 to 10 wt. %. When considering the time dependent NP dispersion model proposed from the SAXS data (breaking up of aggregates during annealing), additional NP structure development pushes the dynamics further and further from the gel point. The extent of stress bearing structure grows as both the NP content increases and the NP structure evolves. It appears that the two processes are correlated through the surprising application of time-concentration superposition (tCS). We have shown that tCS visually represents the correlated relaxation processes across a wide range of timescales and concentrations. We could not locate any accounts in the literature of shifting structure development with respect to composition. Therefore, understanding the applicability of time-concentration superposition to the ttS data requires future investigation.

Additionally, the failure of ttS with PEO composite analog is puzzling assuming the structural evolution is directly related to NP structure formation. A comparison between the two composites suggests that microphase separation is necessary, perhaps facilitating a confinement in the NP dispersion, or a cooperative translation of stress through the two domains (i.e. physical crosslinking akin to spherical morphologies in linear tri-block copolymers). We cannot conclusively describe this phenomena at this time and require additional TRMS studies on the PEO homopolymer analogs with well-defined NP additives.

The thermo-structural and thermo-rheological properties are of interest from a processing standpoint. We understand that the strength and lifetime of the proposed hydrogen bonding interaction between NP and PEO is indirectly proportional to the temperature.[42] The temperature dependent relaxations of the neat F127 template are described by the shift factors a_T and the master curve in Figure 2.14. All experimental timescales are slower than the characteristic chain relaxation time, so the F127 melt behaves like a viscoelastic liquid. We observe that the relaxations change drastically when NPs are added to the systems. The fact that the dynamics change is a signature of NP reinforcement. Polymer dynamics near the particle interface become constrained and adopt a new temperature dependence depending on the number of interactions (which is increased through the NP loading).[43] BCP microphase segregation is also introduced with NP addition, which is well known to further push the characteristic relaxation time to longer time scales. The temperature dependent SAXS measurements presented in Figure 2.13 suggest that the microphase segregation is not static across the experimental temperature range. At loadings above the critical limit of 10 wt.%, segregation strength decreases linearly with increasing temperature, indicated by the increase in FWHM of q^*. Our assumption of the close relationship between hydrogen bonding lifetime and χ_{eff} is supported by these observations. A traditional first order ODT was expected as temperature increased but was not ultimately resolved. The failure of tTS typically accompanies a phase transition.[44] Therefore, the ability to generate a master curve from the ω dependent data suggests that the composites with loadings at or above 20 wt.% do not disorder and that the NPs are dictating the thermorheological response.

The trend of b_T in Figure 2.14b is surprising and implies that the modulus is increasing in the melt up to T = 140 °C. If the applied stress is maintained through an interconnected network of intermolecular interactions, the modulus could increase in the melt if the effective crosslink density increases. While the strength of the intermolecular interactions may be decreasing, the access to more PEO chains is increasing as the BCP mobility increases in the melt. A similar phenomenon was proposed by Kelarakis et al. for surface functionalized clay platelets in PEO melts, where η^* increased with increasing temperature.[45] Our observations are consistent with Kelarakis' observation, as F127 is highly mobile in the melt and can facilitate the additional interactions.

Despite the dense NP packing in the major domain, d_0 decreases linearly with increasing temperature in the strongly segregated composites. A decrease of 2 nm (from d_0 = 13.5 to d_0 = 11.5 nm) is significant on such a length scale, where the d_{NP} and interparticle spacing are on the order of 2-3 nm. Such a transition appears puzzling at first approximation because shrinking of the domains would further constrain the NP packing. Since d_0 is proportional to R_g and χ according the theoretical predictions, there should be a direct proportionality between d_0 and $1/T$.[46,47] As temperature increases, d_0 decreases and any discontinuity in the temperature dependence usually designates an ODT. However, the transition is not universal for all systems, as sometimes, $d_0(T)$ is the same above and below the ODT.[46] Therefore, it is important to simultaneously monitor both *I(q*)* and *FHWM(q*),* which are much stronger indicators of a phase transition. The theory is based on symmetric linear di-block systems, so the application to low N tri-block copolymers may require additional considerations. NPs should impact the trends in d_0 and FWHM according to reports by Zhao et al., who presented the effect of palladium (Pd) NPs on

ODT in poly(styrene)-*block*-poly(isoprene) (PS-*b*-PI) and poly(styrene)-*block*-poly(methyl methacrylate) (PS-*b*-PMMA) BCPs. A small concentration of NP (φ = 1 wt.%) decreased the ODT of PS-*b*-PI by 15 °C. The interactions were not enthalpically favored and the entropic penalty destabilized the microphase separated domains.[48] The characteristic decrease in d_0 was observed with increasing temperature in SAXS in the neat BCP, while for the nanocomposite, a slight increase in d_0 was observed in the vicinity of ODT. In the PS-*b*-PMMA system, the addition of Pd to the favorable PS domain increased the ODT by 10 °C and the microphase separation was stabilized.[49] We do not observe a discontinuity or an increase in d_0 during heating of the composites with 20 wt.% NP or more. However, the resolution of the temperature step (ΔT = 10 °C) is not sensitive enough to detect a subtle transition. The measurement could be improved by using smaller steps or high throughput synchrotron radiation to increase data density. The phase behavior that we can observe for composites with 20 wt.% or greater follow the response predicted for neat linear BCPs at temperatures far from T_{ODT}. Therefore, the NPs must increase χ_{eff} yet cooperatively allow the BCP chain dynamics to independently respond to the temperature change.

Multiple viscoelastic trends with NP loading are obvious from the master curves of $G'(\omega)$ and $G''(\omega)$ in Figure 2.14a. First, the magnitude of G^* increases with NP loading, as well as the degree of elasticity over all measured frequencies. There is a liquid-to-solid transition upon loading from 0 wt.% to 10 wt.% according to the plots of η^* and G^*. The transition appears to be independent of the presence of strong microphase segregation. The time resolved viscoelastic data shows the structure evolving further beyond the critical gel point with higher NP loading and NP structure development. We cannot conclude the

structural origins of the solid-like behavior from this data exclusively due to the convolution of many dynamic pathways between NPs, polymer chains, and microphase separated phases (much like the situation with SAXS data analysis). Therefore, further discussion of $H(\tau)$ in Figure 2.15 is recommended to understand the relaxation patters in the composite and the impact of NPs loading and intermolecular interaction. As previously described, F127 is a viscoelastic liquid with a wide range of power law scaling in $H(\tau)$. The shape of $H(\tau)$ is not entirely self-similar however. The longest mode seems to deviate from the power law regime, further evidence of a liquid far from the critical gel point. We observe a stark transition in the shape of $H(\tau)$ at 10 wt.% as the slope qualitatively increases. Power law scaling across short time scales curves into a plateau at longer times. The regions of self-similarity suggest the structure is clearly beyond the gel point at 10 wt.%. For the strongly segregated composites (above 20 wt.%), the scaling exponent is independent of NP loading on short timescales, but the kink at the plateau region becomes more pronounced. In this regime, the slope becomes positive. For a material near the gel point, a positive exponent in power law scaling of $H(\tau)$ signifies dynamics resulting from a glass transition as opposed to gelation (which adopts a negative slope).[32] Our initial hypothesis was that "glassy" dynamics may arise due to the high NP loading and confinement, which could be measured and resolved with rheology. In concentrated colloidal suspensions with repulsive particles, two relaxation processes (α and β) govern the dynamics. Fast β relaxations correspond to a NP exploring the local environment, or "cage" of neighbors. The α relaxations are cooperative long-range rearrangement of the NP cages and relax much slower. The processes are additive and are represented together by in $H(\tau)$ by a Baumgartel-Schausberger-Winter (BSW) spectrum.[32,50] As the particle system

approaches the liquid-solid transition, the α relaxations begin to dominate. The slope of $H(\tau)$ becomes positive and the characteristic relaxation time increases and begins to diverge. We observe solid relaxation processes in the NP/F127 composites at volume fractions well below the critical limit of crystal formation in colloidal suspensions (φ = 0.54).[51] Therefore, we cannot exclusively describe the dynamics by our understanding of exclusively α and β relaxations. There are repulsive, steric, and attractive enthalpic interactions all contributing to the proposed glassy relaxation processes. Qualitatively, the master curves are reminiscent of typical β relaxations at high ω and the onset of α at low ω. The spectra could be modeled by a BSW or broadened BSW, but the empirical model does not deconvolute the contribution of the different stress bearing structures. More work must be done to develop a system where the relaxation times can be compared (i.e. universal time-temperature relation) to systematically observe the passage through the liquid-solid transition with rheology, and to either isolate the impact of the enthalpic interactions or of the microphase separated morphology.

2.5 Conclusion & Future Directions

We investigate the role of NP loading on the viscoelasticity and phase behavior in microphase separated BCP composites in the limit of small d_0 and high φ of NP. Surface functionalized NPs selectively interact with one segment of a disordered BCP and induce self-assembly up to NP concentrations of 40 wt.%. The evolution toward a well-ordered nanocomposite is investigated with cooperative SAXS and time resolved rheology. Structure development and viscoelasticity scale with NP content, and a general master curve describing behavior across all NP loadings is constructed using time-time and time-concentration superposition. The structure is pushed further from the gel point with

increasing NP content and NP structure development. The melt rheological behavior transitions from liquid-like to solid-like behavior as described by frequency dependent dynamic modulus $G'(\omega)$ and $G''(\omega)$. The addition of stiff nanoparticles to the soft polymer matrix leads to a $x10^3$ increase in the magnitude of G^*. Thermorheological behavior and temperature dependent phase transitions are also investigated. No ODT is detected above 20 wt.%, suggesting the NP additives likely stabilize the microphase segregation and dominate the viscoelasticity of the composite.

Our initial research goals were to understand the impact of NPs on the viscoelasticity in the ordered and disordered state, and the impact of loading on achieving said states in additive driven assembly. In the ZrO_2/F127 system, the transition to an ordered, solid-like material at 20 wt.% did not provide a large window to explore the proposed phase transitions. The additive driven assembly was so effective that we could not detect T_{ODT} above 20 wt.%. The thermostructural and thermorheological properties of the composites exhibit clear trends with temperature, but do not identify any first order phase transitions. Therefore, we tried to model and describe the material properties in the ordered state and correlate the structure to the relaxation dynamics.

The key parameter we proposed to tune and investigate was the intermolecular interactions in the form of hydrogen bonding between NPs and PEO chains. Overall, the impact of hydrogen bonding was not exclusively isolated in this system. Steric repulsion forces between NPs were also present, as well as unaccounted intermolecular interactions from unknown ligands on the NP surface. To tackle the hydrogen bonding impact exclusively, we should utilize alternative additives with well-defined moieties. One possibility is POSS additives with octa(maleamic acid) (OMA) or octa(aminophenyl)

(OAP) functionalization. Preliminary experiments investigating phase transitions in POSS-OMA complexed with F108 were performed. POSS-OMA drives F108 into a cylindrical morphology with loading of 30 wt.%.[14] ODT of the BCP microphase segregation was clearly observed in temperature dependent SAXS upon heating ordered composites through T = 160 °C. In rheology, the response was contrary to the classical signature of the ODT (a drastic decrease in G^* with increasing temperature). The modulus rose rapidly by several orders of magnitude when heating beyond T = 110 °C and the material became stiffer and more solid-like. We hypothesize the increase is due to crosslinking between the maleamic acid functional groups which solidifies the POSS additives into an interconnected inorganic scaffold within the PEO domain. Crosslinking was confirmed by FTIR spectroscopy before and after thermal treatment.[14] POSS-OAP is incapable of thermally induced crosslinking and therefore more desirable to study phase transitions with cooperative rheology and scattering. Daga et al. demonstrated induced phase assembly of F108 at POSS-OAP loadings of 20, 30 and 40 wt. %.[14] In the future, the phase behavior and rheological properties of this system could also be investigated in the same manner and compared to the response of the SM acids, ZrO_2 and POSS-OMA materials. Stronger correlations from the separate SAXS and rheology characterizations require a quantitative analysis approach by comparing either the rate of change in FWHM and $G^*(\omega)$ versus temperature and time or developing a through a more robust model of the scattering intensity.

Our current investigation focused exclusively on linear viscoelastic behavior. The non-linear viscoelasticity of highly filled systems is fascinating and highly relevant for processing. Shear induced jamming of the crowded NPs is expected to occur, which

severely impacts the flow properties of the composite. Here, application of the "soft glassy rheology" (SGR) model may be useful.[52] The application of shear is also used to modify the microphase segregation and morphology, possibly to induce alignment or improve grain sizes.

The approach outlined in this chapter is rooted in a fundamental understanding of the highly filled NP/BCP composites. To practically utilize this material system, it is necessary to resolve the fundamentals of phase behavior, component interactions and dynamics. Our future goal is to apply this knowledge to drive future efforts in material design and feasible means of hybrid material fabrication. The structure-property relationships are not necessarily universal across different combinations of surface functionalized NP and BCP template. Each system will be entirely different depending on the design of the NP surface chemistry as well as the native BCP chain dynamics. For example, the particle-particle interactions between ZrO_2 play a dominate role in the structure development in cooperation with coordinated polymer-particle interactions. Therefore, it is important to develop expertise in both rheology and scattering characterization to access new material properties and transitional phenomenon for specific material systems. Such approaches are the key to provide further insight into the complex structure-property relationships of this class of nanocomposites.

2.6 References

(1) Kao, J.; Thorkelsson, K.; Bai, P.; Rancatore, B. J.; Xu, T. Toward Functional Nanocomposites: Taking the Best of Nanoparticles, Polymers, and Small Molecules. *Chem. Soc. Rev.* **2013**, *42* (7), 2654–2678.

(2) Lin, Y.; Daga, V. K.; Anderson, E. R.; Gido, S. P.; Watkins, J. J. Nanoparticle-Driven Assembly of Block Copolymers: A Simple Route to Ordered Hybrid Materials. *J. Am. Chem. Soc.* **2011**, *133*, 6513–6516.

(3) Moll, J. F.; Akcora, P.; Rungta, A.; Gong, S.; Colby, R. H.; Benicewicz, B. C.; Kumar, S. K. Mechanical Reinforcement in Polymer Melts Filled with Polymer Grafted Nanoparticles. *Macromolecules* **2011**, *44* (18), 7473–7477.

(4) Mendoza, C.; Gindy, N.; Wilhelm, M.; Fahmi, A. Linear and Non-Linear Viscoelastic Rheology of Hybrid Nanostructured Materials from Block Copolymers with Gold Nanoparticles. *Rheol. Acta* **2011**, *50* (3), 257–275.

(5) Kumar, S. K.; Benicewicz, B. C.; Vaia, R. A.; Winey, K. I. 50th Anniversary Perspective : Are Polymer Nanocomposites Practical for Applications? *Macromolecules* **2017**, *50*, 714–731.

(6) Cushen, J. D.; Otsuka, I.; Bates, C. M.; Halila, S.; Fort, S.; Rochas, C.; Easley, J. A.; Rausch, E. L.; Thio, A.; Borsali, R.; et al. Oligosaccharide/Silicon-Containing Block Copolymers with 5 Nm Features for Lithographic Applications. *ACS Nano* **2012**, *6* (4), 3424–3433.

(7) Yao, L.; Lin, Y.; Watkins, J. J. Ultrahigh Loading of Nanoparticles into Ordered Block Copolymer Composites. *Macromolecules* **2014**, *47* (5), 1844–1849.

(8) Chiu, J. J.; Kim, B. J.; Yi, G. R.; Bang, J.; Kramer, E. J.; Pine, D. J. Distribution of Nanoparticles in Lamellar Domains of Block Copolymers. *Macromolecules* **2007**, *40* (9), 3361–3365.

(9) Gai, Y.; Lin, Y.; Song, D.-P.; Yavitt, B. M.; Watkins, J. J. Strong Ligand–Block Copolymer Interactions for Incorporation of Relatively Large Nanoparticles in Ordered Composites. *Macromolecules* **2016**, *49* (9), 3352–3360.

(10) Daga, V. K.; Watkins, J. J. Hydrogen-Bond-Mediated Phase Behavior of Complexes of Small Molecule Additives with Poly(Ethylene Oxide- b -Propylene Oxide- b -Ethylene Oxide) Triblock Copolymer Surfactants. *Macromolecules* **2010**, *43* (23), 9990–9997.

(11) Tirumala, V. R.; Romang, A.; Agarwal, S.; Lin, E. K.; Watkins, J. J. Well Ordered Polymer Melts from Blends of Disordered Triblock Copolymer Surfactants and Functional Homopolymers. *Adv. Mater.* **2008**, *20* (9), 1603–1608.

(12) Tirumala, V. R.; Daga, V. K.; Bosse, A. W.; Romang, A.; Ilavsky, J.; Lin, E. K.; Watkins, J. J. Well-Ordered Polymer Melts with 5 Nm Lamellar Domains from Blends of a Disordered Block Copolymer and a Selectively Associating Homopolymer of Low or High Molar Mass. *Macromolecules* **2008**, *41* (21), 7978–7985.

(13) Fairclough, J. P. A.; Yu, G.-E.; Mai, S.-M.; Crothers, M.; Mortensen, K.; Ryan, A. J.; Booth, C. First Observation of an Ordered Microphase in Melts of Poly(Oxyethylene)-Poly(Oxypropylene) Block Copolymers. *Phys. Chem. Chem. Phys.* **2000**, *2* (7), 1503–1507.

(14) Daga, V. K.; Anderson, E. R.; Gido, S. P.; Watkins, J. J. Hydrogen Bond Assisted Assembly of Well-Ordered Polyhedral Oligomeric Silsesquioxane-Block Copolymer Composites. *Macromolecules* **2011**, *44* (17), 6793–6799.

(15) Kothari, R.; Winter, H. H.; Watkins, J. J. Rheological Study of Order-to-Disorder Transitions and Phase Behavior of Block Copolymer–Surfactant Complexes Containing Hydrogen-Bonded Small Molecule Additives. *Macromolecules* **2014**, *47* (22), 8048–8055.

(16) Bockstaller, M. R.; Mickiewicz, R. A.; Thomas, E. L. Block Copolymer Nanocomposites: Perspectives for Tailored Functional Materials. *Adv. Mater.* **2005**, *17* (11), 1331–1349.

(17) Balazs, A. C.; Emrick, T.; Russell, T. P. Nanoparticle Polymer Composites: Where Two Small Worlds Meet. *Science (80-.).* **2006**, *314* (5802), 1107–1110.

(18) Huh, J.; Ginzburg, V. V.; Balazs, A. C. Thermodynamic Behavior of Particle/Diblock Copolymer Mixtures: Simulation and Theory. *Macromolecules* **2000**, *33* (21), 8085–8096.

(19) Lee, J.-Y.; Thompson, R. B.; Jasnow, D.; Balazs, A. C. Entropically Driven Formation of Hierarchically Ordered Nanocomposites. *Phys. Rev. Lett.* **2002**, *89* (15), 155503.

(20) Mours, M.; Winter, H. H. Time-Resolved Rheometry. *Rheologica Acta*. 1994, pp 385–397.

(21) Winter, H. H.; Mours, M. The Cyber Infrastructure Initiative for Rheology. *Rheol. Acta* **2006**, *45* (4), 331–338.

(22) Song, D.-P.; Li, C.; Li, W.; Watkins, J. J. Block Copolymer Nanocomposites with High Refractive Index Contrast for One-Step Photonics. *ACS Nano* **2016**, *10* (1), 1216–1223.

(23) De Jeu, W. H. *Basic X-Ray Scattering for Soft Matter*, 1st ed.; Oxford University Press: Oxford, 2016.

(24) Adolf, D.; Martin, J. E. Time-Cure Superposition during Cross-Linking. *Macromolecules* **1990**, *23* (15), 3700–3704.

(25) Liu, Y.; Momani, B.; Winter, H. H.; Perry, S. L. Rheological Characterization of Liquid-to-Solid Transitions in Bulk Polyelectrolyte Complexes. *Soft Matter* **2017**, *13* (40), 7332–7340.

(26) Song, Y.; Zheng, Q. Linear Rheology of Nanofilled Polymers. *J. Rheol. (N. Y. N. Y).* **2015**, *59* (1), 155–191.

(27) Genix, A.-C.; Oberdisse, J. Structure and Dynamics of Polymer Nanocomposites

Studied by X-Ray and Neutron Scattering Techniques. *Curr. Opin. Colloid Interface Sci.* **2015**, *20* (4), 293–303.

(28) Winter, H. H. Three Views of Viscoelasticity for Cox-Merz Materials. *Rheol. Acta* **2009**, *48* (3), 241–243.

(29) Osterwinter, C.; Schubert, C.; Tonhauser, C.; Wilms, D.; Frey, H.; Friedrich, C. Rheological Consequences of Hydrogen Bonding: Linear Viscoelastic Response of Linear Polyglycerol and Its Permethylated Analogues as a General Model for Hydroxyl-Functional Polymers. *Macromolecules* **2015**, *48*, 119–130.

(30) Winter, H. H.; Mours, M. Rheology of Polymers near Liquid-Solid Transitions. *Adv. Polym. Sci.* **1997**, *134*, 165–234.

(31) Baumgaertel, M.; Winter, H. H. Determination of Discrete Relaxation and Retardation Time Spectra from Dynamic Mechanical Data. *Rheol. Acta* **1989**, *28* (6), 511–519.

(32) Winter, H. H. Glass Transition as the Rheological Inverse of Gelation. *Macromolecules* **2013**, *46* (6), 2425–2432.

(33) Genix, A.-C.; Oberdisse, J. Nanoparticle Self-Assembly: From Interactions in Suspension to Polymer Nanocomposites. *Soft Matter* **2018**, *14*, 5161–5179.

(34) Song, D.-P.; Li, C.; Colella, N. S.; Xie, W.; Li, S.; Lu, X.; Gido, S. P.; Lee, J.-H.; Watkins, J. J. Large-Volume Self-Organization of Polymer/Nanoparticle Hybrids with Millimeter-Scale Grain Sizes Using Brush Block Copolymers. *J. Am. Chem. Soc.* **2015**, *137*, 12510–12513.

(35) Faure, B.; Salazar-Alvarez, G.; Ahniyaz, A.; Villaluenga, I.; Berriozabal, G.; De Miguel, Y. R.; Bergström, L. Dispersion and Surface Functionalization of Oxide Nanoparticles for Transparent Photocatalytic and UV-Protecting Coatings and Sunscreens. *Sci. Technol. Adv. Mater.* **2013**, *14* (2), 1–23.

(36) Moro, S.; Parneix, C.; Cabane, B.; Sanson, N.; D'Espinose De Lacaillerie, J. B. Hydrophobization of Silica Nanoparticles in Water: Nanostructure and Response to Drying Stress. *Langmuir* **2017**, *33* (19), 4709–4719.

(37) Kim, S.; Hyun, K.; Kim, Y. S.; Struth, B.; Clasen, C.; Ahn, K. H. Drying of a Charge-Stabilized Colloidal Suspension in Situ Monitored by Vertical Small-Angle X-Ray Scattering. *Langmuir* **2013**, *29* (32), 10059–10065.

(38) Kim, S.; Hyun, K.; Struth, B.; Ahn, K. H.; Clasen, C. Structural Development of Nanoparticle Dispersion during Drying in Polymer Nanocomposite Films. *Macromolecules* **2016**, *49* (23), 9068–9079.

(39) Fredrickson, G. H.; Bates, F. S. Dynamics of Block Copolymers: Theory and Experiment. *Annu. Rev. Mater. Sci.* **1996**, *26* (1), 501–550.

(40) Park, D. Y. Direct Calculation of Inter-Particle Distance in Suspension by Image Processing. *Powder Technol.* **2018**, *330*, 252–258.

(41) Chambon, F.; Winter, H. H. Analysis of Linear Viscoelasticity of a Crosslinking Polymer at the Gel Point. *J. Rheol. (N. Y. N. Y).* **1986**, *30* (2), 367.

(42) Sijbesma, R. P.; Beijer, F. H.; Brunsveld, L.; Folmer, B. J. B.; Hirschberg, J. H. K. K.; Lange, R. F. M.; Lowe, J. K. L.; Meijer, E. W. Reversible Polymers Formed from Self-Complementary Monomers Using Quadruple Hydrogen Bonding. *Science (80-.).* **1997**, *278* (5343), 1601–1604.

(43) Berriot, J.; Montes, H.; Lequeux, F.; Long, D.; Sotta, P. Evidence for the Shift of the Glass Transition near the Particles in Silica-Filled Elastomers. *Macromolecules* **2002**, *35* (26), 9756–9762.

(44) Han, C. D.; Kim, J.; Kim, J. K. Determination of the Order-Disorder Transition Temperature of Block Copolymers. *Macromolecules* **1989**, 383–394.

(45) Kelarakis, A.; Giannelis, E. P. Crystallization and Unusual Rheological Behavior in Poly(Ethylene Oxide)-Clay Nanocomposites. *Polymer (Guildf).* **2011**, *52* (10), 2221–2227.

(46) Sakamoto, N.; Hashimoto, T. Order-Disorder Transition of Low Molecular Weight Polystyrene-Block-Polyisoprene. 1. SAXS Analysis of Two Characteristic Temperatures. *Macromolecules* **1995**, *28* (20), 6825–6834.

(47) Bates, F. S.; Rosedale, J. H.; Fredrickson, G. H. Fluctuation Effects in a Symmetric Diblock Copolymer near the Order – Disorder Transition. *J. Chem. Phys.* **1990**, *92* (1990), 6255.

(48) Zhao, Y.; Saijo, K.; Takenaka, M.; Koizumi, S.; Hashimoto, T. Order−Disorder Transition of Nanocomposites: Pd Nanoparticles in Polystyrene- Block - Polyisoprene Microdomain Templates. *Macromolecules* **2009**, *42* (14), 5272–5277.

(49) Zhao, Y.; Saijo, K.; Hashimoto, T. Order − Disorder Transition of Nanocomposites : Polystyrene- Block - Poly(Methyl Methacrylate) with Palladium Nanoparticles. *Macromolecules* **2013**, *46*, 957–970.

(50) Baumgaertel, M.; Schausberger, A.; Winter, H. H. The Relaxation of Polymers with Linear Flexible Chains of Uniform Length. *Rheol. Acta1* **1990**, *29*, 400–408.

(51) Joshi, Y. M. Dynamics of Colloidal Glasses and Gels. *Annu. Rev. Chem. Biomol. Eng.* **2014**, *5*, 181–202.

(52) Sollich, P. Rheological Constitutive Equation for a Model of Soft Glassy Materials. *Phys. Rev. E* **1998**, *58* (1), 738–759.

CHAPTER 3

RHEOLOGY OF MICROPHASE SEPARATED BRUSH BLOCK COPOLYMER MELTS: CORRELATING STRUCTURE AND DYNAMICS

3.1 Introduction & Project Motivation

Despite recent successes in the development of linear BCP templated nanocomposites, there are still several limitations preventing their wide spread use, notably slow dynamics of self-assembly, limited domain sizes, and poor control over long-range order. These limitations highlight current hurdles preventing rapid, scalable and low-cost fabrication of NP/BCP hybrid composites.[1] Alternate architectures of BCP are utilized as a result. In this chapter, we discuss the physical properties of a class of branched polymers referred to as brush (or bottlebrush) block copolymers (BBCP). BBCPs are large macromolecules with discrete block segments of densely grafted side chains tethered to a molecular backbone.[2] Highly extended backbone conformations and significant steric repulsion between grafted side chains suppress chain entanglements in the melt, resulting in rapidly self-assembly into diverse microphase separated morphologies.[2–4] The intrinsic structural features of BBCPs results in fast ordering dynamics (on the order of minutes with assisted thermal or solvent annealing) and large domain spacings over d_0 = 100 nm, offering opportunities for rapid and scalable manufacturing.[1] BBCP have found practical use in a variety of applications such as the development of photonic crystals, templates for porous scaffolds, elastomeric materials, and the bottom up fabrication of well-ordered nanocomposites.[5–13]

The synthesis and preparation of BBCPs is well described in the literature. The basic approach is to attach, or "graft" side chains onto a linear polymeric backbone. The

three primary synthetic routes are: “graft from”, “graft to”, and “graft through”.[2] The “graft from” approach begins by polymerizing a linear backbone decorated with reactive sites along the backbone, followed by initiating polymerization of the side chains from said reactive sites. The first successful report of “graft from” synthesis was by Beers et al. in which a methyl methacrylate backbone was synthesized by controlled atom transfer reversible polymerization (ATRP) with bromine terminated groups along the backbone.[14] Subsequent ATRP of the bromine groups was implemented to polymerize poly(styrene) (PS) and poly(butyl acrylate) (PBA) grafts off of the backbone, resulting in well-defined bottlebrush molecules that were directly imaged with atomic force microscopy (AFM). Conventional free radical polymerization resulted in large dispersity ($Đ$ = 2-3) while ATRP afforded low dispersity around $Đ$ = 1.3. A wide range of molecular weights (up to hundreds of kg/mol) were achieved with ATRP. The “graft from” approach expanded the complexity of the bottlebrush design. Core-shell BBCPs architectures are easily prepared by polymerizing block copolymers directly from the grafting points.[3,4] The core-shell BBCPs display a wide range of interesting solution properties and have been used as effective encapsulants.[15,16] However, multiple protection and deprotection steps are necessary during the grafting, which is synthetically cumbersome.[2] Other downsides of the “graft from” approach are that the backbone is limited to mainly methacrylate-based chemistries and uniform side chain length is not guaranteed, as the side chains are polymerized in-situ.

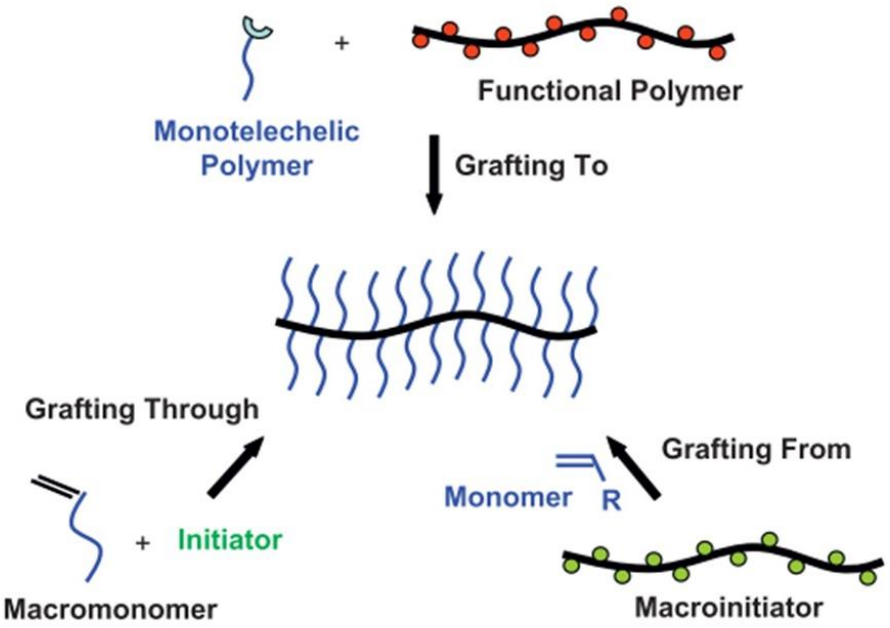

Figure 3.1 Three main strategies for preparing molecular brushes: grafting through, grafting onto, and grafting from. (Modified from Ref. 4)[4]

The "graft to" approach utilizes ATRP and "click" chemistries to prepare bottlebrushes by connecting pre-synthesized side chains to a molecular backbone.[4,17] The "graft to" takes sidechains that are designed and prepared ex-situ, unlike the "graft from" approach, expanding the customization of the molecular design. A broad catalog of backbone chemistries are demonstrated in the literature.[2] However, significant drawbacks arise in the sterics associated with attaching the side chain to the backbone. As grafting progresses, it becomes much harder to connects additional grafts within the dense array of side chains along the backbone, resulting in much lower graft densities (less than 100%) than the "graft from" method.[2] The incomplete conversion of grafts requires additional purification steps and results in larger dispersity.

Recently, an effective "graft through" approach was developed by Xia et al. using ring opening metathesis polymerization (ROMP) of norbornene modified macromonomers

(-NB MM).[18,19] ROMP emulates the side chain customization of the "graft to" method, in that the side chains are prepared ex-situ. Targeted side chain chemistry and molecular weight is designed before synthesis of the backbone. The side chains are further functionalized with a norbornene moiety at one of the chain ends, which is susceptible to ROMP via. Grubbs 2nd or 3rd generation catalyst.[20] ROMP results in well controlled product with narrow dispersity and predictable molecular weight. The cumbersome protection and deprotection in the "graft to" and "graft from" steps are eliminated. Homopolymer bottlebrushes are easily prepared with high grafting density (z) with one side chain per repeat unit in the backbone (z = 1). Copolymers are polymerized by mixing two types of macromonomer into one batch and polymerizing. The configuration is dependent on the reactivity ratios of the two monomers, often resulting in a random copolymer.[19] Well-defined A-B di-block copolymers (BBCP) are prepared with sequential ROMP. Here, the first block is polymerized by completely reacting macromonomer A, followed by addition of macromonomer B that polymerizes off of the reactive site at the end of the first block.[19] The total degree of polymerization, or total backbone length (N_{bb}) may be limited due to the reaction conditions in ROMP and the lifetime of the catalyst.[2] While N_{bb} > 1000 is easily achieved in the ATRP methods, ROMP approaches are typically limited to N_{bb} ~ 100's. This thesis focuses on BBCP synthesized by the "graft through" approach with norbornene macromonomers due to the simple chemistry and high graft densities.

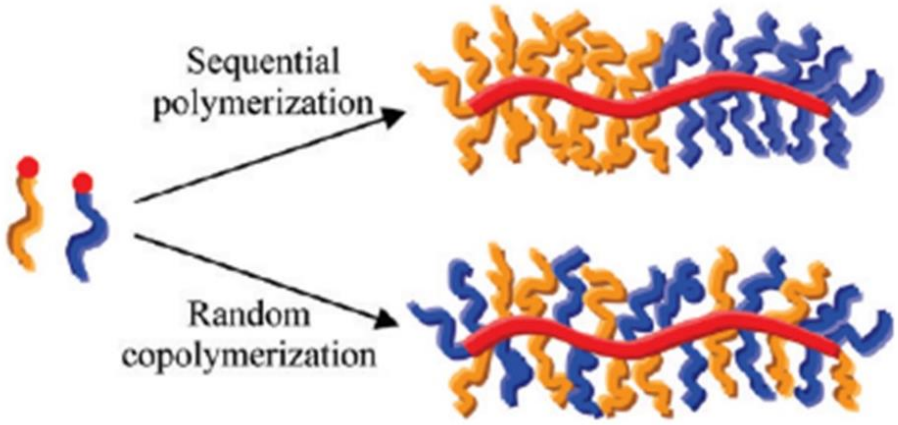

Figure 3.2 Schematic illustration of the synthesis of brush block copolymer through sequential addition (top) and brush random copolymer through random copolymerization (bottom) of MMs. (Modified from Ref. 19)[19]

The parameters that govern linear BCP microphase separation (N, χ, f) are certainly applicable to BBCPs. In A-B di-block BBCPs, additional structural features, such as side chain molecular weight ($M_{n\text{-}A}$), side chain asymmetry ($M_{n\text{-}A}/M_{n\text{-}B}$), grafting density ($z$), and graft distribution heavily influence the phase behavior and must also be considered.[21,22] A comprehensive understanding of the achievable morphologies across the phase diagram is essential when applying BBCPs as templates for nanomaterial fabrication. The self-assembly of di-block BBCPs has been investigated across a wide parameter space of block volume fraction (f), side chain length (N_{sc}), and backbone length (N_{bb}) in both bulk and thin film regimes.[23–26] The relationship between N_{bb} and domain spacing (d_0) is of interest for lamellar forming BBCPs, where lamellar period follows a power law scaling with N_{bb} ($d_0 \sim N_{bb}^{\alpha}$). Mean field theory predicts $\alpha = 0.66$ in the strong segregation limit (SSL) for symmetric LBCPs.[27] BBCPs appear to deviate from this theoretical prediction. Rzayev synthesized a series of high molecular weight poly(styrene)-*b*-poly(lactide) (PS-*b*-PLA) BBCPs with domain spacing ranging from $d_0 = 76$ to $d_0 = 163$ nm and observed a linear relationship between d_0 and N_{bb} ($d_0 \sim N_{bb}$).[26] The linear scaling behavior was unexpected

and suggested a highly extended backbone conformation when compared to Gaussian conformation of linear di-blocks. Further studies by Gu et al. and Hong et al. expanded upon this scaling relationship in two groups of symmetric PS-*b*-PLA BBCPs with variable side chain length (Short chain: PS-NB MM M_n = 2.4 kg/mol & PLA-NB MM M_n = 2.4 kg/mol. Long chains: PS-NB MM M_n = 4.3 kg/mol & PLA-NB MM M_n = 4.5 kg/mol).[24,25] Scaling exponents of α = 0.93 and α = 0.82 were observed for the short and long side chain systems respectively, again confirming the extended backbone conformation in these highly grafted BBCPs. Surprisingly, the short chains resulted in a more extended backbone due to a balance between side chain elasticity and interfacial energy contribution. The researchers proposed that the backbone will also stretch to minimize the cross-sectional area at the interface, which costs more energy in the long side chain system and leads to less backbone extension.[24] The interfacial effects were thought to be more influential that the additional steric hindrance along the backbone due to the longer side chains.[24] Additionally, Hong et al. considered the self-assembly of the PS-*b*-PLA BBCP with GISAXS on thin film samples processed via. solvent annealing.[25] The scaling exponents increased to α = 0.99 and α = 1.03 (short and long side chains respectively) indicating enhanced extension of the backbone when compared to the thermally annealed bulk samples. The increased scaling was attributed to swollen domains that became kinetically trapped during the solvent evaporation.[25] Dalsin et al. investigated the trends in α over a wide range of MW (M_n = 28.3 kg/mol – 696 kg/mol) in atactic poly(propylene)-*block*-poly(styrene) (aPP-*b*-PS) BBCPs of short side chains length (aPP-NB MM M_n = 2.1 kg/mol, PS-NB MM M_n = 4.0 kg/mol).[23] Surprisingly, α was not constant across the wide MW range. At low MW, α < 0.3 and increased to α = 0.88 at the highest MW. Again, the

large scaling exponent was consistent with the previous results for an extended backbone conformation. However, the small MW samples showed a significantly decreased exponent because at low N_{bb}, the lamellar period is dominated by the side chain length rather than the backbone length. The architecture more closely resembles a star-like polymer configuration rather than an elongated worm-like tube.[23] Most recently, Lin et al. explored α through a continuum between linear and bottlebrush architecture by varying z in a series of PS-*b*-PLA BBCPs (Figure 3.3).[21] Here, α systematically increases from the predicted 0.66 at $z = 0$ to highly extended conformations at maximum grafting of $z = 1$. These trends were a direct result of changes in the polymer architecture, rather than the segregation strength, further showing the importance of the side chains structure and backbone conformation on the unique self-assembly of BBCPs.

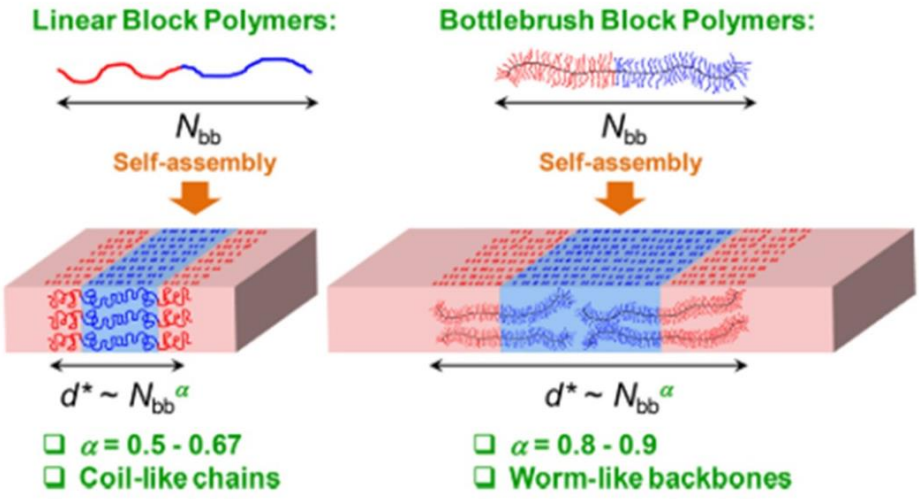

Figure 3.3 Self-assembly of linear and bottlebrush di-block copolymers into lamellae. (Modified from Ref. 21)[21]

Systems with highly asymmetric side chain length ($M_{n\text{-}A} \neq M_{n\text{-}B}$) are less understood. Gai et al. presented a preliminary phase map of a series of poly(styrene)-*block*-poly(ethylene oxide) (PS-*b*-PEO) BBCPs with variable side chain lengths (PS-NB MM M_n = 3.5 kg/mol, PEO-NB MM M_n = 0.75, 2 & 5 kg/mol) (Figure 3.4). The lamellar

morphology persisted up to exceptionally asymmetric volume fractions from f_{PEO} = 0.28 – 0.72, much higher than that predicted in a theoretical LBCP phase diagram.[28] The lamellar window was independent of the side chain length and the side chain asymmetry ($M_{n\text{-}PS}/M_{n\text{-}PEO}$). The desire to minimize the area at the domain interface drives the order-to-order transition.[29] Backbone stiffness opposes the transition to cylindrical morphology until exceptionally asymmetric limits, where the interfacial curvature required to form a different morphology is finally obtained.[12] Simulations suggest that the order-to-order transition is driven more from the side chain asymmetry rather than the volume fraction, but only at exceptionally large side chain asymmetries.[30,31] While several phase maps are presented describing the diversity of nanostructures and morphologies, a complete phase diagram (χN vs. f) has not been experimentally determined for any BBCP system, of symmetric or asymmetric side chain length. It is apparent that careful selection and design of the side chain chemistry and length is crucial for obtaining target morphologies and length scales in BBCP based nanomaterials.

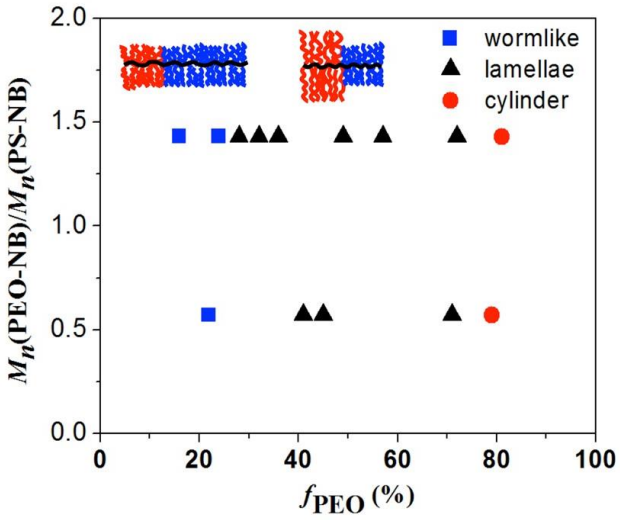

Figure 3.4 Summary of PS-*b*-PEO BBCP phase transition: a plot of side chain length ratio (M_n(PEO-NB)/M_n(PS-NB)) versus PEO volume fraction (f_{PEO}). (Modified from Ref. 28)[28]

While not considered in this thesis, recent demonstrations of tuning graft density and distribution have expanded the scope of our understanding of bottlebrush self-assembly. Chemistries developed by Chang et al. precisely control the space between grafted side chains during "graft through" synthesis with ROMP by adding small molecule norborneyl dialkylesters.[22,32] The diesters act as diluents along the backbone, introducing a blank repeat unit without a sidechain. A complete analysis of the reactivity ratio between various diluents and traditional macromonomers (PS-NB, PLA-NB, and PDMS-NB) led to the development of materials with precise graft densities and distributions along the backbone.[32] The modulation of these two structural parameters was found to impact the self-assembly of three PS-*b*-PDMS BBCPs with equal composition (f = 0.5) but different graft distributions. The graft density was either uniform across the entire molecule or configured in a gradient distribution (with increasing density away from the interface or towards the interface). The BBCP with uniform grafting along the backbone assembled into highly asymmetric lamellae due to the extended backbone conformations in both domains. The samples with higher graft density at the interface self-assembled into the most symmetric lamellae because the backbones segments away from the interface were lightly grafted, more flexible, and could accommodate the backbone asymmetry and demands for equal block volumes.[22] Control of graft distribution was also utilized by Jiang et al. to copolymerize *exo*- and *endo*-norbornene capped macromonomers together in a "one-pot" approach resulting in well-defined gradient copolymers.[33] Kinetic studies revealed that *exo*-PS and *endo*-PLA could be polymerized into a gradient distribution of side chains within the backbone, resulting in copolymers with a mixed interface. The simple straightforward synthesis was the first successful demonstration of gradient BBCP

structures. The mixed interface impacted the phase behavior and resulted in the formation of cylindrical morphology. The structure contrasted analogous di-block BBCPs of equivalent volume fraction and side chain length that preferred a lamellar morphology.

While BBCPs are primarily used to achieve large d_0, highly grafted Janus architectures have shown promise in templating small sub-10 nm spacings on rapid time scales.[34–37] The Janus MMs are prepared by tethering two unique side chains to a single norbornene unit and polymerizing through with ROMP. The side chains microphase separate due to chemical incompatibility and arrange on opposite sides of the backbone. Therefore, the backbone defines the interface between the two domains and d_0 is driven by the side chain dimensions rather than the backbone. Incorporation of short side chains supports rapid self-assembly as the entanglements are minimized.

The ability to rapidly self-assemble is a consistent highlight of the densely grafted bottlebrush architecture, often credited to the lack of entanglements resulting from the short side chain length and backbone extension. Indeed, the densely grafted brush motif impacts the chain dynamics and rheological properties as seen in small amplitude oscillatory shear and creep experiments on homopolymer bottlebrushes synthesized by the "graft through" approach.[38–42] The full dynamic modulus response highlights the relaxation patterns of each component of the architecture, from the individual side chains to the entire molecular backbone. In macromolecules with short side chain length, the formation of an entanglement relaxation is completely suppressed. Dynamic moduli $G'(\omega)$ and $G''(\omega)$, transition directly from liquid behavior at low frequencies to glassy behavior at the highest frequencies (Figure 3.5). As side chain length increases, a plateau in $G'(\omega)$ emerges in the fast relaxation regime, corresponding to the entanglement of those side chains. The

dynamic behavior on longer times scales is driven by the size of the backbone. In this intermediate frequency regime, backbones behave as unentangled semi-flexible chains and the relaxation process and can be described by classical Gaussian chain dynamics theory.[38] Both Rouse-like and Zimm-like scaling behaviors are observed. Only at exceptionally large backbone length, an additional relaxation plateau may emerge leading to "double relaxation" behavior of both side chains and backbone.[41] In the low frequency limit, bottlebrushes exhibit terminal scaling behavior of $G'(\omega) \sim \omega^2$ and $G''(\omega) \sim \omega^1$. Recently, Haugan et al. explored the continuum between linear polymers and densely grafted bottlebrushes by tuning *z*. Bottlebrush backbones with high grafting density began to entangle at exceptionally long backbone length ($N_{bb} >> 1000$) as reptation dynamics set in.[42] The critical backbone length for entanglement was found to be a function of graft density, and various dynamic regimes describing the side chain conformations were identified according to the plateau modulus.

The relaxation processes in microphase separated materials (both linear and brush architecture) are quite different from the homogeneous melts.[43–46] Blocks of exceptionally large MW entangle within the microphase separated domain. The interface between domains additionally confines the polymer chains, which must relax through a hindered reptation process or through arm retraction relaxations. The terminal response transitions to non-liquid scaling, of which is dependent on the condition of the morphology and the defects in the ordered structure. Therefore, the microphase separation in the BBCP systems introduces new considerations for structure-property relationships in comparison to the well-studies homopolymer brush systems.

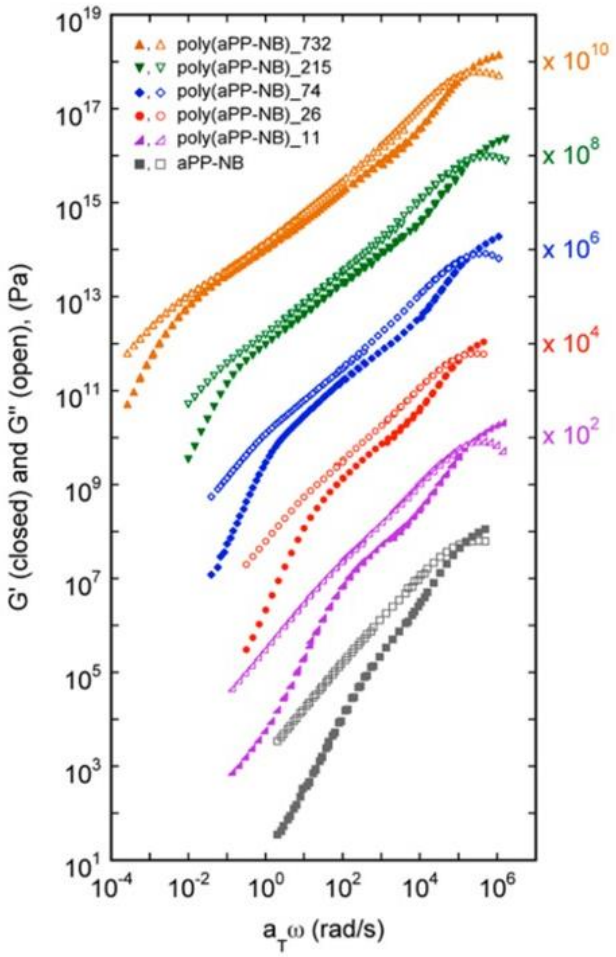

Figure 3.5 Dynamic master curves of G' (closed symbols) and G'' (open symbols) for aPP-NB and poly(aPP-NB)s at a reference temperature of $T_{ref} = T_g$ +34 °C. Curves vertically shifted using the indicated scale factors. (Modified from Ref. 38)[38]

The interplay of the linear viscoelasticity of the brush architecture and those typically associated with entangled LBCPs is puzzling up until this point. There are no direct reports focused on the dynamics of neat BBCP systems with high grafting density and short side chain lengths. A few studies have been conducted on various comb-like/graft copolymer systems, but with much lower grafting densities than the architectures of interest ($z = 1$).[47–51] Dynamic mechanical analysis was conducted on PS-*b*-PEO-*b*-PS ABA triblock brush copolymer ion gel materials by Bates et al., but the full dynamic response was not presented in detail.[52,53] A comprehensive understanding of relaxation and flow properties

through rheological characterization is crucial for understanding the origins of rapid self-assembly in BBCPs, and for the future implementation of these materials in an industrial setting, such as flow coating or roll-to-roll processing.

In this chapter, we wish to investigate this interplay of structure and dynamic properties in model BBCPs with short side chains and $z = 1$ using SAXS and rheology. We explore the linear viscoelasticity and molecular dynamics of BBCPs in the microphase segregated melt state. We test a model system of poly(styrene)-*block*-poly(ethylene oxide) BBCPs with short side chain lengths below entanglement molecular weight and precise control over side chain length (N_{sc}), block composition (f), and overall backbone length (N_{bb}). We specifically study the dynamic mechanical response ($G'(\omega)$ and $G''(\omega)$) over a wide frequency range, as well as the relaxation time spectrum $H(\tau)$. We expect the BBCP materials to combine the response of bottlebrush homopolymers with the heterogeneous microphase segregation characteristics of linear BCPs, each distinctly contributing to the viscoelastic behavior. By combining both dynamics into one molecular design, a new structure-property relationship may emerge.

3.2 Experimental

3.2.1 Synthesis and Material Design

A series of AB di-block poly(styrene)-*block*-poly(ethylene oxide) (PS-*b*-PEO) BBCPs were synthesized by sequential ring opening metathesis polymerization (ROMP) of norbornene modified macromonomers (MM) according to established procedures (Figure 3.6).[28,54] The side chain lengths were controlled at MW below the entanglement molecular weight to take advantage of the fast ordering dynamics observed for such polymers in previous studies.[1,24] Side chain MW of each MM are as follows: PS-NB MM

M_n = 2.9 kg/mol or 3.5 kg/mol & PEO-NB MM M_n = 5 kg/mol. The resulting polymers exhibit an asymmetric molecular shape between each block due to a mismatch between side chain length (Figure 3.7). Chemical characterization (NMR and GPC) available in Appendix A.

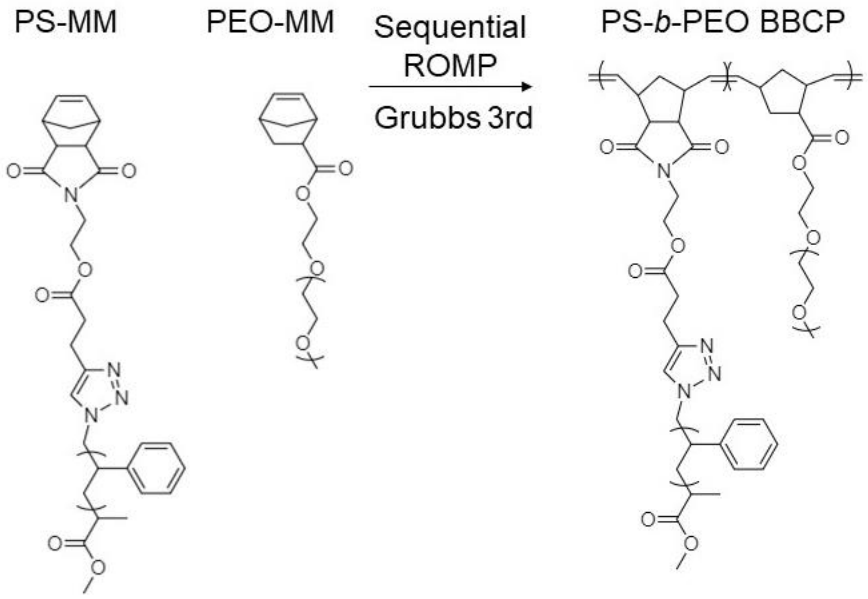

Figure 3.6 Synthetic route for sequential ring opening metathesis polymerization (ROMP) of PS-NB MM and PEO-NB MM to form PS-*b*-PEO BBCPs via. Grubbs 3rd generation catalyst

Two series of BBCPs were prepared to investigate the impact of two structural design parameters on the rheological properties and phase behavior: composition of PEO block (f_{PEO}) and overall backbone degree of polymerization (N_{bb}). The f_{PEO} series was synthesized using PS-NB MM M_n = 3.5 kg/mol & PEO-NB MM M_n = 5 kg/mol. Composition was controlled by varying the feed ratio of macromonomers during sequential polymerization and ranges from f_{PEO} = 0.24 – 0.81. Full molecular characteristics are presented in Table 3.1 for the five samples of the f_{PEO} series.

The N_{bb} series was synthesized using PS-NB MM M_n = 2.9 kg/mol & PEO-NB MM M_n = 5 kg/mol. The overall molecular weight was varied by keeping the feed ratio of the two blocks equal and constant (f_{PEO} = 0.50) while changing the catalyst-to-monomer ratio. N_{bb} ranges from 21 – 119. While the overall composition of the BBCP is symmetric, there are additional asymmetries to consider between each block. For example, the ratio of the calculated block backbone length is asymmetric ($N_{bb\text{-}PS}/N_{bb\text{-}PEO} \approx 1.6$). The asymmetry accommodates the significant difference in side chain length between each block ($N_{sc\text{-}PS}$ = 28, $N_{sc\text{-}PEO}$ = 114) while maintaining equal mass ratio. On the PS side, $N_{sc\text{-}PS} \leq N_{bb\text{-}PS}$ and the molecular shape resembles a traditional worm-like structure, while in the PEO block, $N_{sc\text{-}PEO} > N_{bb\text{-}PEO}$ and the shape is more like a star-like polymer rather than the conventional worm. There is also a contrast in side chain flexibility. The short PS side chains are much stiffer and more sterically hinder than the longer, more flexible PEO side chains. Overall, the BBCP possess a PS block with a long backbone and short, stiff side chains and a PEO block with a shorter backbone and longer flexible side chains. Molecular characteristics are presented in Table 3.2 for the five samples in the N_{bb} series.

Self-assembly dynamics and viscoelasticity of select BBCPs were directly compared to analogous linear AB di-block PS-*b*-PEO purchased from Polymer Source Inc. Three polymers were used as received with f_{PEO} = 0.22 (M_n = 49 kg/mol), f_{PEO} = 0.47 (M_n = 76 kg/mol), and f_{PEO} = 0.81 (M_n = 88 kg/mol).

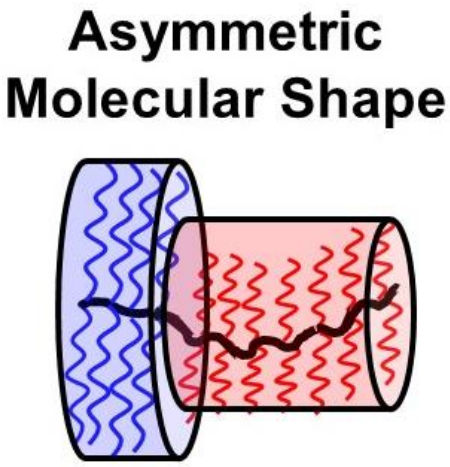

Figure 3.7 Schematic representation of PS-*b*-PEO BBCP with asymmetric molecular shape. At equal composition (f_{PEO} = 0.5), difference in PS (red) and PEO (blue) side chain length results in blocks with asymmetric backbone degree of polymerizations

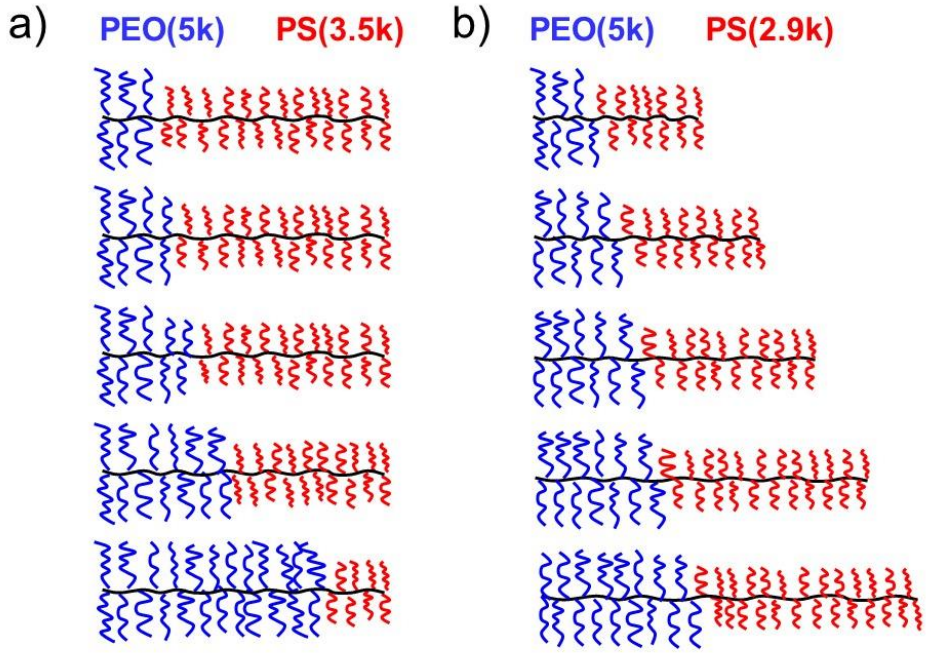

Figure 3.8 (a) Molecular design of PS-*b*-PEO composition series (variable f_{PEO}) with PS side chains (3.5 kg/mol) and PEO side chains (5 kg/mol). **(b)** Molecular design of PS-*b*-PEO with variable backbone length N_{bb} with PS side chains (2.9 kg/mol) and PEO side chains (5 kg/mol).

Table 3.1 Molecular characteristics of PS-*b*-PEO BBCPs with variable f_{PEO}

PS-*b*-PEO Sample Name[a]	*Mw* (kg/mol)[b]	$Đ$[b]	f_{PEO}[c]	N_{bb}[d]	$N_{bb\text{-}PS}$[d]	$N_{bb\text{-}PEO}$[d]	d_0 (nm)[e]
f-24	715	1.28	0.24	148	121	27	43.6
f-28	320	1.10	0.28	76	60	16	41.9
f-32	346	1.12	0.32	80	60	20	51.1
f-49	474	1.09	0.49	105	63	42	59.6
f-81	401	1.16	0.81	75	19	56	34.0

[a]BBCPs are labeled as "*f*-X", where "X" = composition of PEO in di-block. [b]Weight average molecular weight (M_w) and polydispersity ($Đ$) were determined by GPC-MALLS. [c]Theoretical volume fraction of PEO (f_{PEO}) was calculated using mass ratios of PS and PEO obtained from ^{1}H NMR spectra and approximate bulk densities (1.05 and 1.09 g/cm^3 for PS and PEO, respectively). [d]Block backbone degree of polymerizations ($N_{bb\text{-}PEO}$ & $N_{bb\text{-}PS}$) and overall backbone degree of polymerization (N_{bb}= $N_{bb\text{-}PEO}$ + $N_{bb\text{-}PS}$) were calculated using absolute molecular weights and $Đ$ as measured by GPC and mass fraction from NMR. [e]Domain spacings (d_0) of microphase separated BBCPs were calculated using the equation d-spacing = $2\pi/q^*$, where q^* corresponds to the primary peak from small angle X-ray scattering in nm^{-1}.

Table 3.2 Molecular characteristics of PS-*b*-PEO BBCPs with variable N_{bb}

PS-*b*-PEO Sample Name[a]	*Mw* (kg/mol)[b]	$Đ$[b]	f_{PEO}[c]	N_{bb}[d]	$N_{bb\text{-}PS}$[d]	$N_{bb\text{-}PEO}$[d]	d_0 (nm)[e]
N_{bb}-21	86	1.14	0.51	21	13	8	29.3
N_{bb}-40	164	1.12	0.51	40	25	15	36.9
N_{bb}-55	228	1.11	0.51	55	34	21	42.3
N_{bb}-72	304	1.14	0.51	72	45	27	65.4
N_{bb}-119	558	1.27	0.50	119	74	45	90.0

[a]BBCPs are labeled as "N_{bb}-X", where "X" = Total backbone degree of polymerization (N_{bb}). [b]Weight average molecular weight (M_w) and polydispersity ($Đ$) were determined by GPC-MALLS. [c]Theoretical volume fraction of PEO (f_{PEO}) was calculated using mass ratios of PS and PEO obtained from ^{1}H NMR spectra and approximate bulk densities (1.05 and 1.09 g/cm^3 for PS and PEO, respectively). [d]Block backbone degree of polymerizations ($N_{bb\text{-}PEO}$ & $N_{bb\text{-}PS}$) and overall backbone degree of polymerization (N_{bb}= $N_{bb\text{-}PEO}$ + $N_{bb\text{-}PS}$) were calculated using absolute molecular weights and $Đ$ as measured by GPC and mass fraction from NMR. [e]Domain spacings (d_0) of microphase separated BBCPs were calculated using the equation d-spacing = $2\pi/q^*$, where q^* corresponds to the primary peak from small angle X-ray scattering in nm^{-1}.

3.2.2 Sample Preparation

A 5 wt.% solution of BBCP in anhydrous dichloromethane (DCM) was prepared and drop-cast onto glass substrate under a nitrogen atmosphere. After the solvent was evaporated, the dried films were collected with a razor blade. Approximately 30 mg of bulk material was packed into a circular metal mold (diameter = 8 mm, thickness = 1 mm) and sandwiched between pieces of Kapton tape. The samples were annealed under vacuum for 1 or 4 h. at T = 110 °C. The samples were subsequently cooled to room temperature. LBCP materials were used as received and prepared with identical protocols and thermally annealed for 24 h at T = 120 °C.

3.2.3 Characterizations

X-ray Scattering: Microphase segregation and domain spacing (d_0) were measured with small angle X-ray scattering (SAXS) using a Ganesha SAXS-LAB instrument with Cu Kα 0.154 nm line on SAXS or USAXS mode. X-ray beam area was 0.04 mm^2. In-situ temperature controlled SAXS was performed with a Linkam HFS600E-P temperature stage over a temperature range of T = 25 – 200 °C using increments of 30 °C (T = 25, 50, 80, 110, 140, 170, and 200 °C). In some cases, the samples were directly heated from room temperature to elevated temperatures of T = 80 °C or T = 110 °C. The heating rate was 10 °C/min followed by 5-minute thermal equilibration before each isothermal measurement. Domain spacings $d_0 = 2\pi/q^*$ were determined from q^*, the primary peak position in nm^{-1}.

Electron Microscopy: Cryo-microtoming (Leica Ultracut microtome) was used to cut bulk samples into 50 nm thin films. Sections were collected using a carbon film supported by copper grids. Subsequent ruthenium tetroxide (RuO_4) staining was applied to improve

contrast between PS (light) and PEO (dark) domains. The prepared thin films were imaged by Transmission Electron Microscopy (TEM) on a JEOL 2000FX (200 kV).

Rheology: Dynamic moduli $G'(\omega)$ and $G''(\omega)$ were measured using small-amplitude oscillatory shear (SAOS) from ω = 1 - 100 rad/s in a Malvern Kinexus rotational rheometer with an 8-mm parallel plate geometry. Measurements were conducted within the linear viscoelastic regime (LVR) at strain amplitudes of γ = 1 %. SAOS frequency sweeps were obtained over a temperature range from T = 60 °C to 170 °C at 10 °C intervals. The elevated temperatures avoided contributions from PEO crystallization. LBCPs characterization ranged from T = 110 to 170 °C, below which the glass transition (T_g) of PS began to interfere with rheological measurements. The time−temperature superposition (tTS) principle was found to apply over the experimental temperature range. Rheological data were analyzed using IRIS Rheo-Hub 2018 software.[55]

Differential Scanning Calorimetry: Differential scanning calorimetry (DSC) analysis was performed on TA Instruments Q200-1390-RCS. The melting enthalpy of PEO domain was measured on the second heating scan from T = -50 to 120 °C at a rate of 10 °C/min. T_g of PS domain was identified using midpoint method from TA Universal Analysis.

3.3 Results

3.3.1 Phase Behavior of PS-*b*-PEO f_{PEO} Series

After thermal annealing for 1 h. at T = 110 °C, the PS-*b*-PEO BBCPs in the f_{PEO} series strongly microphase segregate according to the presence of a primary scattering peak q^* in 1-D SAXS spectra (Figure 3.9a). The rapid self-assembly on timescales of 1 h. is consistent with previous results of fast ordering dynamics in BBCPs with short side chain length.[1,24] The domain spacings of resulting nanostructures ranged from d_0 = 34 to d_0 = 59

nm. An additional scattering feature at q = 0.4 nm^{-1} emerged due to presence of PEO crystalline lamellae in the samples with high f_{PEO}. The composition significantly impacts the phase behavior and resulting morphology in this series of PS-*b*-PEO BBCPs, and has been described in detail by Gai et al.[28] At the lowest f_{PEO} (*f*-24), a disordered "wormlike" morphology is observed, consisting of a PEO minor phase embedded in a PS matrix. While a primary scattering peak is observed, the absence of any higher order reflection peak indicates weak periodicity and long-range order of the microphase-segregated structure. The worm-like structure was confirmed by TEM analysis (Figure 3.9b). When approaching the equal composition of f_{PEO} (*f*-28, *f*-32, and *f*-49), a lamellar morphology arises according the peak ratio of higher order reflections to the primary scattering peak (q^*:2q^*:3q^*) as well as complementary TEM images (Figure 3.9c). At the highest f_{PEO} (*f*-81), a cylindrical morphology consisting of PS cylinders in a PEO matrix is observed (Figure 3.9d).

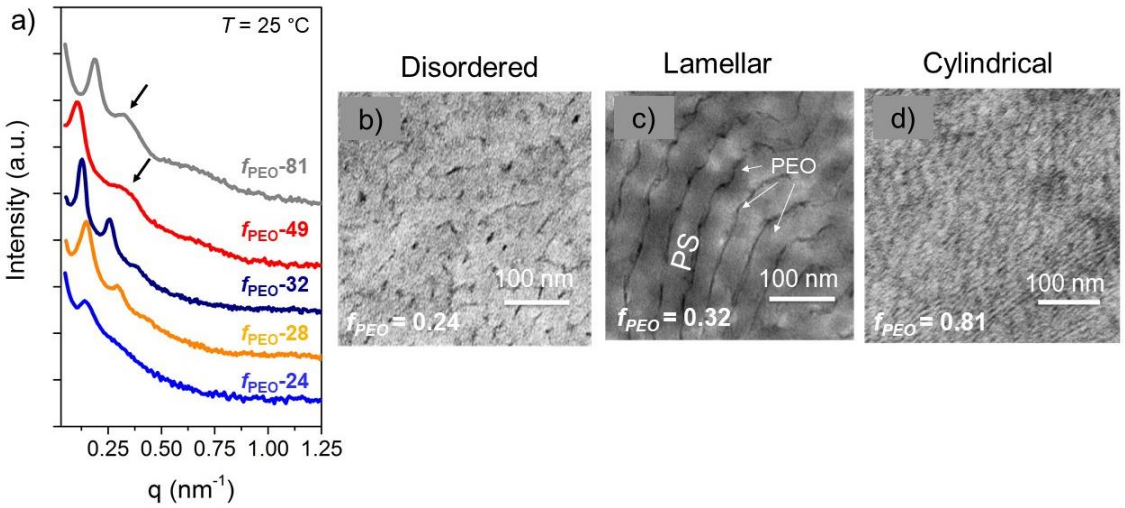

Figure 3.9 (a) Room temperature 1-D SAXS spectra of microphase separated PS-*b*-PEO BBCPs after thermal annealing. Arrow indicates scattering from PEO crystals. **(b) (c) (d)** TEM images of various morphologies for the PS-*b*-PEO BBCPs as a function of block composition. PEO domains (dark) are stained to contrast PS domains (light) (Modified from Ref. 28)[28]

In some cases, the scattering from PEO crystallization extends over the expected q range of high order scattering peaks of the microphase segregated structure. Therefore, the samples were heated above the melting temperature of PEO (T_m ~65 °C) in temperature-controlled SAXS, at which point the PEO peaks disappear and higher order reflections were weakly observed. The lamellar morphology was confirmed for *f*-49 by peak ratios of q^*:2q^*:3q^* (Figure 3.10a), while cylindrical morphology was confirmed for *f*-81 with peak ratios of q^*: √3q^*.

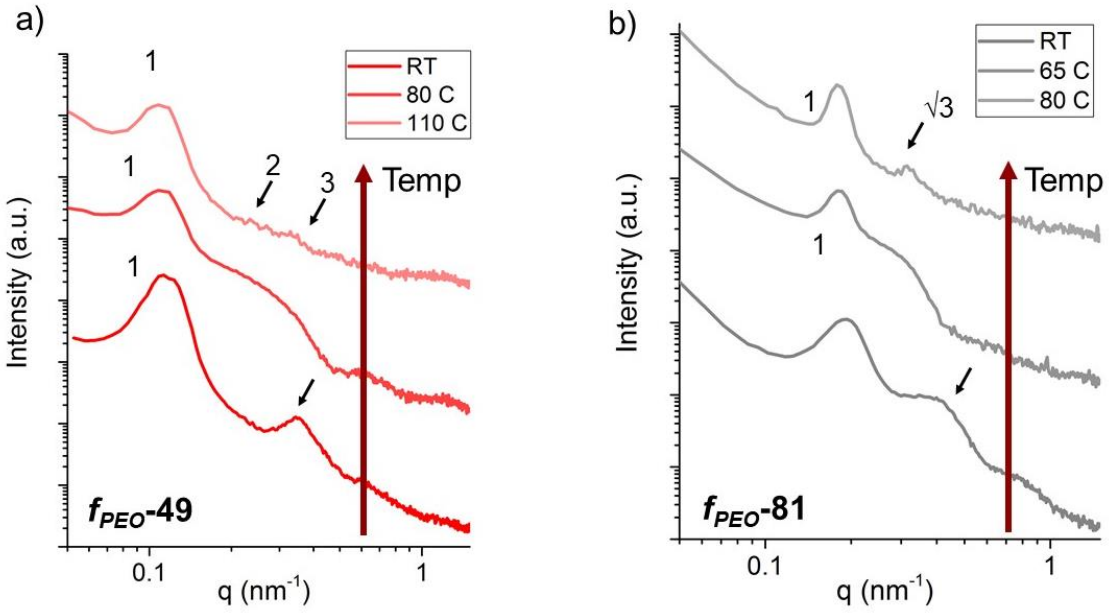

Figure 3.10 (a) Temperature-controlled SAXS of *f*-49 upon heating from room temperature to T = 80 °C and T = 110 °C. After heating the scattering signal from PEO lamellae disappears. At T = 110 °C, weak second- and third-order peaks are resolved at peak ratios q^*:2q^*:3q^* indicating lamellar morphology. **(b)** Temperature-controlled SAXS of *f*-81 upon heating from room temperature to T = 65 °C and T = 80 °C. After heating the scattering signal from PEO lamellae disappears. At T = 80 °C a higher order peak may be resolved at peak ratio q^*:√3q^* indicating cylindrical morphology. (Modified from Ref. 54)[54]

3.3.2 Linear Viscoelasticity of PS-*b*-PEO f_{PEO} Series

The dynamic properties of the PS-*b*-PEO BBCPs were determined by SAOS in the melt state after thermal annealing. The full dynamic response of the BBCPs was tested for

applicability of time-temperature superposition (tTS). The Booij−Palmen plot (phase angle (δ) versus complex modulus (G^*)) is a useful tool for investigating the rheological behavior of bulk polymeric materials as well as confirming the applicability of tTS.[56,57] Booij−Palmen plots were constructed from the dynamic data and are plotted in Figure 3.11, where we use the normalized phase angle ($2\delta/\pi$) versus complex modulus (G^*). In general, tTS can be applied if the individual frequency sweeps at each temperature collapse onto a single curve. The material is considered "thermorheologically simple" if the condition is satisfied. Overall, the BBCP samples display thermorheological simplicity over the experimental temperature range. However, the exception is *f*-81, which does not obey tTS as indicated by the lack of superposition of the $\delta(G^*)$ curves. Here, *f*-81 simply behaves like a soft solid with $G^* \sim 10^4$ Pa. For PS-*b*-PEO BCPs, as f_{PEO} increases, thermorheological simplicity breaks down. We note that a similar phenomenon was identified by Bates et al. The dynamic moduli of PS-*b*-PEO-*b*-PEO triblock brush block copolymers with high volume fraction of PEO (f_{PEO} = 0.75) showed soft solid behavior ($G^* \sim 10^3$ Pa) as well as failure of tTS over a temperature range of 40−105 °C.[53]

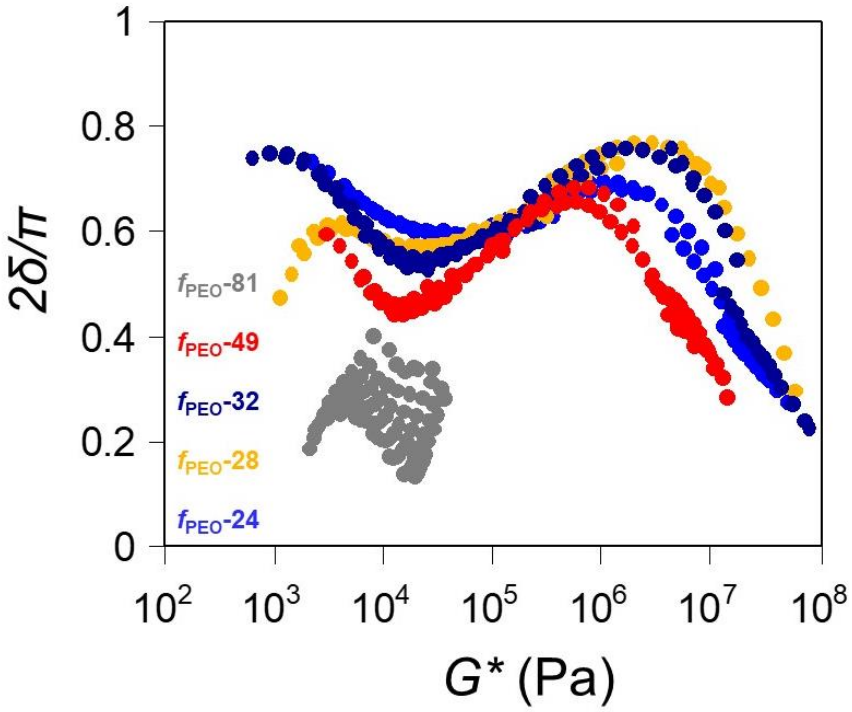

Figure 3.11 Booij−Palmen plot of BBCP materials *f*-24, *f*-28, *f*-32 *f*-49, and *f*-81. tTS cannot be applied to samples with $f_{PEO} \sim 0.8$. The frequency sweep data do not overlap, highlighting the thermorheological complexity of the material.

With tTS confirmed for most of the BBCP materials, master curves of the dynamic response were constructed by shifting frequency sweeps to a reference temperature of T_{ref} = 120 °C (Figure 3.12a). T_{ref} was chosen because it is within the experimental temperature range of all samples and above the approximate T_g of neat PS (100 °C). Shift factors a_T (Figure 3.12b) show fit to the Williams−Landel−Ferry (WLF) equation, suggesting realistic temperature dependence of the dynamic response.[58] Shift factors vary considerable with temperature, indicating the dynamics and characteristic relaxation times are a function of f_{PEO}. Therefore, we select the arbitrary *Tref* to compare the shape of the master curves as opposed to direct quantitative comparison of relaxation times. Vertical shift factors b_T were found to be close to 1. Ideally, the master curves encompass the entire relaxation response, from terminal flow to the glassy regime. At the highest frequencies above $a_T\omega$ =10^4−10^5 rad/s, elastically dominated behavior ($G'(\omega) > G''(\omega)$) is well-defined,

suggesting the cooperative "glassy" dynamics of the PS domain coupled with the amorphous PEO phase (which is well above T_g). At frequencies below $a_T\omega = 10^4$ rad/s, a crossover to viscously dominated behavior is observed where $G''(\omega)$ is larger than $G'(\omega)$. The dynamic response of the BBCPs is primarily viscous over the entire remaining intermediate frequency range extending to the longest time scales. There is no observable rubbery plateau in $G'(\omega)$, generally expected for a highly entangled LBCP systems of comparable MW. The terminal flow regime at the lowest accessible frequencies is viscously dominated but does not reach the classical liquid scaling behavior ($G'(\omega) \sim \omega^2$, $G''(\omega) \sim \omega^1$). Additional data at lower frequency was unobtainable due to instrument and sample limitations, preventing the application of a true power law scaling in $G'(\omega)$ and $G''(\omega)$.

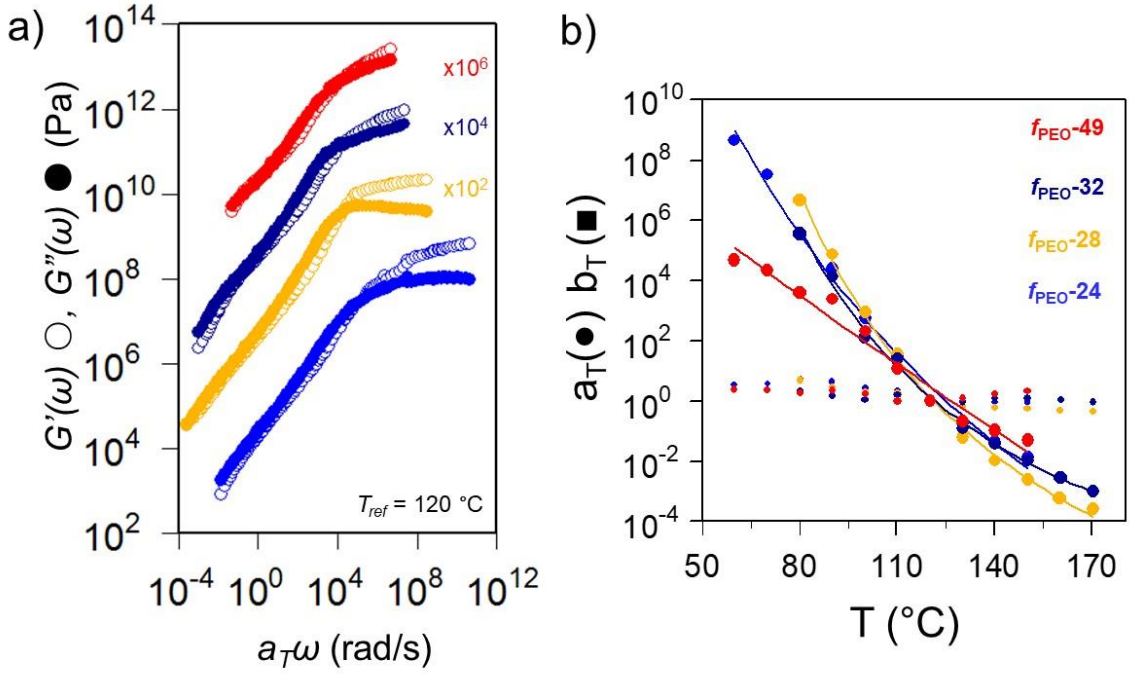

Figure 3.12 (a) Master curves of dynamic moduli $G'(\omega)$ (open symbols) and $G''(\omega)$ (closed symbols) for PS-*b*-PEO BBCP samples at a reference temperature of T_{ref} = 120 °C. Master curve shifted vertically by additional indicated scaling factor to provide clarity. **(b)** Time–temperature superposition shift factors a_T (large circles) and b_T (small squares) determined from master curve construction. Line shows fit to the WLF equation.

After rheological characterization, the samples were cooled down to T = 25 °C and removed from the rheometer for additional SAXS characterization to determine any changes in microphase segregation. In 1-D SAXS, q^* remained constant with minimal changes in d_0, indicating that microphase segregation was maintained after rheological characterization and subsequent quenching back to room temperature.[54]

3.3.3 Viscoelasticity of Linear versus Brush Architectures

Overall, the BBCPs exhibit a highly viscous dynamic response with no detectable elastic plateau across the experimental frequency range. The emergence of highly mobile viscous dynamics supports the instance of rapid self-assembly into microphase segregated morphologies and nanostructures. The rapid ordering dynamics and high mobility in the BBCP systems occur despite high MW (~ 100s of kg/mol). The BBCP architecture was directly compared to PS-*b*-PEO LBCP samples with comparable f_{PEO}. It was necessary to anneal the LBCPs for longer times (t = 24 h) at higher temperatures (T = 120 °C) to adequately compare the rheological response of BBCP and LBCP samples with similar microphase segregation and d_0. For comparison, separate LBCP samples were annealed at identical conditions to the BBCP (1 h at T = 110 °C). 1-D SAXS did not reveal any strong scattering peaks (Figure 3.13a), indicating that longer annealing periods were required to achieve adequate microphase segregation, resulting in domain spacings of d_0 = 32.6, 66.5, and 44.8 nm for LBCP-22, LBCP-47, and LBCP-81 respectively (Figure 3.13b). We propose that the reduced degree of chain entanglements in BBCPs increases mobility while strong chemical differences between blocks (large χ) provides significant driving force for microphase segregation, in turn requiring milder thermal annealing conditions for a steady state structure to assemble.

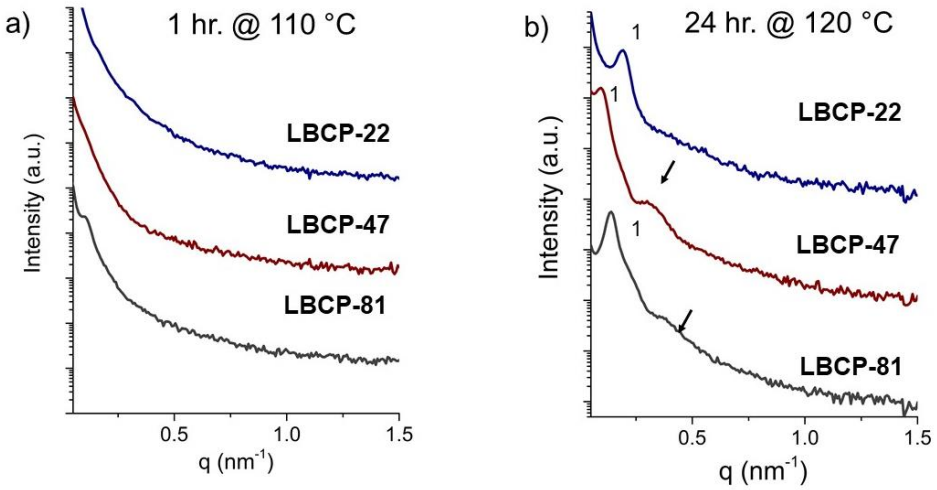

Figure 3.13 (a) 1-D SAXS spectra of PS-*b*-PEO LBCPs after 1 h thermal annealing at T = 110 °C. Note the absence of microphase segregation. **(b)** SAXS spectra of PS-*b*-PEO LBCPs after 24 h thermal annealing at T = 120 °C, which formed microphase segregated structures and were used for rheological characterization. (Modified from Ref. 54)[54]

To compare the linear viscoelasticity of the two architectures, the dynamics of the LBCP samples are presented in the Booij-Palmen plot with identical limits to each axis (Figure 3.14) Identical trends in tTS applicability are observed for LBCPs, mainly the thermorheological complexity at high f_{PEO}. However, at larger G^* values above 10^7 Pa (corresponding to the lowest testing temperatures), discontinuities in the overlap of the curves begin to emerge in the LBCPs, characteristic of a material passing through T_g.[59] At lower values of G^*, relaxation processes are identified by local minima in $\delta(G^*)$.[38,60] Strong minima in both LBCP samples occur at $G^* \sim 10^5$ Pa and are associated with the chain entanglement plateau. In the case of the BBCPs, the minimum in $\delta(G^*)$ is broad and at large δ (primarily viscous behavior). For *f*-49, the minimum is more drastic, but reduced by an order of magnitude in modulus ($G^* \sim 10^4$ Pa) compared to LBCPs. This feature is most likely some other structural relaxation, possibly of the backbone or microphase separation rather than the side chains, which would be expected at much higher G^* values if they were entangled.[38,41] At the lowest modulus values (below 10^4 Pa), the "liquid-like"

behavior of the BBCP is highlighted as the data curves upward to higher δ. Comparatively, the LBCP response immediately begin to slope toward smaller δ and more elastic, solid-like character.

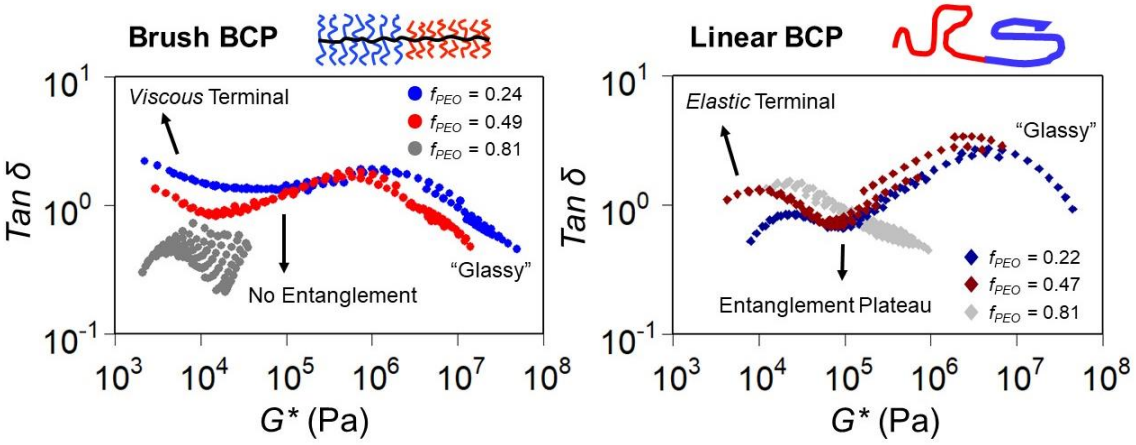

Figure 3.14 Booij–Palmen plot of **(a)** BBCP materials *f*-24, *f*-49, and *f*-81 and **(b)** LBCP samples LBCP-22, LBCP-47, and LBCP-81. tTS cannot be applied to samples with f_{PEO} ~ 80%. The frequency sweep data do not overlap, highlighting the thermorheological complexity of the material. (Modified from Ref. 54)[54]

3.3.4 Phase Behavior of PS-*b*-PEO N_{bb} Series

The viscoelasticity of the BBCPs is clearly distinct from the conventional LBCP. It appears that the BBCPs behave like the homopolymer bottlebrushes despite microphase segregation between the two domains. The viscoelasticity of BCPs is highly dependent on the morphology, especially in the low frequency limit.[61] Therefore, an investigation of rheological properties of BBCPs with a standardized morphology is desired. Here, we study the structure and viscoelasticity of asymmetric PS-*b*-PEO BBCPs again with precise control over $N_{sc,}$ f, and N_{bb} over a controlled range of MW up to 500 kg/mol (Details in Table 3.2). The BBCPs in this series are symmetric in composition (f_{PEO} = 0.5) and exclusively assemble into lamellar morphology. The objectives are to determine viscoelastic patterns, propose possible structural mechanisms responsible for the observed response, and to represent them in a rheological model. Our focus is on the previously

observed fast dynamics of the BBCPs. We further focus on the molecular asymmetry due to a step change in side chain length ($N_{sc\text{-}PEO} \neq N_{sc\text{-}PS}$), which is expected to significantly impact the nature of the self-assembly and the rheological properties.

The BBPCs self-assembled into ordered lamellae after thermal annealing due to microphase separation between the chemically dissimilar blocks. Primary scattering peaks (q^*) appeared in all five samples, as well as high order reflections at peak ratios of q^*:2q^* (Figure 3.15). PEO crystallization was observed at room temperature, especially in the larger N_{bb} samples, evidenced by a Bragg scattering peak at q = 0.4 nm^{-1}. The lamellar domain spacing increases systematically from d_0 = 23 to d_0 = 90 nm with increasing N_{bb}. The relationship between d_o and N_{bb} suggests an extended backbone conformation in close agreement with reports of other lamellae forming BBCP systems in the literature.[21,23–25] The scaling phenomena will be discussed in Section 3.4.

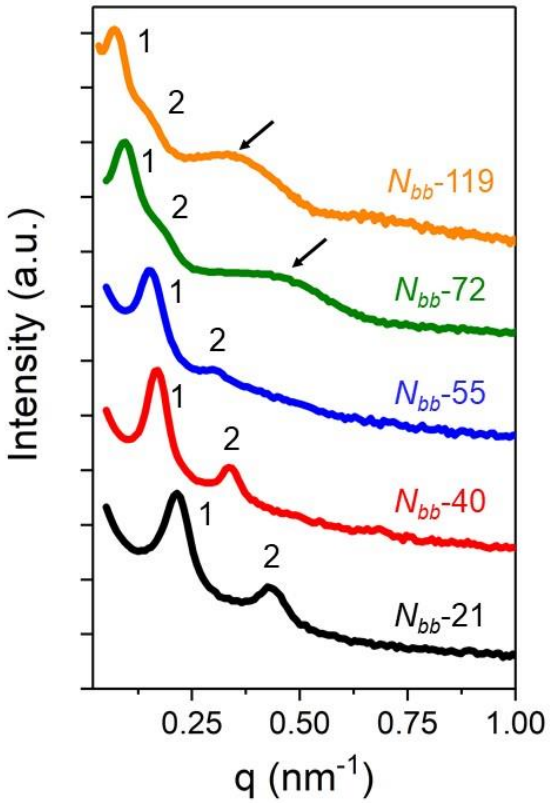

Figure 3.15 Room Temperature 1D SAXS spectra of BBCPs after thermal annealing for 4 h. at T = 120 °C. Higher order Bragg reflections are identified at ratio of q^*:2q^*. Arrow designates scattering peaks from PEO crystal lamellae.

The presence of even order scattering peak (*2q**) as well as corresponding transmission electron microscopy (TEM) images reveals the formation of lamellar structures with asymmetric domain thicknesses d, where $d_{PEO} \neq d_{PS}$. In Figure 3.16a-e, TEM micrographs show the stained PEO domains are much thinner than the brighter PS domains. The asymmetry seems unexpected, as equal mass ratio implies relatively equal volume in each domain (according to bulk density assumptions). Observation of such asymmetric structures is common in bottlebrush systems.[22,24,26,32,62–64] Current discussions suggest that the crowding of brush side chains at high grafting density introduces significant excluded volume effects which are not accounted for by the mean-field approximation of LBCPs. Therefore the local packing may deviate from the bulk density

commonly used for the calculation of volume fraction.[23] The asymmetric layer thickness is also likely due to the contrast between star and worm like conformation in the PEO and PS blocks. The implication of the brush architecture on the lamellar assembly will be elaborated on later in Section 3.4.

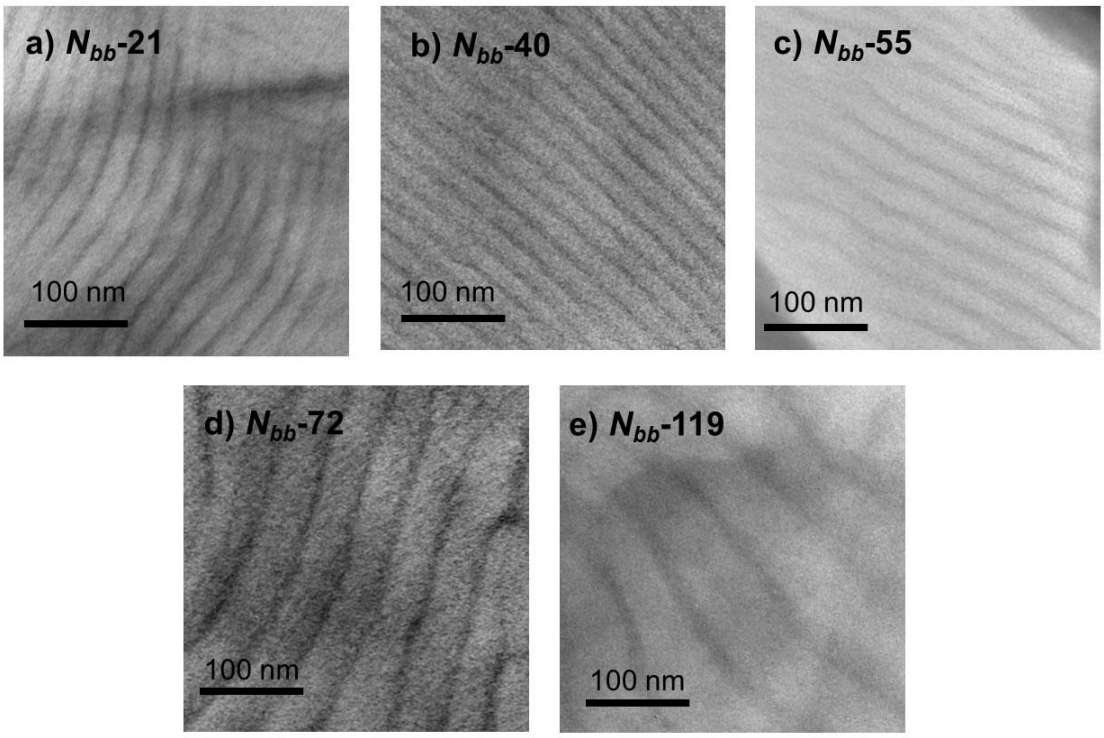

Figure 3.16 Transmission Electron Microscopy (TEM) of cryomicrotomed BBCP samples after thermal annealing. **(a)** N_{bb}-21 **(b)** N_{bb}-40 **(c)** N_{bb}-55 **(d)** N_{bb}-72 **(e)** N_{bb}-119. Dark domains are stained PEO while bright domains correspond to PS. All scale bars are 100 nm.

The temperature dependent phase behavior was characterized by in-situ temperature controlled SAXS. Pre-annealed BBCP samples were heated from room temperature to T = 200 °C using temperature steps of 30 °C (Figure 3.17a-e). Microphase separation (identified by q^*) persists up to T = 170 °C (the highest temperature in rheological characterization by SAOS). The high order peak $2q^*$ disappears upon heating through T = 80 °C (above T_m of the PEO crystals), indicating a loss of long-range order in the lamellar packing. The transition appears to be universal across the range of N_{bb}. While

the intensity of q^* does decrease (likely due to electron density differences between crystalline and amorphous PEO domains), the full width at half maximum (FWHM) of q^* does not shift substantially (Figure 3.18b). Only the long-range order is impacted such that in the mobile melt state, the PS and PEO domains are still microphase segregated, but the long-range lamellar packing is disordered. We consider this an "order-disorder transition" but not through the classical first-order pathway described by theory and experiment for strongly segregated LBCPs.[65–68] At T = 200 °C, a microphase separation transition (MST) to the homogeneous state is ultimately observed, designated by the complete disappearance of q^*. The ordered lamellae reform upon cooling back to room temperature. Here, the MST is accessible (T_{MST} > 170 °C) and rapid ordering can be induced upon quenching. The structure transition highlights the potential for processing of these specific materials and suggests many interesting opportunities for flow induced alignment.

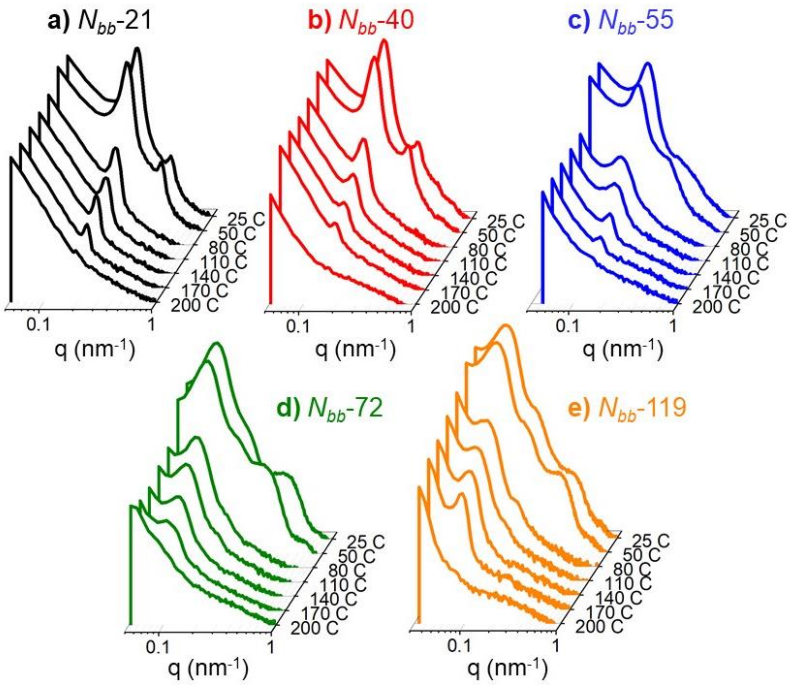

Figure 3.17 Log-log spectra of in-situ temperature controlled SAXS for N_{bb} series from room temperature through T = 200 °C. **(a)** N_{bb}-21 **(b)** N_{bb}-40 **(c)** N_{bb}-55 **(d)** N_{bb}-79 and **(e)** N_{bb}-119. Scattering intensity normalized by intensity of incident beam and a constant sample thickness (0.5 mm).

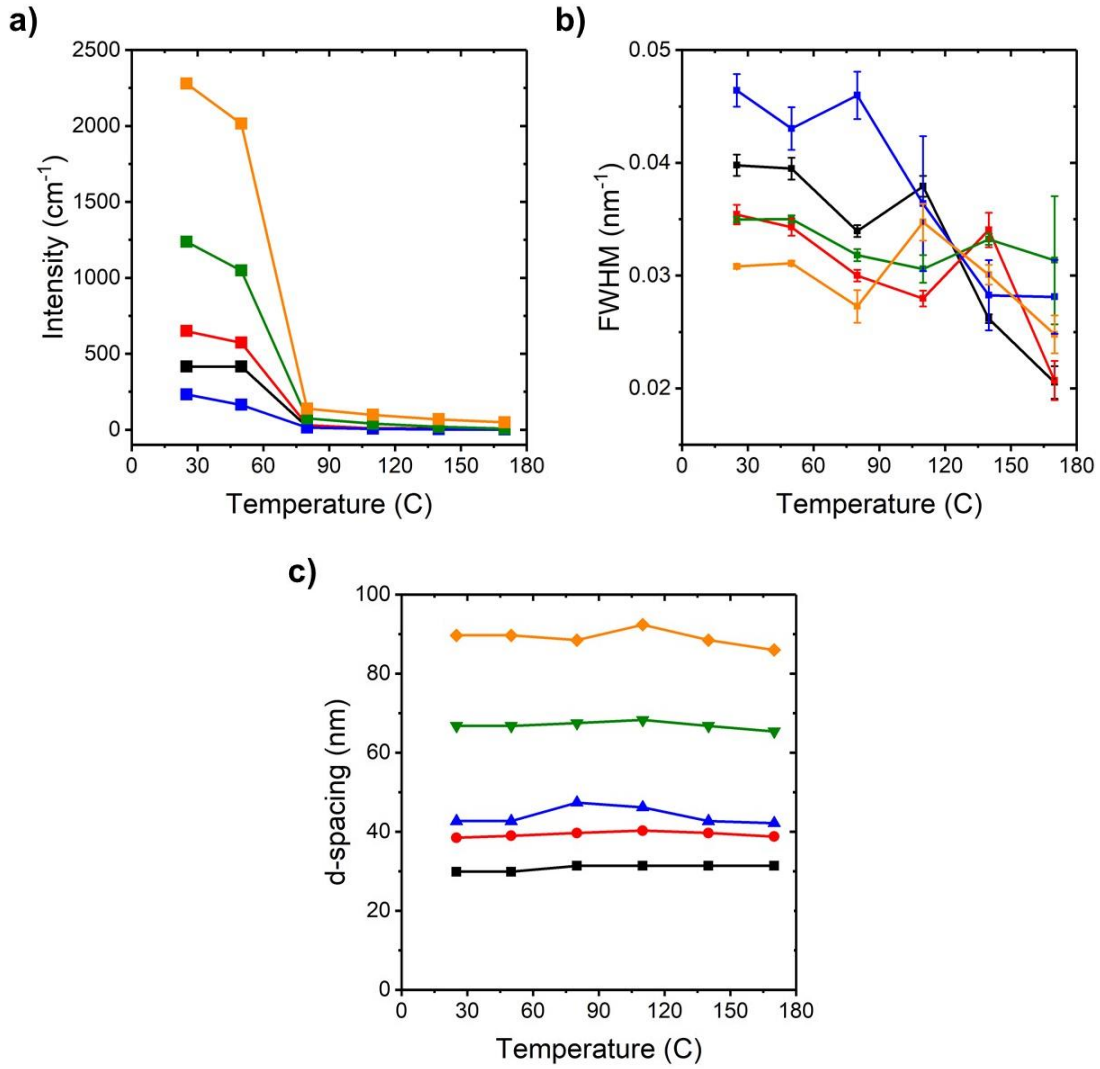

Figure 3.18 Trends in **(a)** Intensity of *q**, **(b)** Full width at half maximum (FWHM) of *q**, and **(c)** d-spacing as a function of temperature. Data compiled from temperature controlled SAXS experiments. Colors correspond to legend in Figure 3.17

DSC was used to further investigate the effect of N_{bb} on thermal transitions in the BBCP series. Melting peaks are observed for all samples around T_m = 55 - 60 °C indicating semi-crystallinity of the PEO domain, consistent with the structural characterization from SAXS. No clear trend in T_m or T_c with N_{bb} is observed. In Figure 3.19b, the enlarged region of the DSC trace reveals a broad glass transition corresponding to the T_g of the PS domain. In a two-phase morphology, the glassy characteristics of each domain are individually

expressed. The PS domain T_g are all below that expected for bulk PS (T_g ~ 100 °C). The reduction in T_g from bulk PS is due to the low MW chains (PS with M_n = 2.9 kg/mol would exhibit a significantly reduced T_g ~ 70 °C) as well as the additional confinement of the chains at one end (i.e. connection to the backbone).[69] The T_g is broad and appears to increase with N_{bb}, contrasting observations in the homopolymer bottlebrushes materials, where T_g is independent of N_{bb}.[38,40] It is possible that in the low N_{bb} samples, star-like architectures and confinement of the sidechains additionally suppress T_g in the PS domain.[70]

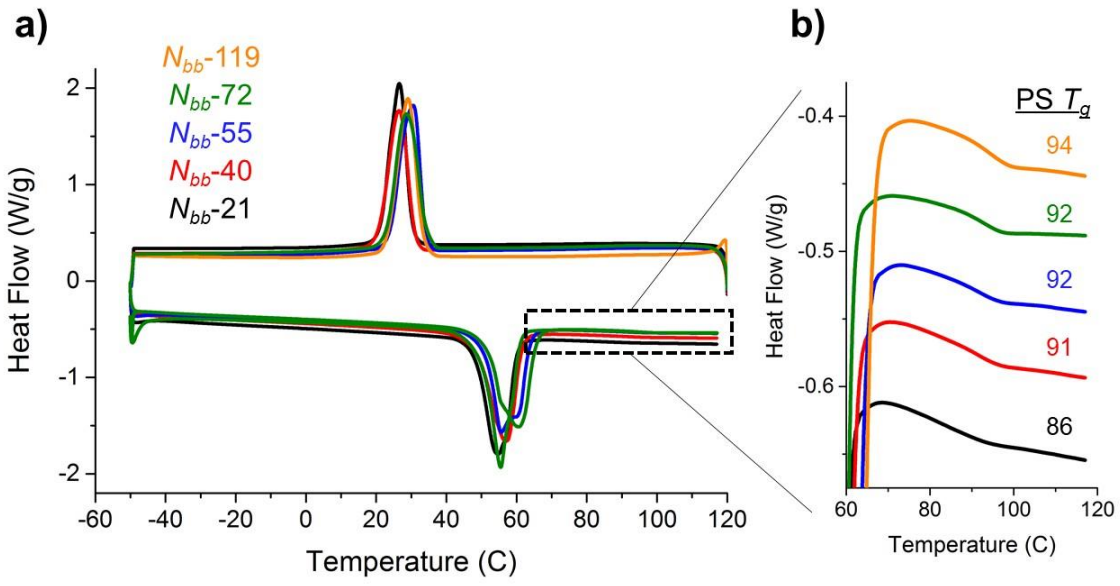

Figure 3.19 (a) Heating and cooling DSC traces of N_{bb} series, indicating melting and crystallization of PEO side chains **(b)** Expanded view of glass transition of PS block. T_g is reported in °C. Qualitatively, T_g is depressed when compared to that of bulk PS (T_g ~ 100 °C). Overall, T_g of PS domain increases with N_{bb} from T = 86 to 94 °C.

3.3.5 Linear Viscoelasticity of PS-*b*-PEO N_{bb} Series

The linear viscoelasticity of the microphase separated BBCPs was characterized using small amplitude oscillatory shear (SAOS) frequency sweeps from T = 90 to 170 °C. The structure is unchanged across the temperature range and the BBCPs are again

thermorheologically simple so that tTS can be applied. The applicability of tTS within the experimental composition range is consistent with previous results that show the onset of tTS failure at $f_{PEO} \sim 0.75$, suggesting that the PS dominates the thermorheological response in this system.[53,54] Master curves of storage and loss modulus ($G'(\omega)$, $G''(\omega)$) at $T_{ref} = T_{g\text{-}PS} + 30$ °C are presented in Figure 3.20a. Horizontal shift factors a_T can be represented with the WLF equation (Figure 3.20b) and are generally independent of N_{bb} with slight variability due to the heterogenous microphase separation. T_{ref} was defined a set distance from $T_{g\text{-}PS}$ determined by DSC in Figure 3.19b to appropriately compare the timescales of the various relaxation processes. In Figure 3.20a, $G'(\omega)$ and $G''(\omega)$ are again vertically separated by an extra factor (A) for clarity. The viscoelastic response is consistent with the f_{PEO} series in Section 3.3.2, notably elastically dominated behavior at the highest frequencies ($a_T\omega > 10^4$ rad/s), and an intermediate frequency regime of viscously dominated behavior, where $G''(\omega) > G'(\omega)$.[54] All samples in the N_{bb} series are unentangled, as no distinct plateau in $G'(\omega)$ is observed. At lower frequencies ($a_T\omega \sim 10^1$ rad/s), a crossover in viscoelastic character occurs. This relaxation feature begins to shift to lower frequency and becomes more pronounced with increasing N_{bb}. At the low frequency limit, the BBCPs do not display liquid terminal scaling limit of $G'(\omega) \sim \omega^2$ and $G''(\omega) \sim \omega^1$, but exhibit power law scaling in $G'(\omega)$ and $G''(\omega)$, as well as a slight increase in elasticity. While difficult to resolve in the master curves of $G'(\omega)$ and $G''(\omega)$, the dynamic data shows multi-modal, sequential relaxation patterns across the entire frequency range. The normalized storage modulus (G'/G^*) in Figure 3.21 delineates these different features most clearly. Notably, the maxima in G'/G^* shifts to lower frequency and is significantly drawn

out over a wider frequency range for the longer backbones. The viscoelastic terminal behavior suggests that there are consequences of the microphase separated structure.

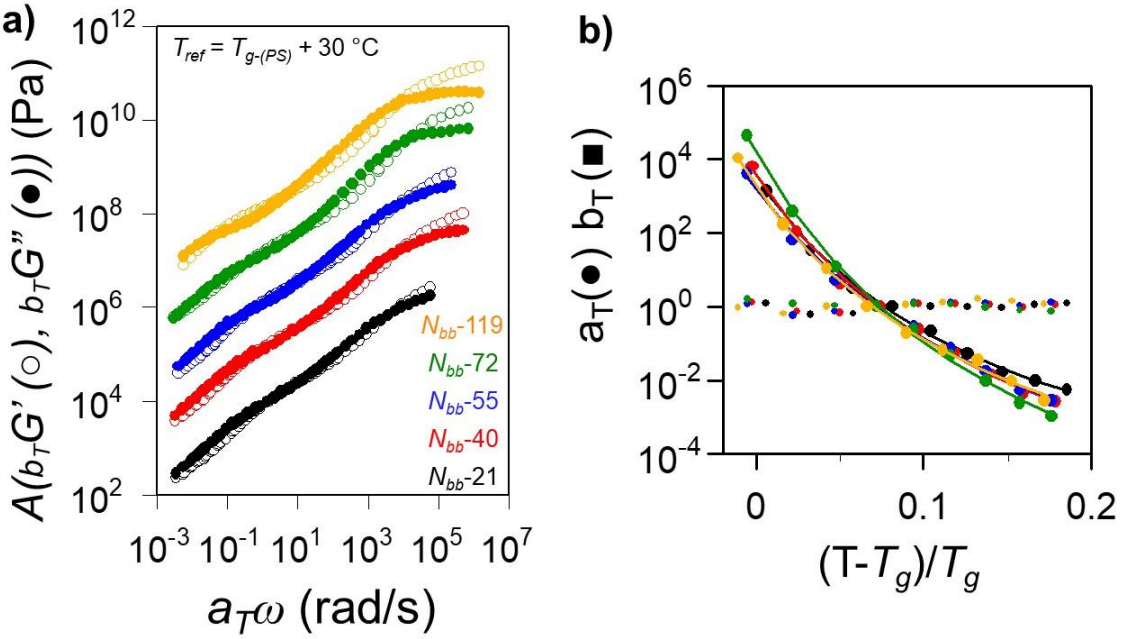

Figure 3.20 (a) Master curves of dynamic moduli *G′(ω)* (open symbols) and *G″(ω)* (closed symbols) for PS-*b*-PEO dbBB samples at a reference temperature of $T_{ref} = T_{g\text{-}PS}$ + 30 °C. Master curves separated vertically (factor *A*) to provide clarity: N_{bb}-21 – x 10^0, N_{bb}-40 – x 10^1, N_{bb}-55 – x 10^2, N_{bb}-72 – x 10^3, N_{bb}-119 – x 10^4 **(b)** Time temperature superposition shift factors a_T (horizontal) and b_T (vertical) at T = 120 °C normalized with respect to T_g: (T - T_g)/T_g. Lines show fit to WLF equation. Shift factors b_T were determined to be close to 1. Temperature dependence in a_T varies slightly with N_{bb} due to heterogeneous nature of the polymeric architecture and morphology.

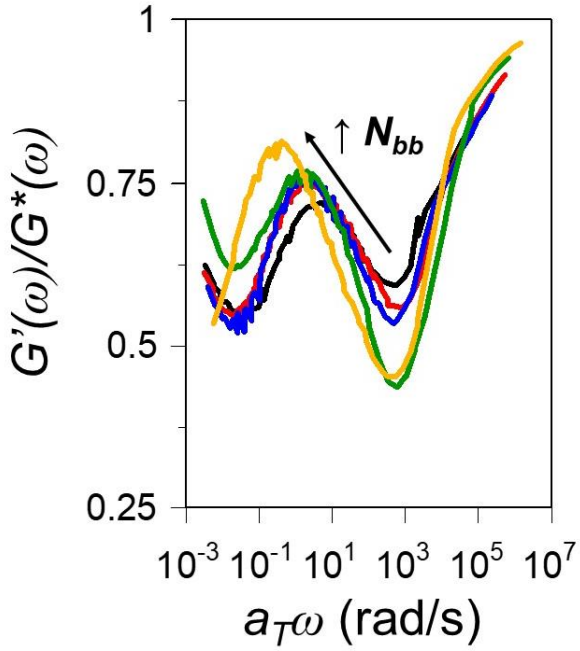

Figure 3.21 Normalized storage modulus (G'/G^*) versus shifted frequency ($a_T\omega$). Data and colors correspond to legend in Figure 3.20a

3.3.6 Relaxation Time Spectra Analysis: Dual Power Law Model

The viscoelasticity of the N_{bb} series is further described by additional analysis of the relaxation modes across the wide range of accessible relaxation times. The relaxation modulus *G(t)* is a powerful parameter when describing the viscoelastic response of a material under all flow conditions, as it expresses the structural rearrangements of a material in time.[71] *G(t)* is a monotonically decaying function which is defined as the integral over relaxation modes from $0 < \tau_i < \tau_{max}$ of the relaxation time spectrum $H(\tau)$ (Eq. 3.1) as described in Chapter 2.[71]

$$G(t) = \int_0^{\tau_{max}} \frac{d\tau}{\tau} H(\tau) e^{-t/\tau} \qquad \text{(Eq. 3.1)}$$

$H(\tau)$ is a continuous function which can be directly calculated from dynamic data, for example through techniques established by Baumgaertel et al.[72] Figure 3.22 shows calculated $H(\tau)$ for all BBCPs in the series (colored circles). All spectra appear to overlap each other and exhibit a similar decaying power law form. Distinct scaling regimes govern

the spectra across all $\tau < \tau_{max}$, much like the sequential relaxations in the dynamic viscoelastic response.

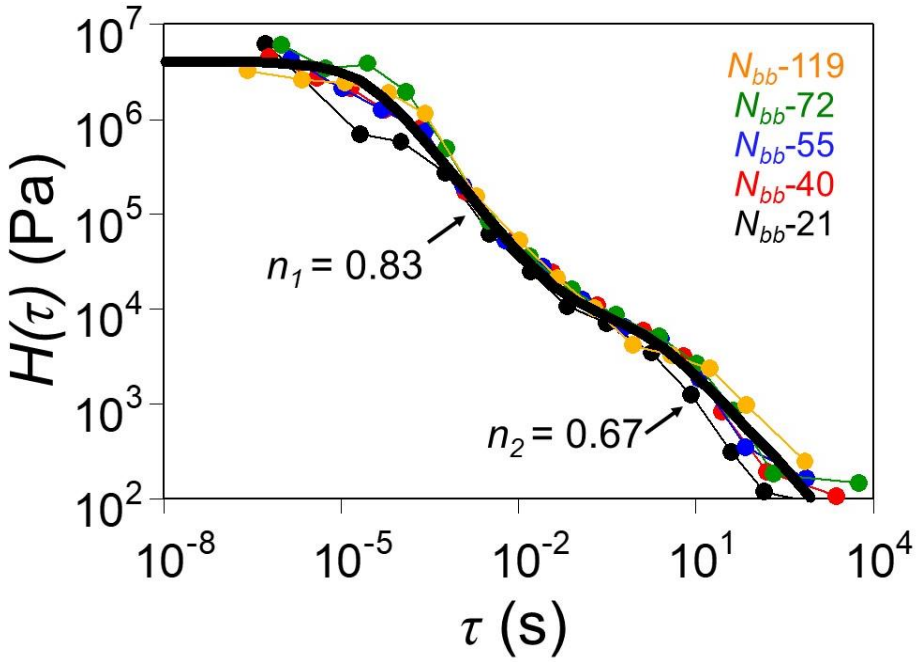

Figure 3.22 Relaxation Time Spectra $H(\tau)$ calculated from dynamic data according to Baumgaertel et al.[72] and fit to general dual power law model (Eq. 3.2) shown in black.

The multi-modal behavior can be crudely represented by a simple power law. Specifically, a dual power law model (Eq. 3.2) is used to represent this behavior more closely:

$$H(\tau) = H_0 + H_1\left(1 + \frac{\tau}{\tau_1}\right)^{-n_1} + H_2\left(1 + \frac{\tau}{\tau_2}\right)^{-n_2} \qquad \text{(Eq. 3.2)}$$

where H_0, H_1, and H_2 are constants, τ_1 and τ_2 are characteristic relaxation times, and n_1 and n_2 are the relaxation exponents. Typically, n_i may adopt a value between $0 < n_i < 1$, where the extreme limit of $n_i = 0$ is a Hookean solid.[71] To represent the experimental data, a cutoff was applied at $\tau_{max} = 10^4$ s. As a result, $H(\tau) = 0$ for all modes $\tau > \tau_{max}$ and we set $H_0 \sim 0$. Various alternative forms of the dual power law are proposed, but Eq. 3.2 represents the response most accurately. A general fit of Eq. 3.2 to all $H(\tau)$ is marked by a solid black line

in Figure 3.22, while individual fits were also made for each spectrum in Figure 3.23 (Parameters in Table 3.3).

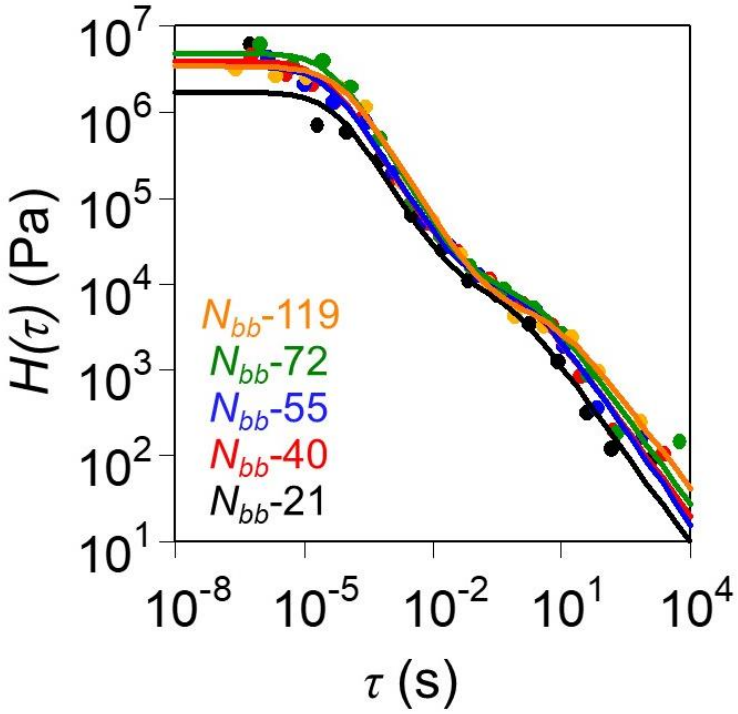

Figure 3.23 Individual fits of dual power law model (Eq. 3.2) to calculated $H(\tau)$ for each BBCP sample. Parameters for fit are presented in Table 3.3.

Table 3.3 Parameters of Dual Power Law Model (τ_{max} = 1x10^4 s, $H_0 \sim 0$):

N_{bb}	H_1 (Pa)	τ_1 (s)	n_1	H_2 (Pa)	τ_2 (s)	n_2
21	1.7 x10^6	4.9 x10^{-5}	0.83	7.5 x10^3	5.4 x10^{-1}	0.68
40	4.0 x10^6	2.9 x10^{-5}	0.83	9.4 x10^3	1.0 x10^{-1}	0.67
55	3.4 x10^6	3.5 x10^{-5}	0.82	9.0 x10^3	1.3 x10^{-1}	0.71
72	4.8 x10^6	4.5 x10^{-4}	0.86	8.3 x10^3	2.0 x10^{-1}	0.67
119	3.4 x10^6	6.4 x10^{-4}	0.81	4.3 x10^3	7.0 x10^{-1}	0.64

The linear superposition of two power laws describes behavior on short and long-time scales respectively. In the first power law regime at the shorter relaxation times (τ = 10^{-4} s), a scaling exponent of $n_1 \approx 0.83$ is observed, which is far from the solid limit. At the

longer relaxation times ($\tau = 10^1$ s), the power law scaling increases slightly to $n_2 \approx 0.67$. The feature is extended to longer relaxation times with increasing N_{bb}, reflected by the increase in τ_2 of over a decade in τ. The shift in relaxation time is consistent with the draw out relaxation feature in Figure 3.21. Surprisingly, the exhibited scaling behavior is remarkably like a critical gel approaching the liquid-to-solid transition, where the structure is self-similar over a large length scale, and on the brink of a sample spanning connectivity limit.[71] The relaxations at long time are usually attributed to structural rearrangements over a larger length scale, where the microphase segregation is expected to dominate. Power law relaxation processes have been identified in strongly segregated lamellar BCPs.[46,73–77] However, here the morphological data depicts a system with unentangled side chains, asymmetric lamellar domains, and a globally disordered morphology in the melt. The new emergence of sequential scaling regimes on short and long timescales suggests the possibility of new relaxation mechanisms arising from the BBCP architecture. The melt state conformation of PS-*b*-PEO BBCPs with asymmetric side chain lengths must be discussed further to accurately describe these phenomena.

3.4 Discussion

A complete assessment of the morphology transitions in PS-*b*-PEO BBCPs was conducted by Gai et al. across a wide range of f_{PEO} and N_{sc}.[28] Notably, the disordered morphology at low f_{PEO} was observed, in which short and irregular shaped PEO domains were dispersed within the PS matrix. Annealing for longer times or at higher temperature did not improve the regularity of packing. The formation of a strongly segregated but disordered morphology was attributed to the highly asymmetric molecular shape which induced severely irregular interfacial curvature. Packing frustration caused by the longer

PEO side chains pushed the system towards disorder, contrasting the formation of ordered cylinders at large f_{PEO} when the minor domain consisted of the shorter PS side chains. The non-uniform morphology evolution is different from that in linear PS-*b*-PEO, in which hexagonally packed PEO cylinders have been observed with f_{PEO} = 0.33.[78] The side asymmetry must be reversed ($N_{sc\text{-}PS} > N_{sc\text{-}PEO}$) to achieve the well-ordered cylinders at low f_{PEO}. For example, PLA cylinders were observed in PS-*b*-PLA BBCP (f_{PLA} = 0.3) when the PLA side chains were much shorter than the PS, introducing a favorable curved interface necessary to facilitate long range order and hexagonal packing. Surprisingly, lamellar morphology is resolved over a much wider range of volume fraction (f_{PEO} = 0.28 – 0.72) when compared to linear BCP systems and was independent of N_{sc}. The lamellar morphology is formed under equalized interfacial area. As previously stated, highly extended backbone conformations oppose the order-order transition to cylindrical morphology until exceptionally asymmetric limits.

We see that the brush architecture introduces new considerations for molecular packing due to the significant excluded volume effects that arise from dense side chain grafting. Scaling arguments have been proposed to describe the conformation and flexibility of homopolymer bottlebrushes and symmetric BBCPs in the melt.[21,42,64,79] The application of these arguments to BBCP with asymmetric side chains and block composition is valid, but has not received as much attention. At high graft density, bottlebrushes are thought of as "worm-like" tubes due to the local backbone unit extension. The side chains may stretch slightly more than their unperturbed Gaussian conformation, but side chain size ($<R_{sc}>$) still scales with $N_{sc}^{1/2}$ despite the dense packing.[79] The flexibility of the backbone is described by the persistence length (l_p), which scales with $<R_{sc}>$ and

graft density z.[79] Therefore, the rigidity of the backbone is influenced by the steric crowding of the side chains. A bottlebrush with norbornene-based backbone is thought to be semi-flexible, with a l_p of 5 backbone repeat units (~ 3.1 nm) according to recent SCFT calculations.[23,64] Therefore, the PS and PEO blocks can be thought of as filaments composed of multiple persistence units. The side chain asymmetry influences the unique l_p of each block, where the PEO side chains should contribute more stiffness to their backbone segment than the PS side chains do to its own backbone. Therefore, the PEO block backbone will be stiffer than the PS block backbone ($l_{p\text{-}PEO} > l_{p\text{-}PS}$).

While the N_{bb} series is symmetric in terms of the composition, the overall configuration of the molecules is highly asymmetric. Realistically, the PEO block resembles a "star-like" polymer, where N_{sc} is the dominating length scale. The star configuration was also identified by Dalsin et al. for aPP-*b*-PS BBCPs with short N_{bb}.[23] In contrast, the PS block resembles a traditional "worm-like" filament, where $N_{bb\text{-}PS}$ dominates the conformation. However, as N_{bb} increases (as well as $N_{bb\text{-}PEO}$), the PEO block approaches the worm-like conformation of the PS block. The transition is apparent in SAXS. The relationship between d_o and N_{bb} (Figure 3.24) is in close agreement with the symmetric aPP-*b*-PS series which spanned the star-to-worm regime.[23] Overall, the power law scaling $d_o \sim N_{bb}^{\alpha}$ for the PS-*b*-PEO depicts an extended backbone conformation resulting in a scaling exponent $\alpha = 0.84$, which is much larger than that predicted for symmetric LBCPs in the strong segregation limit ($\alpha = 0.66$).[27] The scaling exponent is in close agreement with observations by Gu et al. in the PS-*b*-PLA BBCP system ($\alpha = 0.93$ & 0.82 for systems with short and long side chains respectively).[24] The scaling exponent decreases significantly ($\alpha = 0.36$) at low N_{bb} when the lamellar spacing is dominated by N_{sc}

rather than N_{bb}. While such scaling was observed in symmetric BBCPs with equivalent side chain MW, it is quite interesting that the trend also holds for asymmetric systems with conformationally dissimilar blocks in which only one block undergoes the transition.

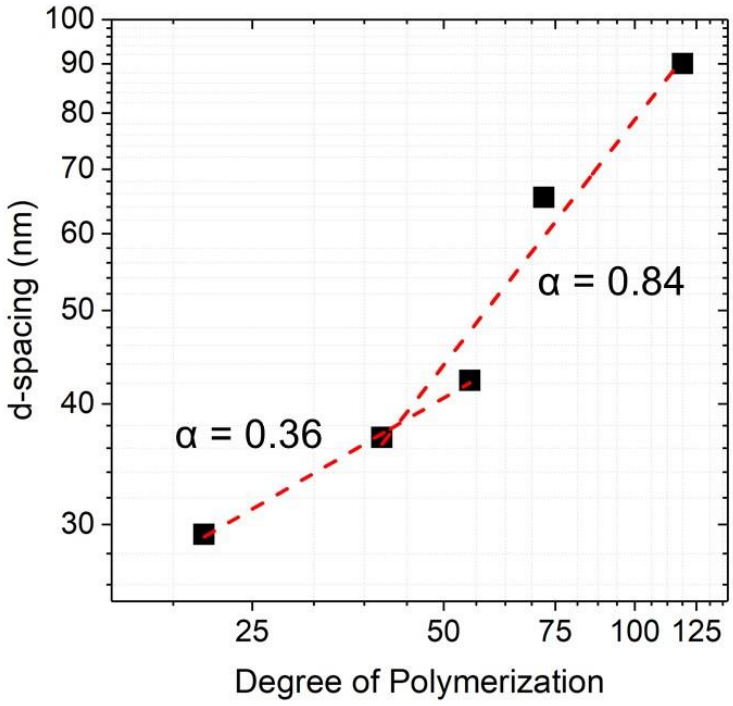

Figure 3.24 Domain spacing (d_0) of lamellar morphology calculated from SAXS vs. backbone degree of polymerization (N_{bb}) for N_{bb} series. Dotted lines follow power law fits to relationship $d_0 \sim N_{bb}{}^{\alpha}$. Fit to N_{bb}-21, N_{bb}-40, and N_{bb}-55 is $\alpha = 0.36$ ($R^2 = 0.99$, std. err. ± 0.02). Fit to N_{bb}-40, N_{bb}-55, N_{bb}-72, and N_{bb}-119 is $\alpha = 0.84$ ($R^2 = 0.96$, std. err. ± 0.12). In the larger N_{bb} regime, the scaling depicts an extended backbone conformation when compared to a scaling of $\alpha = 0.66$ expected for symmetric LBCPs in the strong segregation limit.

A lamellar morphology forms when the curvature at the interface is equalized, resulting in a flat interface.[29] In linear BCPs, the curvature is equalized when the volume fraction between two di-blocks is symmetric. Even though the PS-*b*-PEO BBCP in the N_{bb} series are compositionally symmetric by mass, it is remarkable that they assemble into lamellae with such asymmetric limits in the architectural design. The asymmetric morphology appears striking, but upon further inspection, the asymmetric lamellae in

Figure 3.16 fall in line with observations from several reports in the literature.[21,24,26,28,62,63] Recent experiments have suggested that the backbone will adjust to accommodate asymmetric side chain lengths, graft density, and graft distribution to enable the formation of lamellae.[21,26,32] The difference in molecular shape between blocks leads to a competition of both space and volume filling, and while the demand for uniform packing is desired, inherent constraints in the system can lead to structures with non-equilibrium density distributions throughout the domains.[22] The conformational volume occupied by each block segment plays a crucial role. A PEO block occupies a larger conformational volume per unit mass due to the longer side chains.[42] While the side chains themselves do not overlap significantly (due to the dense packing and steric repulsions), the TEM images in Figure 3.16 suggests that the conformational volume overlap is more significant in the PEO domain than in the PS domain. The overlap could act as a mechanism for equalizing the area at the interface, which drives the lamellar morphology. The PS block is much longer and while semi-flexible, cannot bend towards the interface to satisfy the cross-sectional area requirements. The result is a thicker PS domain driven by the extended backbone size. The PEO domain is semi-crystalline at room temperature according to SAXS and DSC characterizations. The PEO side chains pack and order more efficiently, while the PS side chains are stiff, bulky and in the glassy state. Therefore, the free volume is much higher in the PS domain than the PEO domains and could contribute to the apparent asymmetry between the lamellae. Additional systematic studies are necessary to determine the scaling laws within each asymmetric domain.

It is well known that crystallinity is a strong driving force that dictates self-assembly and the ordering transition.[80–83] The melting of PEO appears to impact the global

ordering of the lamellae but not the local microphase segregation or characteristic domain spacing. Beyond T_m, the interface is still defined by large composition fluctuations, but the interfacial area cannot be equalized to form stable lamellae. The stiff, rigid inner-domain PEO crystallization assists the persistence of long range lamellar order. A similar phenomenon was recently proposed by Chae et al. in BBCPs with crystallizable POSS pendants groups that supported well-ordered lamellar morphology despite asymmetric molecular shape.[63] The reformation of lamellar morphology in the PS-*b*-PEO after cooling back to room temperature is consistent with the hypothesis that the long-range morphology is coupled with the presence of stiff crystallites. While we suggest that the conventional bulk densities (ρ_{PEO} = 1.12 g/cm^3 (crystalline) & 1.09 g/cm^3 (melt)) are not appropriate for the local packing of the brush architecture, a minor change in the PEO brush density should still be expected through the melting transition, which could influence the long range order.[84] It is apparent that the crystallization of densely grafted bottlebrush macromolecules and their co-assembly within BCPs also requires additional investigations. Regardless, PEO crystallization and long-range lamellar order do not appear to impact the rheological properties characterized in the melt state for this material set.

The significance of tTS and thermorheological simplicity should be discussed before elaborating on the unique viscoelasticity of the BBCPs. It is remarkable that the dynamics can be resolved over such a wide range of timescales through tTS. The origins of thermorheological simplicity in heterogenous materials seems counter intuitive, in the sense that relaxation processes from multiple components may express individual temperature dependence.[56] van Gurp et al. tested the applicability of tTS on a wide variety of polymer blends, both miscible and immiscible.[56] Experimental results showed that some

of the blends would fail tTS while others would hold. Possible explanations suggest that if the activation energies or WLF parameters of the components are similar, then tTS may hold. Additionally, the failure of tTS can be subtle and not picked up through experimental methods, especially in asymmetric systems with a small volume fraction of one component. There is no theoretical basis for the determination of shift factors a_T in multiphase polymer systems, but if the viscoelastic contrast is high, the contribution of one component will dominate.[56,85] Considering the significant asymmetry in both block design and side chain length of the PS-*b*-PEO BBCPs, it is possible that the "larger" phase is dominating the relaxation response. Above T_g, PS-rich materials generally display thermorheologically simple behavior.[59] On the other hand, there are few accounts of tTS for PEO-rich materials in the molten state, supporting the emergence of thermorheological complexity in the high f_{PEO} samples.

The viscoelastic response of the f_{PEO} series (Figure 3.11a) is remarkably like that of the bottlebrush homopolymers depicted in the literature, specifically the viscously dominated scaling in $G'(\omega)$ & $G''(\omega)$ at intermediate ω and absence of an entanglement plateau.[38–40] In the melt state, BBCPs *f*-24 through *f*-49 proceed directly from primarily viscous behavior at low frequency to glassy behavior at high frequency ($a_T\omega = 10^4$ rad/s). The relaxation patterns suggest that within the microphase segregated domains, the bottlebrush side chains provide a liquid-like environment for the relaxation of the main backbone chains like that in the homopolymer melt. The worm-like conformation of the BBCP block is crucial. LBCPs with comparable domain spacing would undoubtedly possess an entirely different chain configuration environment within each microphase

separated layer of highly entangled, linear flexible chains, consistent with the comparison in Figure 3.14.

The full dynamic spectrum in the melt state is governed by structures across various length scales, such as the microphase separation, macromolecular architecture, and side chain chemistries. As such, multiple relaxation mechanisms contribute to the total response. We believe the structural features of the BBCP are more systematically controlled in the N_{bb} series compared to the f_{PEO} series. Therefore, we interpret the total dynamic behavior with respect to the data set in Figure 3.20. The segmental relaxations of the side chains (the smallest structural length scale) are resolved in the high ω regime, where the dynamics are elastically dominated.[38,40] The power law scaling of the complex modulus $\eta^*(\omega) \sim \omega^{-0.7}$ (Figure 3.25) in the N_{bb} series is compared to that of aPP homopolymer bottlebrushes with short side chains which scale at $\eta^*(\omega) \sim \omega^{-1}$ in the segmental/glassy regime.[40] The PS-*b*-PEO BBCPs do not approach this limit due to the presence of microphase separation. The convoluted response of both the glassy PS and the amorphous PEO domains lead to a "reduced" glassy response on the shortest timescales. The structure is analogous to hard glassy plates (PS domain) separated by a melted mobile layer (PEO domain).

Surprisingly, scaling of $\eta^*(\omega) \sim \omega^{-0.33}$ was observed in the transition from the highest frequency to the intermediate regime ($a_T\omega \sim 10^4$ rad/s), followed by $\eta^*(\omega) \sim \omega^{-0.5}$ in the intermediate ($a_T\omega < 10^1$ rad/s), and returns to $\eta^*(\omega) \sim \omega^{-0.33}$ at terminal timescales. The quantitative scaling is remarkably comparable to that identified by Dalsin et al. for aPP homopolymer bottlebrushes.[38] The power law scaling of -0.33 and -0.5 indicated Zimm and Rouse-like dynamics respectively, according to calculations from the theoretical

dynamic moduli of each molecular model. While the models were initially developed to describe the dynamics of flexible, linear polymers chains in dilute solution, the qualitative picture and quantitative scaling of each model proved useful in describing the dynamics of homopolymer bottlebrush melts within the intermediate ω range. However, the terminal regime of the BBCPs contrasts the homopolymers, where $\eta^*(\omega)$ plateaus and a zero-shear viscosity (η_0) is ultimately resolved. The viscoelastic terminal behavior confirms that there are consequences of the microphase separated structure that are unique to the BBCPs.

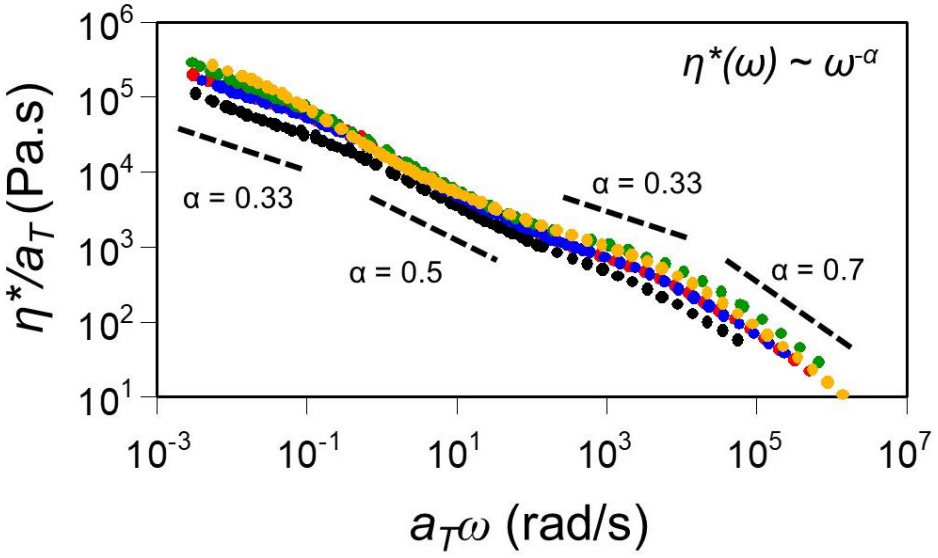

Figure 3.25 Master curves of reduced complex viscosity (η^*) versus shifted frequency ($a_T\omega$) using data from Figure 3.20. Distinct regimes of power law scaling $\eta^*(\omega) \sim \omega^{\alpha}$ are consistently present across all N_{bb}. In the high frequency limit, while all curves do not superimpose, the scaling is approximately $\alpha \approx -0.75$ in each case. Scaling of $\alpha \approx -0.33$ was observed in the transition from the highest frequency to the intermediate regime ($a_T\omega \sim 10^4$ rad/s), followed by $\alpha \approx -0.5$ in the intermediate ($a_T\omega < 10^1$ rad/s), and returns to $\alpha \approx -0.33$ at terminal timescales.

The transition into viscously dominated behavior in Figure 3.20 ($a_T\omega \sim 10^4$ rad/s) or into the first power law regime of $H(\tau)$ in Figure 3.22 ($\tau \sim 10^{-4}$ s) represents a shift away from the fast relaxations dominated by segmental side chains. Here, side chains are unentangled and fully relaxed. Side chains connected to the end of each block, far from the

interface, form a layer of free chain ends in the center of the domain. The blocks may appear constrained schematically, as depicted in Figure 3.26, but the inner-domain structure is essentially a confined liquid melt. The absence of chain entanglements allows the blocks to freely "slide" along each other via. an internal slip layer (ISL). The rapid intradomain relaxation process is resolved by the first relaxation exponent n_1 and dominates the power law behavior at the short time scales. The conventional relaxation of the entire bottlebrush molecule is restricted by the interface, which is consistent with the segregation of the two blocks into their own distinct liquid layers. The PEO and PS layers relax cooperatively in this regime but exhibit different relaxation dynamics due to the asymmetric molecular configurations and difference in segmental friction. Although the semi-flexible backbones have sufficient mobility to slide in both domains, increased configurational volume overlap in the PEO domain may result in hindered dynamics compared to the longer PS backbones. The total response of the cooperative relaxation is likely dominated by the PS dynamics yet convoluted within the spectrum and could contribute to the deviations at $\tau \sim 10^{-4}$ s, which is broader at low N_{bb}. As N_{bb} increases, the scaling of n_1 forms a sharper, more distinct power law regime as the architecture transitions to a more traditional worm-like configuration.

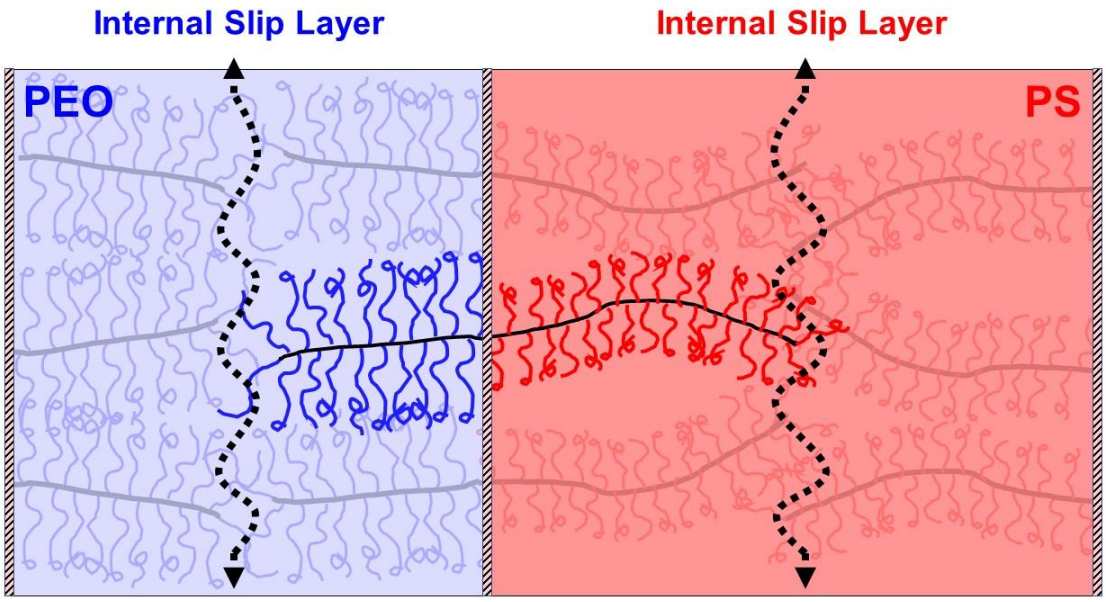

Figure 3.26 Schematic representation of asymmetrically shaped PS-*b*-PEO BBCP locally assembled into a microphase separated layers. Backbone blocks rapidly slide along each other facilitated by an internal slip layer (ISL), producing liquid–like relaxations within each domain (dotted arrows). Side chains avoid overlap due to steric crowding and repulsive forces. The domain interface (dashed lines) is set at junction point between PEO and PS blocks, constraining side chains and preventing composition fluctuations across domains.

In the second regime, n_2 is governed by relaxation processes on a much longer time scale. As previously mentioned, $n_2 \approx 0.67$ is remarkably like a critical gel near the liquid-to-solid transition. According to the SAXS, after the phase transition into the melt state, the lamellae are globally disordered, weakly correlated over large length scales, and likely possess many defects. The structure is qualitatively like the disordered "spinodal pattern" proposed by Bates et al. for symmetric LBCPs near the ODT, where composition fluctuations may be significantly large enough to produce a q^* in scattering, but the equilibrium structure fluctuates spatial in time.[86] However, the scaling of $G'(\omega)$ and $G''(\omega)$ for the symmetric LBCPs is nearly terminal.[86,87] The scaling in the BBCPs is remarkably similar to that found in low MW LBCPs quenched into the ordered state, where power law scaling of $G'(\omega) \sim G''(\omega) \sim \omega^{0.5}$ is described by both theory and experiment.[76,87] Despite

the discrepancy, the BBCP morphology lacks long range order, consistent with that of a material near the gel point, where the structure is on the edge of a sample spanning connectivity limit.[71]

The emergence of a dual relaxation is unique to the BBCP materials. The difference in scaling in n_2 may be due to the interface between the blocks, which is fundamentally different from that found in LBCP systems. For those side chains close to the interface, thermodynamic driving forces induce significant backbone stretching and elongation along with the steric repulsion of side chains.[23] Side chains along the backbone further away from the interface show increased degrees of freedom and orientation compared to the confined arrangement at the interface and contribute to the high mobility of the chain ends in the ISL.[23] The interface is well defined in the melt, and there is minimal composition fluctuation across it due to the large specific interfacial area and strong segregation between the two blocks. The di-blocks are confined perpendicularly to the interface but have mobility to rearrange within the interface itself.[88] The restriction combined with fluctuation effects shifts the terminal relaxation to a much lower frequency. Therefore, the power law behavior likely extends until the MST is reached. In many respects, the schematic picture of semi-flexible, unentangled macromolecules penetrating perpendicularly from a segregated interface is similar to surfactants at a liquid interface, or with the layered liquid super structure of smectic liquid crystals described by Larson et al., where power law scaling at low ω limit is indistinguishable from macroscopically disordered lamellar poly(styrene)-*block*-poly(isoprene).[89]

The impact of the interface is further explained by comparing the scaling of n_2 to that calculated from densely grafted PLA bottlebrushes with short side chains from Haugan

et al. (Figure 3.27).[42] Dynamically, the PLA samples look very similar to critical gels but only show one power law exponent of $n \approx 0.6$ across all experimental time scales. The relaxation of the semi-flexible PLA chains is Rouse-like and not characteristic of the rapid confined ISL process described by n_1. On the longer timescales, the BBCPs exhibit a similar backbone rearrangement mechanism within the interface which is convoluted with the relaxation of the disordered morphology. The onset of this convoluted relaxation feature stretches to longer τ with increasing N_{bb}.

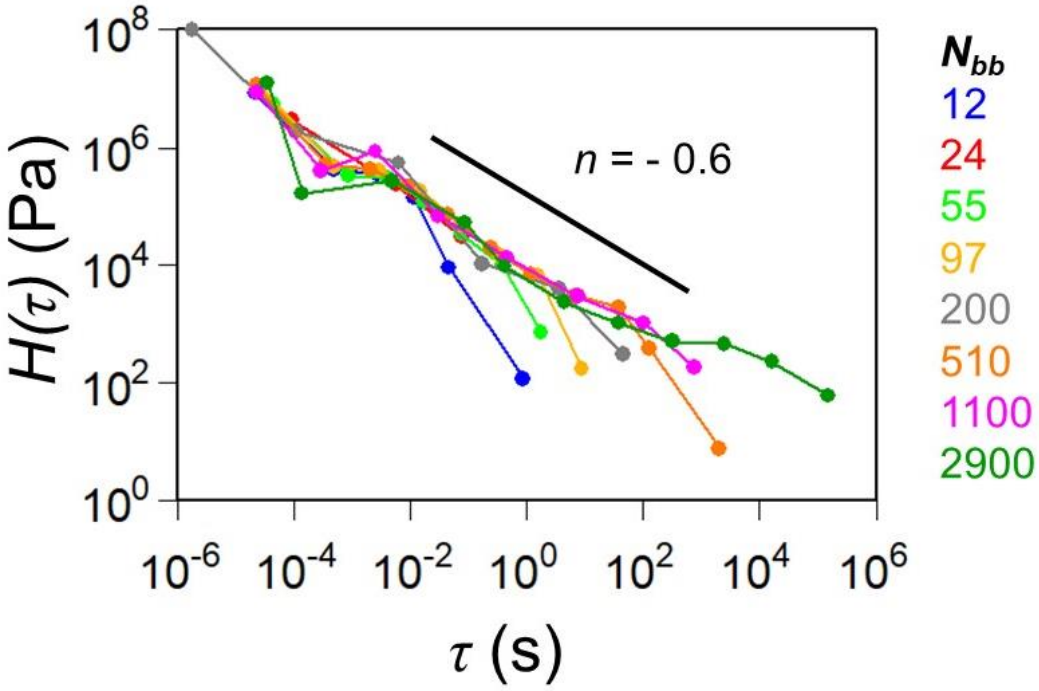

Figure 3.27 Data of Haugan et al.;[42] dynamic data of poly(lactide) (PLA) homopolymer bottlebrushes (hBBs) with side chain M_n = 3.5 kg/mol, graft density z = 1 and backbone degree of polymerization ranging from N_{bb} = 12 - 2900. Relaxation Time Spectra $H(\tau)$ calculated from dynamic data at reference temperature of $T_{ref} = T_g + 34$ °C. Spectra appear to follow single power law model with form $H(\tau) = H_0(\tau)^{-n}$ and power law exponent of n = 0.6.

The emergence of sequential scaling regimes on short and long timescales arises in the BBCP architecture. The BBCPs exhibit classically unentangled dynamics over an exceptionally wide range of backbone lengths and configurations not achieved by LBCPs

of comparable MW. The range of domain spacings can be significantly larger than those realized in LBCPs. The combination of rheological properties of low MW, unentangled systems with the nano-structural characteristics of high MW entangled systems is quite remarkable. Additionally, the application of the dual power law model could be further implemented to compare structure-property relationships in analogous materials exhibiting similar critical gel-like behavior.

3.5 Conclusion & Future Directions

In summary, the linear viscoelastic behavior of PS-*b*-PEO di-block brush copolymers was thoroughly investigated as a function of two primary experimental parameters: block composition (f_{PEO}) and overall backbone length (N_{bb}). BBCPs were synthesized using sequential ROMP and side chain lengths were kept below the entanglement molecular weight to suppress entanglements in the melt state. The viscoelastic response was highlighted by the absence of an entanglement plateau in the master curves of $G'(\omega)$ & $G''(\omega)$, leading to viscously dominated "liquid-like" behavior over a wide ω range while still maintaining microphase segregation and nanostructure. Overall, the BBCPs behave like bottlebrush homopolymers according to SAOS characterizations. The characteristic "liquid-like" response of the BBCPs was compared to the entangled LBCPs with analogous microstructures. The rheological characterization confirms the commonly accepted assumption that reduced chain entanglements produce fast ordering dynamics requiring milder thermal annealing conditions when compared to conventional LBCP materials. However, the unique interplay between dynamics and morphology in the f_{PEO} series was not conclusively resolved. Therefore, we investigated exclusively lamellar BBCPs with constant and symmetric composition (f_{PEO} = 0.5). The

reduced entanglements resulting from short side chains enable rapid self-assembly into microphase segregated lamellar morphologies despite the significant asymmetry between the "molecular shape" of each block. The formation of asymmetric lamellae was observed and suggested a unique molecular packing driven by the excluded volume and steric crowding of densely grafted side chains as well as independent crystallization of the PEO side chains. Microphase separation persisted across the experimental temperature range of the rheological characterization. The bottlebrush architecture governs the rheology across the range of N_{bb}. Most relaxation processes are dominated by two relaxation modes represented by a new dual power law model for the relaxation time spectrum $H(\tau)$ (Eq. 3.2). The PS-*b*-PEO BBCPs in the series generally exhibit scaling exponents of $n_1 \approx 0.83$ and $n_2 \approx 0.67$, typical for materials near the critical-gel point. Therefore, the rheology of the BBCPs is more aptly described as "critical gel like" rather than "liquid like". The faster mode (n_1) is attributed primarily to intradomain dynamics, where unentangled side chains and semi-flexible backbones freely "slide" along each other via an internal slip layer (ISL), facilitated by a liquid region of free chain ends in the center of the layer. The second power law mode (n_2) is attributed to the global morphology and the interface, which is still relatively soft and requires longer times to relax stress. An absence of long range order was observed in the melt at high temperature, consistent with the structure of a weakly percolating network. The response is comparable to low MW unentangled LBCPs in the macroscopically disordered state and lamellar liquid crystal assemblies.

The results in this chapter represent one of the first investigations into the rheological properties of well-defined di-block BBCPs. The full parameter space that defines the structure-property relationship is still relatively unexplored. Of future interest

are systems with alternative side group chemistry with drastic contrast in steric bulkiness and interaction parameter χ. Specifically; acrylates, silicones, and butadiene derivative side chains. While significant synthetic work must be undertaken to prepare these materials, many of the methods are outlined in the literature. The addition of an amorphous, rubbery block (such as poly(dimethyl siloxane), PDMS) to replace the semi-crystalline PEO block could be used to create thermoplastic elastomer analogs, which are used in a wide range of applications. The structure-property relationships in the BBCP architecture may be an advantageous approach to achieve diverse phases and unique rheological properties when compared to that of the well know conventional LBCP materials.

The phase transition in the melt state appears to define the viscoelasticity of the PS-*b*-PEO BBCPs. The highly mobile rheology arises from the disordered structure, while well-ordered morphologies are reformed after quenching back to room temperature. The solidification of the PEO crystallization is important and could be used to the advantage for flow induced processing. These findings emphasize the desirability and potential of the BBCP architectures for ease of processability in future applications. There are many undiscovered structure-property relationships concerning well-ordered structures, such as stabilized lamellae in the melt, or cylindrical and spherical morphologies. The power law relaxation behavior is expected to be fundamentally different for these additional structures.

As an outlook, this work emphasizes the importance of rheological characterization and that it should be implemented more widely. Besides useful time-dependent dynamic data, rheology is useful for determining mechanical properties, processing conditions, and optimizing material properties like damping, extensibility or recovery. The groundwork for

future applications of BBCP rheology is laid out in this chapter. In addition, we believe that the dual power law model elegantly captures sequential relaxation process and is applicable to other complex macromolecular architectures that exhibit similar power law relaxations. For example, the dual model will help quantitatively differentiate the relaxation processes in homopolymer systems with long entangled side chains as well as the systems with strong long-range order in the melt state (either lamellar, cylindrical, or spherical morphology). Analysis of $H(\tau)$ and quantification of the relaxation processes in such systems will certainly improve our understanding of the structure-property relationships in these emergent materials.

3.6 References

(1) Song, D.-P.; Li, C.; Colella, N. S.; Xie, W.; Li, S.; Lu, X.; Gido, S. P.; Lee, J.-H.; Watkins, J. J. Large-Volume Self-Organization of Polymer/Nanoparticle Hybrids with Millimeter-Scale Grain Sizes Using Brush Block Copolymers. *J. Am. Chem. Soc.* **2015**, *137*, 12510–12513.

(2) Verduzco, R.; Li, X.; Pesek, S. L.; Stein, G. E. Structure, Function, Self-Assembly, and Applications of Bottlebrush Copolymers. *Chem. Soc. Rev.* **2015**, *44*, 2405–2420.

(3) Rzayev, J. Molecular Bottlebrushes: New Opportunities in Nanomaterials Fabrication. *ACS Macro Lett.* **2012**, *1* (9), 1146–1149.

(4) Sheiko, S. S.; Sumerlin, B. S.; Matyjaszewski, K. Cylindrical Molecular Brushes: Synthesis, Characterization, and Properties. *Prog. Polym. Sci.* **2008**, *33* (7), 759–785.

(5) Liberman-Martin, A. L.; Chu, C. K.; Grubbs, R. H. Application of Bottlebrush Block Copolymers as Photonic Crystals. *Macromol. Rapid Commun.* **2017**, *38*, 1700058.

(6) Daniel, W. F. M.; Xie, G.; Vatankhah Varnoosfaderani, M.; Burdyńska, J.; Li, Q.; Nykypanchuk, D.; Gang, O.; Matyjaszewski, K.; Sheiko, S. S. Bottlebrush-Guided Polymer Crystallization Resulting in Supersoft and Reversibly Moldable Physical Networks. *Macromolecules* **2017**, *50*, 2103–2111.

(7) Song, D.-P.; Jacucci, G.; Dundar, F.; Naik, A.; Fei, H.-F.; Vignolini, S.; Watkins, J. J. Photonic Resins: Designing Optical Appearance via Block Copolymer Self-Assembly. *Macromolecules* **2018**, *51* (6), 2395–2400.

(8) Song, D.-P.; Lin, Y.; Gai, Y.; Colella, N. S.; Li, C.; Liu, X.-H.; Gido, S. P.; Watkins, J. J. Controlled Supramolecular Self-Assembly of Large Nanoparticles in Amphiphilic Brush Block Copolymers. *J. Am. Chem. Soc.* **2015**, *137* (11), 3771–3774.

(9) Song, D.-P.; Li, C.; Li, W.; Watkins, J. J. Block Copolymer Nanocomposites with High Refractive Index Contrast for One-Step Photonics. *ACS Nano* **2016**, *10* (1), 1216–1223.

(10) Song, D.-P.; Naik, A.; Li, S.; Ribbe, A.; Watkins, J. J. Rapid, Large-Area Synthesis of Hierarchical Nanoporous Silica Hybrid Films on Flexible Substrates. *J. Am. Chem. Soc.* **2016**, *138* (41), 13473–13476.

(11) Altay, E.; Nykypanchuk, D.; Rzayev, J. Mesoporous Polymer Frameworks from End-Reactive Bottlebrush Copolymers. *ACS Nano* **2017**, *11* (8), 8207–8214.

(12) Bolton, J.; Bailey, T. S.; Rzayev, J. Large Pore Size Nanoporous Materials from the Self-Assembly of Asymmetric Bottlebrush Block Copolymers. *Nano Lett.* **2011**, *11* (3), 998–1001.

(13) Sveinbjornsson, B. R.; Weitekamp, R. a.; Miyake, G. M.; Xia, Y.; Atwater, H. a.; Grubbs, R. H. Rapid Self-Assembly of Brush Block Copolymers to Photonic Crystals. *Proc. Natl. Acad. Sci.* **2012**, *109* (36), 14332–14336.

(14) Beers, K. L.; Gaynor, S. G.; Matyjaszewski, K.; Sheiko, S. S.; Moeller, M. Synthesis of Densely Grafted Copolymers by Atom Transfer Radical Polymerization. *Macromolecules* **1998**, *31* (26), 9413–9415.

(15) Huang, K.; Canterbury, D. P.; Rzayev, J. Synthesis of Segmented Polylactide Molecular Brushes and Their Transformation to Open-End Nanotubes. *Macromolecules* **2010**, *43* (16), 6632–6638.

(16) Huang, K.; Rzayev, J. Well-Defined Organic Nanotubes from Multicomponent Bottlebrush Copolymers. *J. Am. Chem. Soc.* **2009**, *131* (19), 6880–6885.

(17) Gao, H.; Matyjaszewski, K. Synthesis of Molecular Brushes by "Grafting onto" Method: Combination of ATRP and Click Reactions. *J. Am. Chem. Soc.* **2007**, *129* (20), 6633–6639.

(18) Xia, Y.; Kornfield, J. A.; Grubbs, R. H. Efficient Synthesis of Narrowly Dispersed Brush Polymers via Living Ring-Opening Metathesis Polymerization of Macromonomers. *Macromolecules* **2009**, *42* (11), 3761–3766.

(19) Xia, Y.; Olsen, B. D.; Kornfield, J. A.; Grubbs, R. H. Efficient Synthesis of Narrowly Dispersed Brush Copolymers and Study of Their Assemblies: The Importance of Side Chain Arrangement. *J. Am. Chem. Soc.* **2009**, *131* (51), 18525–18532.

(20) Love, J. A.; Morgan, J. P.; Trnka, T. M.; Grubbs, R. H. A Practical and Highly Active Ruthenium-Based Catalyst That Effects the Cross Metathesis of Acrylonitrile. *Angew. Chemie - Int. Ed.* **2002**, *41* (21), 4035–4037.

(21) Lin, T.-P.; Chang, A. B.; Luo, S.-X.; Chen, H.-Y.; Lee, B.; Grubbs, R. H. Effects of Grafting Density on Block Polymer Self-Assembly: From Linear to Bottlebrush. *ACS Nano* **2017**, *11* (11), 11632–11641.

(22) Chang, A. B.; Lin, T.-P.; Thompson, N. B.; Luo, S.-X.; Liberman-Martin, A. L.; Chen, H.-Y.; Lee, B.; Grubbs, R. H. Design, Synthesis, and Self-Assembly of Polymers with Tailored Graft Distributions. *J. Am. Chem. Soc.* **2017**, *139* (48), 17683–17693.

(23) Dalsin, S. J.; Rions-maehren, T. G.; Beam, M. D.; Bates, F. S.; Hillmyer, M. A.; Matsen, M. W. Bottlebrush Block Polymers : Quantitative Theory and Experiments. *ACS Nano* **2015**, *9* (12), 12233–12245.

(24) Gu, W.; Huh, J.; Hong, S. W.; Sveinbjornsson, B. R.; Park, C.; Grubbs, R. H.; Russell, T. P. Self-Assembly of Symmetric Brush Diblock Copolymers. *ACS Nano* **2013**, *7* (3), 2551–2558.

(25) Hong, S. W.; Gu, W.; Huh, J.; Sveinbjornsson, B. R.; Jeong, G.; Grubbs, R. H.; Russell, T. P. On the Self-Assembly of Brush Block Copolymers in Thin Films. *ACS Nano* **2013**, *7* (11), 9684–9692.

(26) Rzayev, J. Synthesis of Polystyrene-Polylactide Bottlebrush Block Copolymers and Their Melt Self-Assembly into Large Domain Nanostructures. *Macromolecules* **2009**, *42* (6), 2135–2141.

(27) Semenov, A. N. Contribution to the Theory of Microphase Layering in Block-Copolymer Melts. *Zh. Eksp. Teor. Fiz* **1985**, *88* (4), 1242–1256.

(28) Gai, Y.; Song, D.-P.; Yavitt, B. M.; Watkins, J. J. Polystyrene- Block -Poly(Ethylene Oxide) Bottlebrush Block Copolymer Morphology Transitions: Influence of Side Chain Length and Volume Fraction. *Macromolecules* **2017**, *50*, 1503–1511.

(29) Bates, F. S.; Fredrickson, G. H. Block Copolymers—Designer Soft Materials. *Phys. Today* **1999**, *52* (2), 32.

(30) Chremos, A.; Theodorakis, P. E. Morphologies of Bottle-Brush Block Copolymers. *ACS Macro Lett.* **2014**, *3* (10), 1096–1100.

(31) Chremos, A.; Theodorakis, P. E. Impact of Intrinsic Backbone Chain Stiffness on the Morphologies of Bottle-Brush Diblock Copolymers. *Polym. (United Kingdom)* **2016**, *97*, 191–195.

(32) Lin, T.-P.; Chang, A. B.; Chen, H.-Y.; Liberman-Martin, A. L.; Bates, C. M.; Voegtle, M. J.; Bauer, C. A.; Grubbs, R. H. Control of Grafting Density and

Distribution in Graft Polymers by Living Ring-Opening Metathesis Copolymerization. *J. Am. Chem. Soc.* **2017**, *139*, 3896–3903.

(33) Jiang, L.; Nykypanchuk, D.; Ribbe, A. E.; Rzayev, J. One-Shot Synthesis and Melt Self-Assembly of Bottlebrush Copolymers with a Gradient Compositional Profile. *ACS Macro Lett.* **2018**, *7*, 619–623.

(34) Kawamoto, K.; Zhong, M.; Gadelrab, K. R.; Cheng, L. C.; Ross, C. A.; Alexander-Katz, A.; Johnson, J. A. Graft-through Synthesis and Assembly of Janus Bottlebrush Polymers from A-Branch-B Diblock Macromonomers. *J. Am. Chem. Soc.* **2016**, *138* (36), 11501–11504.

(35) Guo, Z.; Le, A. N.; Feng, X.; Choo, Y.; Liu, B.; Wang, D.; Wan, Z.; Gu, Y.; Li, V.; Osuji, C. O.; et al. Janus Graft Block Copolymers: Design of Polymer Architecture for Independently Tuned Nanostructures and Polymer Properties. *Angew. Chemie Int. Ed.* **2018**, *130*, 8629.

(36) Cheng, L.; Gadelrab, K. R.; Kawamoto, K.; Yager, K. G.; Johnson, J. A.; Alexander-Katz, A.; Ross, C. A. Templated Self-Assembly of a PS- Branch -PDMS Bottlebrush Copolymer. *Nano Lett.* **2018**, *18*, 4360–4369.

(37) Rokhlenko, Y.; Kawamoto, K.; Johnson, J. A.; Osuji, C. O. Sub-10 Nm Self-Assembly of Mesogen-Containing Grafted Macromonomers and Their Bottlebrush Polymers. *Macromolecules* **2018**, *51*, 3680–3690.

(38) Dalsin, S. J.; Hillmyer, M. A.; Bates, F. S. Linear Rheology of Polyolefin-Based Bottlebrush Polymers. *Macromolecules* **2015**, *48*, 4680–4691.

(39) Dalsin, S. J.; Hillmyer, M. A.; Bates, F. S. Molecular Weight Dependence of Zero-Shear Viscosity in Atactic Polypropylene Bottlebrush Polymers. *ACS Macro Lett.* **2014**, *3* (5), 423–427.

(40) López-Barrón, C. R.; Brant, P.; Eberle, A. P. R.; Crowther, D. J. Linear Rheology and Structure of Molecular Bottlebrushes with Short Side Chains. *J. Rheol. (N. Y. N. Y).* **2015**, *59* (3), 865–883.

(41) Hu, M.; Xia, Y.; McKenna, G. B.; Kornfield, J. A.; Grubbs, R. H. Linear Rheological Response of a Series of Densely Branched Brush Polymers. *Macromolecules* **2011**, *44* (17), 6935–6943.

(42) Haugan, I. N.; Maher, M. J.; Chang, A. B.; Lin, T.-P.; Grubbs, R. H.; Hillmyer, M. A.; Bates, F. S. Consequences of Grafting Density on the Linear Viscoelastic Behavior of Graft Polymers. *ACS Macro Lett.* **2018**, *7*, 525–530.

(43) Bates, F. S. Block Copolymers near the Microphase Separation Transition. 2. Linear Dynamic Mechanical Properties. *Macromolecules* **1984**, *17* (12), 2607–2613.

(44) Winey, K. I.; Sanjay, J.; Larson, R. G.; Watanabe, H. Interdependence of Shear

Deformations and Block Copolymer Morphology. *Macromolecules* **1993**, *26*, 2542–2549.

(45) Koppi, K. A.; Tirrell, M.; Bates, F. S.; Almdal, K.; Colby, R. H. Lamellae Orientation in Dynamically Sheared Diblock Copolymer Melts. *J. Phys. II* **1992**, *2*, 1941–1959.

(46) Rubinstein, M.; Obukhov, S. P. Power-Law-Like Stress Relaxation of Block Copolymers: Disentanglement Regimes. *Macromolecules* **1993**, *26* (7), 1740–1750.

(47) Lin, Y.; Gu, Y.; Chen, Z.; Zhang, S.; Zhang, G.; Wang, Y.; Xing, H.; Tang, T. Morphology and Linear Rheology of Comb-like Copolymer Melts with High Grafting Density: I. PVSt- g -(PS- b -PE) Comb-like Block Copolymers. *Polymer (Guildf).* **2017**, *122*, 87–95.

(48) Lin, Y.; Wang, Y.; Zheng, J.; Yao, K.; Tan, H.; Wang, Y.; Tang, T.; Xu, D. Nanostructure and Linear Rheological Response of Comb-like Copolymer PSVS- g -PE Melts: Influences of Branching Densities and Branching Chain Length. *Macromolecules* **2015**, *48* (20), 7640–7648.

(49) Wang, L.; Yang, H.; Tan, H.; Yao, K.; Gong, J.; Wan, D.; Qiu, J.; Tang, T. Synthesis and Structure-Property Relationships of Polypropylene-g- Polystyrene and Polypropylene-g-Poly(n-Butyl Acrylate) Graft Copolymers with Well-Defined Molecular Structures. *Polym. (United Kingdom)* **2013**, *54* (14), 3641–3653.

(50) De La Fuente, J. L.; Fernandez-Garcia, M.; Cerrada, M. L.; Spiess, H. W.; Wilhelm, M. Small-Angle X-Ray Scattering and Linear Melt Rheologyof Poly(Tert-Butyl Acrylate-g-Styrene) Graft Copolymers. *Polymer (Guildf).* **2006**, *47* (5), 1487–1495.

(51) De La Fuente, J. L.; Wilhelm, M.; Spiess, H. W.; Madruga, E. L.; Fernandez-Garcia, M.; Cerrada, M. L. Thermal, Morphological and Rheological Characterization of Poly(Acrylic Acid-g-Styrene) Amphiphilic Graft Copolymers. *Polymer (Guildf).* **2005**, *46* (13), 4544–4553.

(52) Bates, C. M.; Chang, A. B.; Schulze, M. W.; Momcilovic, N.; Jones, S. C.; Grubbs, R. H. Brush Polymer Ion Gels. *J. Polym. Sci. Part B Polym. Phys.* **2015**, *54*, 292–300.

(53) Bates, C. M.; Chang, A. B.; Momcilovic, N.; Jones, S. C.; Grubbs, R. H. ABA Triblock Brush Polymers: Synthesis, Self-Assembly, Conductivity, and Rheological Properties. *Macromolecules* **2015**, *48* (14), 4967–4973.

(54) Yavitt, B. M.; Gai, Y.; Song, D.-P.; Winter, H. H.; Watkins, J. J. High Molecular Mobility and Viscoelasticity of Microphase-Separated Bottlebrush Diblock Copolymer Melts. *Macromolecules* **2017**, *50* (1), 396–405.

(55) Winter, H. H.; Mours, M. The Cyber Infrastructure Initiative for Rheology. *Rheol. Acta* **2006**, *45* (4), 331–338.

(56) van Gurp, M.; Palmen, J. Time-Temperature Superposition for Polymeric Blends. *J Rheol Bull* **1998**, *65*, 5–8.

(57) Booij, H. C.; Palmen, J. Some Aspects of Linear and Nonlinear Viscoelastic Behavior of Polymer Melts in Shear. *Rheol. Acta* **1982**, *21* (4), 376–387.

(58) Williams, M. L.; Landel, R. F.; Ferry, J. D. The Temperature Dependence of Relaxation Mechanisms in Amorphous Polymers and Other Glass-Forming Liquids1. *J. Am. Chem. Soc.* **1955**, *679* (12), 3701–3707.

(59) Morrison, F.; Bourvellec, G. LE; Winter, H. H. Flow-Induced Structure and Rheology of a Triblock Copolymer. *J. Appl. Polym. Sci.* **1987**, *33*, 1585–1600.

(60) Trinkle, S.; Freidrich, C. Van Gurp-Palmen-Plot: A Way to Characterize Polydispersity of Linear Polymers. *Rheol. Acta* **2001**, *40* (4), 322–328.

(61) Colby, R. H. Melt Rheology of Block Copolymers. In *Encyclopedia of Materials: Science and Technology*; 2001; pp 727–730.

(62) Yu, Y.; Chae, C.; Kim, M.; Seo, H.; Grubbs, R. H.; Lee, J. Precise Synthesis of Bottlebrush Block Copolymers from ω - End-Norbornyl Polystyrene and Poly(4-Tert -Butoxystyrene) via Living Anionic Polymerization and Ring-Opening Metathesis Polymerization. *Macromolecules* **2018**, *51* (2), 447–455.

(63) Chae, C.; Yu, Y.; Seo, H.; Kim, M.; Grubbs, R. H.; Lee, J. Experimental Formulation of Photonic Crystal Properties for Hierarchically Self-Assembled POSS − Bottlebrush Block Copolymers. *Macromolecules* **2018**, *51* (9), 3458–3466.

(64) Chang, A. B.; Bates, C. M.; Lee, B.; Garland, C. M.; Jones, S. C.; Spencer, R. K. W.; Matsen, M. W.; Grubbs, R. H. Manipulating the ABCs of Self-Assembly via Low-X Block Polymer Design. *Proc. Natl. Acad. Sci.* **2017**, *114* (25), 6462–6467.

(65) Bates, F. S.; Fredrickson, G. H. Block Copolymer Thermodynamics: Theory and Experiment. *Annu. Rev. Phys. Chem.* **1990**, *41* (1), 525–557.

(66) Shibayama, M.; Hashimoto, T. Small-Angle X-Ray Scattering Analyses of Lamellar Microdomains Based on a Model of One-Dimensional Paracrystal with Uniaxial Orientation. *Macromolecules* **1986**, *19*, 740–749.

(67) Matsen, M. W.; Bates, F. S. Unifying Weak- and Strong-Segregation Block Copolymer Theories. *Macromolecules* **1996**, *29* (4), 1091–1098.

(68) Almdal, K.; Koppi, K. A.; Bates, F. S.; Mortensen, K. Multiple Ordered Phases in a Block Copolymer Melt. *Macromolecules* **1992**, *25* (6), 1743–1751.

(69) Fox, T. G.; Flory, P. J. The Glass Temperature and Related Properties of Poly-Styrene. Influence of Molecular Weight. *J. Polym. Sci.* **1954**, *14*, 315–319.

(70) Ren, J. M.; McKenzie, T. G.; Fu, Q.; Wong, E. H. H.; Xu, J.; An, Z.; Shanmugam, S.; Davis, T. P.; Boyer, C.; Qiao, G. G. Star Polymers. *Chem. Rev.* **2016**, *116* (12), 6743–6836.

(71) Winter, H. H.; Mours, M. Rheology of Polymers near Liquid-Solid Transitions. *Adv. Polym. Sci.* **1997**, *134*, 165–234.

(72) Baumgaertel, M.; Winter, H. H. Determination of Discrete Relaxation and Retardation Time Spectra from Dynamic Mechanical Data. *Rheologica Acta*. 1989, pp 511–519.

(73) Winter, H. H. The Occurance of Self Similar Relaxation in Polymers. *J. Non. Cryst. Solids* **1994**, *172*, 1158–1167.

(74) Colby, R. H. Block Copolymer Dynamics. *Curr. Opin. Colloid Interface Sci.* **1996**, *1*, 454–465.

(75) Witten, T. A.; Leibler, L.; Pincus, P. A. Stress Relaxation in the Lamellar Copolymer Mesophase. *Macromolecules* **1990**, *23* (3), 824–829.

(76) Kawasaki, K.; Onuki, A. Dynamics and Rheology of Diblock Copolymers Quenched into Microphase-Separated States. *Phys. Rev. A* **1990**, *42* (6), 3664–3666.

(77) Fredrickson, G. H.; Bates, F. S. Dynamics of Block Copolymers: Theory and Experiment. *Annu. Rev. Mater. Sci.* **1996**, *26* (1), 501–550.

(78) Kim, D. H.; Sun, Z.; Russell, T. P.; Knoll, W.; Gutmann, J. S. Organic-Inorganic Nanohybridization by Block Copolymer Thin Films. *Adv. Funct. Mater.* **2005**, *15* (7), 1160–1164.

(79) Paturej, J.; Sheiko, S. S.; Panyukov, S.; Rubinstein, M. Molecular Structure of Bottlebrush Polymers in Melts. *Sci. Adv.* **2016**, *2* (11), e1601478.

(80) Huang, P.; Zhu, L.; Guo, Y.; Ge, Q.; Jing, A. J.; Chen, W. Y.; Quirk, R. P.; Cheng, S. Z. D.; Thomas, E. L.; Lotz, B.; et al. Confinement Size Effect on Crystal Orientation Changes of Poly(Ethylene Oxide) Blocks in Poly(Ethylene Oxide)- b -Polystyrene Diblock Copolymers. *Macromolecules* **2004**, *37* (10), 3689–3698.

(81) Loo, Y. L.; Register, R. A.; Ryan, A. J. Modes of Crystallization in Block Copolymer Microdomains: Breakout, Templated, and Confined. *Macromolecules* **2002**, *35* (6), 2365–2374.

(82) Quiram, D. J.; Register, R. A.; Marchand, G. R. Crystallization of Asymmetric Diblock Copolymers from Microphase-Separated Melts. *Macromolecules* **1997**, *30* (16), 4551–4558.

(83) Ryan, A. J.; Hamley, I. W.; Bras, W.; Bates, F. S. Structure Development in Semicrystalline Diblock Copolymers Crystallizing from the Ordered Melt.

Macromolecules **1995**, *28* (11), 3860–3868.

(84) Zhu, L.; Cheng, S. Z. D.; Calhoun, B. H.; Ge, Q.; Quirk, R. P.; Thomas, E. L.; Hsiao, B. S.; Yeh, F.; Lotz, B. Phase Structures and Morphologies Determined by Self-Organization, Vitrification, and Crystallization: Confined Crystallization in an Ordered Lamellar Phase of PEO-b-PS Diblock Copolymer. *Polymer (Guildf).* **2001**, *42*, 5829–5839.

(85) Han, C. D.; Kim, J. K. On the Use of Time-Temperature Superposition in Multicomponent/Multiphase Polymer Systems. *Polymer (Guildf).* **1993**, *34* (12), 2533–2539.

(86) Bates, F. S.; Rosedale, J. H.; Fredrickson, G. H. Fluctuation Effects in a Symmetric Diblock Copolymer near the Order – Disorder Transition. *J. Chem. Phys.* **1990**, *92* (1990), 6255.

(87) Rosedale, J. H.; Bates, F. S. Rheology of Ordered and Disordered Symmetric Poly(Ethylenepropylene)-Poly(Ethylethylene) Diblock Copolymers. *Macromolecules* **1990**, *23* (8), 2329–2338.

(88) Zhang, Y.; Wiesner, U. B. Rheology of Lamellar Polystyrene- Block - Polyisoprene Diblock Copolymers. *Macromol. Chem. Phys.* **1998**, *199*, 1771–1784.

(89) Larson, R. G.; Winey, K. I.; Patel, S. S.; Watanabe, H.; Bruinsma, R. The Rheology of Layered Liquids: Lamellar Block Copolymers and Smectic Liquid Crystals. *Rheol. Acta* **1993**, *32*, 245–253.

CHAPTER 4

ALIGNMENT OF WELL-ORDERED LAMELLAE IN BRUSH BLOCK COPOLYMERS WITH CONTROLLED OSCILLATORY SHEAR

4.1 Introduction & Project Motivation

Long range, defect-free structural order enhances the utility of nanoscale devices. For example, optically active photonic crystals require multiple stacks of repeating layers packed into long-range, single crystalline order.[1–3] Polycrystallinity, packing defects, and stacking faults disrupt the constructive interference of the incident light.[4] In membranes of ion conducting materials, well-ordered continuous pathways are required throughout the matrix to transport the ions. In proton exchange membranes (PEMs) fabricated from lamellar BCPs, the conductivity is dependent on the orientation of the lamellar layers.[5,6] PEMs with isotropically disordered domains and significant grain boundaries have reduced conductivity compared to those with anisotropic, aligned structures. Some heterogenous materials spontaneously form large grains of oriented structure (on order of hundreds of microns), but directing the structure into a single crystal with defined orientation is desired to optimize material performance.[1,7] Therefore, understanding pathways to control long range order during material preparation and processing is critical. The pursuit of controlling long range order and orientation in BCPs has led to the field of *directed self-assembly* (DSA), and is applicable to both BCP templates and self-assembled nanocomposites.[8,9] Chemoepitaxy (chemically-driven) and graphoepitaxy (topologically-driven) are two primary approaches for thin film assemblies.[8] In bulk materials, the application of an external field (electrical, magnetic, mechanical) is necessary.[8,10] Electrical field alignment

relies on the difference in dielectric permittivity between the block segments.[5,11,12] Domains align along the field direction through field induced de-mixing and reformation processes.[9] Measurement by Ruppel et al. utilized in-situ time-resolved X-ray to determine the dynamic pathways of ordering, and correlate the electric field strength to the observed phase transitions and phase behavior.[11,13] Strong orientation was achieved under electric fields near the order-to-disorder transition. Three primary mechanisms were proposed and evaluated through both experiment and theory; rotation of grains, nucleation and growth, and selective disintegration of lamellar grains.[11] BCPs alignment with magnetic fields was elegantly demonstrated in work from Osuji and coworkers.[9,14–16] Magnetic field alignment relies on anisotropy in the magnetic susceptibility of the two blocks, which arise from either permanent magnetic material properties, or induced magnetic dipoles. Conventional BCP systems are aligned under exceptionally high field strengths (4.5 - 6 T) using powerful NMR magnets. However, the setup is cumbersome and energy intensive. Low magnetic fields (0.5 – 1 T) are used in conjunction with specialty BCP chemistries, requiring incorporation of magnetically active substituents (such as inorganic NPs or liquid crystals).[15] Magnetic and electrical alignment possess many advantages and feasible pathways towards well-ordered nanostructures, however introducing significant contrast between the two blocks remains a barrier to universal use.[8]

An alternative approach is through mechanical methods, such as the application of stress. Specifically, shear stress was used to align BCP morphologies as far back as 1970, when Keller et al. first discovered flow induced ordering in styrene-butadiene-styrene (SBS) BCPs.[17] Several years later, reports of induced alignment by oscillatory shear were presented by Koppi et al. in poly(ethylene propylene)-*block*-poly(ethylene ethylene) (PEP-

b-PEE) BCP melts (φ_{PEP} = 0.55), which strongly microphase separated into lamellar morphologies.[18,19] The lamellar grains were initially small in size after thermal annealing and melt pressing according to the isotropic powder diffraction pattern observed in small angle neutron scattering (SANS) experiments. When the isotropic samples were subjected to oscillatory shear at low frequency (ω = 0.2 rad/s), the lamellae were found to orient along to the velocity-gradient direction after 15 hours of continuous shearing at large strain amplitude (γ = 100 %). However, at higher frequencies (ω = 1 rad/s), the lamellae oriented normal to the velocity-gradient. The crossover in orientation was explained by the relationship between the applied ω and the relaxation time of the slow local domains or the faster chain relaxations. Oscillating at either relaxation time facilitates that respective structure to reorient with or against the shear field. When shearing at temperatures well below T_{ODT}, the orientation was independent of the applied ω with lamellar layers always forming along the velocity-gradient.[18] Two mechanisms were proposed to describe the experimental results. First, the lamellae aligned along the velocity-gradient were thought to arise through a pathway referred to as "defect mediated stress relaxation". At low ω, the defects in the lamellae become the stress bearing structures and have the ability reorder over other structural features, resulting in the progressive removal of grain boundaries. The removal of such defects in the quenched state lowered the overall energy of the system. The second pathway was through a "shear induced disordering", where the lamellae are destroyed from the energy input of the intense shear and reform along the vorticity direction of the shear flow. The primary characterization technique to determine the orientation of the PEP-*b*-PEE lamellae was SANS, which required significant sample

preparation as sufficient deuteration is necessary to introduce contrast between the microphase separated domains.[18]

Poly(styrene)-*block*-poly(isoprene) (PS-*b*-PI) is the standard BCP template to study shear induced alignment and has been demonstrated in detail.[20–24] A series of papers from Chen et al. explores the large parameter space of processing parameters under large amplitude oscillatory shear (LAOS) of PS-*b*-PI BCPs with lamellar morphology.[20–22] The final orientation is dependent on strain amplitude (γ), temperature (T), time (t), and frequency (ω). In terms of the polymer dynamics, two characteristic frequencies are proposed to explain the frequency-dependent alignment in a similar approach to Koppi et al. The first frequency is associated with the time scale of chain dynamics (ω_c') while the second relates to longer range domain relaxations (ω_d). The characteristic frequencies were used to define four dynamic regimes in which a different lamellar orientation will form. Three primary orientations of lamellae can form with respect to the applied shear field: parallel, perpendicular, and transverse (Figure 4.1). Structural characterization by laser optical methods concluded that the perpendicular orientation was possible at frequencies below ω_c' and above ω_d ($\omega_d < \omega < \omega_c'$) where the dynamics are coupled with nanostructure and oscillations are slow enough that the chains segments are fully relaxed. Parallel alignment was observed at the high frequencies above ω_c' as well as below ω_d on time scales dominated by the microphase separated domains. At timescales well above ω_c' (i.e. the highest accessible frequencies), a bimodal distribution of parallel and transverse orientations was observed.

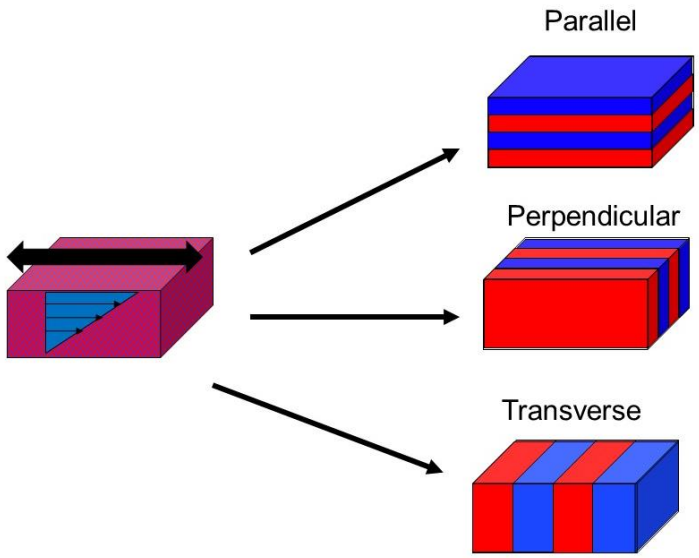

Figure 4.1 Three potential orientations of lamellar morphology with respect to applied shear deformation

Complementary experiments were performed by Zhang and Wiesner on PS-*b*-PI BCPs around the same time.[23,24] Here, the molecular weight and temperature dependence was more thoroughly considered. In addition to the high molecular weight samples, low molecular weight samples (below entanglement molecular weight) form lamellar morphology with strong microphase segregation despite the low block length *N*. The dynamics of the unentangled samples exhibited entanglement-like effects, despite each block being much lower than the expected entanglement MW of a corresponding homopolymer. The experimental results were rationalized by the introduction of additional constrains placed on the PS and PI chains by the block junction at the interface. The junction acts as a "physical crosslink" and convolutes the transition zone from segmental relaxations to structure dominated relaxation at the lowest ω.[23] The junction has significantly more freedom to move within the interface (parallel) than it does across the interface (perpendicular). The additional conformational freedom contributed to correlated motion of the interfaces under large amplitude shear, resulting in parallel orientation.[24] The

major findings of this study are summarized in Figure 4.2, where the various alignment mechanisms are defined with respect to the power law scaling of complex viscosity (η^*) with reduced oscillatory frequency ($a_T\omega$).

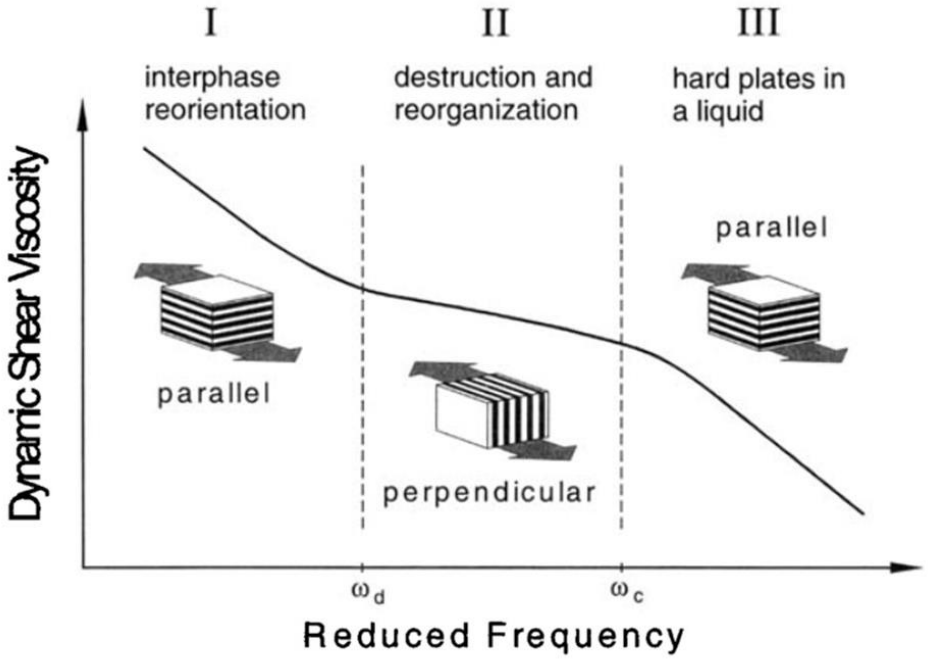

Figure 4.2 Schematic representation of the three frequency regimes of orientation I-III related to the dynamic shear viscosity observed for lamellar diblock copolymers (Modified from Ref. 24)[24]

Winey et al. expanded the evaluation of the PS-*b*-PI BCPs by considering the effect of shear on alignment at both intermediate and global length scales, utilizing electron microscopy as standard technique to quantify domain alignment.[25] Alignment was observed at relatively low strains (γ = 5 %) at temperatures only 20 °C above T_g of the PS domain. The findings suggested that a commonly accepted "grain rotation" mechanism, in which locally ordered grains of lamellae re-orient as hard bodies into the shear field, was not occurring in their samples. The initial structure (before shear alignment) was disordered, suggesting there were no grains to rotate. It appeared that "destruction and reformation" of the lamellae was the primary mechanisms for alignment, supported by the

presence of focal conic defects after shearing, which can only form through destruction and reformation.[25]

In-situ experimental setups are ultimately necessary to directly observe the dynamic re-orientation pathways during oscillatory shear alignment. Several set ups are proposed for a wide range of shear geometries and measurement orientations.[26–32] A concentric couette flow cell is used for predominantly viscous complex fluids. The sampling volume is often very large, limiting the application to BCP melts and NP/BCP composites. Therefore, parallel plate or linear shear cells are necessary. The collection of data on relevant time scales requires the intensity of synchrotron SAXS or neutron sources, limiting the availability of the in-situ set ups.

The lamellar systems have been considered extensively. While not discussed in this thesis, alignment of other morphologies, such as hexagonally packed cylinders or cubic lattice spheres, follows entirely different dynamics and alignment pathways.[33–36] The focus on oscillatory shear does not exclude steady shear and flow induced ordering as possible processing approaches to align BCP domains, which deserve to be considered in a separate arena.[37]

Traditionally, LBCP materials are aligned through intense nonlinear shear deformations (γ = 10 – 100 %), which is necessary to overcome thermodynamic stability in the system and induce grain rotation or destruction/reformation mechanisms. The processing temperatures are also often controlled at a temperature near T_{ODT} to increase the chain mobility. In a practical sense, lower operating temperature may be more desired and of concern for large scale processing and coating applications, or with materials that are thermally degradable. The application of oscillatory shear alignment to BBCPs is of

significant interest. We have demonstrated that BBCPs are unentangled in the melt, and exhibit critical gel-like, highly mobile rheology. Therefore, the energy input may not be as high as in traditional entangled LBCP systems. Additionally, BBCPs naturally self-organize into large ordered grains.[1,38] However, the orientation of said grains have not been controlled in any particular direction. Therefore, shear is a practical candidate for DSA of microphase separated BBCP morphologies. As of now, the systematic relationship between the viscoelasticity and domain orientation in BBCPs has not been explored or described in detail.

In this work, we report the alignment of microphase separated lamellae in BBCPs when subjected to oscillatory shearing conditions with respect to characteristic relaxation dynamics inspired by the approach established by Koppi and Wiesner.[18,24] Specifically, we investigate two different types of lamellae forming BBCP templates which exhibit multiple dynamic regimes as defined by their linear viscoelasticity. We wish to understand the effect of controlled oscillatory shearing within each established frequency regime on the local and global orientation of the lamellar morphology.

4.2 Experimental

4.2.1 Material Selection

Two separate lamellae forming AB di-block BBCPs were synthesized by sequential ring opening metathesis polymerization (ROMP) according to established procedures: Poly(styrene)-*block*-poly(ethylene oxide) (PS-*b*-PEO) BBCP (f_{PEO} ~ 0.5, PS-NB MM M_n = 2.9 or 3.5 kg/mol and PEO-NB MM M_n = 5 kg/mol) and poly(tert butyl acrylate)-*block*-poly(ethylene oxide) (PtBA-*b*-PEO) (f_{PEO} ~ 0.4, PtBA-NB MM M_n = 7.6 kg/mol and PEO-NB MM M_n = 5 kg/mol).[1,39] Synthetic characterizations (NMR and GPC) are presented in

Appendix A. Consideration was taken in the molecular design to keep side chain lengths low to reduce entanglements and maintain high molecular mobility according to previous studies.[1] PS-*b*-PEO was chosen as we have systematically evaluated the linear viscoelastic properties of model materials and have described the various structural relaxation processes and mechanisms (See Chapter 3). PtBA-*b*-PEO was selected to compare directly with the conclusions drawn by Song et al. concerning self-organization of lamellar arrays into large volume grains.[1]

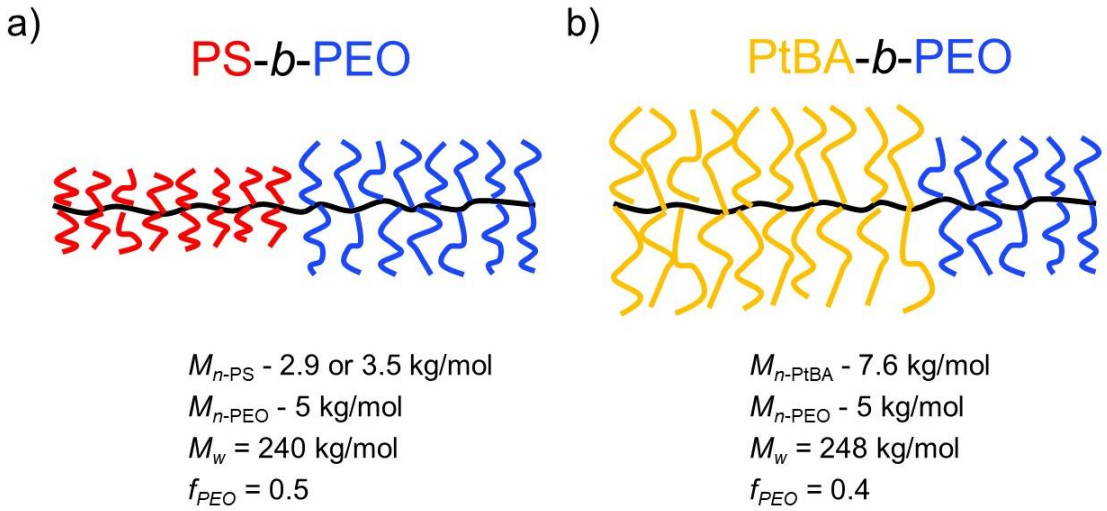

Figure 4.3 Molecular Design of **(a)** PS-*b*-PEO and **(b)** PtBA-*b*-PEO BBCPs

4.2.2 Sample Preparation, Characterization and Shearing Protocols

BBCPs were drop cast from 1.5 wt.% solutions of dichloromethane (DCM) through 0.45 μm PTFE filters onto flat glass substrates, which were covered immediately with glass Petri dishes. After adequate solvent evaporation (~ 1 day), the films were additionally dried under nitrogen purge to completely remove excess solvent. The dried films were removed by razor blade. Bulk samples were prepared for rheological characterization of linear and non-linear viscoelastic properties, while additional material was collected and prepared for shear processing.

For viscoelastic characterization, approximately 40 mg of bulk material was packed into a circular metal mold and sandwiched between pieces of Kapton tape. The samples were annealed under vacuum for 1 h at T = 120 °C (PS-*b*-PEO) or 15 min at T = 100 °C (PtBA-*b*-PEO). The samples were subsequently cooled to room temperature (T ~ 25 °C). Dynamic moduli were measured by small-amplitude oscillatory shear (SAOS) between ω = 1 - 100 rad/s using a Malvern Kinexus rotational rheometer and an 8 mm parallel plate geometry. Measurements were conducted within the linear viscoelastic regime (LVR) at strain amplitudes of γ = 1 %, confirmed by strain amplitude sweeps at ω = 1 rad/s from γ = 0.1 % to γ = 100 % at three separate temperatures. SAOS isothermal frequency sweeps were performed from T = 50 - 170 °C in 10 °C intervals. The time−temperature superposition (tTS) principle was found to apply over a wide temperature range. Rheological data were analyzed using IRIS Rheo-Hub 2018 software.[40]

A preliminary shear alignment study was conducted in the Kinexus with PS(3.1k)-*b*-PEO(5k) BBCP. A melt pressed, thermally annealed circular sample (R = 4 mm) was prepared and characterized by SAXS before and after shearing in the parallel plate geometry in the rheometer. 2-D SAXS patterns were collected at locations along the radial direction on the circular sample from the center (r = 0) to the outer edge ($r \approx R$ = 4 mm). The sample was subjected to single frequency oscillatory time sweeps at constant frequency (ω = 1 rad/s), constant strain amplitude (γ = 1 %), and constant temperature (T = 110 °C) for an extended time (t = 2 h). After cooling down to room temperature, the sample was scanned by SAXS at positions along the radial direction as well as 8 points equally distributed azimuthally near the edge of the disk-shaped sample (r ~ R).

All other shear alignment studies were conducted in a Linkam CSS450 Optical Shearing Device by placing approximately 5-10 mg of BBCP on a strip of Kapton tape placed over the optical window (Fig 4.4). Bulk sample dimensions were approximately 2 mm x 2 mm x 1 mm (V = 4 mm^3). The shearing stage was heated and held at a thermal annealing temperature (1 h at T = 120 °C (PS-*b*-PEO) or 15 min at T = 100 °C (PtBA-*b*-PEO)) to allow microphase separation and self-assembly of the morphology. After thermal annealing, the gap height between the two shearing plates was set to h = 0.7 mm and the shearing stage temperature was either heated or cooled to a desired shearing temperature (T_{shear}), after which controlled oscillatory shear was immediately applied for t = 6 h. The shearing parameters were selected according to the analysis of the linear and non-linear viscoelastic characterization (Figure 4.6 and Figure 4.16 for PS-*b*-PEO and PtBA-*b*-PEO respectively). Three separate regimes were selected as a function of ω, denoted as high, intermediate, and low ω. γ was selected as 50 %, within the non-linear viscoelastic regime at all selected shearing frequencies. The shearing time was chosen to be t = 6 h. to provide adequate time for structure development. Due to experimental limitations of the CSS450, the applied frequency was set constant at ω = 1 rad/s, while the shearing temperature was changed, allowing access to the different relaxation times through the tTS relationship. Shearing conditions are presented in Table 4.1 for PS-*b*-PEO and Table 4.2 for PtBA-*b*-PEO. After shearing, the stage was cooled to room temperature (T = 25 °C) and the sample was carefully removed and placed onto a strip of double sided tape, keeping the sample orientation consistent with the shearing direction. For comparison, a control sample was prepared through the same pre-annealing procedure but in the absence of shear (referred to as “static anneal”).

Table 4.1: Shearing Conditions for PS-*b*-PEO determined from SAOS

Shearing Regime	T_{shear} (°C)	Frequency ω (rad/s)	Strain Amplitude γ *(%)*	Time *t* (hr.)
High	95	1	50	6
Intermediate	115	1	50	6
Low	145	1	50	6
Static Anneal	120	--	--	1

Table 4.2: Shearing Conditions for PtBA-*b*-PEO determined from SAOS

Shearing Regime	T_{shear} (°C)	Frequency ω (rad/s)	Strain Amplitude γ *(%)*	Time *t* (hr.)
High	50	1	50	6
Intermediate	65	1	50	6
Low	110	1	50	6
Static Anneal	100	--	--	0.25

Microphase segregation, domain spacing, and domain orientation of the sheared BBCP samples were characterized using small-angle X-ray scattering (SAXS) on a Ganesha SAXS-LAB instrument with Cu Kα 0.154 nm line. Domain spacings $d_0 = 2\pi/q^*$ were determined from q^* = primary peak position. 2-D scattering patterns were collected at three orthogonal direction according to the orientation of the applied shear (Figure 4.4c) Bulk shear aligned samples were positioned in front of X-ray beam in each direction and manually rotated after each measurement. Intensity (*I(q)*) of each measurement was normalized for incident beam intensity and sample thickness. The 2-D scattering pattern represents sampling volume with incident surface area of 0.3 x 0.3 mm, which is the approximate area of the X-ray beam. Large volume orientation data was collected by synchrotron SAXS on beamline 11-BM (Complex Materials Scattering, CMS) at the National Synchrotron Light Source II (NSLS-II), Brookhaven National Laboratory (BNL).

A silver behenate standard was used for the calibration of all 2-D scattering data. Select shear aligned samples were oriented onto the sample stage with respect to the shearing direction in similar fashion to the Ganesha set up. The sample stage was translated and scanned with continuous SAXS exposures with a beam size of 0.1 x 0.1 mm. Measurements were taken across the entire top surface of the bulk samples (through the gradient direction) and along the edge of the sample (through the flow and vorticity directions). The space between each scattering pixel is approximately 0.1 mm. 2-D scattering patterns were processed by integrating *I* versus *q* into 1-D spectra plots as well as *I(q*)* versus azimuthal angle (*θ)*. Orientationally order parameter *S* was calculated for each 2-D scattering pattern and plotted into order parameter maps (Details in Section 4.3.3).

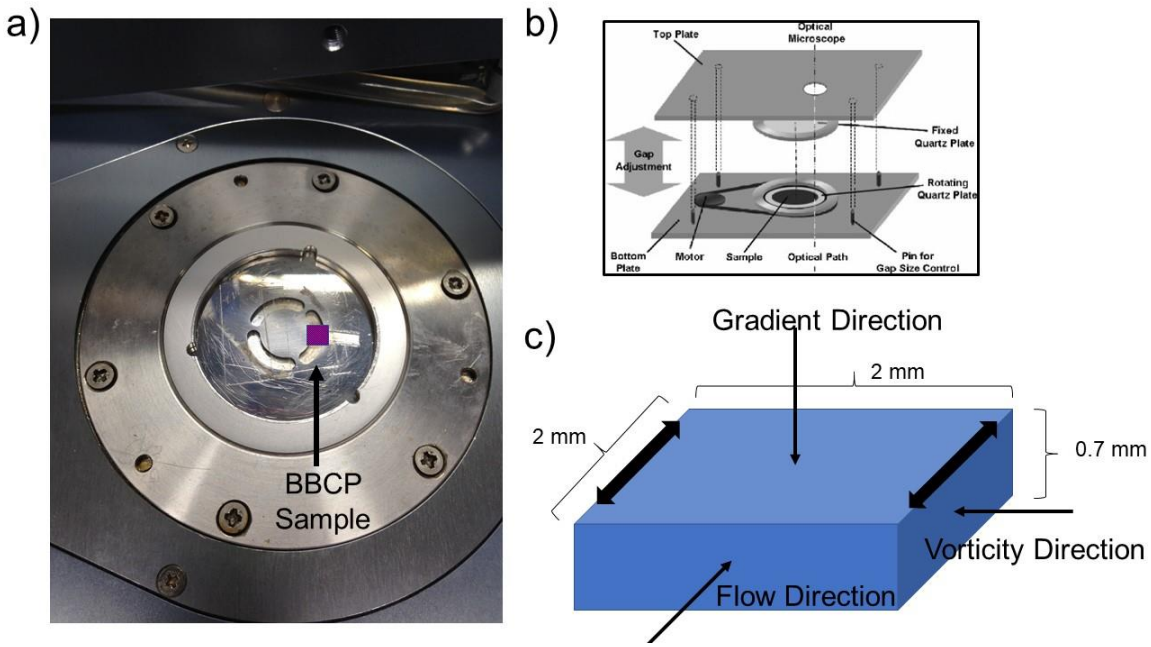

Figure 4.4 (a) Linkam CSS450 shear cell **(b)** Schematic of Linkam CSS450 construction **(c)** Sample geometry with approximate dimensions and orientations of flow (*v*), gradient (∇*v*), and vorticity (∇x*v)* directions.

4.3 Results

4.3.1 Alignment of PS-*b*-PEO BBCPs with SAOS

Shear alignment on PS-*b*-PEO BBCP was conducted with controlled shearing in the rheometer at low strain and low temperature, inspired by the approach outlined by Winey et al.[25] Before shear alignment, 2-D SAXS patterns of separately prepared PS(3.5k)-*b*-PEO(5k) BBCP were collected along the radial axis. After thermal annealing, there was no apparent preferred orientation of the microphase segregated domains (Figure 4.5). An isotropic powder diffraction pattern for the primary peak was observed at most points along the radial axis from the center of the sample ($r = 0$) to the edge ($r \approx R$). The sample was subjected to single frequency oscillatory time sweeps (ω = 1 rad/s) for t = 2 h at a strain amplitude of γ = 1% and constant temperature T = 110 °C. After shearing, the radial axis was scanned again. While no changes in the G^* were observed during shearing, a very distinct transition in the preferred orientation of the lamellar domains was evident from the 2-D SAXS patterns.[41] At the center of the sample, a powder diffraction pattern was still present indicating no preferred orientation of the lamellar structure. At radial locations closer to the edge ($r \rightarrow R$), the intensity of the primary peak began to increase as well as the preferred azimuthal angle θ. At the very outer edge, strong scattering signal arising from domain alignment was observed as shown in the 2-D SAXS pattern (Figure 4.5b). Strain amplitude is linearly proportional to radial distance in the parallel plate geometry.[42] As the applied strain amplitude increased with increased distance from the center, a preferred orientation begins to emerge. At r/R = 0.75, the beginning of a preferred azimuthal angle dependence appears and becomes very strong at $r/R \approx 1$. The 2-D SAXS pattern suggests that the lamellae are aligned normal to the vorticity plane of the shear

(perpendicular orientation). The 1-D *I(q)* spectra indicate that the microphase segregation was unchanged after the application of shear. Spectra at $r/R \approx 1$ before and after shearing have identical microphase segregation strength and domain spacing.[41] Additionally, the microphase separation persists at the shearing temperature (T = 110 °C) well below T_{MST}, as shown by temperature-controlled SAXS in Chapter 3. 2-D SAXS patterns were collected at points along the outer edge ($r/R \approx 1$) where anisotropy was the strongest (Figure 4.5c) to determine the global orientation across the sample. The preferred domain direction correlates to the applied shear direction. Normalized intensities of the primary peak were shifted according to the applied oscillatory shear direction at each location on the outer edge (Figure 4.5d). At all points around the edges, the primary peaks align perpendicular (at θ = 90° and 270°) to the applied shear direction. The correlated orientation over several millimeters is impressive and suggests that large volume grains may be processed.

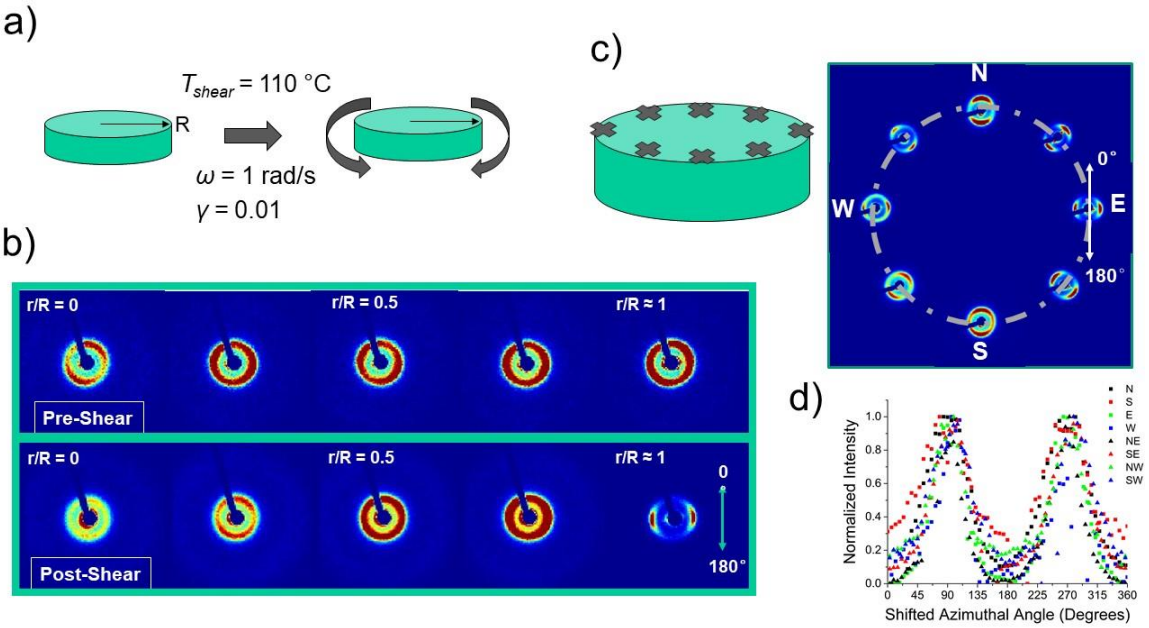

Figure 4.5 Controlled shearing of PS-*b*-PEO in Kinexus Rheometer. **(a)** Sample geometry and shear conditions. **(b)** 2-D SAXS patterns taken along radial direction before and after shear alignment. Orientation arises at the sample edge (r/R = 1) after shearing. **(c)** 2-D SAXS patterns taken at equidistant locations on the sample edge. All orientations are correlated to the shear direction. **(d)** Normalized intensity of q^* as a

function of shifted azimuthal angle according to shear direction formalism in (c). All orientations align with $\theta = 0$ and 180° (Modified from Ref. 41)[41]

4.3.2 Frequency Dependent Shearing of PS-*b*-PEO BBCP

The initial observations of shear induced alignment is surprising, especially considering the low strain amplitude. While some orientation is induced with small amplitude oscillatory shear, the majority of reorientation occurs under larger amplitude. We observed that a critical shear amplitude of γ = 1 % was necessary to induce domain orientation. Therefore, a systematic analysis of large amplitude strains was conducted to achieve higher degree of orientation over larger areas and identify the other possible orientations. Here, we approach the correlation between dynamic response and lamellar orientation described by Wiesner et al.[24] For subsequent studies, a new PS(2.9k)-*b*-PEO(5k) BBCP system was prepared. Overall, the rheology is consistent with previous reports, as well as the analysis and discussion in Chapter 3. In the melt state, PS-*b*-PEO is thermorheologically simple and obeys tTS. Figure 4.6a shows the dynamic response plotted as complex viscosity (η^*/a_T) versus shifted frequency ($a_T\omega$) at a reference temperature of T_{ref} = 120 °C (shift factors inset). The curve is partitioned into four distinct scaling regimes, defined by exponent x in power law scaling $\eta^*(\omega) \sim \omega^{-x}$. According to observations by Chen and Wiesner, each regime corresponds to a unique relaxation transition across the self-assembled structure. In BBCPs, high frequency response is associated with sequential relaxation processes resulting from the unentangled side chains, while lower frequency is a consequence of the highly mobile morphology. Within each regime, a single oscillatory frequency at the midpoint is defined and denoted for shearing as low ω, intermediate ω, or high ω. The response at the highest accessible frequencies ($a_T\omega > 10^4$ rad/s) begins to enter the segmental/glassy relaxation and was avoided. The

non-linear viscoelastic response was determined at each ω by strain sweeps from γ = 0.1 % to 100 % (Figure 4.6b). Complex modulus G^* is constant at low γ and begins to deviate as γ is increased. We define the extent of the linear viscoelastic regime (LVR) up to the drop off in G^*. The LVR extends to the highest strain at the low frequency limit, up to γ ~ 10 %. At high ω, the LVR is considerable shorter, extending to around γ ~ 2-3 %, and the drop off in G^* is the most drastic.

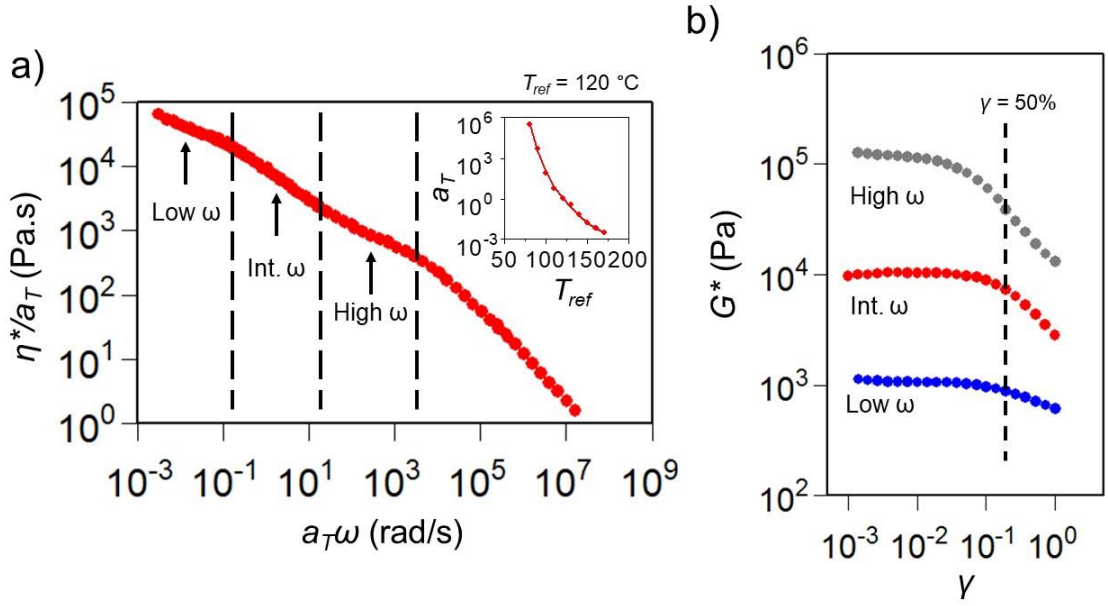

Figure 4.6 (a) Complex Viscosity (η^*) versus shifted frequency at reference temperature of T_{ref} = 120 °C. Shift factors a_T shown inset. Solid line is fit to WLF equation. **(b)** Non-linear viscoelasticity plotted as G^* versus oscillatory shear strain amplitude (γ) at selected frequencies (ω) within each dynamic regime

The shear alignment conditions were selected according to the viscoelastic response as previously described. Unique PS-*b*-PEO BBCP samples were sheared at each condition reported in Table 4.1. After shearing, each sample was carefully removed from the shear stage. The microphase segregation, morphology, and grain structure at each shear condition were investigated by SAXS. Figure 4.7 shows the reconstructions of 2-D scattering patterns at orthogonal directions for each of the four conditions (static anneal, high ω, intermediate

ω, and low ω). Double sided arrow denotes the coordinates with respect to shearing direction (referred throughout as *gradient* (∇v), *flow* (v), and *vorticity* ($\nabla x v$)). In all directions, microphase segregation is indicated by diffraction rings corresponding to strong primary peak q^* in 1-D SAXS spectra (Figure 4.8).

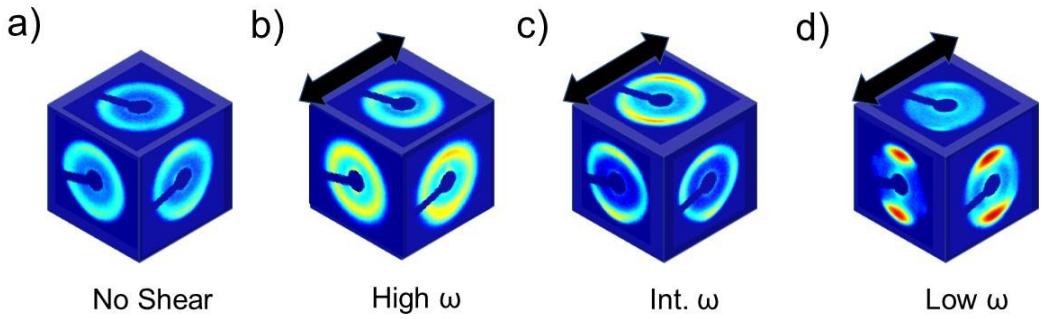

Figure 4.7 2-D SAXS patterns in three orthogonal directions for bulk PS-*b*-PEO samples after **(a)** thermal annealing under static conditions as well as shearing at **(b)** high ω **(c)** intermediate ω and **(d)** low ω. Arrow represents shearing direction. 2-D images scaled to standardized intensity scale.

Lamellar morphology was resolved by appearance of high order scattering peaks at a ratio of q^*:2q^*:3q^*. The orientation of the lamellae through the bulk sample is described by the anisotropy in the 2-D scattering patterns. Isotropic patterns in all three directions suggest no preferred orientation of the structure over the bulk sample volume in the PS-*b*-PEO sample under no shear (Figure 4.7a). After shearing in the high ω regime (Figure 4.7b), the diffraction pattern is still isotropic and not as sharp as the static condition. The intensity of q^* in the 1-D spectra is much lower than the other shearing conditions and the high order scattering peaks are much weaker (Figure 4.8b). However, the scattering patterns begin to express significant anisotropy after intermediate and low ω shearing (Figure 4.7c and 4.7d respectively). 2-fold symmetric scattering patterns emerge at the low ω condition in all three directions. In the gradient direction, the ring is weak and diffuse, while in the flow and vorticity directions, the diffraction ring is very intense and forms a

symmetric arc pattern. The intermediate ω also has intense scattering rings in the flow and vorticity directions, however, the anisotropy is not as prevalent. *I(q*)* is more intense in the gradient direction of intermediate ω when compared to the gradient direction in the low ω condition.

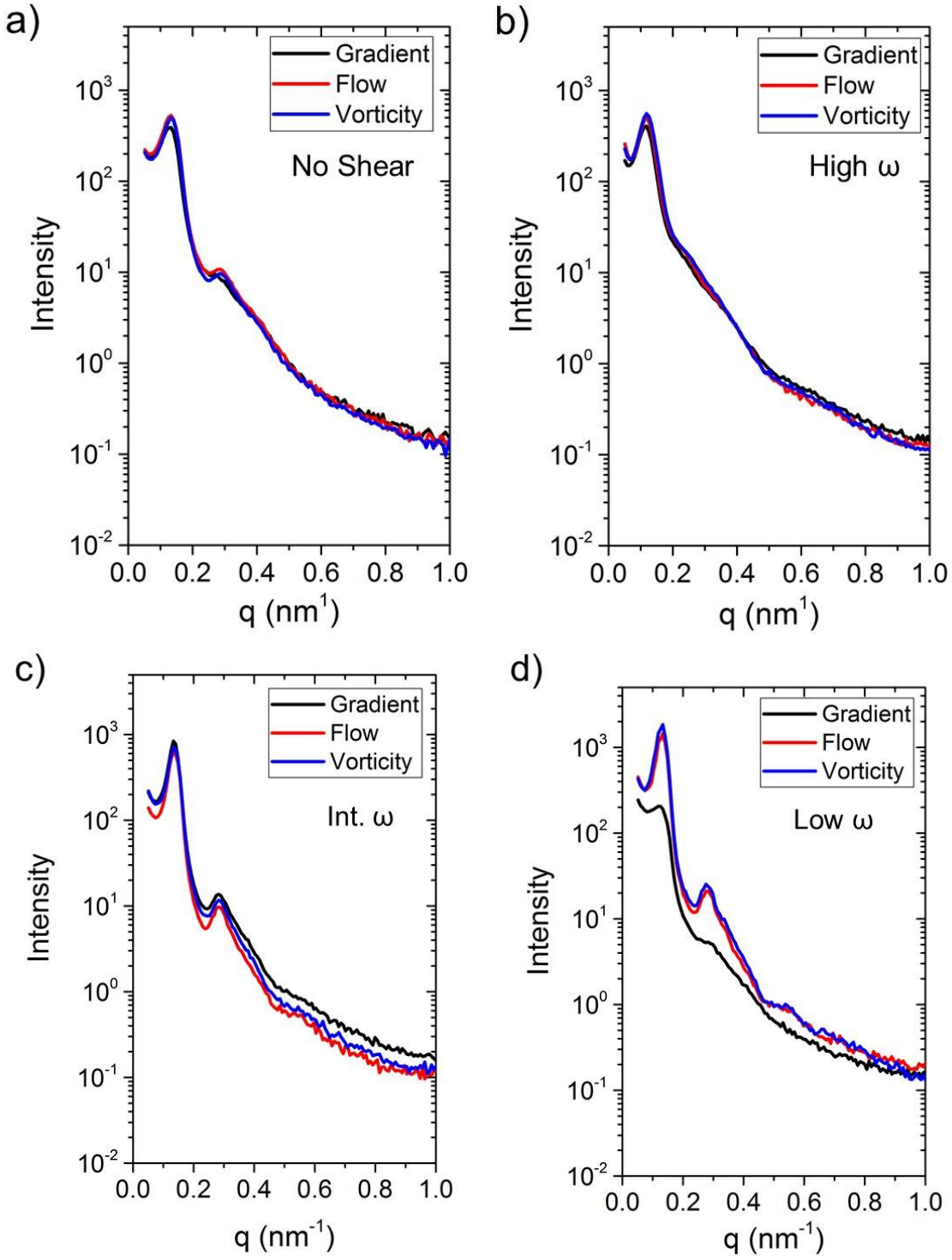

Figure 4.8 Orientation dependent 1-D SAXS spectra of PS-*b*-PEO (d_0 = 52 nm) at different shearing conditions: **(a)** thermal annealing under static conditions as well as shearing at **(b)** high ω **(c)** intermediate ω and **(d)** low ω. Plots of intensity I versus scattering vector q are generated by integrating 2-D scattering patters in Figure 4.7.

Azimuthal integrations about q^* are plotted in Figure 4.9 to quantitatively visualize the anisotropy in the 2-D scattering patterns. Azimuthal integrations are processed by taking a 2-D scattering pattern and integrating the intensity of q^* as a function of azimuthal angle θ from 0° to 360° (θ = 0° is oriented vertical up, and θ increases clockwise). While mild θ dependence is observed at high and intermediate ω (Figure 4.9b and 4.9c respectively), the most drastic intensity in the azimuthal plots is clearly in the low ω regime (Figure 4.9d), where the peak intensity is centered on θ = 0° and 180°, highlighting the 2-fold symmetric pattern. The symmetric patterns in each direction suggest a parallel orientation of the lamellae is strongest at the low ω shearing condition.

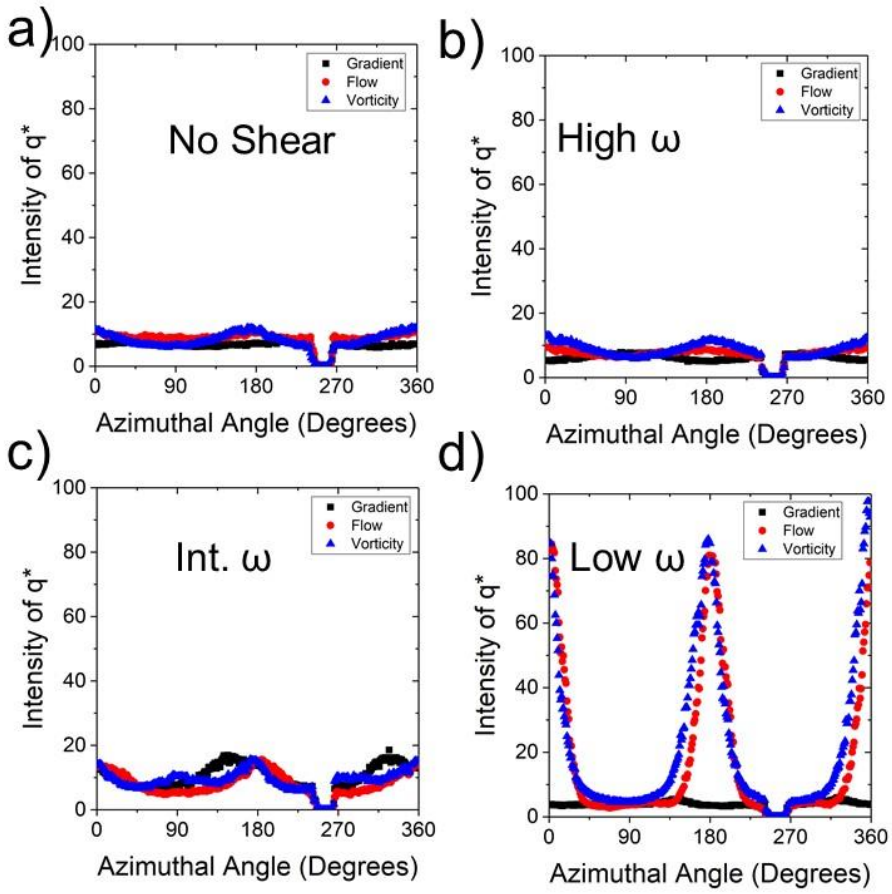

Figure 4.9 Azimuthal integration of primary scattering peak q^* in three orthogonal directions for PS-*b*-PEO after **(a)** thermal annealing under static conditions as well as shearing at **(b)** high ω **(c)** intermediate ω and **(d)** low ω.

4.3.3 Global Ordering in PS-*b*-PEO via. Scanning SAXS

The 2-D SAXS patterns and azimuthal integrations of q^* indicate that oscillatory shear either induces or enhances the collective orientation of the lamellar grain structure and that the strongest effect is observed after low ω oscillation. We investigate the impact of low ω shear on the global/macroscale orientation with high throughput synchrotron SAXS characterizations by continuously scanning along the entire surface of the bulk shear aligned sample, as described in Section 4.2.2. Select 2-D scattering patterns are reconstructed in the same format as Figure 4.7 to qualitatively visualize the anisotropy at each location on the bulk surface. A grid of 5 x 5 images is presented for the gradient surface, while the flow and vorticity surfaces are reconstructed as grids of 1 x 5 images. Each 2-D image represents a scattering volume with an incident area of 0.1 mm x 0.1 mm, and each location is spaced 0.4 mm apart (total sample area in gradient direction = 1.6 mm x 1.6 mm). The 2-D images in the gradient direction suggest that the scattering intensity is weak. A large grain is observed in the bottom section of the sample where there is no powder ring at all, consistent with parallel oriented lamellae, which would not produce any scattering signal in that direction if perfectly aligned.[43] In the upper corner of the gradient surface, more intense scattering is present, as well as minor signatures of anisotropic rings. The scattering is likely due to some fraction of the structure that is not completely aligned in the parallel orientation. However, despite this grain, the anisotropy in $I(q^*)$ is very strong at θ = 0° and 180° across the entire flow and vorticity surface, consistent with the results presented in Figure 4.9d. Here, alignment is achieved across an exceptional length scale on the order of almost 2 mm, indicating the uniformity of the parallel orientation over a large sample volume.

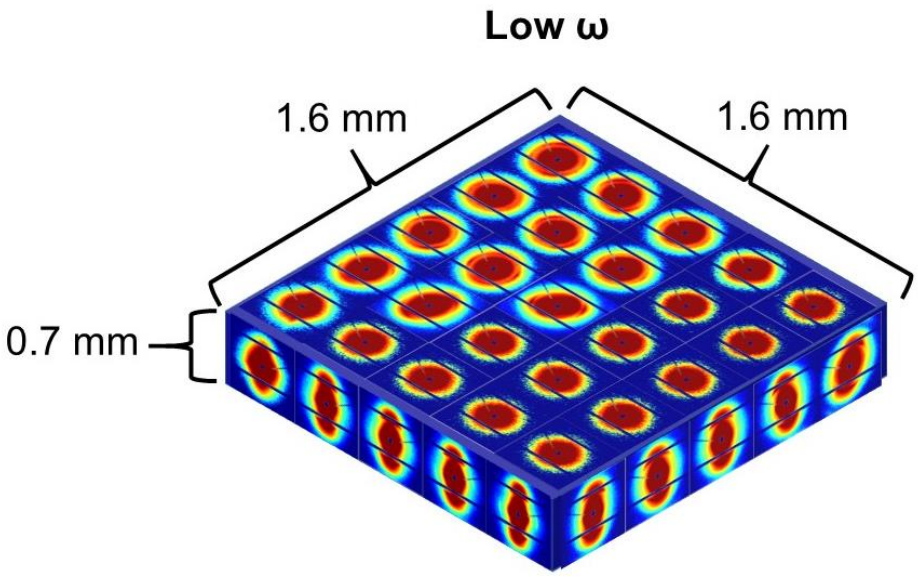

Figure 4.10 Reconstruction of select 2-D SAXS patterns from large volume scanning of low ω shearing condition. Images represent a sample volume of 1.6 x 1.6 x 0.7 mm.

The reconstruction in Figure 4.10 does not represent the entire data set collected from high throughput scanning SAXS measurements, which contains scattering patterns for over 1000 discrete locations across the sample. Therefore, to represent the orientation at all locations, we calculate the orientation order parameter *S* from the azimuthal integration of q^* in the resulting 2-D scattering patterns as

$$S = \frac{1}{2}(3\langle cos^2(\theta)\rangle - 1) \qquad \text{Eq. 4.1}$$

$$\langle cos^2(\theta)\rangle = \frac{\int_0^{2\pi} I(\theta)\sin(\theta)cos^2(\theta)d\theta}{\int_0^{2\pi} I(\theta)\sin(\theta)d\theta} \qquad \text{Eq. 4.2}$$

where θ is the azimuthal angle and $\langle cos^2(\theta)\rangle$ is the ensemble average of the azimuthal intensity, defined by Eq. 4.2. $I(\theta)$ is calculated by fitting a Gaussian distribution to the raw azimuthal data. *S* is commonly used to determine order in liquid crystals, BCPs, and other oriented nanoscale materials, accounting for orientation over all three dimensions.[44] Here, *S* ranges from 0 - 1 according to the orientation of the 2-D pattern ($\theta = 0°$ is oriented vertical

up, and θ increases clockwise). S is calculated at each location along the surface of the sheared sample and is mapped for the entire volume through the gradient, flow and vorticity planes (Figure 4.11). While the surface in the gradient direction exhibits some non-uniformity (as previously described in Figure 4.10), S is low (between S = -0.2 and S = 0.2) and generally within the isotropic limit, suggesting poor orientation of the lamellae along that direction. Plots of S along the flow and vorticity surfaces show increased orientation up to S = 0.7 and S = 0.8 over the entire 2 mm sample length, suggesting strong alignment normal to the gradient direction over an exceptionally large volume. The dip along the vorticity direction to S = 0.5 may be due to sample inhomogeneity factors such as scattering off an uneven surface. Overall, mapping of S further confirms that the lamellae are highly aligned in a parallel orientation.

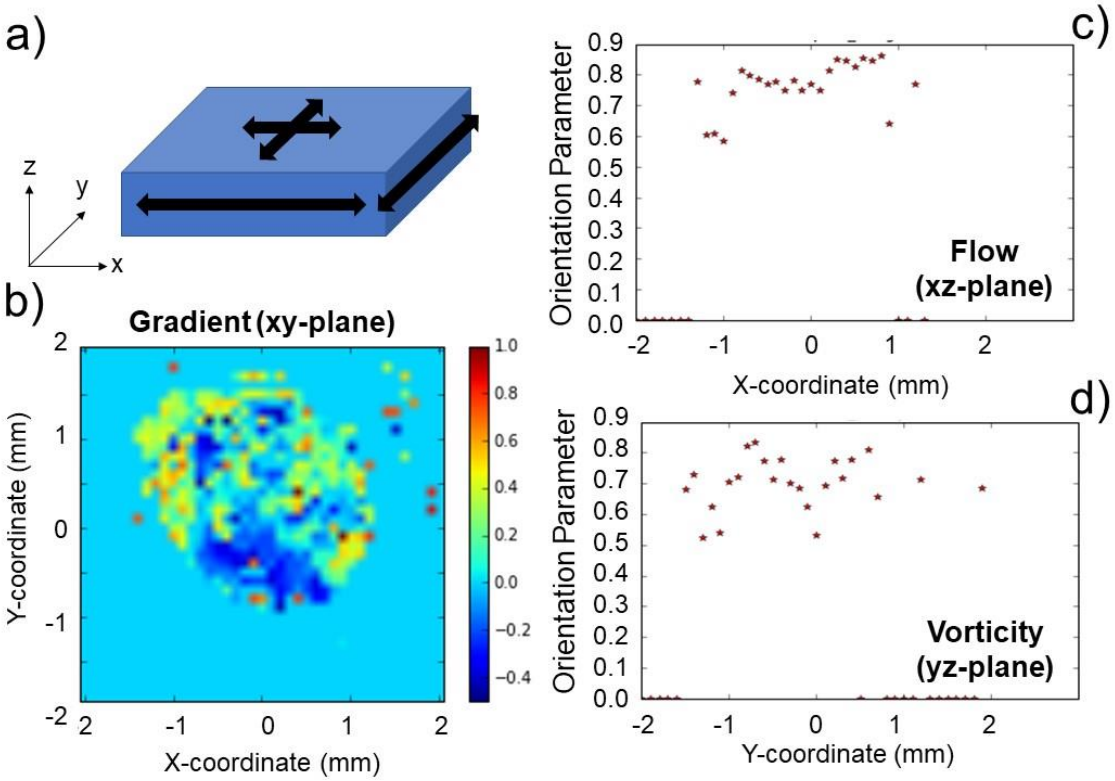

Figure 4.11 (a) Schematic of SAXS scanning technique across each orthogonal face of the bulk shear aligned BBCP samples. **(b)** 2-D map of orientation order parameter S compiled from 2-D scattering patterns at each location on the gradient (xy-plane). **(c)**

Orientation order parameter *S* along the edge of the sample in the flow plane. *S* is consistently ~ 0.8 along entire edge of almost 2 mm. **(d)** Orientation order parameter *S* along the edge of the sample in the vorticity plane. *S* is ~ 0.7 - 0.8 along entire edge of almost 2 mm. Strong orientation in flow and vorticity plane suggests alignment of lamellae parallel to applied shear.

Large volume scanning of the shear aligned sample was compared to the statically thermal annealed sample, revealing the impact of the shear on the directed global orientation over self-organization. A reconstruction analogous to Figure 4.10 is presented in Figure 4.12. According to orientation maps in Figure 4.13, the thermally annealed sample shows significantly large grains with $S = 0.4$ and $S = -0.2$ in the gradient direction, yet they are not uniformly aligned across the entire sample. *S* fluctuates significantly along the entire edge of the sample in both flow and vorticity directions, suggesting there are some areas of orientation, but the grain size is small and not well oriented.

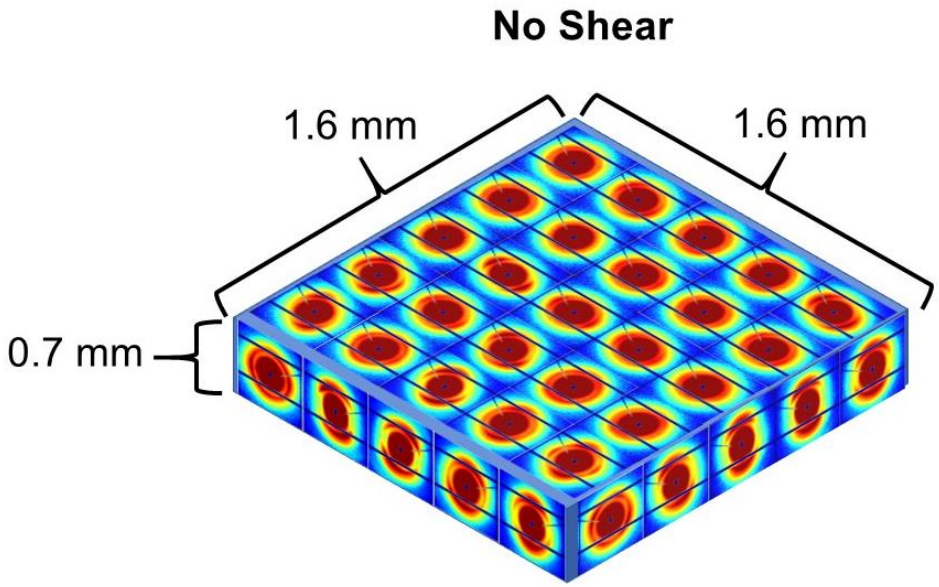

Figure 4.12 Reconstruction of select 2-D SAXS patterns from large volume scanning of static annealing condition. Images represent a sample volume of 1.6 x 1.6 x 0.7 mm.

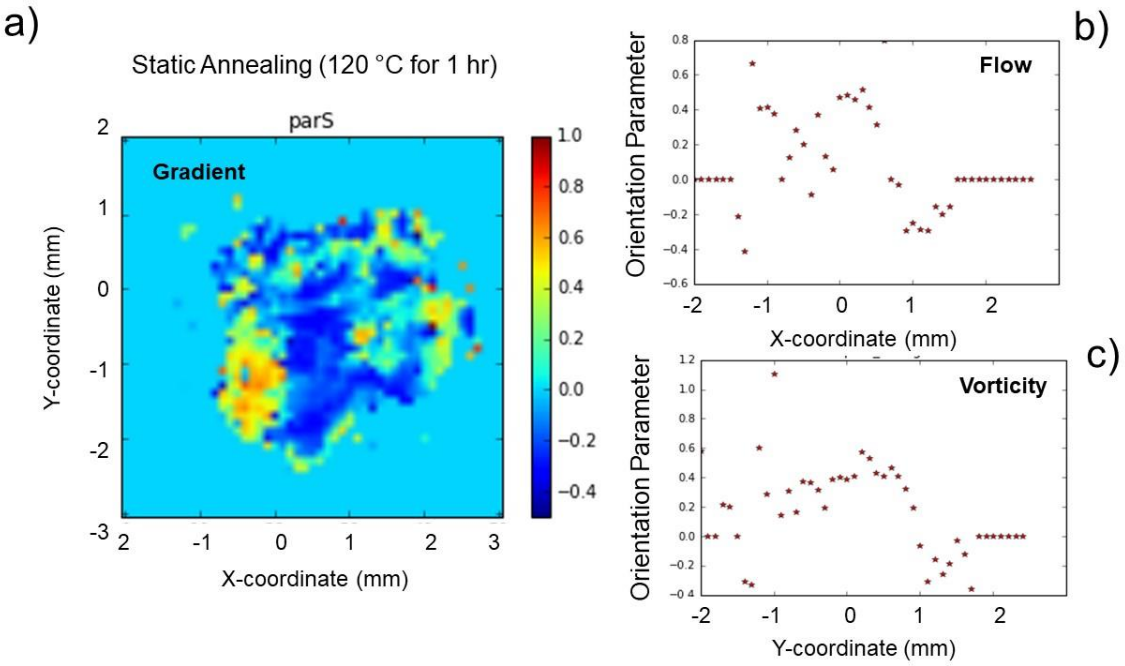

Figure 4.13 (a) 2-D map of orientation order parameter *S* compiled from 2-D scattering patterns at each location on the gradient (xy-plane) of thermally annealed PS-*b*-PEO. **(b)** Orientation order parameter *S* along the edge of the sample in the flow plane. *S* is highly non-uniform along entire edge of almost 2 mm, adopting both positive and negative values **(c)** Orientation order parameter *S* along the edge of the sample in the vorticity plane. Trend in *S* is analogous to the flow direction, suggesting poor control and order of the lamellae.

4.3.4 Effect of Temperature on Global Ordering of PS-*b*-PEO

An additional sample was thermally annealed at T = 145 °C for t = 6 h (the same thermal conditions as the low ω regime) but in the absence of shear to elucidate the effect of the high thermal annealing temperature on the orientation of the large volume grains exclusively. At T = 145 °C, the thermal energy may be sufficient to induce self-organization of the lamellar domains, as suggested by Song et al.[1] In the latter case, perpendicularly oriented lamellae were reported, possibly suggesting the lamellae prefers a different orientation than that achieved with shear alignment. A bulk sample was prepared and annealed in the Linkam CSS450 and identically characterized by SAXS. 2-D scattering patterns, 1-D spectra, and azimuthal integrations are presented in Figure 4.14. The 2-D

patterns look like the shear aligned sample, however the anisotropy is much less intense. Well-ordered lamellae are assembled with consistent d_0 according to strong peak reflections in the 1-D spectra. Azimuthal integrations of q^* do exhibit some tendency towards the θ = 0° and 180° orientation in the flow and vorticity direction (i.e. parallel alignment). However, $I(q^*)$ is much weaker compared to low ω shearing (Figure 4.9d). Significant scattering is detected in the vorticity direction at θ = 90° and 270° as well, suggesting some fraction of the lamellae may be oriented orthogonally to the preferential parallel direction.

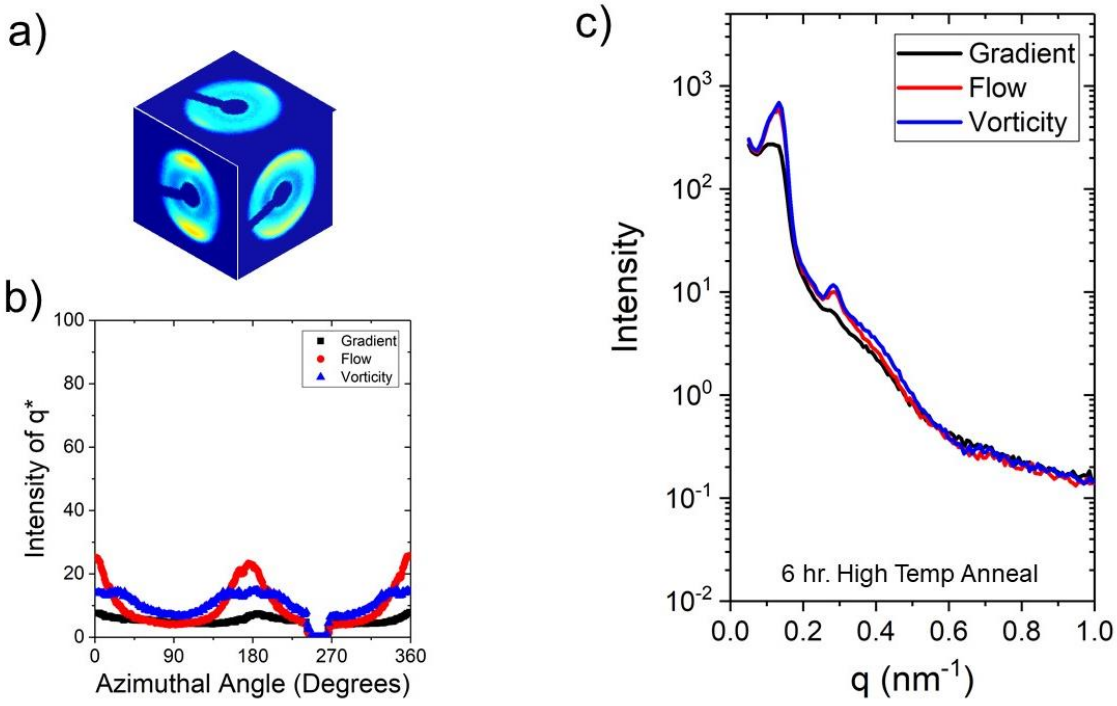

Figure 4.14 (a) 2-D SAXS patterns in three orthogonal directions for bulk PS-*b*-PEO samples after thermal annealing under static conditions at T = 145 °C. **(b)** Azimuthal integration of primary scattering peak q^* in three orthogonal directions for PS-*b*-PEO and **(c)** orientation dependent 1-D SAXS spectra

Large volume scanning was subsequently performed, and S is mapped across the entire sample volume in Figure 4.15. While S increases significantly along the flow and vorticity directions, there are large oriented grains visible through the gradient, suggesting

that the lamellae are not completely aligned into the parallel orientation as they are when shear is applied. The large volume scanning results appear consistent with observations by Song et al.[1] The increased thermal annealing temperature produces locally ordered grains with strong orientation, but the direction is not correlated over the large sample volume. Convolutions of scattering signal from the local orientations contribute to non-uniform values of *S* over the entire sample. Therefore, elevated annealing temperature is useful in forming large grains of well-ordered lamellae, however the directed global parallel orientation is weaker when compared to the shear aligned sample.

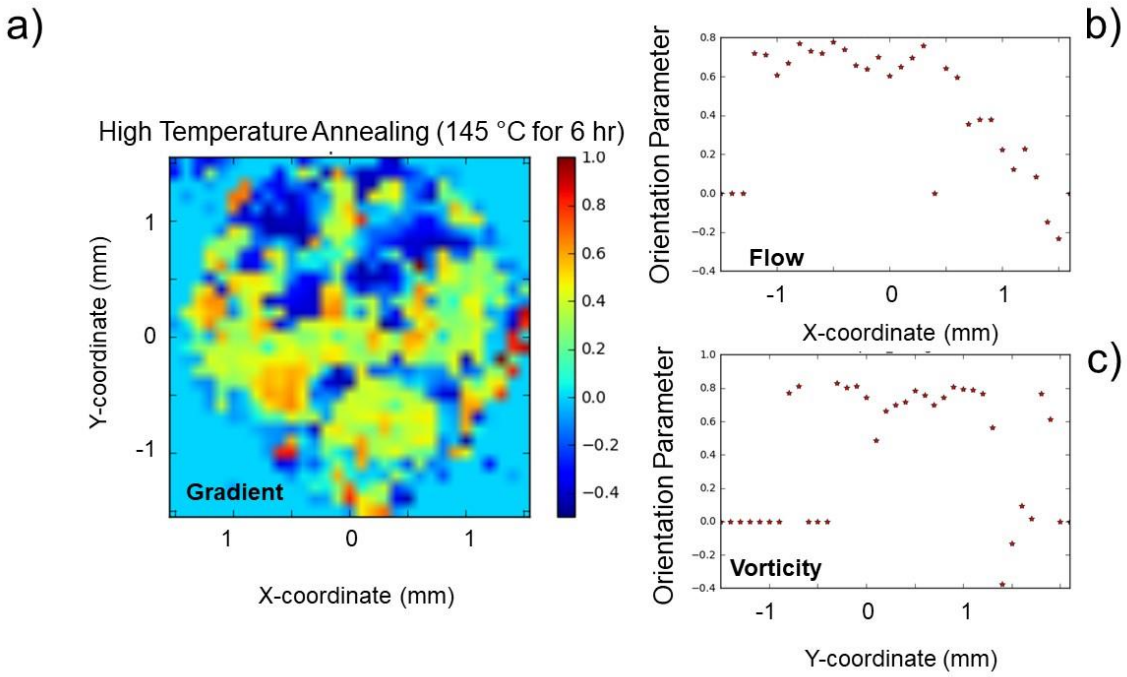

Figure 4.15 (a) 2-D map of orientation order parameter *S* compiled from 2-D scattering patterns at each location on the gradient (xy-plane) of T = 145 °C thermally annealed PS-*b*-PEO. **(b)** Orientation order parameter *S* along the edge of the sample in the flow plane. **(c)** Orientation order parameter *S* along the edge of the sample in the vorticity plane.

4.3.5 Frequency Dependent Shearing of PtBA-*b*-PEO BBCP

An investigation into PtBA-*b*-PEO was conducted to directly compare observations by Song et al. of the self-organization of large volume nanostructures after thermal

annealing in the same system. PtBA-*b*-PEO has enhanced mobility compared to PS-*b*-PEO due lower T_g of the PtBA block and increased steric repulsion between side chains from the longer side chain M_n (M_n(PtBA) > M_n(PS)).[1] While some self-organization was observed in PS-*b*-PEO, we expect the structure in PtBA-*b*-PEO to be much more apparent. Here, we hypothesize that shearing can be used to improve the global order of the self-organized grains in a large bulk sample. Linear and non-linear viscoelasticity of the PtBA-*b*-PEO was measured (Figure 4.16) and is comparable to the response from the PS-*b*-PEO template. Four power law scaling regimes in $\eta^*(\omega)$ are identified and partitioned into low, intermediate, and high ω. Similar limits of the LVR are observed. Therefore, γ = 50 % is again selected for the shear alignment conditions. Once again, we apply LAOS within each regime and investigate the effect of the shearing parameters on lamellar alignment.

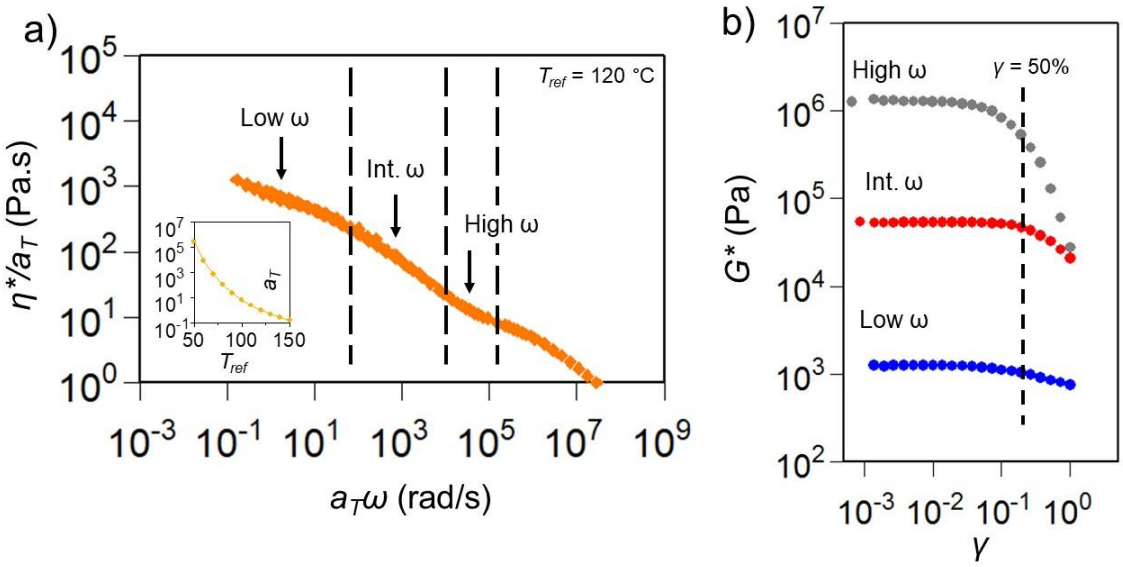

Figure 4.16 (a) Complex Viscosity (η^*) versus shifted frequency at reference temperature of T_{ref} = 120 °C. **(b)** Non-linear viscoelasticity plotted as G^* versus oscillatory shear strain amplitude (γ) at selected frequencies (ω) within each dynamic regime

Shear alignment processing parameters are detailed in Table 4.2. The shearing conditions differ from PS-*b*-PEO (notably lower processing temperatures) due to the

significantly reduced T_g of the PtBA block compared to a PS block. After shearing, anisotropy is observed across all shearing conditions, even the static thermally annealed samples, indicate the presence of some alignment even without application of shear (Figure 4.17a). The results are consistent with previous reports where the natural self-assembly of ordered grains is observed, but not directed into a specific orientation or direction. At high ω, anisotropy is observed in all three directions, with preference to θ = 0° and 180° in the flow and vorticity. The grain improves at intermediate ω, where the anisotropy sharpens and centers in the flow and vorticity direction, while the anisotropy in the gradient decreases in intensity. Qualitatively, the patterns describe parallel orientation of the lamellae across a larger frequency range than the PS-*b*-PEO system. The low ω patterns are particularly interesting. The flow direction is anisotropic with broad arcs oriented vertically, while the vorticity exhibits very sharp vertical peaks and some additional scattering on the horizontal axis θ = 90° and 270°. The trends are also expressed in the 1-D plots, where the higher order peaks are the strongest for the low frequency (Figure 4.18).

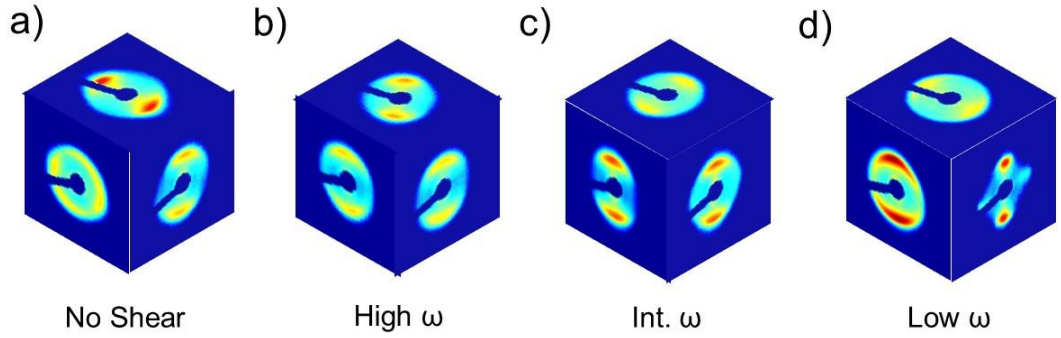

Figure 4.17 2-D SAXS patterns in three orthogonal directions for bulk PtBA-*b*-PEO samples after **(a)** thermal annealing under static conditions as well as shearing at **(b)** high ω **(c)** intermediate ω and **(d)** low ω. 2-D images scaled to standardized intensity scale.

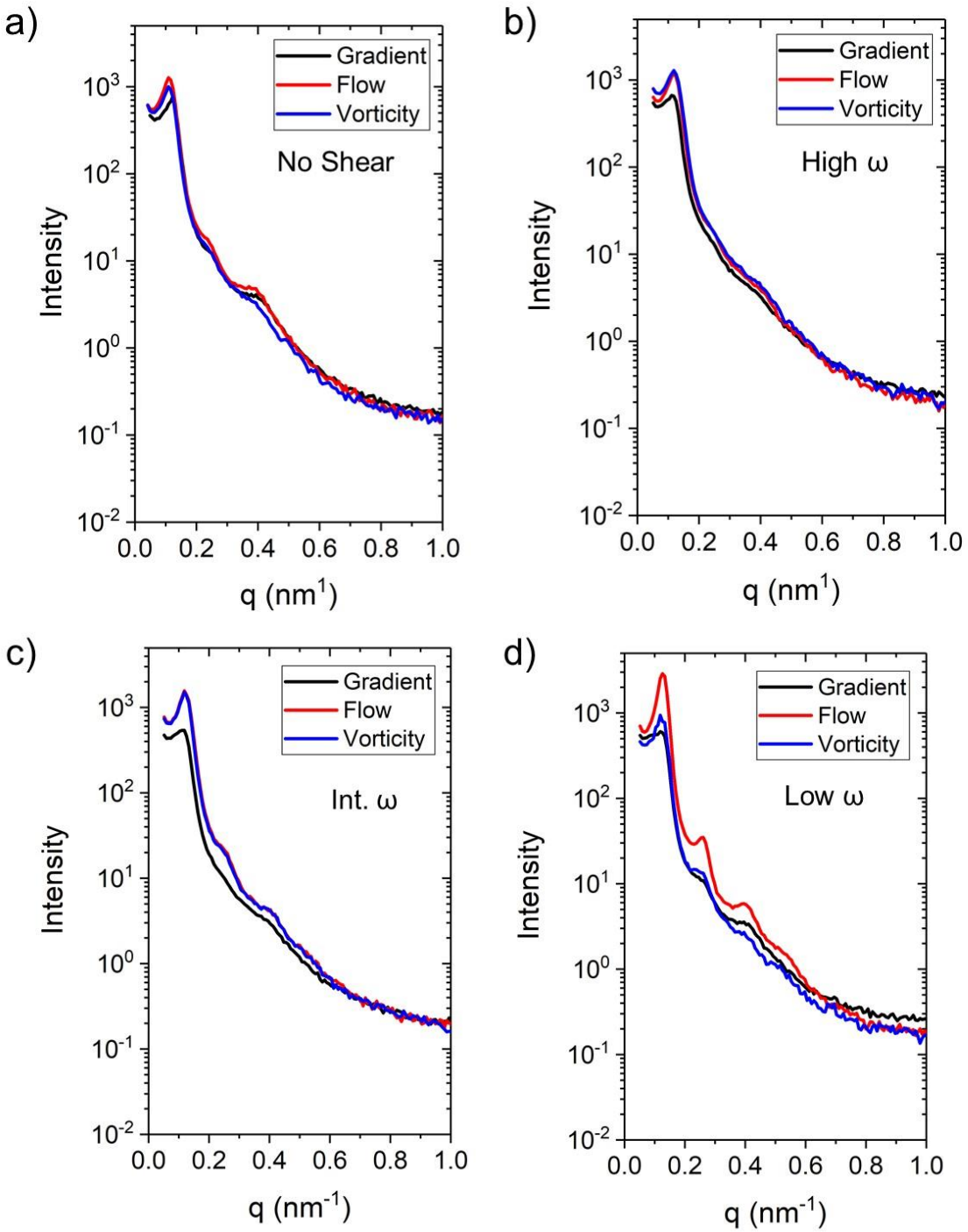

Figure 4.18 Orientation dependent 1-D SAXS spectra of PtBA-*b*-PEO at different shearing conditions: **(a)** thermal annealing under static conditions as well as shearing at **(b)** high ω **(c)** intermediate ω and **(d)** low ω. Plots of intensity versus scattering vector q are generated by integrating 2-D scattering patters in Figure 4.17

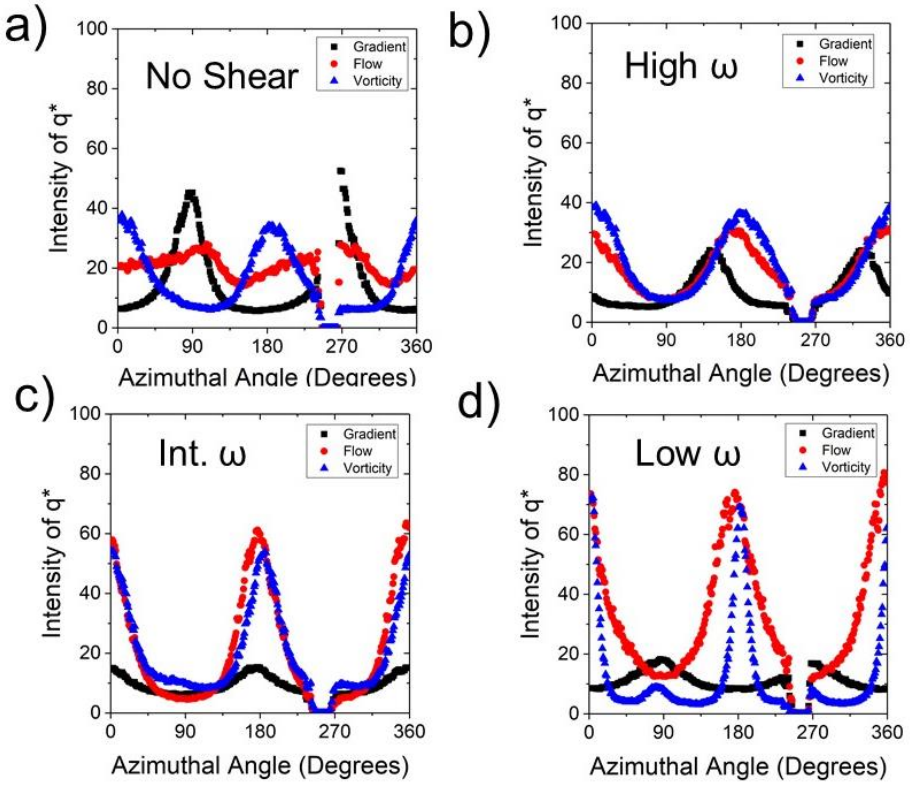

Figure 4.19 Azimuthal integration of primary scattering peak q^* in three orthogonal directions for PtBA-*b*-PEO after **(a)** thermal annealing under static conditions as well as shearing at **(b)** high ω **(c)** intermediate ω and **(d)** low ω.

4.3.6 Global Ordering in PtBA-*b*-PEO via. Scanning SAXS

Orientation maps of S in the gradient, flow and vorticity directions are presented in Figure 4.20 for the low ω condition. The surface in the gradient direction is generally uniform, with S = -0.2. A negative value of S correlates to azimuthal intensity at θ = 90 and 270°. Therefore, any lamellae scattering in the gradient direction would be in the perpendicular orientation, with the lamellar domains directed along the flow direction. However, there are some grains with positive values of S along the outer edge of the sample. Plots of S along the flow and vorticity surfaces show significantly increased S values over the entire 2 mm sample length like the PS-*b*-PEO sample, suggesting much stronger alignment normal to the gradient direction over an exceptionally large volume.

The vorticity direction is particularly striking. Order is extremely uniform and S = 0.9 across the entire edge. In the flow direction, S is slightly lower around S = 0.6, yet still uniform over 2 mm. The 2-D scattering patterns and values of S are consistent with parallel orientation however some population of lamellae may be oriented orthogonally to the flow direction. The origins of this peculiar behavior will be discussed in Section 4.4.

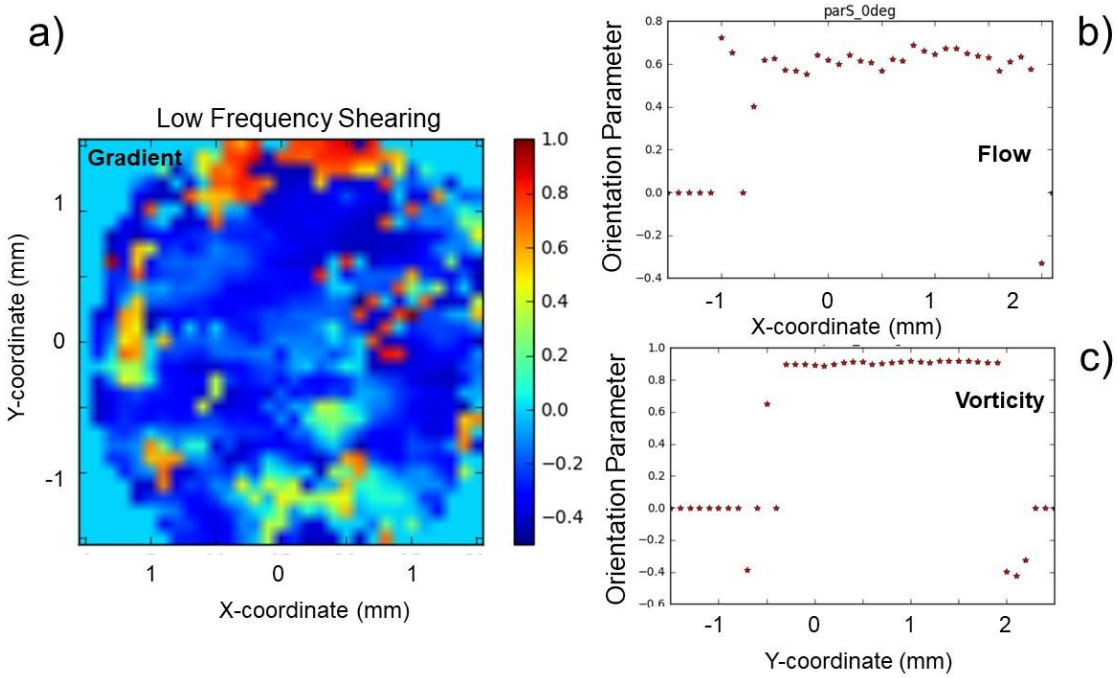

Figure 4.20 (a) 2-D map of orientation order parameter S compiled from 2-D scattering patterns at each location on the gradient (xy-plane) of low ω shear aligned PtBA-*b*-PEO sample **(b)** Orientation order parameter S along the edge of the sample in the flow plane. **(c)** Orientation order parameter S along the edge of the sample in the vorticity plane.

Large volume scanning of the shear aligned PtBA-*b*-PEO sample was compared to a static thermally annealed sample. In Figure 4.21, the thermally annealed sample is heterogeneous in the gradient direction with several grains ranging from S = 0.5 to S = -0.4. S fluctuates widely along the entire edge of the sample in both the flow and vorticity direction. Some locations display orientations as large as S = 0.8, but the uniformity is not strong. The results appear to be consistent with the large volume self-organization with

Song et al.[1] However, in the latter case only the top surface of the sample was characterized and the full 3-D orientation was not considered. Here, we see that the grains orient in all directions, and while they may appear oriented from the top surface, the orientation may be much stronger along an orthogonal direction.

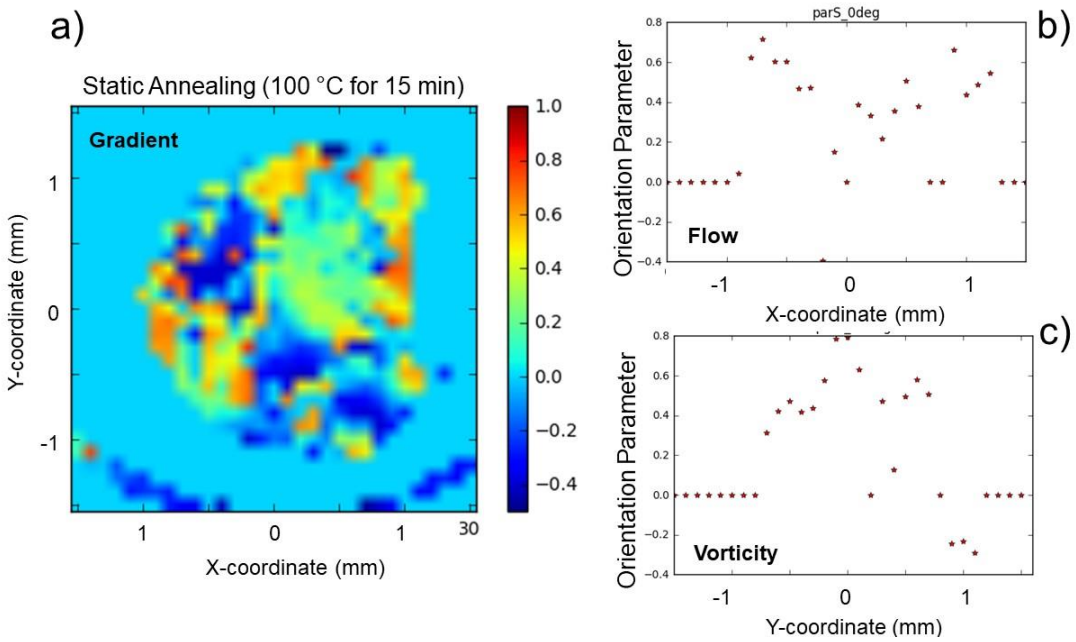

Figure 4.21 (a) 2-D map of orientation order parameter *S* compiled from 2-D scattering patterns at each location on the gradient (xy-plane) of static annealed PtBA-*b*-PEO sample. **(b)** Orientation order parameter *S* along the edge of the sample in the flow plane. **(c)** Orientation order parameter *S* along the edge of the sample in the vorticity plane.

4.3.7 Effect of Temperature on Global Ordering of PtBA-*b*-PEO

An additional sample was thermally annealed at T = 110 °C for t = 6 h (the same thermal conditions as the low ω regime) in the absence of shear to elucidate the effect of the high thermal annealing temperature in the PtBA-*b*-PEO system as well. 2-D scattering patterns, 1-D spectra, and azimuthal integrations are presented in Figure 4.22. The 2-D patterns show anisotropy in all three directions. The azimuthal intensity in the flow and vorticity directions appear to be centered at θ = 0° and 180°, however the preferential intensity in the gradient orientation is not correlated to either of these directions and seems

to be randomly directed (Figure 4.22b). Therefore, a significant fraction of the lamellae is likely in the parallel orientation, however off-axis orientations are still prevalent. The scattering intensity and sharpness of high order scattering peaks in 1-D spectra (Figure 4.22c) are independent of the observation direction, further suggesting that the grain sizes may be large, but not globally directed in any specific orientation. The results are consistent with the statically annealed control in Figure 4.17a.

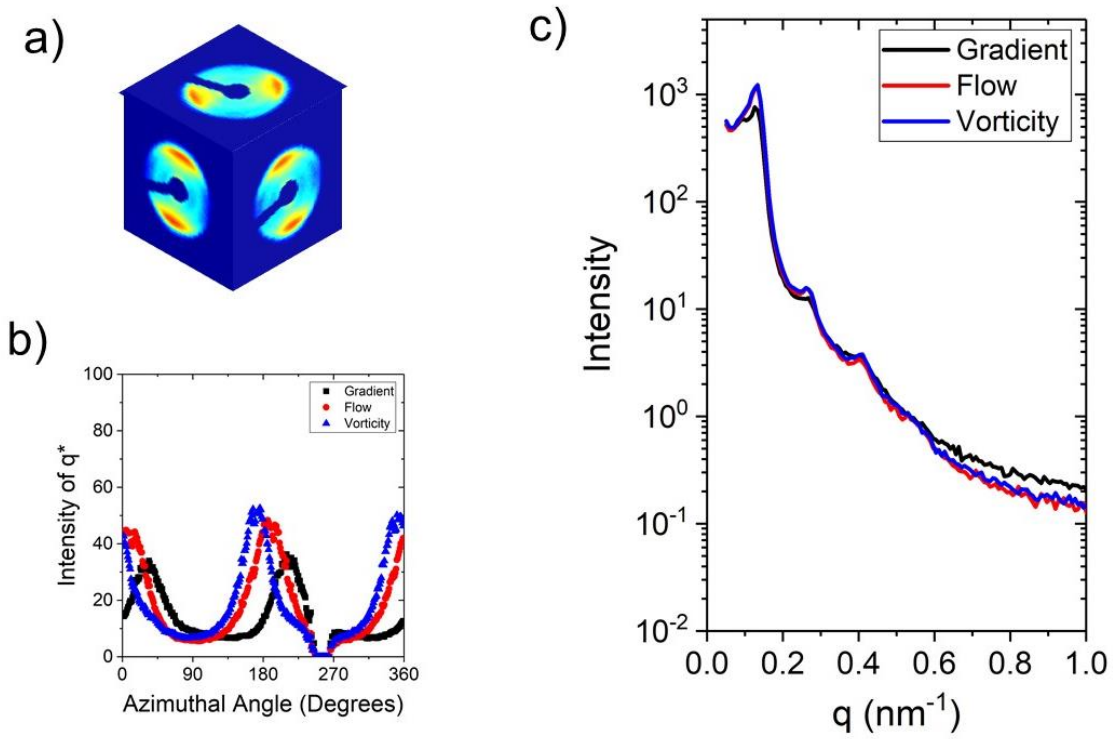

Figure 4.22 (a) 2-D SAXS patterns in three orthogonal directions for bulk PtBA-*b*-PEO samples after thermal annealing under static conditions at T = 110 °C. **(b)** Azimuthal integration of primary scattering peak q^* in three orthogonal directions and **(c)** orientation dependent 1-D SAXS spectra

Large volume scanning was performed, and S is mapped across the entire sample volume in Figure 4.23. At least three large grains appear in the gradient surface in Figure 4.23a. Alignment across a mm^2 area is impressive, but the heterogeneity suggests that application of shear is important to achieve universal orientation. S varies between each

grain significantly, reflecting the same results observed in the statically annealed sample (Figure 4.21). Again, the order is primarily positive along the sample edges (Figure 4.23b and Figure 4.23c), but highly non-uniform in comparison to the sheared sample in Figure 4.20.

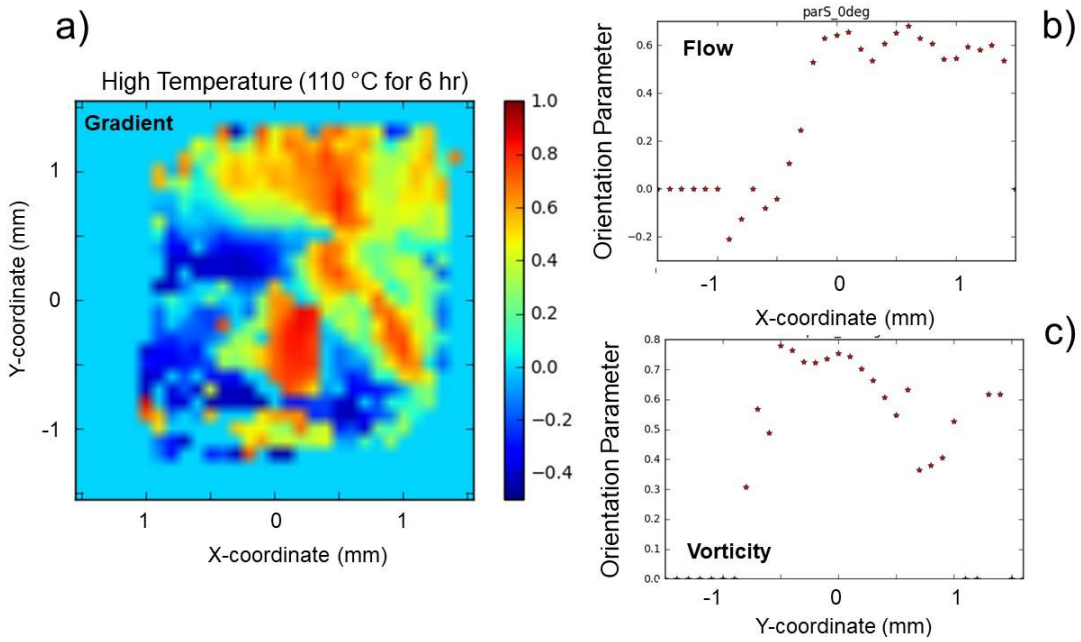

Figure 4.23 (a) 2-D map of orientation order parameter *S* compiled from 2-D scattering patterns at each location on the gradient (xy-plane) of T = 110 °C thermally annealed PtBA-*b*-PEO. **(b)** Orientation order parameter *S* along the edge of the sample in the flow plane. **(c)** Orientation order parameter *S* along the edge of the sample in the vorticity plane.

4.4 Discussion

The clear observation of anisotropic scattering patterns in the SAXS characterization suggests that highly ordered and aligned lamellar nanostructures are present in the microphase separated BBCP samples both after shearing and after static annealing. While in some cases, these nanostructures appear to be self-organized into locally ordered grains, the application of shear is used to improve the global grain ordering and direct the lamellae into primarily parallel orientations with respect to the applied shear. Our key objective is to understand the correlation between the rheological

properties/dynamic relaxation processes and the reorientation mechanisms that result in the well-ordered structures. Connecting the fundamental physical behavior to bulk structural properties is essential for improving final material performance through processing. The linear viscoelastic behavior of model PS-*b*-PEO BBCPs and mechanisms of structural relaxation have been thoroughly discussed in Chapter 3. Here, we draw upon those conclusions of the unique structure-property relationship in BBCP melts to describe the experimentally observed results while also revisiting the proposed pathways of alignment in lamellar forming LBCP systems.

Despite the breadth of work, the proposed alignment mechanisms for LBCPs are not universal due to differences in χ and viscoelastic contrast between various di-block combinations.[24] The parameter space is very complicated. Therefore, we focus on the low ω regime, as this produced the strongest alignment in the BBCP templates. It is understood that low ω oscillations target the slowest relaxation processes.[18] Koppi et al. proposed that structure aligns through a "defect mediated stress relaxation process", where defects in the long-range order become the stress bearing structures that respond on the longest time scales.[18] The defects along grain boundaries in an isotropic, quenched state will reorder, resulting in parallel alignment of the lamellae. The defect driven mechanism seems plausible in the PS-*b*-PEO BBCPs, which is globally isotropic after static thermal annealing according to Figure 4.7a. Hard body grain rotation is also widely accepted as a route to parallel aligned domains. However, there are two key differences between the classical behavior of LBCPs and that which we determined for BBCPs: the confined liquid layers resulting from unentangled side chains, and the highly disordered structure in the melt state reminiscent of a critical gel approaching the solid transition. Any discussion that requires

"well ordered" lamellae under shear must be modified and reconsidered for the BBCP materials. As far as the temperature dependent SAXS data can reveal, the large grain structure disappears completely in the melt state, whether under shear or at static conditions. Therefore, the "grain rotation" mechanism is highly unlikely in the BBCP melts because the morphology is disordered in the melt and there is no "hard body" grain to rotate. The existence of a disordered melt morphology provides more support for the defect mediated mechanism, as the structure is most likely riddled with defects. The reorientation of such defects can only be accessed at low ω shearing conditions. The lack of entanglements reduces topological constraints found in the entangled LBCPs, and therefore enhances the rapid rearrangement and relaxation of the global structure at low ω. We acknowledge that in the PS-*b*-PEO and PtBA-*b*-PEO systems, it is possible that temporal fluctuations of lamellar structure cannot be resolved on the timescale of the SAXS characterization. Therefore, it is difficult to determine the degree of alignment directly under shear. There must be some memory of the defect elimination at the interfaces so that after shear is removed, the oriented structure sets in as the temperature is quenched back to room temperature and dynamics slow down.

The higher ω regime is associated with the rapid, internal slip layer relaxations within each microphase separated domain. Therefore, at high ω, we expect the inner liquid layer to bear the primary stress response. Experimental results show that shearing on the timescale of segmental side chain relaxations does not produce much directed order or long-range alignment of the lamellae. The time scale is too fast to correlate over longer length scales. Therefore, local grains may form but the entire sample volume is not directionally oriented.

The apparent formation of off-axis lamellae in the PtBA-*b*-PEO sample is puzzling (Figure 4.17d). The 4-fold symmetry appears along the vorticity direction, which would suggest *transverse* orientation, where lamellar layers also align normal to the flow direction. Transverse is often considered the most thermodynamically unstable orientation and is rare.[21] When assessing the global orientation along the other two orthogonal directions, the proposed transverse structure is not consistent with a truly transverse orientation. According to our formalism for *S*, transverse lamellae correspond to an order parameter of $S = 1$ in the gradient direction. However, *S* clearly trends towards negative values, more closely resembling the perpendicular orientation. We hypothesize that the off-axis orientation is a non-stable structure that forms during shear alignment. A similar phenomenon was observed in the PS-*b*-PI low molecular weight BCPs, where anomalistic orientations arose after short amounts of shearing, but disappeared after extended periods of shearing.[24] In the PS-*b*-PI templates, such orientations were only found it at the highest shearing ω, which is inconsistent with our results. Another explanation could be the formation of perforated lamellae, which produce off-axis intensity much like the 4-fold pattern observed in the 2-D scattering patterns. However, the most common structure, hexagonal perforated lamellae (HPL) produces a 6-fold symmetric pattern.[45,46] Precise TEM measurements along the shear plane are required to confirm. Even if the transverse structure exists, the contribution to the scattering intensity is low, suggesting a minor population in comparison to parallel orientations. *S* represents an ensemble average of all orientations, so overall the order is much stronger in the parallel orientation.

The assembly of the lamellar morphology coexists with the recrystallization of the PEO domain according the results presented in Chapter 3. However, the alignment and

orientation of the crystalline domains is independent of the order-disorder transition from ordered lamellae to disordered melt. 2-D WAXS patterns of both PS-*b*-PEO and PtBA-*b*-PEO samples are presented in Figure 4.24. There is no observable orientation of the PEO crystals along the flow direction after cooling to room temperature. The thermal annealed sample (static) and low ω shear samples are indistinguishable. The PEO crystals support long range lamellar order, but within the PEO domain, the crystals are not oriented with the alignment of the microphase separated lamellae. Such a phenomenon is inconsistent with results of crystallization in lamellar PS-*b*-PEO LBCPs after shear alignment where aligned PEO crystals are induced within a confined lamellar layer.[47–49] The crystals are highly uniform and the orientation (perpendicular, inclined, parallel) is dependent on the crystallization temperature.[47] The "confined crystallization" effect relies on retaining the lamellar morphology throughout the melting-crystallization transition ($T_m < T_{ODT}$). In the case of BBCPs, T_m coexists with the ODT to disordered morphology upon heating. During the reordering transition, the dynamics in the glassy domain will slow down first upon cooling from the melt, which will likely constrain and "lock up" the aligned structure produced from the shearing. The lamellar orientation is dependent on domains defects and interfaces, while the PEO crystallization transition is independent of those processes. The crystallization behavior of short side chains in densely grafted BBCPs is a topic of considerable research interest, and not well understood at this time. The cooling rate and crystallization temperature was not defined or well controlled in this investigation. The samples were quenched to room temperature by simply turning off the heating element and allowing the system to cooldown to room temperature, which took about 10 minutes to

equilibrate. Systematic investigations into the recrystallization process will resolve the complex behavior of confined PEO crystallization in the BBCP systems.

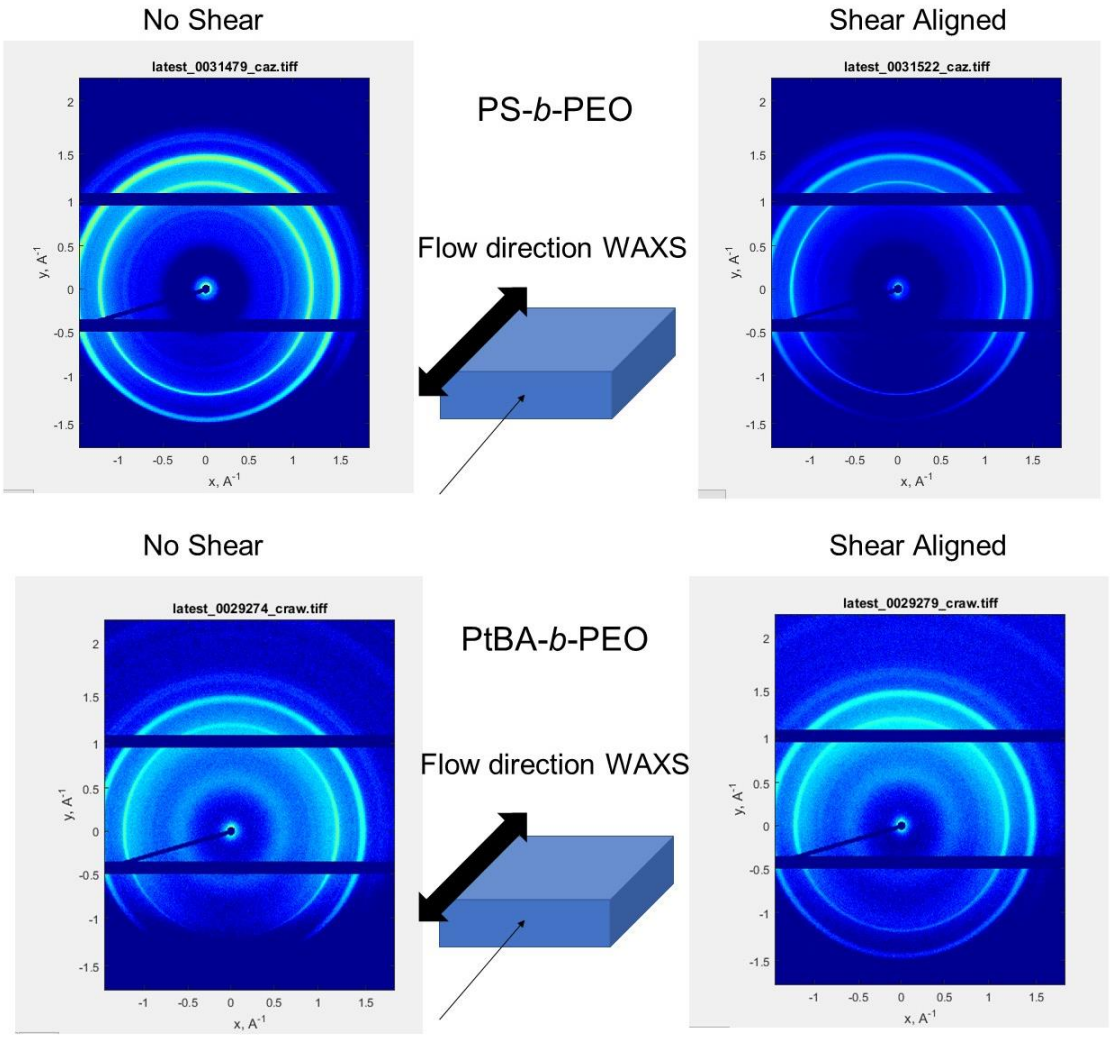

Figure 4.24 2-D wide angle X-ray scattering (WAXS) patterns of PS-*b*-PEO and PtBA-*b*-PEO along the "flow" direction after no shear and shear alignment in the low ω regime. Diffraction rings are a result of crystalline segments of the PEO domain. No preferred orientation observed at any processing condition, suggesting the PEO crystal orientation is decoupled from microphase lamellar orientation.

In the BBCPs, the onset of shear alignment within the LVR is striking (Figure 4.5). Traditionally, shear induced domain orientation is produced by high shear strains required to overcome the thermodynamic barriers associated with local destructions and re-formations (i.e., mixing) of the microphase segregated domains and to remove grain

boundaries.[18,25,34] The existence and percolation of the grain boundaries define the critical gel-like relaxations. At low strain, where structure is not perturbed, any removal or reorganization of defects by shear alignment would not noticeable by rheological experiments. After SAOS, the scattering patterns indicate a perpendicular alignment of the domains, which was not observed at any of the LAOS conditions. Parallel orientations are most stable and most common, so the appearance of perpendicular orientation is surprising. We believe that the perpendicular orientation was not a complete transition, but a transient state that formed at low strain. We could not confirm the 3-D structure by scattering through the flow or vorticity directions. The additional information should confirm if the orientation is completely perpendicular or if the observed structure is a small fraction of the entire population.

The demonstration of shear-induced alignment in the BBCP materials is interesting and especially appealing for implementation in future processing applications. As previously stated, the controlled domain ordering at small strain amplitude (within the LVR) and at low temperature ($T_g < T \ll T_{MST}$) is advantageous and achieved with the BBCP architecture. This provides an entirely new regime of potential processing conditions for the controlled assembly of BBCP domains via shear deformation. Advantages of reducing the processing temperature include speeding up processing time, reduced energy use, and reducing the chance of sample degradation. These highlights all convey the potential for BBCP implementation in applications where nanoscale domain alignment must be easily and efficiently controlled.

While the Linkam CSS450 is a well-known conventional shearing apparatus, establishment of uniform shear deformation requires that the entire sample cell be filled

with material (volume ~ 1000 mm^3). Batch synthesis of BBCPs is limited to ~ 300 mg, which is significantly lower than the shear cell volume. Therefore, we are limited to characterizing a much smaller bulk sample positioned directly at the optical window where the applied strain is defined. The small sample size inherently breaks the ideal shearing assumption due to free surfaces and edge effects. The top surfaces are in contact with the shear plates, while the edges are in contact with air, and behave as free surfaces (Figure 4.25). The shear tensor does not accommodate this artifact and the boundary conditions are un-defined at the air/sample interface.[42] The impact of this edge effect decreases for those volume elements closer into the bulk of the material. However, the data suggests that any uncertainty at the interface does not make a difference in the overall directed alignment of the structure. The order parameters are uniform along the edges despite the interface. In the future, the edge effect must be reconciled when processing highly aligned nanostructures for applications.

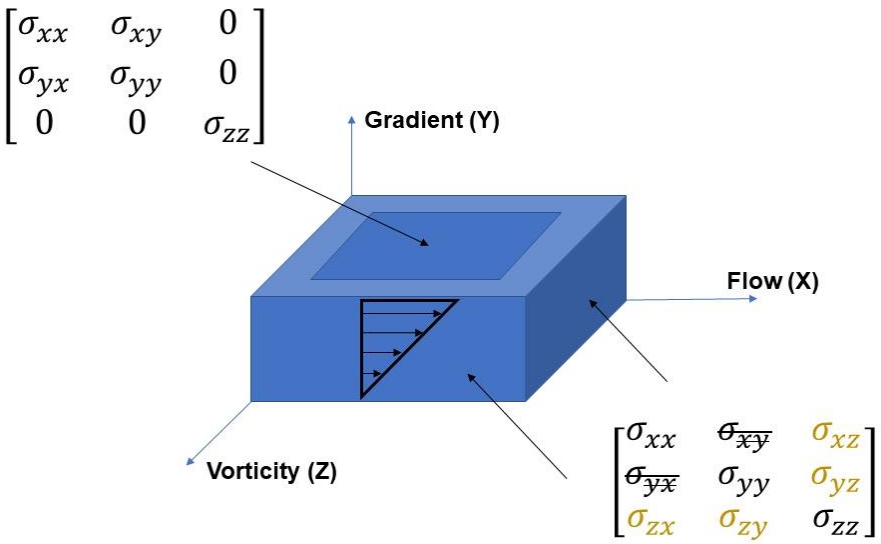

Figure 4.25 Consideration of edge effects. When evaluating the boundary conditions, shear tensor is undefined for those volume elements on the edge of the bulk sample at the sample/air interface. Symmetry in stress tensor is broken ($\sigma_{yx} \neq \sigma_{yx}$)

Also, it is well known that surface effects at the interface can direct and drive oriented assembly in thin films (i.e. chemoepitaxy and graphoepitaxy).[12,50] While such a driving force only applies to those layers in the vicinity of the interface (within a few hundreds of nanometers), the surface energy could play a larger effect in BBCPs, which exhibit unique templating and thin film assembly behavior compared to typical LBCPs.[10,51] We only performed shearing on Kapton substrates, which has a surface energy of $\gamma \sim 40$ mJ/m^2.[52] PS, PtBA, and PEO all have similar surface energies so we should not expect any domain to have a preferential attraction to Kapton. Preferential surface interactions may have a reduced impact in BBCP systems according to experimental observations by Hong et al. for thin film assemblies of PS-*b*-PLA BBCPs which formed lamellar domains normal to the silicon substrate despite PLA having a strong attraction to the oxide layer on Si.[51] The entropic gain from assembling in such a conformation was stronger than the thermodynamic surface interactions. In future studies, it would be advantageous to design substrate interactions to direct or improve alignment in cooperation with shearing, utilizing both techniques as a route to achieving transverse or perpendicular orientations, which were not observed in our conventional shear alignment investigation.

4.5 Conclusion & Future Directions

In summary, we build upon the natural self-organization of microphase separated lamellar BBCPs and demonstrate the ability to control lamellar alignment using oscillatory shearing techniques. Preliminary experiments revealed that orientation was induced over a large sample area and generally directed using small amplitude shear strains and low processing temperature. We expand the relationship between the relaxation processes in the melt (determined from linear viscoelastic measurements) and the resulting lamellar

orientation after large amplitude oscillatory shear. Small angle X-ray scattering was used to characterize and define the lamellar orientation, as well as the strength of orientation and correlation to the applied shear direction through the order parameter *S*. Parallel orientation was achieved over an exceptionally large bulk sample volume ($V \sim 1$ mm^3). We propose a defect mediated rearrangement process occurs in the inherently disordered melt state structure when shearing at low ω as opposed to conventional grain rotation.

While shear alignment has been demonstrated for BBCPs, the full parameter space has yet to be resolved. Of interest is the effect of applied strain γ. Minor alignment was observed after SAOS, but the orientation was inconsistent with follow up studies. LAOS was much more effective and produced strong orientation and high *S* values. Only one strain amplitude was used ($\gamma = 50$ %). Other amplitudes are of interest, for example strains that are the same "distance" into the non-linear viscoelastic regime. The microphase separated structure could be permanently destroyed at exceptionally large strains. These limits must be established before developing processing protocols. We also chose an arbitrary shearing time of $t = 6$ h. and would like to investigate time dependent behavior of transient and final structure formation.

The absence of confined crystallization is puzzling and deviates from our understanding of the LBCP systems. Controlling the cooling temperature and quenching will be used in future investigations to understand crystallization of the PEO side chains within the orientated lamellae.

As presented, the characterizations are entirely ex-situ representations of the structure and morphology. While orientation mechanisms may be proposed and discussed by looking at material states before and after shearing, direct in-situ measurements are

desired to quantitatively investigate the onset and evolution of lamellar orientation. Such experiments were planned out and conducted through collaborations with various external partners. Preliminary in-situ Rheo/SAXS experiments were performed at the Scattering Facility in Physical Chemistry I, University of Bayreuth (Germany), where the Linkam CSS450 was placed in line with the Ganesha SAXS-LAB. We determined the linear viscoelastic behavior of a model PtBA-*b*-PEO BBCP and targeted the low and intermediate ω regimes. For each regime, the sample was sheared for t = 30 min. at γ = 25 %. During shearing, one continuous exposure was taken to collect a 2-D SAXS pattern under shear. After the shear, the sample was cooled to room temperature and held for t = 30 min, during which another exposure was taken. The cycle was repeated 8 times for a total of t = 4 h. of discontinuous shearing. Unfortunately, the results from both the low and intermediate ω shearing were inconclusive. In the melt state, $I(q^*)$ decreases significantly, and as a result, the azimuthal integration was noisy, and the lamellar orientation could not be defined. Background scattering was very strong due to a thick Kapton window and excess scattering in air (as opposed to vacuum), which further convoluted the data. The structure was easier to resolve after cooling down to room temperature after each shearing operation. The azimuthal integrations suggested slight improvement in anisotropy upon shearing in the low ω regime, however shearing at the intermediate ω produced an isotropic scattering pattern. These results were inconclusive and were not consistent with other experiments.

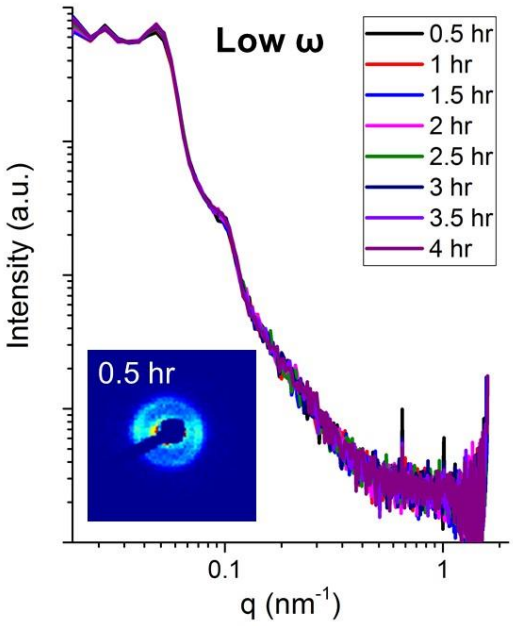

Figure 4.26 In-situ SAXS spectra of PtBA-*b*-PEO under controlled oscillatory shear in Linkam CSS 450 shear cell. Scattering signal is very weak and independent of shearing time. Inset shows representative 2-D scattering pattern. Weak anisotropy in *q** is observed

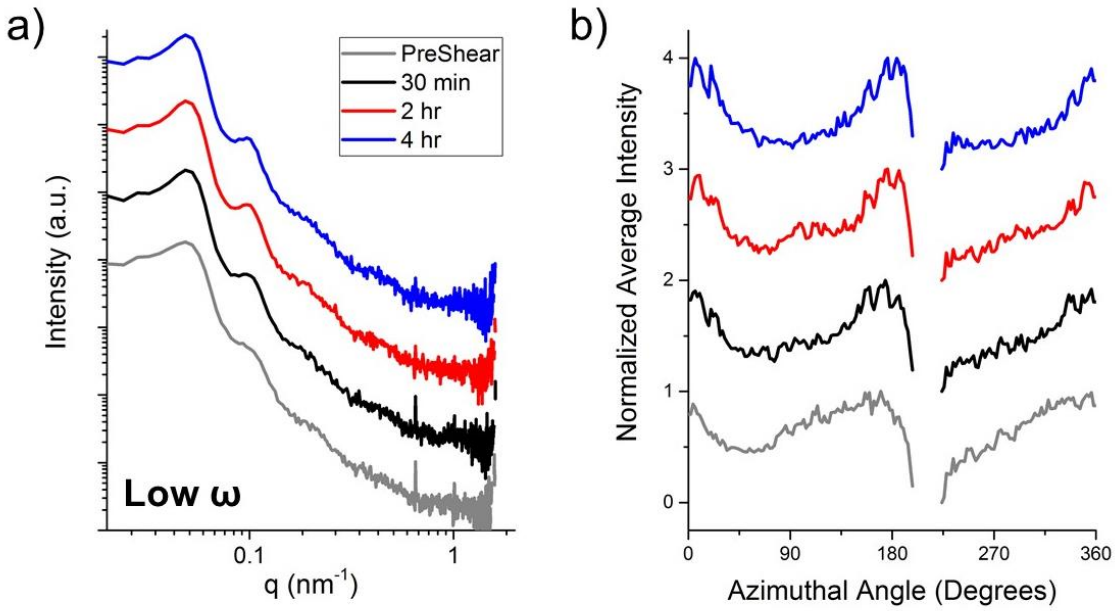

Figure 4.27 (a) SAXS spectra of PtBA-*b*-PEO upon cooling down to room temperature after varying times of controlled shearing. Spectra are vertically shifted for clarity **(b)** Azimuthal integration of *q** from 2-D scattering patterns. Spectra are vertically shifted for clarity

The Linkam CSS450 set up orients the flow direction perpendicularly to the scattering direction. Therefore, only structure in the gradient direction can be resolved under shear. At the time of these measurements, the three-dimensional orientation and morphology was not of interest and was not considered. In hindsight, the orientation of parallel lamellae would not contribute any scattering signal in the Linkam set up, as the lamellar layers would be perpendicular to the incident X-rays.

The result of Rheo/SAXS experiments revealed two experimental limitations. First, the in-house radiation source of the Ganesha is not bright enough to collect scattering patters on a reasonable time scale. Therefore, synchrotron radiation is necessary to resolve true time resolved data. The second limitation is the constraint to the gradient direction in the Linkam CSS450. The BBCPs consistently orient into the parallel orientation, which would not be observed in such a set up. Despite the experimental constrains, low ω shearing of both PS-*b*-PEO and PtBA-*b*-PEO were performed with in-situ Rheo/SAXS at beamline 11-BM (NSLS II, BNL). The results were consistent with the full analysis and understanding of the BBCP systems. During shear, the primary peak became weak and eventually disappeared in the melt state, suggesting the lamellae are weakly arranged or ordering in the orthogonal direction. After shearing, the samples were removed, and SAXS patterns collected along both the flow and vorticity directions displayed extremely high orders of orientation consistent with the parallel orientation. There are other shear devices designed to view through the different planes of the shear profile (as discussed in Section 4.1) Future investigations of processes resulting in parallel lamellae must utilize these set ups. Moving forward, PEO based materials may not be an ideal system to use. The scattering intensity is inherently weak in the melt and the morphology is disordered, so

there is not much information to extract in-situ and analyze. A system with higher χ and significant electron density contrast is required. The analysis is much simpler without crystallization, which is eliminated by using amorphous blocks (such as the classic template, PS-*b*-PI). Within the framework of current BBCP synthesis, PS-*b*-PLA or PS-*b*-PDMS are reasonable candidates for future shear alignment studies.

This simple strategy for the long-range alignment applies to a wide range of potential functional materials and applications and invites the manipulation of composite materials containing small molecules, quantum dots, anisotropic NPs, magnetic NPs, etc. The well-aligned NP arrays may serve as new age materials in the fabrication of high-performance plasmonic devices or optical materials. The ultrafast kinetics of BBCP ordering offers new opportunities for efficient, low-energy, and cost effective scalable processes.

4.6 References

(1) Song, D.-P.; Li, C.; Colella, N. S.; Xie, W.; Li, S.; Lu, X.; Gido, S. P.; Lee, J.-H.; Watkins, J. J. Large-Volume Self-Organization of Polymer/Nanoparticle Hybrids with Millimeter-Scale Grain Sizes Using Brush Block Copolymers. *J. Am. Chem. Soc.* **2015**, *137*, 12510–12513.

(2) Song, D.-P.; Li, C.; Li, W.; Watkins, J. J. Block Copolymer Nanocomposites with High Refractive Index Contrast for One-Step Photonics. *ACS Nano* **2016**, *10* (1), 1216–1223.

(3) Song, D.-P.; Jacucci, G.; Dundar, F.; Naik, A.; Fei, H.-F.; Vignolini, S.; Watkins, J. J. Photonic Resins: Designing Optical Appearance via Block Copolymer Self-Assembly. *Macromolecules* **2018**, *51* (6), 2395–2400.

(4) Parnell, A. J.; Tzokova, N.; Pryke, A.; Howse, J. R.; Mykhaylyk, O. O.; Ryan, A. J.; Panine, P.; Fairclough, J. P. A. Shear Ordered Diblock Copolymers with Tuneable Optical Properties. *Phys. Chem. Chem. Phys.* **2011**, *13* (8), 3179–3186.

(5) Park, M. J.; Balsara, N. P. Anisotropie Proton Conduction in Aligned Block Copolymer Electrolyte Membranes at Equilibrium with Humid Air. *Macromolecules* **2010**, *43* (1), 292–298.

(6) Phillip, W. A.; O'Neill, B.; Rodwogin, M.; Hillmyer, M. A.; Cussler, E. L. Self-Assembled Block Copolymer Thin Films as Water Filtration Membranes. *ACS Appl. Mater. Interfaces* **2010**, *2* (3), 847–853.

(7) Bodycomb, J.; Funaki, Y.; Kimishima, K.; Hashimoto, T. Single-Grain Lamellar Microdomain from a Diblock Copolymer. *Macromolecules* **1999**, *32* (6), 2075–2077.

(8) Darling, S. B. Directing the Self-Assembly of Block Copolymers. *Prog. Polym. Sci.* **2007**, *32* (10), 1152–1204.

(9) Hu, H.; Gopinadhan, M.; Osuji, C. O. Directed Self-Assembly of Block Copolymers: A Tutorial Review of Strategies for Enabling Nanotechnology with Soft Matter. *Soft Matter* **2014**, *10* (22), 3867–3889.

(10) Cheng, L.; Gadelrab, K. R.; Kawamoto, K.; Yager, K. G.; Johnson, J. A.; Alexander-Katz, A.; Ross, C. A. Templated Self-Assembly of a PS- Branch -PDMS Bottlebrush Copolymer. *Nano Lett.* **2018**, *18*, 4360–4369.

(11) Ruppel, M.; Pester, C. W.; Langner, K. M.; Sevink, G. J. A.; Schoberth, H. G.; Schmidt, K.; Urban, V. S.; Mays, J. W.; Böker, A. Electric Field Induced Selective Disordering in Lamellar Block Copolymers. *ACS Nano* **2013**, *7* (5), 3854–3867.

(12) Morkved, T. L.; Lu, M.; Urbas, a. M.; Ehrichs, E. E.; Jaeger, H. M.; Mansky, P.; Russell, T. P. Local Control of Microdomain Orientation in Diblock Copolymer Thin Films with Electric Fields. *Science (80-.).* **1996**, *273* (5277), 931–933.

(13) Pester, C. W.; Schmidt, K.; Ruppel, M.; Schoberth, H. G.; Boker, A. Electric-Field-Induced Order-Order Transition from Hexagonally Perforated Lamellae to Lamellae. *Macromolecules* **2015**, *48* (17), 6206–6213.

(14) Rokhlenko, Y.; Gopinadhan, M.; Osuji, C. O.; Zhang, K.; O'Hern, C. S.; Larson, S. R.; Gopalan, P.; Majewski, P. W.; Yager, K. G. Magnetic Alignment of Block Copolymer Microdomains by Intrinsic Chain Anisotropy. *Phys. Rev. Lett.* **2015**, *115* (25), 2–6.

(15) Gopinadhan, M.; Choo, Y.; Kawabata, K.; Kaufman, G.; Feng, X.; Di, X.; Rokhlenko, Y.; Mahajan, L. H.; Ndaya, D.; Kasi, R. M.; et al. Controlling Orientational Order in Block Copolymers Using Low-Intensity Magnetic Fields. *Proc. Natl. Acad. Sci.* **2017**, *114* (45), E9437–E9444.

(16) Tousley, M. E.; Feng, X.; Elimelech, M.; Osuji, C. O. Aligned Nanostructured Polymers by Magnetic-Field-Directed Self-Assembly of a Polymerizable Lyotropic Mesophase. *ACS Appl. Mater. Interfaces* **2014**, *6* (22), 19710–19717.

(17) Keller, A.; Pedemonte, E.; Willmouth, F. M. Macro Lattice from Segregated Amorphous Phases of a Three Block Copolymer. *Kolloid-Z.u.Z.Polymere* **1970**, *238*, 385–389.

(18) Koppi, K. A.; Tirrell, M.; Bates, F. S.; Almdal, K.; Colby, R. H. Lamellae Orientation in Dynamically Sheared Diblock Copolymer Melts. *J. Phys. II* **1992**, *2*, 1941–1959.

(19) Riise, B. L.; Fredrickson, G. H.; Larson, R. G.; Pearson, D. S. Rheology and Shear-Induced Alignment of Lamellar Diblock and Triblock Copolymers. *Macromolecules* **1995**, *28* (23), 7653–7659.

(20) Gupta, V. K.; Krishnamoorti, R.; Chen, Z.-R.; Kornfield, J. A.; Smith, S. D.; Satkowski, M. M.; Grothaus, J. T. Dynamics of Shear Alignment in a Lamellar Diblock Copolymer: Interplay of Frequency, Strain Amplitude, and Temperature. *Macromolecules* **1996**, *29* (3), 875–884.

(21) Chen, Z.-R.; Kornfield, J. A. Flow-Induced Alignment of Lamellar Block Copolymer Melts. *Polymer (Guildf).* **1998**, *39* (19), 4679–4699.

(22) Chen, Z.-R.; Kornfield, J. A.; Smith, S. D.; Grothaus, J. T.; Satkowski, M. M. Pathways to Macroscale Order in Nanostructured Block Copolymers. *Science (80-.).* **1997**, *277* (5330), 1248–1253.

(23) Zhang, Y.; Wiesner, U. B. Rheology of Lamellar Polystyrene- Block - Polyisoprene Diblock Copolymers. *Macromol. Chem. Phys.* **1998**, *199*, 1771–1784.

(24) Wiesner, U. B. Lamellar Diblock Copolymers under Large Amplitude Oscillatory Shear Flow: Order and Dynamics. *Macromol. Chem. Phys.* **1997**, *198* (11), 3319–3352.

(25) Winey, K. I.; Sanjay, J.; Larson, R. G.; Watanabe, H. Interdependence of Shear Deformations and Block Copolymer Morphology. *Macromolecules* **1993**, *26*, 2542–2549.

(26) Rendon, S.; Fang, J.; Burghardt, W. R.; Bubeck, R. A. An Apparatus for in Situ X-Ray Scattering Measurements during Polymer Injection Molding. *Rev. Sci. Instrum.* **2009**, *80* (4), 043902.

(27) Caputo, F. E.; Burghardt, W. R.; Krishnan, K.; Bates, F. S.; Lodge, T. P. Time-Resolved Small-Angle x-Ray Scattering Measurements of a Polymer Bicontinuous Microemulsion Structure Factor under Shear. *Phys. Rev. E - Stat. Nonlinear, Soft Matter Phys.* **2002**, *66* (4), 1–18.

(28) Caputo, F. E.; Burghardt, W. R. Real-Time 1-2 Plane SAXS Measurements of Molecular Orientation in Sheared Liquid Crystalline Polymers. *Macromolecules* **2001**, *34* (19), 6684–6694.

(29) Mortensen, K.; Almdal, K.; Bates, F. S.; Koppi, K. A.; Tirrell, M. V.; Nordén, B. Shear Devices for in Situ Structural Studies of Block-Copolymer Melts and Solutions. *Phys. B Phys. Condens. Matter* **1995**, *213–214* (C), 682–684.

(30) Pfleiderer, P.; Baik, S. J.; Zhang, Z.; Vleminckx, G.; Lettinga, M. P.; Grelet, E.; Vermant, J.; Clasen, C. X-Ray Scattering in the Vorticity Direction and Rheometry from Confined Fluids. *Rev. Sci. Instrum.* **2014**, *85* (6), 065108.

(31) Mykhaylyk, O. O.; Parnell, A. J.; Pryke, A.; Fairclough, J. P. A. Direct Imaging of the Orientational Dynamics of Block Copolymer Lamellar Phase Subjected to Shear Flow. *Macromolecules* **2012**, *45* (12), 5260–5272.

(32) Okamoto, S.; Saijo, K.; Hashimoto, T. Real-Time SAXS Observations of Lamella-Forming Block Copolymers under Large Oscillatory Shear Deformation. *Macromolecules* **1994**, *27* (20), 5547–5555.

(33) Scott, D. B.; Waddon, A. J.; Lin, Y. G.; Karasz, F. E.; Winter, H. H. Shear-Induced Orientation Transitions in Triblock Copolymer Styrene-Butadiene-Styrene with Cylindrical Domain Morphology. *Macromolecules* **1992**, *25* (16), 4175–4181.

(34) Morrison, F.; Winter, H. H. The Effect of Unidirectional Shear on the Structure of Triblock Copolymers. I. Polystyrene-Polybutadiene-Polystyrene. *Macromolecules* **1989**, *22*, 3533–3540.

(35) Morrison, F.; Bourvellec, G. LE; Winter, H. H. Flow-Induced Structure and Rheology of a Triblock Copolymer. *J. Appl. Polym. Sci.* **1987**, *33*, 1585–1600.

(36) Mortensen, K.; Theunissen, E.; Kleppinger, R.; Almdal, K.; Reynaers, H. Shear-Induced Morphologies of Cubic Ordered Block Copolymer Micellar Networks Studied by in Situ Small-Angle Neutron Scattering and Rheology. *Macromolecules* **2002**, *35* (20), 7773–7781.

(37) Zalusky, A. S.; Olayo-Valles, R.; Wolf, J. H.; Hillmyer, M. A. Ordered Nanoporous Polymers from Polystyrene-Polylactide Block Copolymers. *J. Am. Chem. Soc.* **2002**, *124* (43), 12761–12773.

(38) Chang, A. B.; Lin, T.-P.; Thompson, N. B.; Luo, S.-X.; Liberman-Martin, A. L.; Chen, H.-Y.; Lee, B.; Grubbs, R. H. Design, Synthesis, and Self-Assembly of Polymers with Tailored Graft Distributions. *J. Am. Chem. Soc.* **2017**, *139* (48), 17683–17693.

(39) Gai, Y.; Song, D.-P.; Yavitt, B. M.; Watkins, J. J. Polystyrene- Block -Poly(Ethylene Oxide) Bottlebrush Block Copolymer Morphology Transitions: Influence of Side Chain Length and Volume Fraction. *Macromolecules* **2017**, *50*, 1503–1511.

(40) Winter, H. H.; Mours, M. The Cyber Infrastructure Initiative for Rheology. *Rheol. Acta* **2006**, *45* (4), 331–338.

(41) Yavitt, B. M.; Gai, Y.; Song, D.-P.; Winter, H. H.; Watkins, J. J. High Molecular Mobility and Viscoelasticity of Microphase-Separated Bottlebrush Diblock Copolymer Melts. *Macromolecules* **2017**, *50* (1), 396–405.

(42) Macosko, C. W. *Rheology: Principles, Measurements, and Applications*; Wiley VCH: New York, 1994.

(43) De Jeu, W. H. *Basic X-Ray Scattering for Soft Matter*, 1st ed.; Oxford University Press: Oxford, 2016.

(44) Zhang, C.; Cavicchi, K. A.; Li, R.; Yager, K. G.; Fukuto, M.; Vogt, B. D. Thickness Limit for Alignment of Block Copolymer Films Using Solvent Vapor Annealing with Shear. *Macromolecules* **2018**, *51*, 4213.

(45) Hashimoto, T.; Koizumi, S.; Hasegawa, H.; Izumitani, T.; Hyde, S. T. Observation of "Mesh" and "Strut" Structures in Block Copolymer/Homopolymer Mixtures. *Macromolecules* **1992**, *25* (5), 1433–1439.

(46) Almdal, K.; Koppi, K. A.; Bates, F. S.; Mortensen, K. Multiple Ordered Phases in a Block Copolymer Melt. *Macromolecules* **1992**, *25* (6), 1743–1751.

(47) Zhu, L.; Cheng, S. Z. D.; Calhoun, B. H.; Ge, Q.; Quirk, R. P.; Thomas, E. L.; Hsiao, B. S.; Yeh, F.; Lotz, B. Crystallization Temperature-Dependent Crystal Orientations within Nanoscale Confined Lamellae of a Self-Assembled Crystalline - Amorphous Diblock Copolymer. *J. Am. Chem. Soc.* **2000**, *122* (25), 5957–5967.

(48) Huang, P.; Zhu, L.; Guo, Y.; Ge, Q.; Jing, A. J.; Chen, W. Y.; Quirk, R. P.; Cheng, S. Z. D.; Thomas, E. L.; Lotz, B.; et al. Confinement Size Effect on Crystal Orientation Changes of Poly(Ethylene Oxide) Blocks in Poly(Ethylene Oxide)- b -Polystyrene Diblock Copolymers. *Macromolecules* **2004**, *37* (10), 3689–3698.

(49) Zhu, L.; Cheng, S. Z. D.; Calhoun, B. H.; Ge, Q.; Quirk, R. P.; Thomas, E. L.; Hsiao, B. S.; Yeh, F.; Lotz, B. Phase Structures and Morphologies Determined by Self-Organization, Vitrification, and Crystallization: Confined Crystallization in an Ordered Lamellar Phase of PEO-b-PS Diblock Copolymer. *Polymer (Guildf).* **2001**, *42*, 5829–5839.

(50) Cavicchi, K. A.; Russell, T. P. Solvent Annealed Thin Films of Asymmetric Polyisoprene - Polylactide Diblock Copolymers. *Macromolecules* **2007**, *40* (4), 1181–1186.

(51) Hong, S. W.; Gu, W.; Huh, J.; Sveinbjornsson, B. R.; Jeong, G.; Grubbs, R. H.; Russell, T. P. On the Self-Assembly of Brush Block Copolymers in Thin Films. *ACS Nano* **2013**, *7* (11), 9684–9692.

(52) Mittal, K. L. *Polymer Science Modification: Relevance to Adhesion Volume 3*; 2004.

CHAPTER 5

PHASE TRANSITIONS AND RHEOLOGICAL PROPERTIES OF BRUSH BLOCK COPOLYMER NANOCOMPOSITES

5.1 Introduction & Project Motivation

The bottlebrush block copolymer template exhibits promise in overcoming many of the limitations preventing the scalable, low-cost fabrication of NP/BCP composites. In comparison to conventional nanocomposites derived from LBCPs, the BBCP templates possess attractive features desired for scale up, such as rapid self-assembly (timescale of minutes as opposed to hours or even several days), large domain spacing (d_0 > 100 nm), large grain sizes (hundreds of microns) and high loading of nanoparticles (φ > 70 wt.%).[1] Amphiphilic BBCPs are used to direct functionalized gold NPs into highly ordered arrays.[2–4] Several examples of NP/BBCP assemblies with unique and desirable physical properties have been described by our group and others in applications such as photonic crystals, non-linear optical materials, and metamaterials.[1,5,6] Rapid self-assembly and solution processability is desirable for implementation in roll-to-roll manufacturing of low-cost and flexible devices.

Understanding the rheological behavior and processing of these hybrid materials (in both the solution and melt state) is a non-trivial matter, as the addition of inorganic material into the matrix imparts significant constraints on the relaxation and dynamics of the polymer chains.[7] These effects are considered in detail in Chapter 2 for additive driven assembly systems of low χN BCPs. The same considerations are valid for highly filled NP/BBCP systems. The highly mobile, critical-gel rheology of the BBCP architecture and absence of chain entanglements is highly attractive and believed to be necessary for the

rapid assembly. Any adverse effects on the rheological properties from the addition of NPs must be considered when designing mechanical performance and processing guidelines.

In this chapter, we will resolve the governing principles of NP/BBCP phase behavior and rheological properties using model systems of amphiphilic BBCPs and surface functionalized ZrO_2 NPs. The temperature dependent behavior is of interest. We hypothesize that the addition of NPs into the microphase separated BBCP template will inhibit the sequential relaxation processes described in Chapter 3. Therefore, we determine the frequency dependent viscoelasticity as a function of NP loading and analyze the relaxation time spectrum $H(\tau)$ to describe the restriction of such relaxation mechanisms. The morphology of the NP/BBCP composites is impacted by the addition of NPs as well and is described in a recent publication.[4] However, temperature dependent phase transitions have not been defined as a function of NP loading. Our goal is to correlate viscoelasticity and phase behavior in the melt state to understand how to control mechanical properties and optimize the processing windows for such materials

5.2 Experimental

5.2.1 Material Selection

Two separate families of PEO-based amphiphilic BBCPs were synthesized by sequential ring opening metathesis polymerization (ROMP) of norbornene functionalized macromonomers.[4,8] Densely grafted PS-*b*-PEO and PtBA-*b*-PEO BBCPs are prepared according to procedures declared in Chapter 3 and Chapter 4. The side chain molecular weight is kept below entanglement molecular weight in both domains to reduce chain entanglements (PS-NB MM M_n = 2.9 kg/mol, PtBA-NB MM M_n = 7.6 kg/mol, PEO-NB MM M_n = 5kg/mol). Within each family, three separate BBCPs were prepared with

increasing overall MW referred to as Small (*S*), Medium (*M*), and Large (*L*) according to their overall backbone length (N_{bb}), schematically represented in Figure 5.1a and Figure 5.1b for PS-*b*-PEO and PtBA-*b*-PEO respectively. Molecular details are presented in Table 5.1 and Table 5.2.

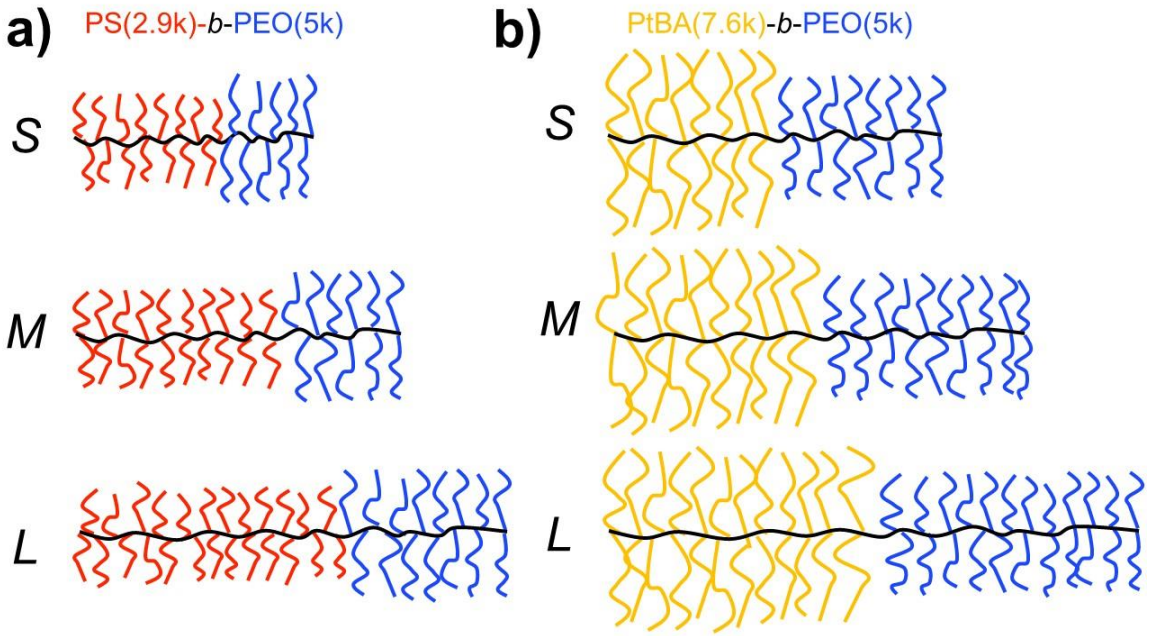

Figure 5.1 Molecular design of **a)** PS-*b*-PEO (S, M, and L) and **b)** PtBA-*b*-PEO BBCPs (S, M, and L)

Table 5.1 Molecular Details of PS-*b*-PEO BBCPs

PS-*b*-PEO Sample Name[a]	*Mw* (kg/mol)[b]	*Đ*[b]	f_{PEO}[c]	N_{bb}[d]	$N_{bb\text{-}PS}$[d]	$N_{bb\text{-}PEO}$[d]	d_0 (nm)[e]
PS-S	204	1.17	0.5	47	29	18	40
PS-M	364	1.21	0.5	81	50	30	67.5
PS-L	900	1.40	0.5	135	84	51	88

[a]BBCPs are labeled as "*PS*-X", where "X" = S, M, or L. [b]Weight average molecular weight (M_w) and polydispersity (*Đ*) were determined by GPC-MALLS. [c]Theoretical volume fraction of PEO (f_{PEO}) was calculated using mass ratios of PS and PEO obtained from ^{1}H NMR spectra and approximate bulk densities (1.05 and 1.09 g/cm^3 for PS and PEO, respectively). [d]Block backbone degree of polymerizations ($N_{bb\text{-}PEO}$ & $N_{bb\text{-}PS}$) and overall backbone degree of polymerization (N_{bb}= $N_{bb\text{-}PEO}$ + $N_{bb\text{-}PS}$) were calculated using absolute molecular weights and *Đ* as measured by GPC and mass fraction from NMR. [e]Domain spacings (d_0) were calculated using the equation d-spacing = $2\pi/q^*$, where q^* corresponds to the primary peak from small angle X-ray scattering in nm^{-1}.

Table 5.2 Molecular Details of PtBA-*b*-PEO BBCPs

PtBA-*b*-PEO Sample Name[a]	*Mw* (kg/mol)[b]	Đ[b]	f_{PEO}[c]	N_{bb}[d]	$N_{bb\text{-}PtBA}$[d]	$N_{bb\text{-}PEO}$[d]	d_0 (nm)[e]
PtBA-S	246	1.22	0.4	32	16	16	50.5
PtBA-M	440	1.3	0.4	54	27	27	75
PtBA-L	581	1.6	0.4	71	35	36	103.4

[a]BBCPs are labeled as "*PtBA*-X", where "X" = S, M, or L. [b]Weight average molecular weight (M_w) and polydispersity ($Đ$) were determined by GPC-MALLS. [c]Theoretical volume fraction of PEO (f_{PEO}) was calculated using mass ratios of PtBA and PEO obtained from ^{1}H NMR spectra and approximate bulk densities (1.05 and 1.09 g/cm^3 for PtBA and PEO, respectively). [d]Block backbone degree of polymerizations ($N_{bb\text{-}PEO}$ & $N_{bb\text{-}PtBA}$) and overall backbone degree of polymerization (N_{bb}= $N_{bb\text{-}PEO}$ + $N_{bb\text{-}PtBA}$) were calculated using absolute molecular weights and $Đ$ as measured by GPC and mass fraction from NMR. [e]Domain spacings (d_0) were calculated using the equation d-spacing = $2\pi/q^*$, where q^* corresponds to the primary peak from small angle X-ray scattering in nm^{-1}.

Zirconium dioxide (ZrO_2) NPs (d_{NP} = 5-6 nm) are used as the inorganic additive. The diameter was selected to be commensurate with the lamellar thickness constraint and to reduce entropic penalty associated with adding NPs into BCP matrix. NPs dispersed in toluene (PCNI-TOL-50) were purchased from Pixelligent Inc. The toluene was evaporated under nitrogen flow followed by re-dispersion in THF via ultrasonication (concentration = 10 mg/ml). NP surface was modified with gallic acid (GA) to improve hydrogen bonding coordination with PEO side chains (Figure 5.2a).[1] Surface modification was carried out by adding 5 wt. % of GA relative to the mass of NPs directly to the NP solution. The resulting mixture was stirred overnight with assisted magnetic stirring. The exchange of the original surface ligands with GA was rapid and efficient, visually evident by a color change from clear to translucent brown. The resulting solution was used for sample preparation without further purifications.

5.2.2 Sample Preparation

Bulk BBCPs were weighed and dissolved in anhydrous THF (solid mass ~ 50 mg). NP solutions (in THF) were added directly to the BBCP solutions to form 1.5 wt.% solutions. The solutions were homogeneously mixed and cast through 0.45 μm PTFE filter onto horizontal glass slides, which were covered immediately with glass Petri dishes. After complete solvent evaporation, the dried films were collected with a razor blade. For SAXS sample preparation, the composite films were filled in a washer at T = 100 °C and melt pressed using a Kapton sheet. The resulting bulk samples were sealed using Kapton tape and annealed at under vacuum (PS: T = 120 °C for 8 h. & PtBA: T = 100 °C for 4 h.), followed by cooling to room temperature under nitrogen. The sample thickness was approximately 0.50 mm. Rheology samples were prepared in identical fashion using a larger washer (diam. = 8 mm).

Throughout, the overall composition of the nanocomposite is defined as the weight percentage of NP solids with respect to the total composite mass. Additional mass and volume fractions are calculated by thermogravimetric analysis (TGA) data and the density of components and are presented in Table 5.3.

Table 5.3: Various compositions of modified ZrO_2 in composites

Composition	PS-*b*-PEO		PtBA-*b*-PEO	
(Core + ligand) wt.%	**15**	**30**	**15**	**30**
Core wt.%	12.3	24.6	12.3	26.6
(Core + ligand) vol.%	5.3	11.9	5.3	11.9
Core vol.%	2.6	6.1	2.6	6.1
(Core + ligand) wt.% in PEO	26.1	46.2	30.6	51.7
Core wt.% in PEO	21.4	37.8	25.1	42.4
(Core + ligand) vol.% in PEO	10.0	21.2	12.2	25.2
Core vol.% in PEO	5.1	11.5	6.3	14

The weight percentages of the NPs in composite samples were converted into volume percentages using approximate density of block copolymer (1.05 g/cm^3), the densities of the ZrO_2 (5.68 g/cm^3), approximate density of original ligand (1.05 g/cm^3), and gallic acid (1.70 g/cm^3). The volume fraction of NPs in the composite is defined as $f = V_{NP}/(V_{NP} + V_{BCP})$, where V_{NP} and V_{BCP} are the volumes of NPs and BCPs, respectively. The volume fraction of NPs in the PEO domain is defined as $f_{NP/PEO} = V_{NP}/(V_{NP} + V_{PEO})$.

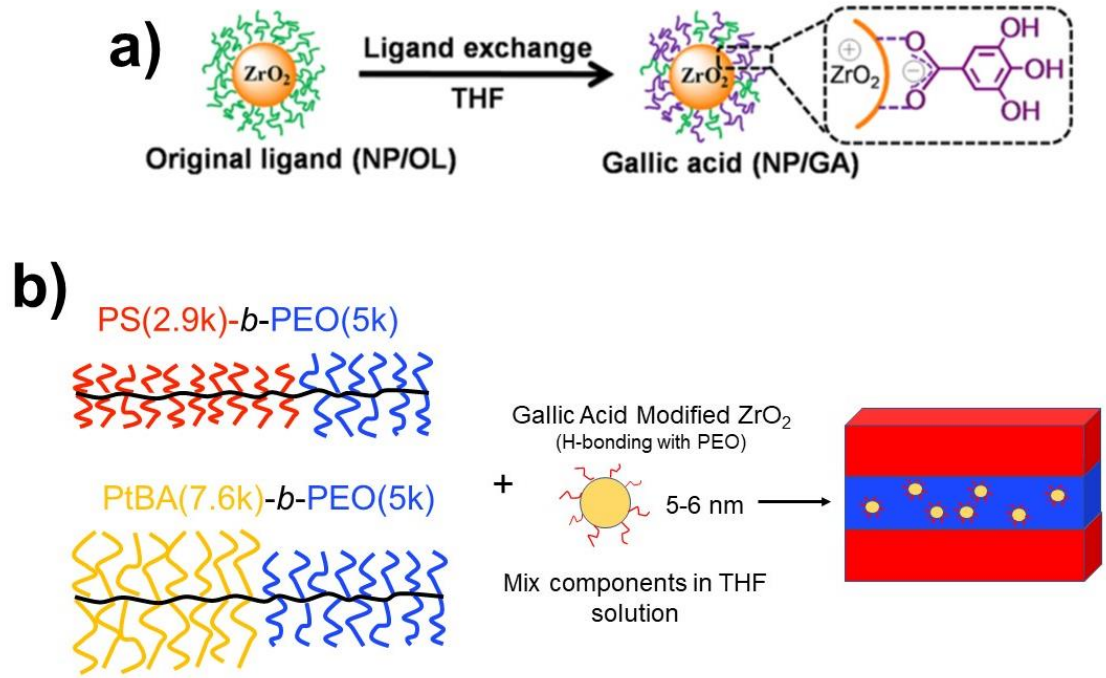

Figure 5.2 (a) Gallic acid modification of ZrO_2 NPs **(b)** Directed self-assembly of ZrO_2 NPs with densely grafted amphiphilic BBCPs. Hydrogen bonding via gallic acid selectively assembles NPs into PEO domain during microphase segregation. (Modified from Ref. 1)[1]

5.2.3 Characterizations

Thermogravimetric analysis (TGA) was performed on a TGA2950 with a heating rate of 10 °C/min under nitrogen. *Fourier transform infrared spectroscopy (FTIR)* measurements were performed using a PerkinElmer FTIR spectrometer in the range from υ = 4000 to 650 cm^{-1} with an ATR crystal window. *Transmission electron microscopy (TEM)* measurements were conducted with a JEOL 2000FX TEM operated at an accelerating voltage of 200 kV. Thin sections (thickness ~ 50 nm) were prepared using a Leica Ultracut UCT microtome equipped with a Leica EM FCS cryogenic sample chamber operated at T = -100 °C. Subsequent staining with ruthenium tetroxide (RuO_4) was used for neat BBCP

to provide enhanced contrast between PS/PtBA and PEO domains. *Differential Scanning Calorimetry (DSC)* measurements were performed using a TA Instruments Q100 DSC equipped with an RCS cooling system and nitrogen gas purge with a flow rate of 50 mL/min. All measurements were conducted in the temperature range of T = -30 to 100 °C at a constant heating and cooling rate of 10 °C/min under a nitrogen atmosphere. *Small-angle X-ray Scattering (SAXS)* measurements were performed on Beamline 11-BM (Complex Material Scattering) at NSLS II (Brookhaven National Lab). In-situ temperature-controlled measurements were conducted on a thermal heating stage (CMS). Bulk samples were heated at a constant heating rate of 0.5 °C/min, while continuous SAXS measurements (~ 10 second exposure) were taken from room temperature (T = 30 °C) to T = 200 °C at temperature intervals of ~ 3 °C/exposure. *Rheology* measurements were performed on a Malvern Kinexus stress-controlled oscillatory rheometer with an 8 mm parallel plate fixture. The dynamic response was probed with small amplitude oscillatory shear (SAOS) frequency sweeps at γ = 1% strain amplitude from T = 50 to 150 °C in increments of 10 °C across a frequency range of ω = 1-100 rad/s. The time-temperature superposition principle was applied to temperature dependent frequency sweeps. Rheological data was analyzed using IRIS-RheoHub 2018 software.

5.3 Results

5.3.1 Nanoparticle Characterization

Surface modification of ZrO_2 was carried out to improve hydrogen bonding interaction between the NP and PEO side chains. The original organic ligand leads to severe NP aggregation and disordered morphologies according to observations by Song et al.[1] NP co-assembly and selective dispersion within PtBA-*b*-PEO BBCP was achieved only

after GA surface modification. The carboxylic acid and hydroxyl groups on GA provide strong hydrogen bonding interaction with the PEO domain necessary to improve dispersion and reach high loading. After surface modification, the NPs remain well dispersed with uniform size distribution according to TEM images in Figure 5.3a. Average particle size remains d_0 ~ 6 nm even after ligand exchange. TGA and FTIR were used to confirm successful ligand exchange. Before GA modification, the inorganic NP core comprises 86 wt.% according to TGA (Figure 5.3b). After modification, the core content is reduced to 83 wt.% suggesting attachment of additional GA ligands to the NP surface. FTIR spectra of the commercial and modified NPs both display a strong C=O carbonyl peak around ν = 1700 cm^{-1}, consistent with FTIR spectra presented by Song et al.[1] After modification, the carboxylic acid peak shifts to lower wavenumber due to selective association towards the NP core, while the three -OH groups extend out towards the periphery of the particle.[9] The broad peak at ν = 3300 cm^{-1} on the modified particles suggests that the -OH functional groups are present and able to hydrogen bond with ether -O- in the PEO side chains.

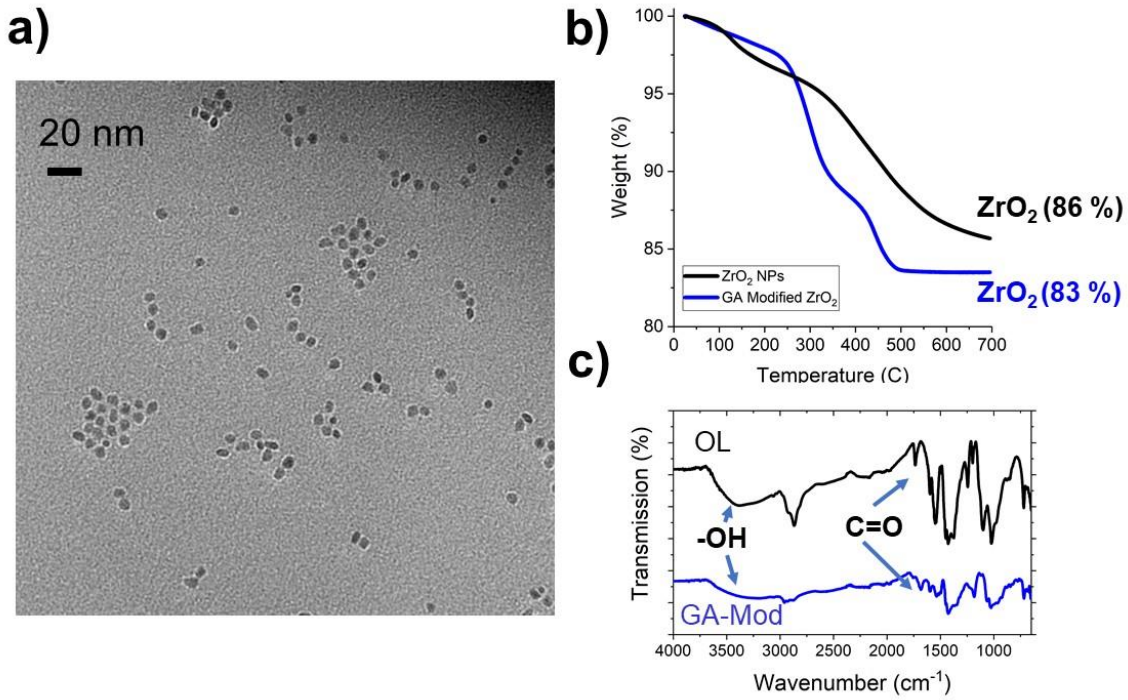

Figure 5.3 (a) TEM micrograph of drop-cast ZrO_2 NPs. NPs are spherical in shape and uniform in size **(b)** TGA of original (black) and modified (blue) ZrO_2 NPs upon heating to T = 700 °C **(c)** FTIR of original (black) and modified (blue) ZrO_2 NPs. Spectra is consistent with reports from Song et al. considering identical NP modification scheme.[1]

5.3.2 Self-Assembly of BBCP Templates with Modified ZrO_2 NPs

Composites were prepared by mixing BBCP and NP solutions at various concentrations according to Table 5.3, followed by drop casting and melt pressing. After melt pressing, the BCP morphology and NP assembly was investigated with small angle X-ray scattering (SAXS) at room temperature. Figure 5.4 shows SAXS spectra of each composite in the PS-*b*-PEO series with increasing loading of NPs (0, 15, and 30 wt.%). Curves are vertically shifted for clarity. In the *S* series (Figure 5.4a) a primary scattering peak q^* is observed in the neat BBCP sample indicating microphase segregation due to chemically dissimilar blocks. The ratio of high order scattering peaks positions to q^* suggests a lamellar morphology with a domain spacing of d_0 = 40 nm. The lamellar morphology is consistent with the mass composition and the architectural configuration of

the side chains.[8] With the addition of 15 wt.% NP, a peak emerges at $q \approx 1.1$ nm^{-1} due to the form factor of the spherical NPs. The form factor intensity increases significantly with loading up to 30 wt.%. The addition of NPs also impacts the scattering at low q, which is primarily dominated by the BCP microphase segregation. Most notably, in PS-*S*-15 (15 wt.% NP), q^* shifts to lower q, suggesting an increase in the d_0 as the NPs occupy space within the PEO domain which swells the microphase separated layer. The high order scattering peak disappears, implying that the long-range order of the lamellae is disrupted or that the structure is inconclusive. q^* and all higher order peaks disappear at the highest loading in PS-*S*-30. The disappearance of q^* is consistent with a disordering transition. At exceptionally large NP loading, the PEO domain cannot accommodate the additional volumetric constrain necessary to form an equalized interfacial area, resulting in an ODT.[10] The strong intensity of the NP scattering peak at high q also suggests NP aggregation. Well-dispersed NPs within the polymer matrix result in a broad peak, while highly aggregated NPs contribute significantly to the scattering intensity and result in a sharp peak.[11] Qualitatively, the form factor is broad enough to suggest decent NP dispersion in PS-*S*-30. Therefore, the disordering transition is more likely related the volume filling constraints. Similar trends in the progression of q^* and high order scattering peaks are observed in the PS-*M* and PS-*L* series (Figure 5.4b and Figure 5.4c). Most notably, PS-*M* and PS-*L* both self-assemble into lamellar morphologies analogous to PS-*S*, with spacings of $d_0 = 67.5$ and $d_0 = 88$ nm respectively. PS-*L* spectra exhibit a characteristic PEO crystallization peak at $q = 0.4$ nm^{-1}. While q^* is distinct in PS-*M*-15 and PS-*L*-15, high order peaks are difficult to resolve, again suggesting a disordered morphology. The NPs appear to be sequestered and dispersed in the polymer matrix but disrupt the formation of well-ordered microphase

separated layers. PS-*M*-30 clearly transitions to a fully disordered structure, like PS-*S*-30, however PS-*L*-30 displays a defined q^* corresponding to d_0 = 104 nm, suggesting the PS and PEO domains are microphase separated. q^* is broad and scatters near the low q limit of the detector, distorting the determination of d_0. According to the observations across this range of N_{bb}, it appears that the longer backbone BBCPs are more successful at incorporating NPs into the templated lamellar structure. The characteristic ratio of the particle diameter to the domain thickness (in this case d_{NP}/d_{PEO}) must be commensurate to achieve successful self-assembly, and has been well studied in NP/LBCP systems as described in Chapter 1 and 2.[12,13] Application to the dense brush systems is valid, but the limits of d_{NP}/d_{PEO} are less understood. In the PS-*b*-PEO BBCP system with asymmetric side chain lengths (PS-NB MM M_n < PEO-NB MM M_n) lamellar domain thickness is also asymmetric according to electron microscopy analysis. The PEO domain appears much thinner with respect to the PS domain despite the PEO side chains being larger than the PS side chains. The size constraint is more significant in BBCPs with small d_0 (i.e. PS-*S*). Therefore, we propose that PS-*L* is near the critical d_{PEO} limit necessary to incorporate the ZrO_2 NPs (d_{NP} = 5 nm) into an ordered assembly. Even within this limit, the lamellae are disordered and not well defined, suggesting that additional physical factors disrupt the self-assembly.

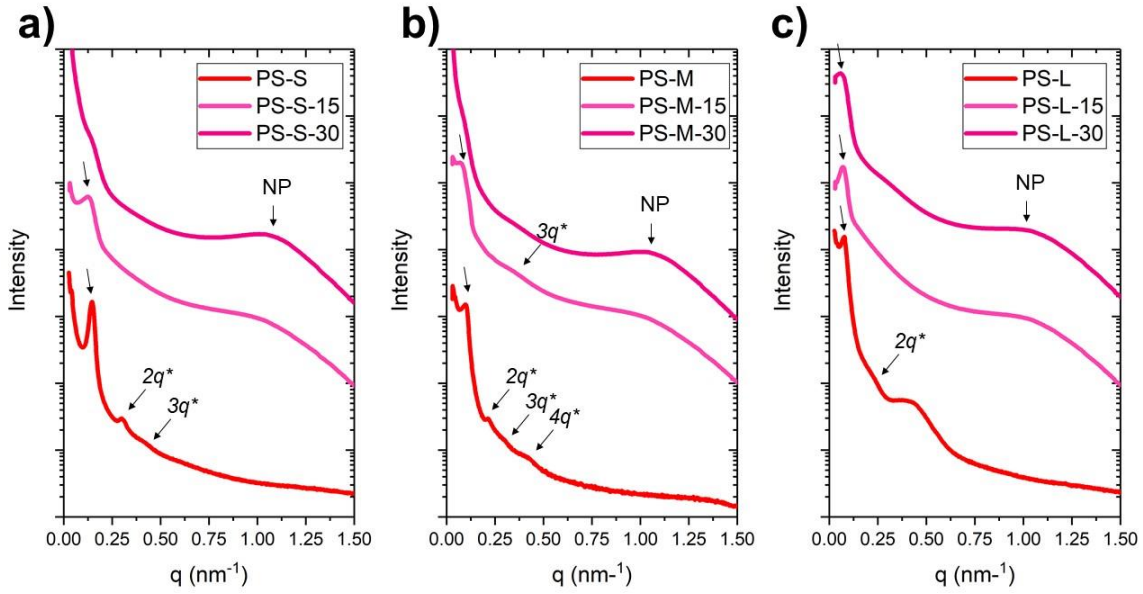

Figure 5.4 Room Temperature SAXS of PS-*b*-PEO series after drop casting and thermal annealing. **(a)** PS-*S*, PS-*S*-15 and PS-*S*-30 **(b)** PS-*M*, PS-*M*-15 and PS-*M*-30 **(c)** PS-*L*, PS-*L*-15 and PS-*L*-30

The BBCP morphology and NP assembly was confirmed with transmission electron microscopy (TEM) of cryomicrotomed slices of bulk composite. Figure 5.5 shows images of PS-*M*, PS-*M*-15 and PS-*M*-30, of which the latter two appeared disordered in SAXS. Neat BBCP sample (PS-*M*) was stained with RuO_4 while composite samples were left unstained as contrast arises from the differences in nuclear mass between NPs and the polymer matrix. The asymmetric lamellae are certainly apparent in PS-*M*, where the dark stained PEO domain is much thinner than the unstained PS domain. One would expect the NPs to selectively assemble into the PEO domain in a well-ordered system by the strong hydrogen bonding. Domains of high NP concentration are observed, but not within any well-defined lamellar structure. The assembly pattern is highly disordered and consistent with the SAXS spectra in Figure 5.4b. There are many possibilities for the trend toward the disordered morphology (such as the d_{NP}/d_{PEO} ratio) that will be discussed in detail in the Discussion (Section 5.4).

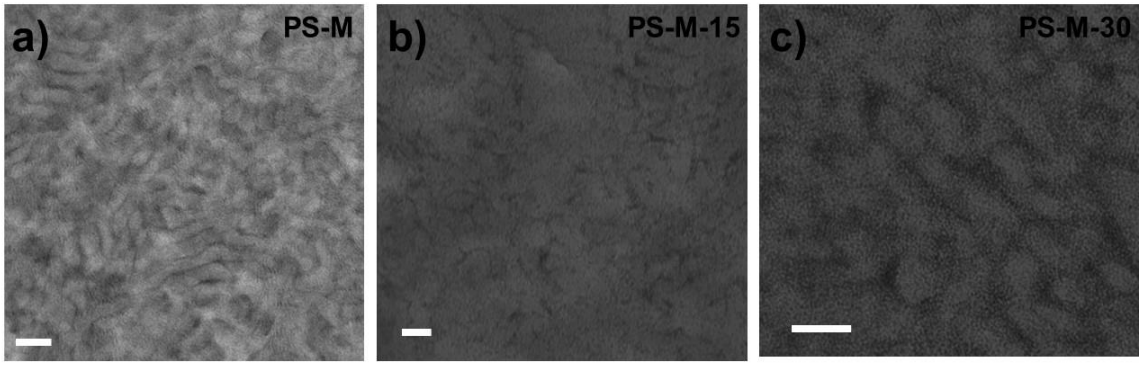

Figure 5.5 Assorted TEMs PS-*b*-PEO from cryomicrotomed slices **(a)** PS-*M* **(b)** PS-*M*-15 and **(c)** PS-*M*-30. All scale bars are 100 nm.

The PtBA-*b*-PEO templates successfully assembled the ZrO_2 NPs into well-ordered nanocomposites with tunable photonic properties as described in previous work.[1] Here, we investigate the co-assembly of this system over a range of N_{bb} and determine the temperature dependent phase behavior. The PtBA-*b*-PEO series of composites were prepared through identical procedures and characterized by SAXS. Figure 5.6 shows the spectra for PtBA-*S*, PtBA-*M*, and PtBA-*L* with NP loadings of 0, 15, and 30 wt.% respectively. All neat BBCP samples (0 wt.%) assemble into well-ordered lamellar morphologies. Multiple high order reflections are detected. The calculated domain spacing from q^* are: PtBA-*S* = 50.5 nm, PtBA-*M* = 75 nm and PtBA-*L* = 103.4 nm. In the PtBA-*b*-PEO series, microphase segregation and lamellar morphologies are generally preserved upon addition of NPs, unlike in the PS-*b*-PEO composites. NP scattering is observed in the high q regime, and the form factor peak is broad suggesting significant NP dispersion. q^* remains sharp up to 30 wt.% NP in PtBA-*M* and PtBA-*L* and shifts to lower q (i.e. increasing d_0). The detection of high order scattering peaks in the composite spectra suggests that NPs co-assemble into the microphase separated BBCP template, consistent with previous investigations of ZrO_2 self-assembly with PtBA-*b*-PEO BBCPs.[1,4]

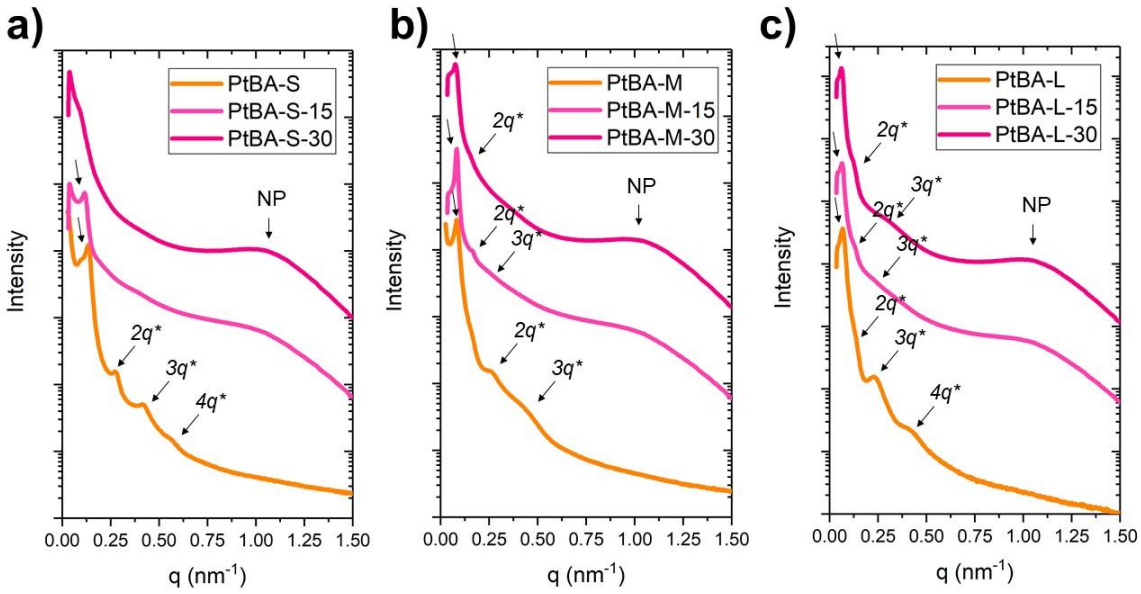

Figure 5.6 Room Temperature SAXS of PtBA-*b*-PEO series after drop casting and thermal annealing. **(a)** PtBA-*S*, PtBA-*S*-15 and PtBA-*S*-30 **(b)** PtBA-*M*, PtBA-*M*-15 and PtBA-*M*-30 **(c)** PtBA-*L*, PtBA-*L*-15 and PtBA-*L*-30

TEM micrographs of PtBA-*b*-PEO composites were prepared by identical experimental procedures and are presented in Figure 5.7. Again, neat BBCP samples were stained while composites were left unstained. Here, the selectively assembly of NPs into the PEO domain is much cleared than in the PS-*b*-PEO template, resulting in significant contrast between the filled and unfilled domains. Well-ordered lamellae are observed at both 15 wt.% and 30 wt.% NP loading (Figure 5.7b and Figure 5.7c respectively), suggesting high NP concentrations can be accommodated with the PtBA-*b*-PEO template. The domain spacings are consistent with those determined from SAXS. In PtBA-*M*, d_0 was found to increase with increasing NP content (from d_0 = 75 nm to d_0 = 83 nm at 30 wt.% loading). The specific location of NPs within the microphase separated domain is of interest (uniformly dispersed, segregated at interface, or segregated at the center of the domain).[14] The TEM micrographs show that the NPs are dispersed homogeneously throughout the PEO domain, with no apparent preference to assembling at the interface or

the center of the domain. The improved co-assembly in the PtBA-*b*-PEO template is consistent with previous results and likely due to several changes to the architectural design of the BBCP. The comparison with the PS-*b*-PEO BBCP will be discussed in the Discussion (Section 5.4).

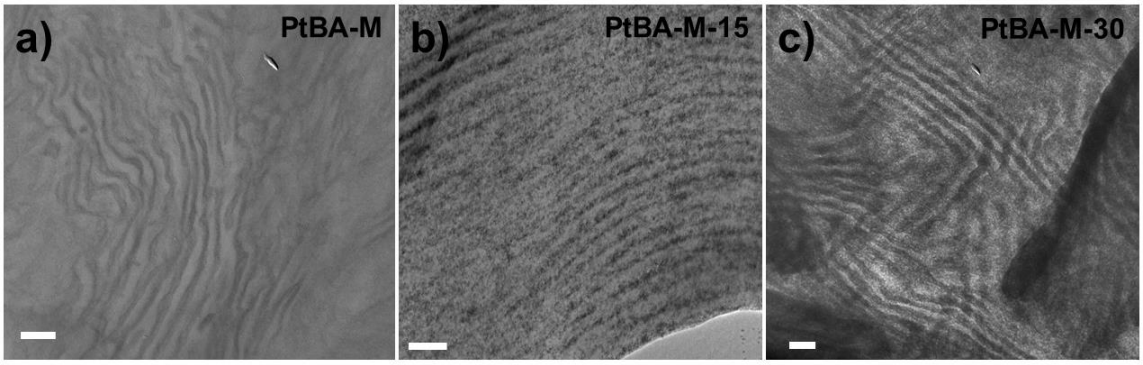

Figure 5.7 Assorted TEMs PtBA-*b*-PEO from cryomicrotomed slices **(a)** PtBA-*M* **(b)** PtBA-*M*-15 and **(c)** PtBA-*M*-30. All scale bars are 100 nm.

5.3.3 Phase Transitions Investigated by in-situ SAXS

Temperature dependent phase transitions were determined by in-situ temperature SAXS of bulk NP/BBCP composites. As previously described, samples were prepared in a metal washer, sandwiched with Kapton tape and secured to a thermal heating stage at Beamline 11-BM. The samples were heated from room temperature to T = 200 °C at a constant ramp rate of 0.5 °C/min and continuously measured in both SAXS and WAXS regimes. 2-D scattering patterns were converted to 1-D scattering spectra at temperature intervals of ~ 3°C. Phase transitions were determined by analyzing plots of 1-D scattering spectra (Scattering intensity (I) versus scattering vector (q)) versus temperature (T) on an x-y-z waterfall plot. Results for the PS-*b*-PEO composites are plotted in Figure 5.8, 5.9, and 5.10 for PS-*S*, PS-*M*, and PS-*L* respectively. Microphase separation, indicated by the presence of primary scattering peak q^*, is consistent with the results from Figure 5.4. The neat BBCPs exhibit strong microphase segregation and lamellar morphology. Upon

heating, the intensity of q^* decreases at the PEO melting temperature ($T_m \approx 60$ °C), consistent with trends outlined in Chapter 3 regarding phase transitions in PS-*b*-PEO BBCPs of asymmetric molecular shape. In general, the high order reflections also disappear beyond T_m, suggesting a transition to a disordered morphology in the melt. Melting transition in PS-*L* (Figure 5.10a) is highlighted by an evolution in the PEO crystalline peak at $q = 0.4$ nm^{-1}. The peak shifts to lower q upon the approach to T_m and begins to broaden before eventually disappearing.

The addition of NPs appears to disrupt ordering and self-assembly in the PS-*b*-PEO template according to room temperature SAXS and TEM analysis of the PS-*S*, PS-*M*, and PS-*L* composites. Therefore, we should not expect any temperature induced ODT in the microphase morphology as the structure is initially disordered. However, the NPs are dispersed within the polymer matrix through targeted intermolecular interactions (hydrogen bonding). The strength and lifetime of the interactions, as well as the polymer chain dynamics, are inherently temperature dependent (as described in Chapter 1). While a typical ODT associated with BCP microphase separation is not expected, other transitions in the NP dispersion or structure may be resolved. Upon heating through the temperature ramp, the spectra do not change qualitatively across all PS-*b*-PEO templates and NP loadings. In Figure 5.8b and 5.8c, the spectra are remarkable static, especially in the high q regime where the NP form factor is resolved. The NP size, shape, and dispersion does not change throughout the heating ramp, suggesting thermal stability of ZrO_2 in the BBCP matrix. Only PS-*L* was able to accommodate loading of NPs up to 30 wt.% and exhibited signatures of microphase separation, yet the structure was primarily disordered. In both PS-*L*-15 and PS-*L*-30, the position and peak width of q^* does not shift with increasing

temperature. However, there is a slight decrease in $I(q^*)$ at the PEO melting transition in PS-*L*-15, which is attributed to the melting of any remaining PEO crystals. Overall, the NPs appear to stabilize the morphology that is initially formed and present at room temperature. While we hypothesize hydrogen bonding becomes energetically weaker at higher temperatures, any additional dispersion of NPs or phase transitions are surprisingly suppressed. Observation of the phase behavior during subsequent cooling is of interest to understand the reversibility of structure. Characterization of the samples cooling down from T = 200 °C back to room temperature was attempted, but insufficient data was collected due to various experimental artifacts relating to sample integrity and defect formation. Under high vacuum and temperature, the neat BBCPs are highly viscous, and can be "sucked out" of the mold if the Kapton seal is not maintained. In many cases, voids caused by the air bubbles interfered with the scattering signal, resulting in inconclusive 2-D patterns. We found that most of the NP composites did not flow out of the mold, but bubbles and voids were introduced during the cooling ramp and convoluted the data.

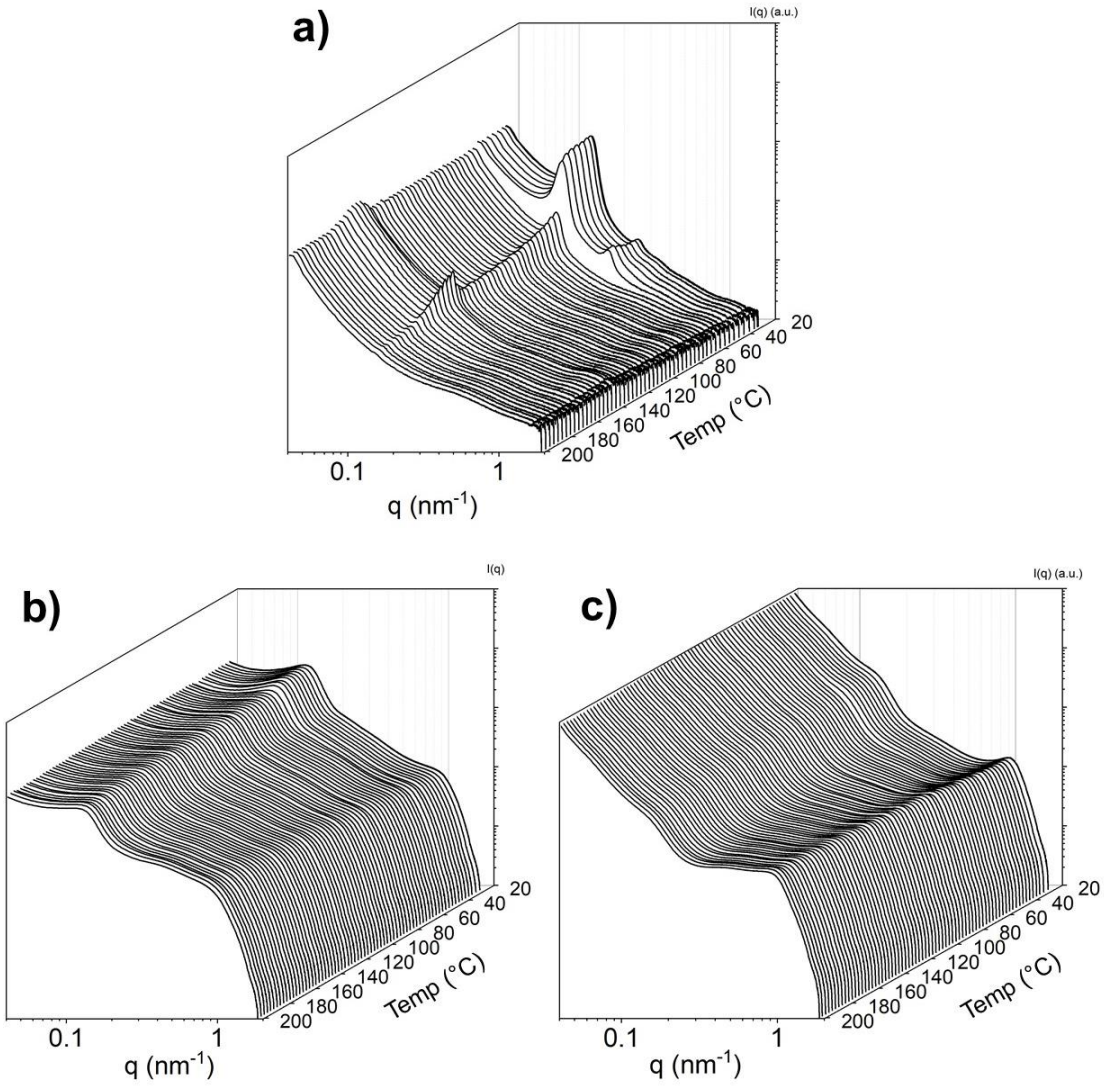

Figure 5.8 Temperature Sweep SAXS of PS-*b*-PEO *S* series represented as plots of *I(q)* versus *T* from *T* = 30 – 200 °C at constant heating rate of 0.5 °C/min **(a)** PS-*S* **(b)** PS-*S*-15 and **(c)** PS-*S*-30

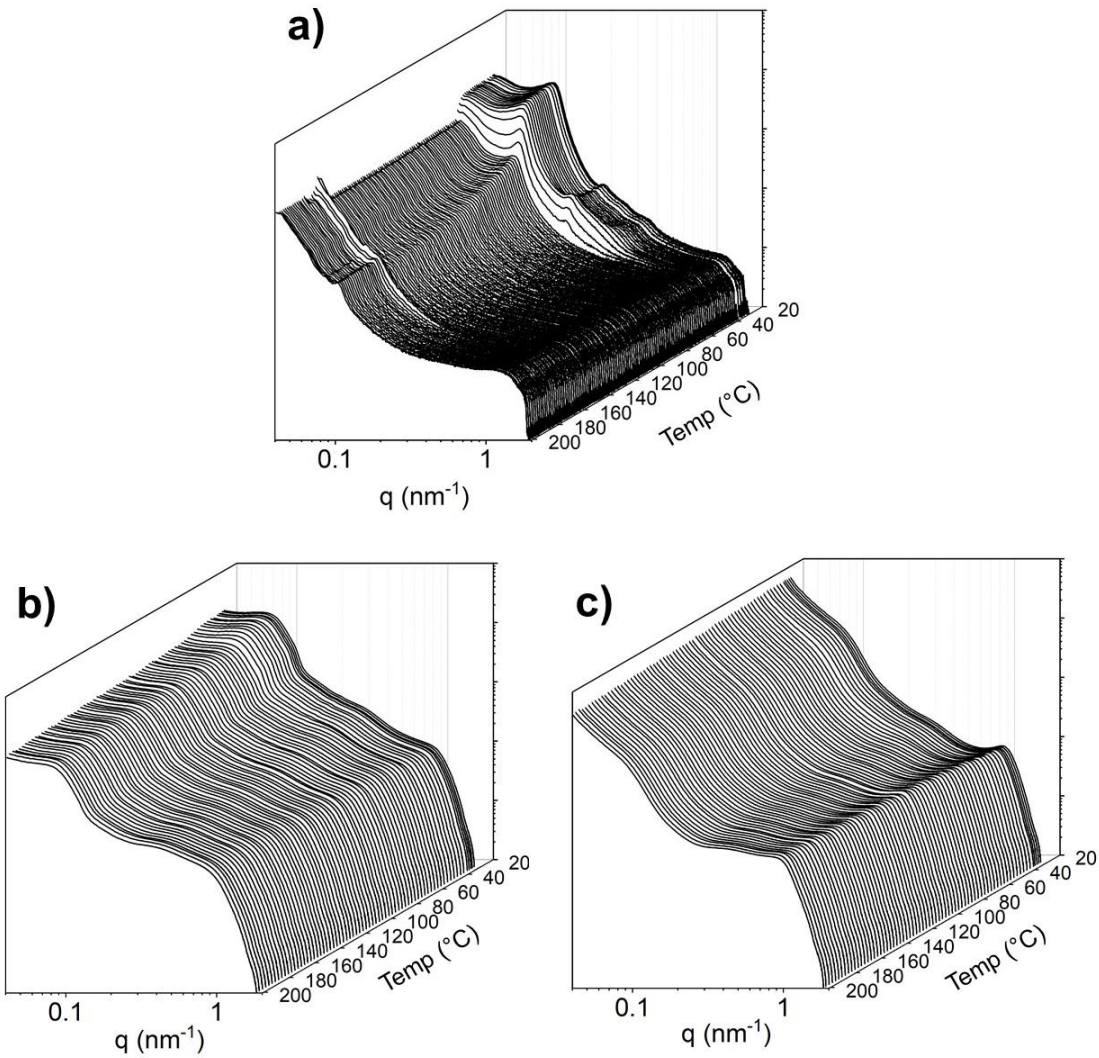

Figure 5.9 Temperature Sweep SAXS of PS-*b*-PEO *M* series represented as plots of *I(q)* versus *T* from *T* = 30 – 200 °C at constant heating rate of 0.5 °C/min **(a)** PS-*M* **(b)** PS-*M* -15 and **(c)** PS-*M* -30

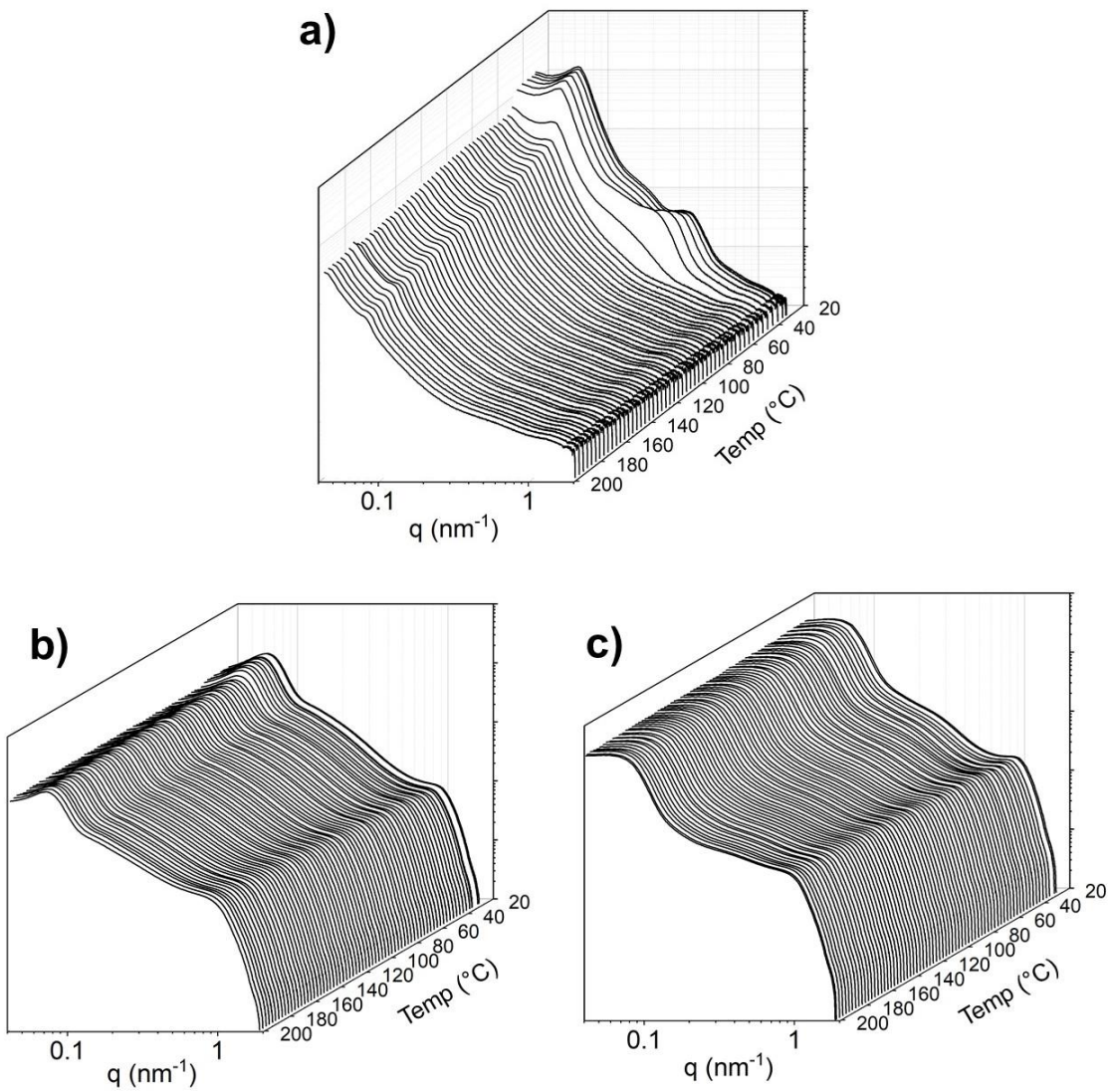

Figure 5.10 Temperature Sweep SAXS of PS-*b*-PEO *L* series represented as plots of *I(q)* versus *T* from *T* = 30 – 200 °C at constant heating rate of 0.5 °C/min **(a)** PS-*L* **(b)** PS-*L*-15 and **(c)** PS-*L*-30

We expect distinct phase transitions in the PtBA-*b*-PEO composite systems due to the improved NP co-assembly compared to the PS-*b*-PEO template. Analogous plots of *I* versus *q* versus *T* are plotted in Figure 5.11, 5.12, and 5.13 for PtBA-*S*, PtBA-*M*, and PtBA-*L* respectively. Again, microphase separation within the neat BBCP persists throughout the experimental temperature range. The PEO melting transition is universally observed over the three neat samples (PtBA-*S*, PtBA-*M*, and PtBA-*L*). The existence of high order peak

3q* in the melt is evidence of some residual long-range order of the lamellar morphology, suggesting an extended percolation of structure when compared to the fully disordered melt state of the PS-*b*-PEO BBCPs. The persistence of high order peaks after the melting transition appears to be unique to the PtBA system, possibly due to the lamellar asymmetry or the conformation of PtBA side chains in the melt. The disappearance of the even order peaks (exclusively) suggests that the lamellar structure is much more symmetric (i.e. equal domain thicknesses) in the melt state.[15] However, it is unlikely that the domains spatially reorder or swell in size as d_0 does not change significantly after the melting transition. Some of the spectra at high temperature appear noisy or inconsistent with the progression of structure. For example, in Figure 5.11a, the spectra at T = 100 °C does not display a strong q*, but the scattering signal returns at T = 120 °C and continues to fluctuate until it is completely lost at T = 170 °C. These abnormal trends are attributed to the formation of bubbles in the melt that interfere with scattering from BBCP structure. Measurements were repeated several times, but the bubble formation was persistent. Securing and properly sealing the sample is necessary to prevent experimental artifacts in future experiments.

Despite the observed abnormalities, qualitative and quantitative phase behavior trends are analyzed and discussed. The persistence of q* is also observed up to T = 200 °C across all composite samples. The decrease in the scattering intensity beyond the melting transition is reduced significantly with increased NP loading, for example in Figure 5.12 (PtBA-*M*) and Figure 5.13 (PtBA-*L*). The decrease is due to a change in the electron density difference between the amorphous and crystalline PEO, as was described earlier for the PS-*b*-PEO materials. The initial morphology and structure of the composites are static

across the temperature range when compared to the neat BBCP samples, also consistent with observations of the PS-*b*-PEO samples.

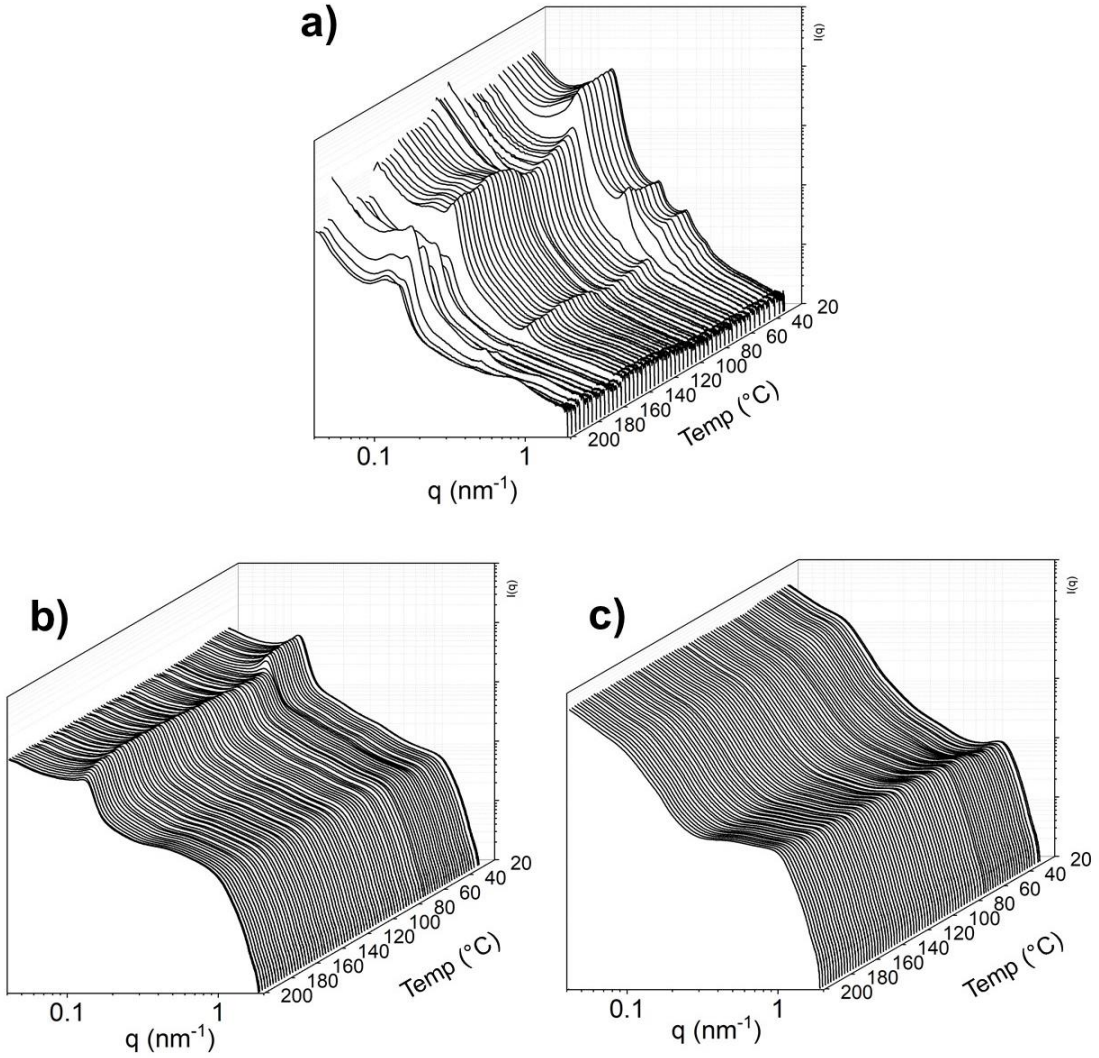

Figure 5.11 Temperature Sweep SAXS of PtBA-*b*-PEO *S* series represented as plots of *I(q)* versus *T* from *T* = 30 – 200 °C at constant heating rate of 0.5 °C/min **(a)** PtBA-*S* **(b)** PtBA-*S*-15 and **(c)** PtBA-*S*-30

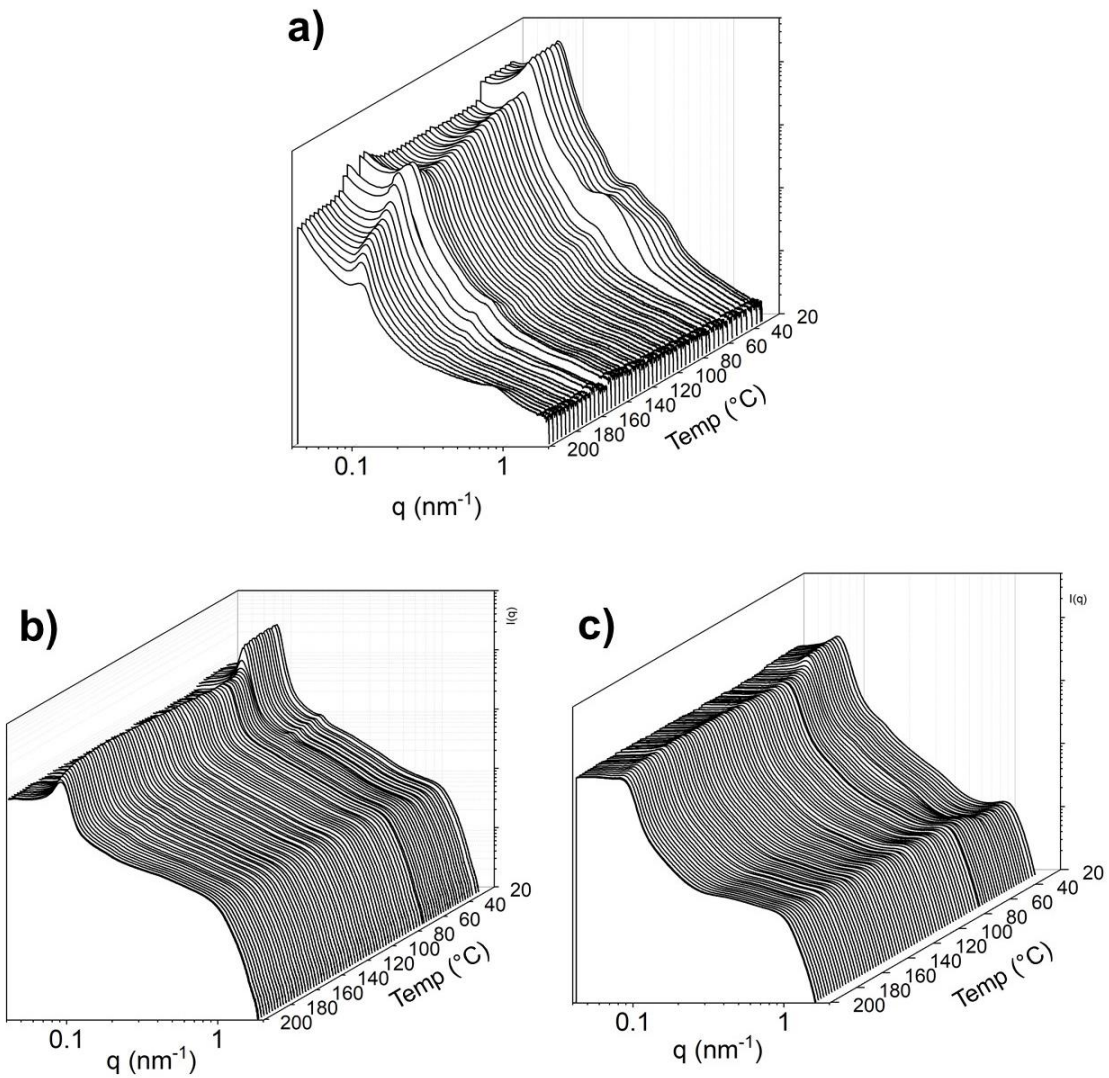

Figure 5.12 Temperature Sweep SAXS of PtBA-*b*-PEO *M* series represented as plots of *I(q)* versus *T* from *T* = 30 – 200 °C at constant heating rate of 0.5 °C/min **(a)** PtBA-*M* **(b)** PtBA-*M*-15 and **(c)** PtBA-*M*-30

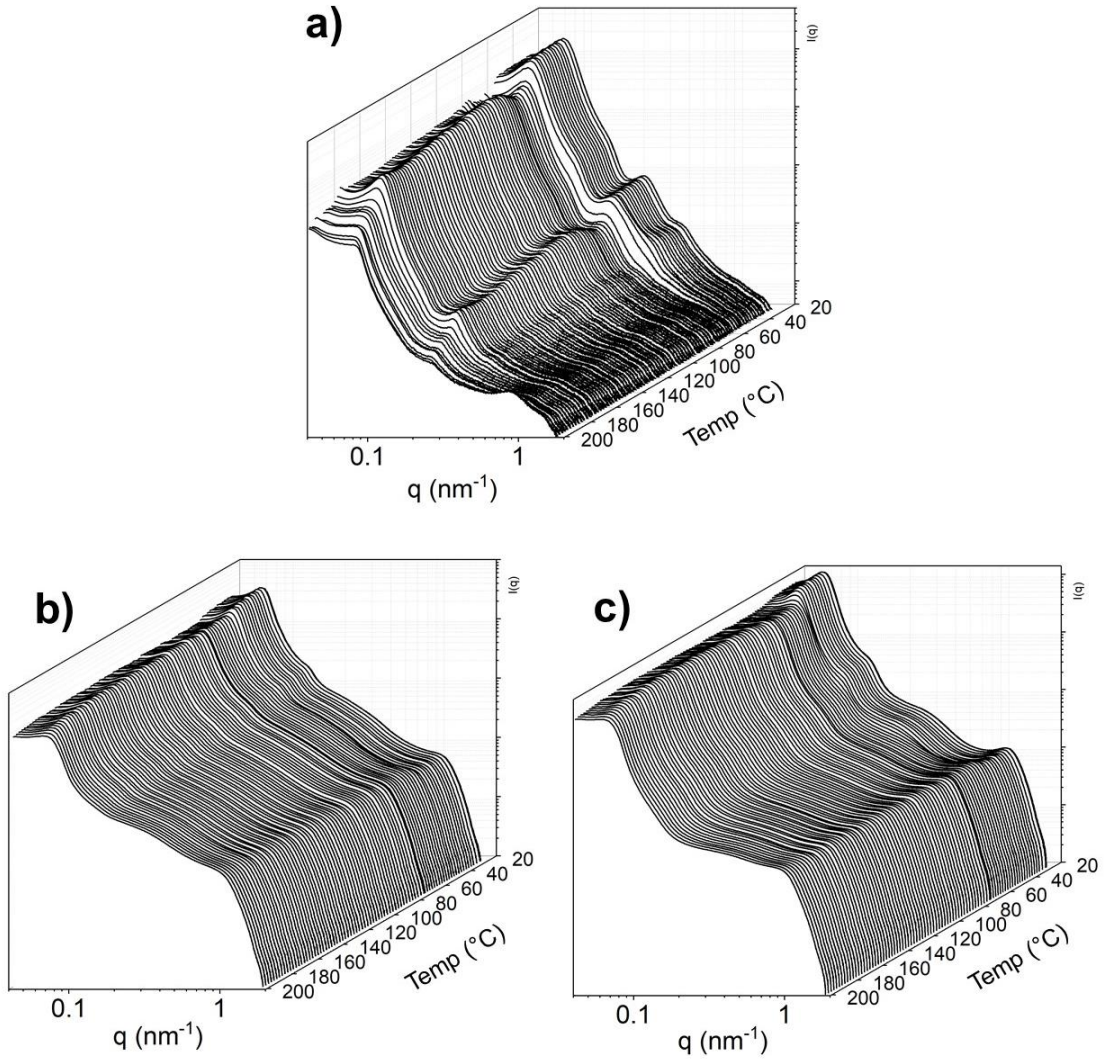

Figure 5.13 Temperature Sweep SAXS of PtBA-*b*-PEO *L* series represented as plots of *I(q)* versus *T* from *T* = 30 – 200 °C at constant heating rate of 0.5 °C/min **(a)** PtBA-*L* **(b)** PtBA-*L*-15 and **(c)** PtBA-*L*-30

5.3.4 Effect of NP Loading on Viscoelasticity of PtBA-*b*-PEO BBCP

The investigation and determination of morphology and phase transitions in model NP/BBCP composites reveals that the PtBA-*b*-PEO is a superior template for the directed assembly of surface modified ZrO_2. As previously discussed, the thermorheological properties are of significant interest in these well-defined NP/BBCP systems. Therefore, we exclusively consider the PtBA-*b*-PEO template for rheological studies. Addition

samples were prepared with NP loadings of 10, 20, and 30 wt.% in PtBA-*M*. The morphology is summarized in Figure 5.14. Overall, the results are consistent with findings in Section 5.3.2. Log-log plots of scattering intensity I vs. scattering vector (q) (Figure 5.14a) indicate microphase segregation due to chemically dissimilar blocks in all samples. The ratio of high order reflection peak positions to q^* reveals lamellar morphology with a d_0 = 75.7 nm for the neat BBCP. In the composites, the form factor is clear at high q and the intensity increases with NP loading. Identification of high order reflections suggests that the lamellar morphology is preserved after NP addition. d_0 varies significantly with NP loading, from d_0 = 76.6 nm at 10 wt.%, d_0 = 72.2 nm at 20 wt.%, and increasing to d_0 = 82.5 nm at 30 wt.%. The decrease in d_0 at 20 wt.% and subsequent increase at higher loading was not observed in the previous series of samples but is consistent within our understanding of the strong microphase segregation. An increase in phase segregation strength and sharpening of the interface shrinks the apparent lamellar thickness despite the change in overall volume fraction between each domain.[16]

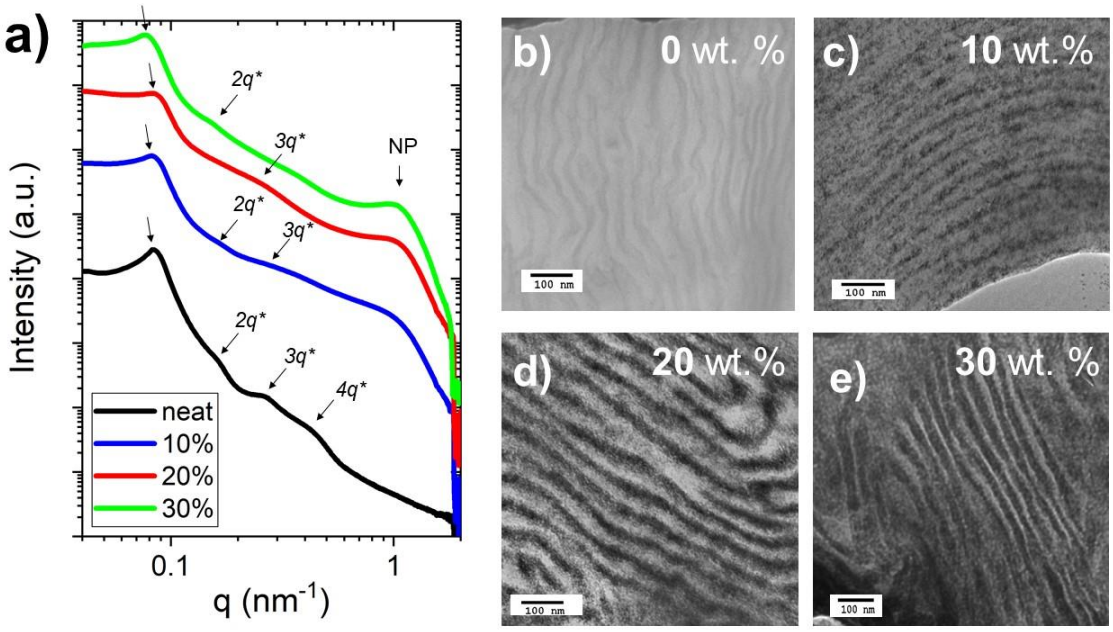

Figure 5.14 (a) Small angle X-ray scattering (SAXS) of PtBA-*b*-PEO BBCP (PtBA-*M*) and composites with various loading of ZrO_2 NP. Spectra are at T = 25 °C. **(b-e)** Transmission electron microscopy images of cryomicrotomed composite samples

The NPs selectively assemble into the PEO domain due to the hydrogen bonding, which results in significant contrast between the filled and unfilled domain. Well-ordered lamellae are observed in TEM (Figure 5.14b-e). The domain spacings appear to be consistent with those determined from SAXS. Again, the NPs are dispersed homogeneously throughout the PEO domain, with no apparent preference to assembling at the interface or the center of the domain.

Separate melt pressed samples were heated from T = 25 to 150 °C as SAXS patterns were continuously collected (Figure 5.15). Results are consistent with those in Figure 5.12. Microphase separation within the neat BBCP persists throughout the experimental temperature range (up to T = 150 °C). The behavior of the 10 wt.% sample is comparable with 15 wt.%, suggesting the stabilization of the lamellae could be achieved with a lower concentration of NP. The drop in $I(q^*)$ at T_m of PEO crystals is clear at 0 and 10 wt.% and reduced significantly at 20 and 30 wt.% loading.

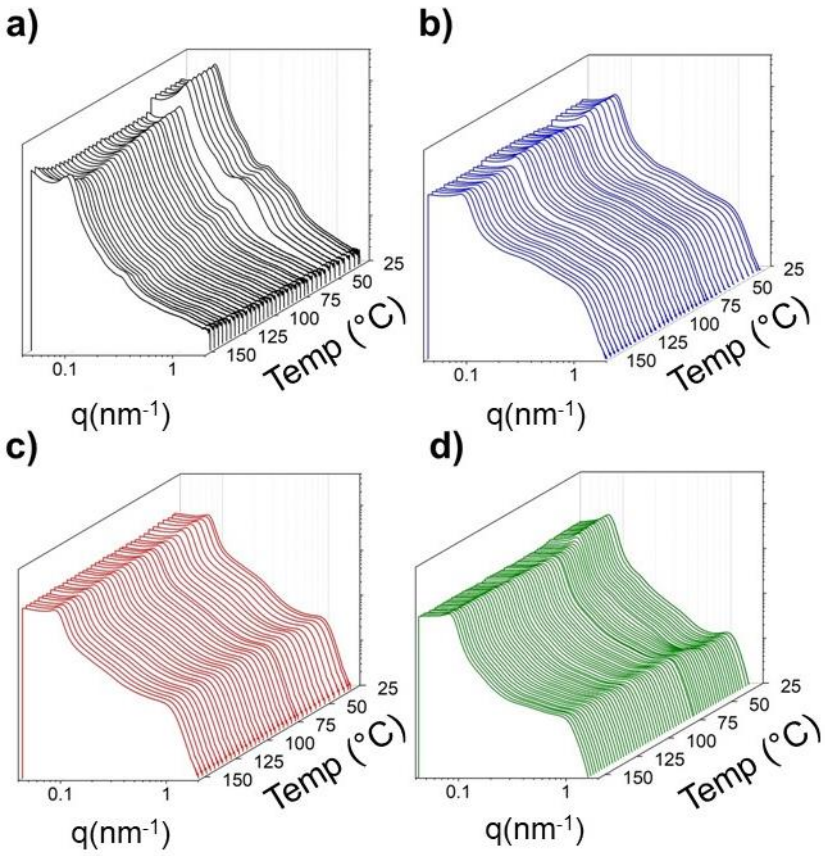

Figure 5.15 Log-log spectra of in-situ temperature controlled SAXS of PtBA-*M* represented as plots of *I(q)* versus *T* from *T* = 30 – 150 °C at constant heating rate of 0.5 °C/min **(a)** 0 wt.% **(b)** 10 wt.% **(c)** 20 wt.% and **(d)** 30 wt.% NP

Differential scanning calorimetry (DSC) is used to further determine the impact of NP addition on the melting and crystallization of PEO side chains. We quantify the degree of crystallinity in the composites to describe the origins of the decrease in *I(q*).* Crystallinity suppression is also a measure of the favorable enthalpic interactions between the NP and PEO.[16,17] Endothermic and exothermic events are observed upon heating and cooling respectively (Figure 5.16). The position of the endothermic peak corresponding to the PEO melting is reduced with increasing NP loading, which means that T_m is depressed from T_m = 55 °C at 0 wt.% to T_m = 50 °C at 30 wt.%. The recrystallization (exothermic peak upon cooling) is also significantly depressed from T_c = 35 °C at 0 wt.% to T_c = 10 °C at 30

wt.%, suggesting the NPs significantly inhibit crystallization of the side chains when cooling from the melt. The normalized percent crystallinity is calculated from the heat of melting (ΔH_m) using the same formalism proposed in Chapter 2 (Section 2.3.1). The PEO crystallinity is linearly suppressed with NP loading down to $X = 0.62$ at 30 wt.%, which is significant and consistent with the SAXS measurements. For context, the crystallinity with respect to total mass of PEO in the 30 wt.% sample is $X = 0.3$ (compared to $X = 0.5$ for neat PtBA-*M*).

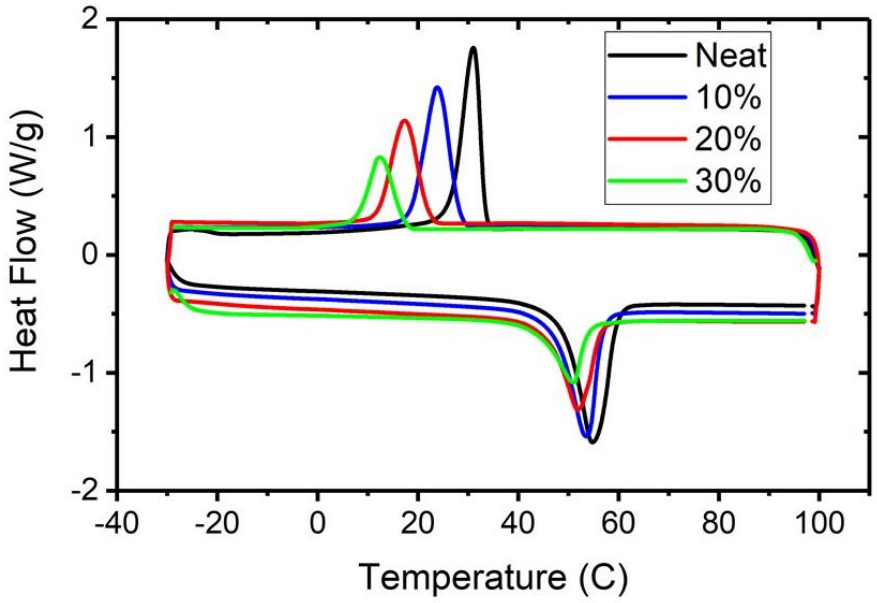

Figure 5.16 DSC curves of composites with various NP loading with a heating and cooling rate of 10 °C/min. A normalized percent crystallinity per gram of PEO is calculated where $X = 1$ for the neat BBCP (0 wt.% NP). $X_{10\%} = 0.88$, $X_{20\%} = 0.76$ and $X_{30\%} = 0.62$.

After full characterization of the morphological thermal transitions, the rheological properties of each composite were determined by small amplitude oscillatory shear with a parallel plate geometry. Storage modulus $G'(\omega)$ and loss modulus $G''(\omega)$ were measured by frequency sweeps at applied strain within the linear viscoelastic limit from $\omega = 1$ -100 rad/s over a temperature range from $T = 50 – 150$ °C (at 10 °C intervals). The

time−temperature superposition (tTS) principle was found to apply over the entire temperature range. Figure 5.17a shows master curves of *G'* and *G"* versus shifted frequency ($a_T\omega$) at a reference temperature of T_{ref} = 50 °C. Master curves are shifted in Figure 5.17a by an additional vertical shift factor *A* for clarity. Shift factors a_T are generally independent of NP loading (Figure 5.18). The dynamic response of the neat PtBA-*M* is consistent and comparable with results in Chapter 3 and Chapter 4, notably the viscously dominated behavior across a wide frequency window and critical gel-like power law scaling ($G'(\omega) \sim G''(\omega) \sim \omega^{0.7}$) at low frequency ($a_T\omega < 10^{-3}$ rad/s).[18] The addition of NPs significantly impacts the classical relaxation response, especially at low frequency. With just 10 wt.% of NP, the overall magnitude of both $G'(\omega)$ and $G''(\omega)$ increases as well as the power law scaling exponent. A crossover from viscously dominated to elastically dominated ($G' > G''$) behavior is clearly observed in the intermediate frequency regime ($a_T\omega \sim 10^{-2}$ rad/s) at a loading of 10 wt.%, followed by a full crossover at 20 wt.% ($G' > G''$ over the remaining range of accessible ω). The viscoelastic transition is clearly depicted in Figure 5.17b, where the dynamic data from the master curve is plotted in the form of complex viscosity (η^*) versus complex modulus (G^*).[19] To reiterate, the power law scaling in this plot describes the liquid−solid characteristic, in which small negative slopes (horizontal) correspond to liquid-like behavior and larger negative slopes (vertical) correspond to solid-like behavior. Distinct sequential relaxation patterns in the neat sample begin to merge into one single, solid-like response upon loading up to 30 wt.%. The transition reveals that the composites develop a structural mechanism to support more stress across the experimental frequency range with increasing NP loading.

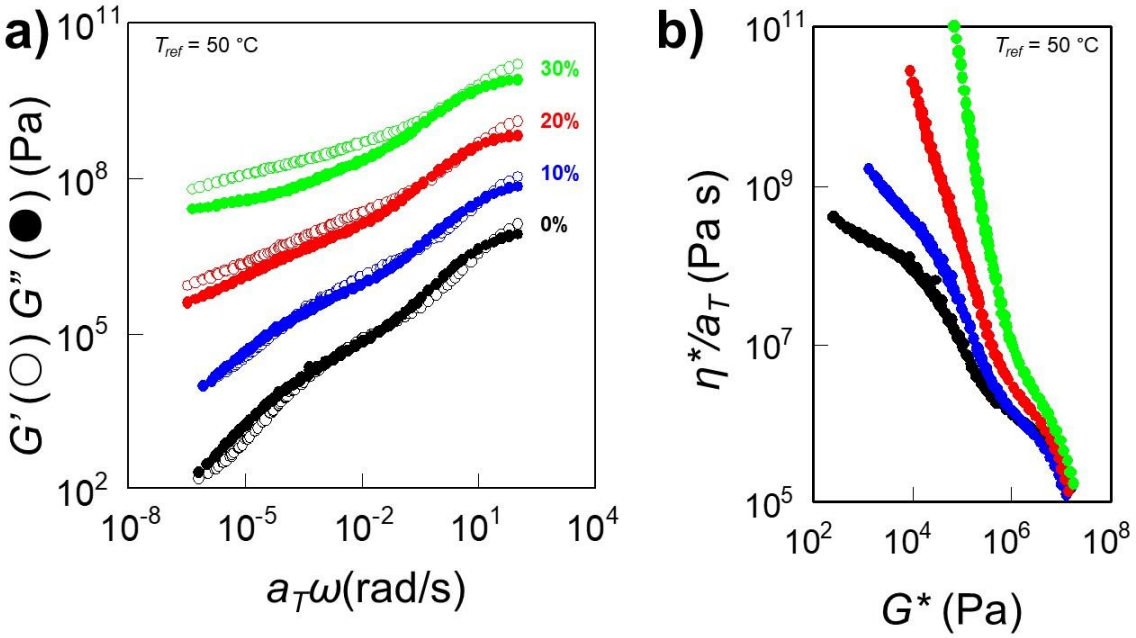

Figure 5.17 (a) Master curves of *G'* and *G"* of BBCPs and composites. Additional vertical shift factor *A* applied: 10 wt.% x10^1, 20 wt.% x10^2, 30 wt.% x10^3 **(b)** Winter plot (η^* vs *G**) of BBCP composites at T_{ref} = 50 °C using master curve data.

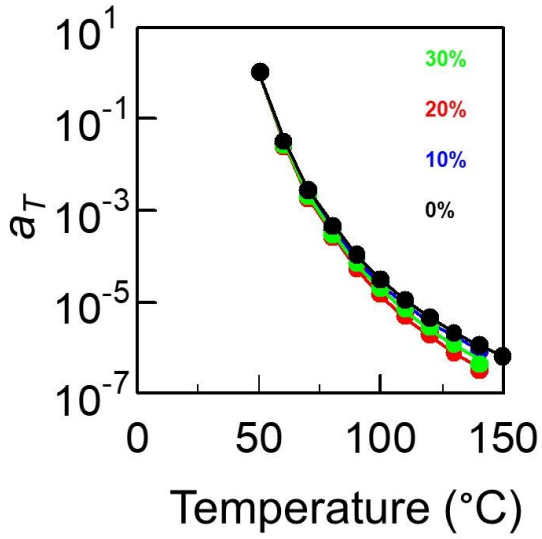

Figure 5.18 Shift factors a_T determined for time-temperature superposition at T_{ref} = 50 °C. Line shows fit to WLF equation.

The evolution in viscoelasticity with NP loading is further described by analysis of the relaxation time spectrum *H(τ)*, which represents the relaxation and rearrangement of macroscopic structures in time.[20] *H(τ)* is directly calculated from the dynamic data according to approaches established by Baumgaertel et al.[21] In Figure 5.19, each spectrum

decays monotonically with time, and various power law scaling regimes are identified. We utilize our analytical approach from Section 3.3.6, where the dual power law expression (Eq. 3.2) is now used model the full dynamic behavior of the NP/BBCP composites from $0 < \tau < \tau_{max}$. The dual model utilizes a linear superposition of two power law functions to describe relaxation processes on short and longtime scales respectively. The calculated spectra were individually fit to the model (fitting parameters are reported in Table 5.4). Here, we define a cutoff at $\tau_{max} = 10^8$ s and apply the third term H_0 to accommodate for the shift in scaling at low ω. We previously set $H_0 \sim 0$ for the neat BBCPs which were viscous at low ω and did not show any signatures of a plateau in *G'*. However, we find that for the composites, a non-zero H_0 and a longtime cutoff in $H(\tau)$ is necessary to model the material behavior at long relaxation times. After fitting the data, we find that power law scaling on both short (n_1) and long (n_2) timescales increases with NP loading. Exponent at short time scales increases slightly while the scaling at longer times increases significantly (from $n_2 = 0.83$ at 0 wt.% to $n_2 = 0.34$ at 30 wt.%). The trend suggests the self-similar relaxations transition towards the solid limit on both short and long-time scales (in the context of $n = 0$ for a Hookean solid). While the composites with 10 wt.% and 20 wt.% still show the dual relaxation features, the response at 30 wt.% appears solid-like over most timescales with a significant plateau extending to τ_{max}. Increased exponents in both n_1 and n_2 imply that the structure is changing across multiple length scales, and additional structural mechanisms are arising. A discussion of the NP impact on melt state morphology is necessary to describe the proposed phenomenon.

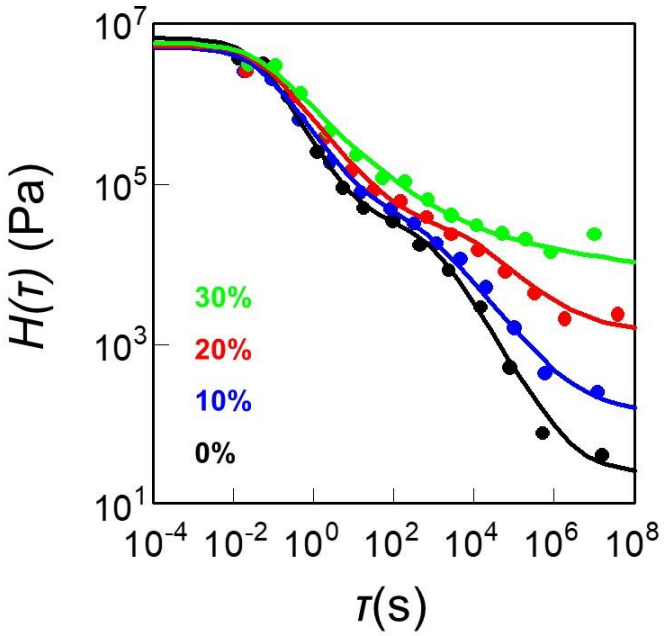

Figure 5.19 Relaxation time spectrum $H(\tau)$ calculated from master curves at T_{ref} = 50 °C according to Baumgaertel et al. Data points represent calculated spectra of each composite. Solid line is the fit to dual power law model (Eq. 3.2) (Fitting parameters in Table 5.4)

Table 5.4 Fitting parameters for dual power law function (Eq. 3.2)

NP loading	H_0 (Pa)	H_1 (Pa)	τ_1 (s)	n_1	H_2 (Pa)	τ_2 (s)	n_2
0 wt.%	$2.5\text{x}10^{1}$	$6.5\text{x}10^{6}$	$3.2\text{x}10^{-2}$	0.89	$3.1\text{x}10^{4}$	$6.3\text{x}10^{2}$	0.83
10 wt.%	$1.4\text{x}10^{2}$	$4.9\text{x}10^{6}$	$3.1\text{x}10^{-2}$	0.72	$3.3\text{x}10^{4}$	$4.4\text{x}10^{2}$	0.60
20 wt.%	$1.4\text{x}10^{3}$	$5.2\text{x}10^{6}$	$3.2\text{x}10^{-1}$	0.63	$2.5\text{x}10^{4}$	$6.4\text{x}10^{2}$	0.50
30 wt.%	$6.3\text{x}10^{3}$	$5.5\text{x}10^{6}$	$2.7\text{x}10^{-1}$	0.52	$2.9\text{x}10^{4}$	$3.1\text{x}10^{2}$	0.34

5.4 Discussion

Two families of amphiphilic BBCPs were used to direct the assembly of surface functionalized ZrO_2 NPs into lamellar morphologies across a range of different nanometer length scales. The temperature dependent phase behavior and rheological properties were investigated to gain a physical understanding of the impact of NPs on the unique structure-property relationships in BBCP melts. Densely grafted PS-*b*-PEO and PtBA-*b*-PEO were both used as templates for directed self-assembly with varying results. The PS-*b*-PEO BBCP morphology disordered upon the addition of NPs and did not exhibit any

temperature dependent phase transitions, while the PtBA-*b*-PEO template successfully incorporated up to 30 wt.% NP into the lamellar morphology which stabilized the microphase separated layers well into the melt state. There are several possibilities for the trend towards disordered morphology in the PS-*b*-PEO template. For example, the ratio d_{NP}/d_{PEO} ratio must be below a critical limit to prevent NP aggregation and expulsion from the microphase separated domain. However, the TEM image in Figure 5.5 provides critical evidence suggesting that the selectivity of the intermolecular interactions between the NP and the PEO side chains is not sufficient. While there are significantly darker regions with high concentration of NP (presumably the PEO domains), NPs are also dispersed within lighter contrast regions, suggesting that the particles are not assembled into the PEO domain exclusively. The main driving force for NP assembly is facilitated hydrogen bonding between the additional GA ligands and the PEO side chains. However, it is possible that interactions from the remaining original ligand preferentially associate with the PS domain (through π-π stacking or van der Waals). The NPs were originally dispersed in toluene, which is a non-polar solvent and a good solvent for PS. The competition between the favorable interactions with the PS side chains as well as PEO side chains may be driving the disruption of microphase segregation.

The improved co-assembly in the PtBA-*b*-PEO template is likely due to several changes to the architectural design of the BBCP. The first is due to the interactions between PtBA and the NP resulting from the original ligands, which appear to be less favorable than those present between the NP and PS side chains. Therefore, the selectivity of the NP towards the PEO domain is enhanced, resulting in improved assembly and the formation of ordered lamellar layers. The second consideration is due to the ratio d_{NP}/d_{PEO}. The neat

PtBA-*b*-PEO BBCP template forms more symmetric lamellae ($d_{PtBA} \sim d_{PEO}$) according TEM, resulting in a thicker PEO domain relative to a PS-*b*-PEO BBCP of comparable MW or d_0. Therefore, the ratio d_{NP}/d_{PEO} is decreased in PtBA-*b*-PEO with the same ZrO_2 NPs. The increased PEO domain thickness provides additional space, volumetric degrees of freedom, and reduces the entropic chain stretching cost for NP accommodation. As discussed in Chapter 3, the packing and assembly of densely grafted sidechains into lamellar layers is directly impacted by excluded volume effects due to steric repulsions of those sidechains.[22,23] We hypothesize the NPs are able to occupy the additional free volume in densely grafted brush systems, which facilitates the exceptionally high loading compared to LBCP systems. Despite this analysis, the structural packing model of the side chains in BBCPs is not well understood and certainly requires additional investigations.

Hydrogen bonding between NPs and the PEO side chain is considered the primary intermolecular interaction of interest when evaluating the temperature dependent phase behavior and rheological properties of the composites. As discussed in Chapter 2, strong hydrogen bonding is expected to suppress/eliminate crystallization in the PEO domain. Crystallinity suppression is resolved in the PtBA-*b*-PEO system, suggesting hydrogen bonding is active and sufficient, and will directly impact the thermostructural and thermorheological properties. In the absence of NP effects, evidence of PEO melting (sudden decrease in $I(q^*)$) is observed in all samples of 0 wt.% (PtBA-*S*, PtBA-*M*, and PtBA-*L*). However, the morphology of the NP composites is static across the experimental temperature range. The amount of crystalline PEO that melts is significantly reduced and the contribution to $I(q)$ is reduced so much that a transition cannot be resolved. The NPs stabilize the structure and remain assembled and dispersed within their respective domain

(whether that be the PEO domain in the well assembled PtBA-*b*-PEO system or both the PS and PEO domain in the disordered PS-*b*-PEO system). The suppression of any additional transition in microphase segregation could be expected due to the increase in χ resulting from the enthalpic contribution of the NP-PEO hydrogen bonding. The temperature dependent phase transitions are understood by considering the NP as a stabilizer of the lamellar structure.[24,25] In the absence of any enthalpic intermolecular interaction, the additional volume occupied by the NP decreases the conformational energy of the polymer chains (in this case the densely grafted side chains). As a result, there is a rise in the cost of extra elastic free energy within the domain and interfacial free energy at the domain interface.[25] We could expect the impact of NP addition in the BBCP materials to have a smaller effect on the entropic conformation loss compared to an analogous LBCP because there is significantly more free volume to occupy.[4] Intermolecular interactions suppress chain dynamics near the NP surface, which hinder interfacial fluctuations across the domain that accompany the disordering transition as the NPs crowd the interface. The lamellar morphology is persistent across all accessed NP loading. Extreme loading of 30 wt.% does not induce an order-order transition or severely impact the interfacial curvature. Despite the universal lamellar structure at all experimental loadings, the NP composites begin to develop an additionally structural mechanism that can sustain applied stress as evidenced by the subsequent rheological investigations. We propose that the high loading of NPs results in a physical crosslinking effect throughout the percolating lamellar domains.

The occurrence of power law relaxations in the dynamic data and in $H(\tau)$ is evaluated as a function of NP loading. The viscoelasticity of the PtBA-*b*-PEO composites

is compared to the rheological model proposed for densely grafted BBCPs in Chapter 3. To summarize, the relaxation processes on short time scales (in the first power law regime n_1) are rapid and generally described as critical-gel like, but far from the Hookean solid limit where $n = 0$. Here, the primary structural mechanism for relaxation is the cooperative movement of confined internal slip layers within each microphase separated domain, facilitated by a high density of free chain ends in the center of each layer. The side chains within each block are unentangled and fully relaxed in the melt, which allows the backbone segments to rapidly slide along each other, like relaxation processes identified in low MW, unentangled BCPs and liquid crystal assemblies.[26,27] The relaxation processes at longer times depend on the largest connected material structure that can still relax, implying the scaling of n_2 is governed by the long-range order of the morphology.[20] From the power law fits, n_1 clearly increases with increasing NP loading, implying the liquid layer becomes constrained with the addition of NPs and that the relaxations change over the same range of τ. As previously mentioned, the NPs occupy significant free volume in the PEO domain, which likely results in increase segmental friction as the PEO segments slide along each other in the melt.[4,7] The intermolecular interactions and entropic penalties associated with the NP sequestration further restrict the native relaxation of the PEO side chains. We propose that the relaxation in the short time regime is a convolution (or cooperative response) of both domains which becomes influenced by the stiff NP/PEO domain as NP loading increases. The viscoelasticity of the neat system is mostly dominated by the PtBA domain (the major phase by mass). Since the NPs are well segregated into the PEO domain, the native liquid layer relaxations in the PtBA domain are independent of the NP loading. Such a response is consistent with the temperature dependence of a_T being independent of

NP loading The NP loading does not impact the temperature dependence of the bulk relaxations which are mostly derived from PtBA content. The PEO side chains "lock up" from the intermolecular and topological constraints, producing a noticeable transition towards the solid limit. The dual model fits surprisingly well at 10 and 20 wt.%, so the sequential relaxation processes still dominate. Therefore, a "self-similar structure" analogy may still apply, or more generally, the characteristic BBCP relaxation processes are still expressed. Additionally, the impact of NPs on chains at the interface should be considered. χ_{eff} is increasing with NP addition which introduces additional stretching penalty on PtBA side chains as well as the PEO side chains. With a sharper interface, the side chains directly at the interface become constrained and elongated to satisfy the interfacial area, further restricting the relaxations resolved in the short time scales.[28]

The impact of NP loading is significant on longer timescales, quantified by the power law scaling of n_2. The physical crosslinking of coordinated hydrogen bonding interactions between the NP and PEO side chains produces a transition to solid-like behavior. The plateau modulus at long time scales (quantified by H_0) scales exponentially with NP loading. Higher NP content increases the percolation of such a network, pushing the response to the solid limit at 30 wt.%. The sequential power law relaxation characteristic of the neat BBCPs disappears at 30 wt.%. The response can be modeled with the dual power law, however the impact of the H_0 term significantly dominates across a wide range of τ. The regime of scale invariant relaxations shrinks, so the structural description used for the BBCP melts is not applicable as a larger sample spanning structure begins to dominate over the accessible time scales.

The strength and lifetime of the hydrogen bonding facilitating the assembly of the NPs is inversely related to temperature.[29] Surprisingly, any weakening of the hydrogen bonds does not soften the elastic modulus in the melt state. In a strongly segregated system, the hydrogen bonding may still be appreciably strong even at elevated temperatures in the melt.[30] Additional mechanisms associated with steric constraints, frictional effects, and NP-NP repulsive forces near the NP surface come into play, but are much more difficult to quantitatively evaluate exclusively from rheology in this material system.

The implications of the solid transition at longtime are rather important for the processing of BBCP nanocomposites, especially considering the advantage of rapid self-assembly in bottom up fabrication approaches such as solution processing or flow induced processing. The self-assembly dynamics of the composite structure should be restricted due to the physical crosslinking effect, possibly resulting in poor structures or kinetically trapped morphologies. However, well-ordered structures are still achieved after sufficient thermal annealing. We propose that there is significant molecular mobility overall within the PtBA domain, which rapidly relaxes through the liquid layer mechanism even with the addition of NPs to the system. Therefore, on short timescales the material is soft, viscous and relaxes rapidly. The solid like response is resolved over much longer time scales (~ 10^3 s at T = 50 °C). Long range order and large grains in microphase separated BBCP systems have been induced primarily by combined thermal and solvent annealing.[1,5,31] Significant structure development is likely formed during the drop-casting and solvent evaporation as well as during post thermal annealing. The solvent adds additional mobility to the polymer chains and screens the interactions between NPs and side chains.[31,32] In the current study, thermal annealing is used to apply uniform thermal history and control PEO

crystallization. Thermal annealing is more applicable to the melt rheological properties considering the absence of excess solvent in the system during rheological testing. After cooling down from the melt state, the percolating network of NP interactions restrict the high mobility of the PEO side chains and the temporally fluctuating microphase separated lamellae. Meanwhile, the rheological investigation reveals that the addition of NPs significantly increases the mechanical properties and the stiffness across the range of accessible timescales. BBCPs templates are often cited for their weak mechanical properties or softness.[33–35] The controlled assembly of NPs within the BBCP template can be used to tune and improve the stiffness and durability of these composites for a range of more demanding applications.

5.5 Conclusion & Future Directions

In conclusion, two amphiphilic BBCPs templates were used to direct the assembly of ZrO_2 NP into ordered lamellar nanostructures. PS-*b*-PEO and PtBA-*b*-PEO BBCP with densely grafted, unentangled side chains were synthesized over a range of backbone lengths (N_{bb}). In the PS-*b*-PEO systems, the lamellar morphology transitioned to a disordered structure upon the addition of NPs due to a combination of incompatibility between the length scales of the PEO domain thickness and the NP diameter, as well as competing intermolecular forces within each respective microphase separated domain. The PtBA-*b*-PEO template successfully incorporated up to 30 wt.% selectively in the PEO domain, consistent with previous investigations. The temperature dependent phase behavior was investigated with high throughput synchrotron SAXS. Despite the disordered morphology, the NPs were stable within the PS-*b*-PEO matrix and no clear transitions were observed in the NP size or distribution with increasing temperature. In the PtBA-*b*-PEO

system, the NPs appeared to stabilize the initial lamellar morphology well into the melt state.

The enhanced structure and co-assembly of the NPs with the PtBA-*b*-PEO BBCP was further investigated by determining the linear viscoelastic properties of ZrO_2/PtBA-*b*-PEO BBCP nanocomposites with SAOS rheology. The objective was to correlate the structure (at variable NPs loadings) to the dynamic relaxation processes unique to the BBCP architecture. The relaxation processes on short and long timescales transition from liquid to solid-like behavior according to power law scaling in the low frequency regime in master curves of *G'* and *G"* and analysis of the relaxation time spectrum $H(\tau)$. The dual power law model reveals a systematic increase in both scaling exponents n_1 and n_2. The progression from liquid-to-solid results primarily from the formation of sample spanning connectivity through the physical crosslinking between the NP surface and the PEO side chains. The highly desirable unentangled/liquid-like rheology characteristic of the BBCP architecture is significantly impacted by the addition of NPs and must be considered when developing processing techniques and optimizing mechanical properties.

The findings suggest that the mechanical properties of the composites can be manipulated by controlling the loading of functional additive, and that significant modification of the NP ligand is necessary to drive favorable intermolecular interactions. However, quantifying and isolating the origins of the important intermolecular interactions (i.e. hydrogen bonding) remained a challenge. The introduction of hydrogen bonding between GA on the NP surface and PEO side chains was successful and contributed to the co-assembly of a well-ordered composite. PEO crystallization was observed in the filled NP/PtBA-*b*-PEO system, but the impact of NP-NP repulsive forces and additional NP

induced frictional effects cannot be decoupled at this time. To isolate the effect of hydrogen bonding on the connection between the phase behavior and rheological properties, we must turn to the SM acid systems discussed in Chapter 2. For example, benzoic acid derivatives containing a defined number of hydrogen bonding moieties (-OH or -COOH functional groups). The advantage of using NPs is to obtain size dependent property enhancement and engineering utility. To conduct a systematic investigation of hydrogen bonding effects on physical crosslinked network formation in the composites, SM additives are advantageous. The SM acids emulate the intermolecular interactions introduced from the surface functionalized NPs but reduce the extent of additional attractive and repulsive forces such as those from the original NP ligands. There are self-associating hydrogen bonding effects between the SM functional groups to consider, as well as a tendency to crystallize. Larger SM crystals are broken up and suppressed during sample preparation by fully dissolving the SM in a favorable solvent (such as THF or DMF). The volume per mol of additive is much smaller than for the NPs which may reduce the entropic penalties in chain stretching while keeping the relative enthalpic contributions high. By adding in variable loading of SM additive with different number of moieties per molecule (from one to six), we can evaluate the trends in power law scaling and correlate the relationship between extent of hydrogen bonding and mechanical enhancement through physical crosslinking. At the solid limit, we expect the plateau modulus G_0 (the extrapolation of G' to low ω limit) to scale with the mol of hydrogen bonding groups and the strength of the interaction (-OH versus -COOH). Alternatively, the functionalized POSS additives discussed in Section 2.5 are desirable as a model material. The POSS cages are geometrically reminiscent of spherical NP but have a defined number of hydrogen bonding groups, important for quantifying the

impact of the favorable intermolecular interactions between the additive and the PEO side chains.

This chapter considers structure-property relationships in NP/BBCP composites in the ordered state after significant sample preparation and processing. There is considerable interest in understanding the dynamics of the self-assembly in the composites and evaluating the impact of NPs on structure development pathways. Rapid self-assembly of the neat BBCP templates from the disordered state has been described in recent publications.[2,36] Clear DOTs were observed within a few minutes of thermal annealing, characterized by SAXS. These two investigations propose that the reduced entanglements in densely grafted BBCP melts contribute to rapid self-assembly dynamics. Our rheological investigations reveal suppressed dynamics in the NP composites due to a physical crosslinking effect. Therefore, the timescales of structure development may be a function of NP loading. We proposed to investigate self-assembly dynamics in NP/BBCP composites experimentally using in-situ temperature controlled SAXS by resolving the structure transitions from the disordered state into the ordered state upon quenching from deep in the melt (T > 200 °C) to a thermal annealing temperature. The proposed transition pathway is fundamentally different from previous investigations, which accessed T_{DOT} from room temperature. The approach from the melt state is appropriate for practical processing methods such as flow and melt processing. Preliminary investigations were performed with PS-*S* samples using inhouse SAXS (Figure 5.20). At room temperature, microphase segregation is resolved and the MST is accessed by heating to T = 200 °C, at which point q^* disappears. After passing through the MST, the temperature control was turned off and the sample was quenched to room temperature. The microphase separation

and lamellar morphology returned upon reaching an equilibrium at T = 45 °C after 30 minutes of cooling, demonstrating the rapid self-assembly dynamics from deep in the melt state. Surprisingly, the grain size was improved according to the preferential alignment of the lamellar structure in the 2-D scattering patterns (Figure 5.20).

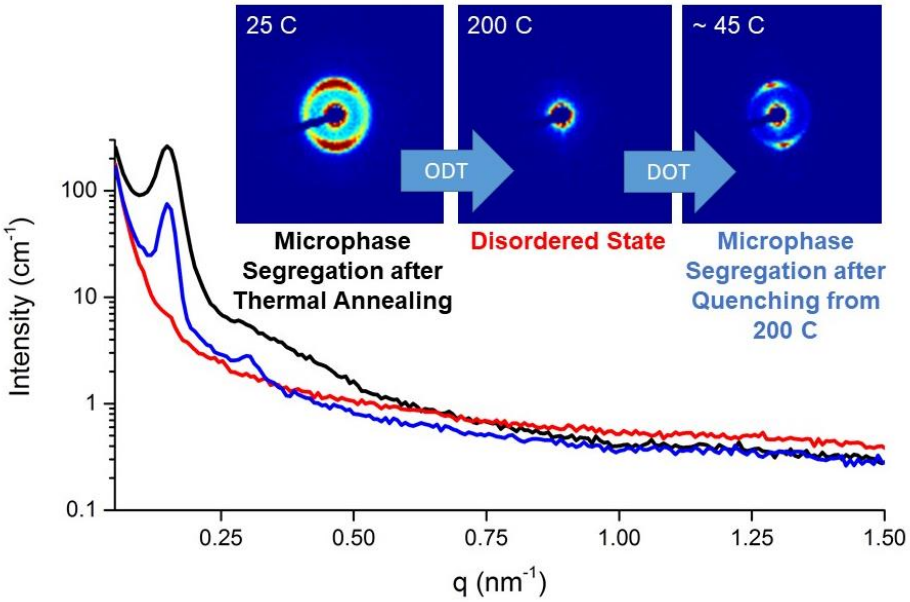

Figure 5.20 SAXS spectra of PS-*b*-PEO BBCP at various temperatures demonstrating rapid self-assembly. Microphase separated sample (black line) was heated from room temperature (T = 25 °C) to T = 200 °C (red line), as which the structure disordered and q^* disappeared. Structure rapidly reforms after quenching to T = 45 °C (blue line). Measurements performed on inhouse SAXS (SAXSLab Ganesha)

Unfortunately, the radiation source on the inhouse SAXS is not bright enough to collect meaningful time resolved measurements. The measurement is on the same order of timescale as the self-assembly. Therefore, we cannot extract information about the structure formation during the temperature quench or shortly after reaching thermal equilibrium (like the limitation of observing in-situ shear alignment, outlined in Section 4.5). Therefore, identical experiments were proposed to utilize high throughput synchrotron radiation and performed at NSLS-II. After measuring the temperature

dependent phase transitions (in Section 5.3.3), separate neat BBCP and NP/BBCP composites were heated from room temperature to T = 200 °C and rapidly quenched to various thermal annealing temperatures (T = 25 °C, 60 °C and 120 °C). Unfortunately, we could not observe any phase transitions during the quenches due to several factors. We soon found out that the morphology of the composites was static in the melt state up to 200 °C. Therefore, the DOT could not be induced up to the maximum temperature. Consequently, the static structure was present upon quenching to the thermal annealing temperature and did not appear to evolve any further with additional thermal annealing. We expected to see consistent results from the neat BBCPs samples that passed through the MST at T = 200 °C. However, significant bubble formation within the sample convoluted the scattering signal. Additionally, the temperature quench was not nearly rapid enough to collect true temperature independent measurements. A quench from T = 200 °C to T = 25 °C took 30 min, comparable with the inhouse set up. Within that time, non-isothermal ordering begins to occur, which is not accounted for in the final characterization. In the future, sample preparation and temperature control must be improved to accurately measure the dynamics of self-assembly in NP/BBCP composites in-situ. Another possible route would be to decouple structure formation from solvent annealing and thermal annealing. Here, in-situ structure formation would be resolved in thin films directly after drop casting with grazing incident SAXS (GI-SAXS). Experimentally, the sample chamber would be purged with a selective solvent for either the NP filled domain or the glassy domain for extended time while rapid SAXS spectra are collected. Additional work must be undertaken to understand structure orientation and surface interactions before committing to the dynamics of self-assembly in the thin film limit.

We planned to use the shear alignment procedure developed in Chapter 4 to process highly aligned NP/BBCP composites with large grain size. The objective was to enhance material properties by introducing additional alignment to the ordered lamellar layers. We concluded that the critical gel-like relaxation behavior on the longest time scales and high mobility of the morphology was crucial for obtaining high order parameters and global alignment over several millimeters. The NPs clearly shift the critical gel relaxations to the solid limit at 30 wt.% loading, undoubtingly inhibiting the lamellar structure from aligning through a defect-mediated relaxation process. On such a time scale, the percolation of the intermolecular interaction network becomes the dominating structure that responds to the stress. Therefore, the defects in lamellar order cannot be manipulated and reordered by the stress field at similar shearing conditions. To align structures of the highly filled NP composites, the interactions must be suppressed or screened during processing. Swelling the PEO domain with a selective solvent will screen the hydrogen bonding between GA and the PEO side chains. However, it will be difficult to control the saturated environment within the Linkam shear cell, so a new sample chamber must be developed. Considering the progression of the solid-like response at long time scales gradually with NP loading, alignment may be induced at lower NP content (~ 10 wt.%). A tradeoff between material property enhancement by NP content or structure alignment arises and could be optimized. A new systematic study would be undertaken to understand the non-linear shear deformation limits and effects in the NP/BBCP composites.

5.6 References

(1) Song, D.-P.; Li, C.; Li, W.; Watkins, J. J. Block Copolymer Nanocomposites with High Refractive Index Contrast for One-Step Photonics. *ACS Nano* **2016**, *10* (1), 1216–1223.

(2) Song, D.-P.; Li, C.; Colella, N. S.; Xie, W.; Li, S.; Lu, X.; Gido, S. P.; Lee, J.-H.;

Watkins, J. J. Large-Volume Self-Organization of Polymer/Nanoparticle Hybrids with Millimeter-Scale Grain Sizes Using Brush Block Copolymers. *J. Am. Chem. Soc.* **2015**, *137*, 12510–12513.

(3) Song, D.-P.; Shahin, S.; Xie, W.; Mehravar, S.; Liu, X.; Li, C.; Norwood, R. A.; Lee, J.-H.; Watkins, J. J. Directed Assembly of Quantum Dots Using Brush Block Copolymers for Well-Ordered Nonlinear Optical Nanocomposites. *Macromolecules* **2016**, *49* (14), 5068–5075.

(4) Song, D.-P.; Gai, Y.; Yavitt, B. M.; Ribbe, A.; Gido, S.; Watkins, J. J. Structural Diversity and Phase Behavior of Brush Block Copolymer Nanocomposites. *Macromolecules* **2016**, *49*, 6480–6488.

(5) Song, D.-P.; Li, C.; Colella, N. S.; Lu, X.; Lee, J.-H.; Watkins, J. J. Thermally Tunable Metallodielectric Photonic Crystals from the Self-Assembly of Brush Block Copolymers and Gold Nanoparticles. *Adv. Opt. Mater.* **2015**, *3* (9), 1169–1175.

(6) Song, D.-P.; Naik, A.; Li, S.; Ribbe, A.; Watkins, J. J. Rapid, Large-Area Synthesis of Hierarchical Nanoporous Silica Hybrid Films on Flexible Substrates. *J. Am. Chem. Soc.* **2016**, *138* (41), 13473–13476.

(7) Berriot, J.; Montes, H.; Lequeux, F.; Long, D.; Sotta, P. Evidence for the Shift of the Glass Transition near the Particles in Silica-Filled Elastomers. *Macromolecules* **2002**, *35* (26), 9756–9762.

(8) Gai, Y.; Song, D.-P.; Yavitt, B. M.; Watkins, J. J. Polystyrene- Block -Poly(Ethylene Oxide) Bottlebrush Block Copolymer Morphology Transitions: Influence of Side Chain Length and Volume Fraction. *Macromolecules* **2017**, *50*, 1503–1511.

(9) Buonsanti, R.; Pick, T. E.; Krins, N.; Richardson, T. J.; Helms, B. A.; Milliron, D. J. Assembly of Ligand-Stripped Nanocrystals into Precisely Controlled Mesoporous Architectures. *Nano Lett.* **2012**, *12* (7), 3872–3877.

(10) Bockstaller, M. R.; Mickiewicz, R. A.; Thomas, E. L. Block Copolymer Nanocomposites: Perspectives for Tailored Functional Materials. *Adv. Mater.* **2005**, *17* (11), 1331–1349.

(11) Genix, A.-C.; Oberdisse, J. Structure and Dynamics of Polymer Nanocomposites Studied by X-Ray and Neutron Scattering Techniques. *Curr. Opin. Colloid Interface Sci.* **2015**, *20* (4), 293–303.

(12) Chiu, J. J.; Kim, B. J.; Kramer, E. J.; Pine, D. J. Control of Nanoparticle Location in Block Copolymers. *J. Am. Chem. Soc.* **2005**, *127* (14), 5036–5037.

(13) Gai, Y.; Lin, Y.; Song, D.-P.; Yavitt, B. M.; Watkins, J. J. Strong Ligand–Block Copolymer Interactions for Incorporation of Relatively Large Nanoparticles in Ordered Composites. *Macromolecules* **2016**, *49* (9), 3352–3360.

(14) Chiu, J. J.; Kim, B. J.; Yi, G. R.; Bang, J.; Kramer, E. J.; Pine, D. J. Distribution of Nanoparticles in Lamellar Domains of Block Copolymers. *Macromolecules* **2007**, *40* (9), 3361–3365.

(15) Chang, A. B.; Lin, T.-P.; Thompson, N. B.; Luo, S.-X.; Liberman-Martin, A. L.; Chen, H.-Y.; Lee, B.; Grubbs, R. H. Design, Synthesis, and Self-Assembly of Polymers with Tailored Graft Distributions. *J. Am. Chem. Soc.* **2017**, *139* (48), 17683–17693.

(16) Lin, Y.; Daga, V. K.; Anderson, E. R.; Gido, S. P.; Watkins, J. J. Nanoparticle-Driven Assembly of Block Copolymers: A Simple Route to Ordered Hybrid Materials. *J. Am. Chem. Soc.* **2011**, *133*, 6513–6516.

(17) Daga, V. K.; Watkins, J. J. Hydrogen-Bond-Mediated Phase Behavior of Complexes of Small Molecule Additives with Poly(Ethylene Oxide- b -Propylene Oxide- b -Ethylene Oxide) Triblock Copolymer Surfactants. *Macromolecules* **2010**, *43* (23), 9990–9997.

(18) Yavitt, B. M.; Gai, Y.; Song, D.-P.; Winter, H. H.; Watkins, J. J. High Molecular Mobility and Viscoelasticity of Microphase-Separated Bottlebrush Diblock Copolymer Melts. *Macromolecules* **2017**, *50* (1), 396–405.

(19) Winter, H. H. Three Views of Viscoelasticity for Cox-Merz Materials. *Rheol. Acta* **2009**, *48* (3), 241–243.

(20) Winter, H. H. Glass Transition as the Rheological Inverse of Gelation. *Macromolecules* **2013**, *46* (6), 2425–2432.

(21) Baumgaertel, M.; Winter, H. H. Determination of Discrete Relaxation and Retardation Time Spectra from Dynamic Mechanical Data. *Rheol. Acta* **1989**, *28* (6), 511–519.

(22) Paturej, J.; Sheiko, S. S.; Panyukov, S.; Rubinstein, M. Molecular Structure of Bottlebrush Polymers in Melts. *Sci. Adv.* **2016**, *2* (11), e1601478.

(23) Lin, T.-P.; Chang, A. B.; Chen, H.-Y.; Liberman-Martin, A. L.; Bates, C. M.; Voegtle, M. J.; Bauer, C. A.; Grubbs, R. H. Control of Grafting Density and Distribution in Graft Polymers by Living Ring-Opening Metathesis Copolymerization. *J. Am. Chem. Soc.* **2017**, *139*, 3896–3903.

(24) Zhao, Y.; Saijo, K.; Hashimoto, T. Order − Disorder Transition of Nanocomposites : Polystyrene- Block - Poly(Methyl Methacrylate) with Palladium Nanoparticles. *Macromolecules* **2013**, *46*, 957–970.

(25) Zhao, Y.; Saijo, K.; Takenaka, M.; Koizumi, S.; Hashimoto, T. Order−Disorder Transition of Nanocomposites: Pd Nanoparticles in Polystyrene- Block - Polyisoprene Microdomain Templates. *Macromolecules* **2009**, *42* (14), 5272–5277.

(26) Larson, R. G.; Winey, K. I.; Patel, S. S.; Watanabe, H.; Bruinsma, R. The Rheology of Layered Liquids: Lamellar Block Copolymers and Smectic Liquid Crystals. *Rheol. Acta* **1993**, *32*, 245–253.

(27) Rubinstein, M.; Obukhov, S. P. Power-Law-Like Stress Relaxation of Block Copolymers: Disentanglement Regimes. *Macromolecules* **1993**, *26* (7), 1740–1750.

(28) Dalsin, S. J.; Rions-maehren, T. G.; Beam, M. D.; Bates, F. S.; Hillmyer, M. A.; Matsen, M. W. Bottlebrush Block Polymers : Quantitative Theory and Experiments. *ACS Nano* **2015**, *9* (12), 12233–12245.

(29) Van Ruymbeke, E. Preface: Special Issue on Associating Polymers. *J. Rheol. (N. Y. N. Y).* **2017**, *61* (6), 1099–1102.

(30) Zhao, Y.; Thorkelsson, K.; Mastroianni, A. J.; Schilling, T.; Luther, J. M.; Rancatore, B. J.; Matsunaga, K.; Jinnai, H.; Wu, Y.; Poulsen, D.; et al. Small-Molecule-Directed Nanoparticle Assembly towards Stimuli-Responsive Nanocomposites. *Nat. Mater.* **2009**, *8* (October), 979–985.

(31) Hong, S. W.; Gu, W.; Huh, J.; Sveinbjornsson, B. R.; Jeong, G.; Grubbs, R. H.; Russell, T. P. On the Self-Assembly of Brush Block Copolymers in Thin Films. *ACS Nano* **2013**, *7* (11), 9684–9692.

(32) Roulet, M.; Vayer, M.; Sinturel, C. A Simple Route to Ordered Metal Oxide Nanoparticle Arrays Using Block Copolymer Thin Films. *Eur. Polym. J.* **2013**, *49* (12), 3897–3903.

(33) Song, D.-P.; Jacucci, G.; Dundar, F.; Naik, A.; Fei, H.-F.; Vignolini, S.; Watkins, J. J. Photonic Resins: Designing Optical Appearance via Block Copolymer Self-Assembly. *Macromolecules* **2018**, *51* (6), 2395–2400.

(34) Bates, C. M.; Chang, A. B.; Momcilovic, N.; Jones, S. C.; Grubbs, R. H. ABA Triblock Brush Polymers: Synthesis, Self-Assembly, Conductivity, and Rheological Properties. *Macromolecules* **2015**, *48* (14), 4967–4973.

(35) Bates, C. M.; Chang, A. B.; Schulze, M. W.; Momcilovic, N.; Jones, S. C.; Grubbs, R. H. Brush Polymer Ion Gels. *J. Polym. Sci. Part B Polym. Phys.* **2015**, *54*, 292–300.

(36) Gu, W.; Huh, J.; Hong, S. W.; Sveinbjornsson, B. R.; Park, C.; Grubbs, R. H.; Russell, T. P. Self-Assembly of Symmetric Brush Diblock Copolymers. *ACS Nano* **2013**, *7* (3), 2551–2558.

APPENDIX

NMR AND GPC SPECTRA OF SIDE CHAIN MACROMONOMERS AND BOTTLE BRUSH BLOCK COPOLYMERS

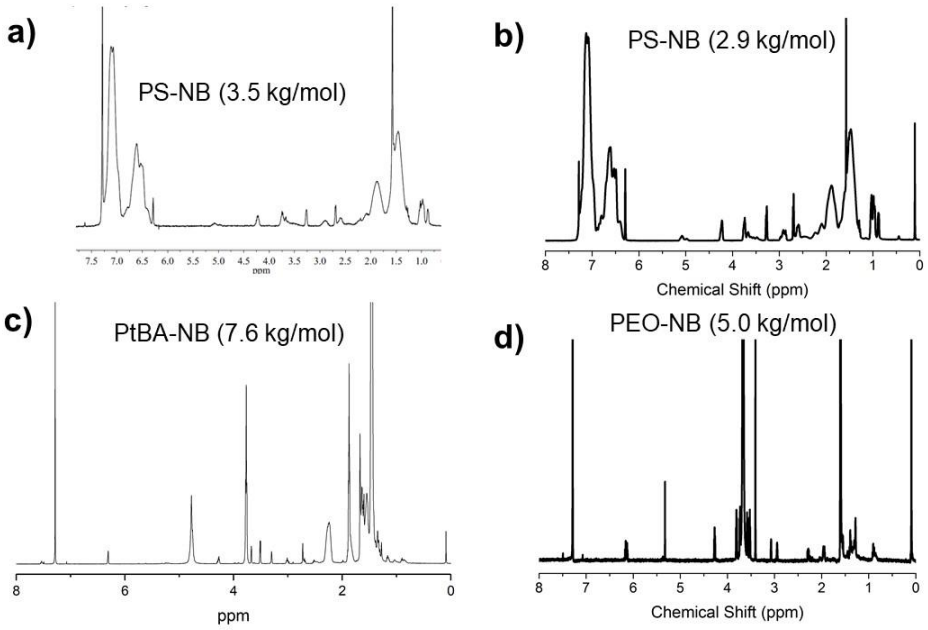

Figure A.1 ^{1}H-NMR spectrum of **(a)** PS-NB MM of 3.5 kg/mol, **(b)** PS-NB MM of 2.9 kg/mol, **(c)** PtBA-NB MM of 7.6 kg/mol, and **(d)** PEO-NB MM of 5.0 kg/mol

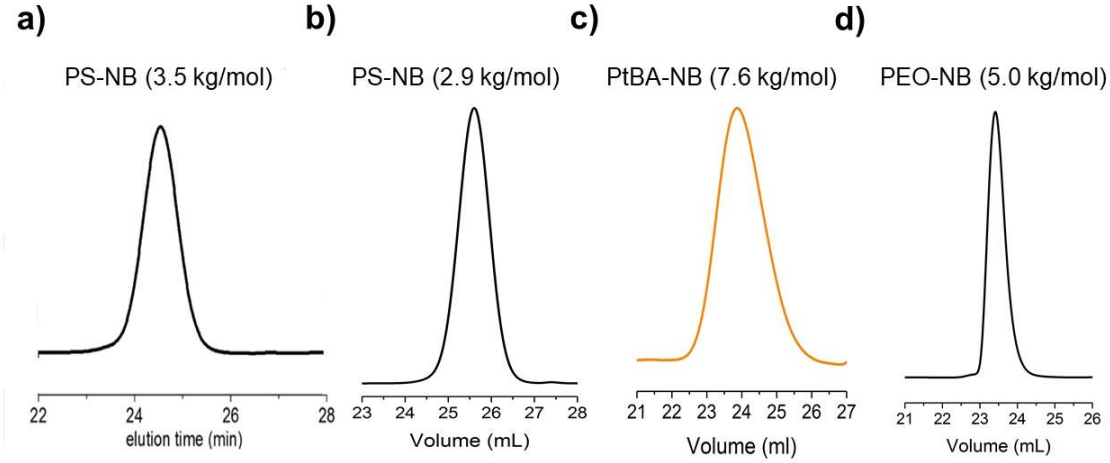

Figure A.2 GPC traces of PS-NB, PtBA-NB and PEO-NB MM for BBCP synthesis: **(a)** PS-NB MM of 3.5 kg/mol, **(b)** PS-NB MM of 2.9 kg/mol, **(c)** PtBA-NB MM of 7.6 kg/mol, and **(d)** PEO-NB MM of 5.0 kg/mol

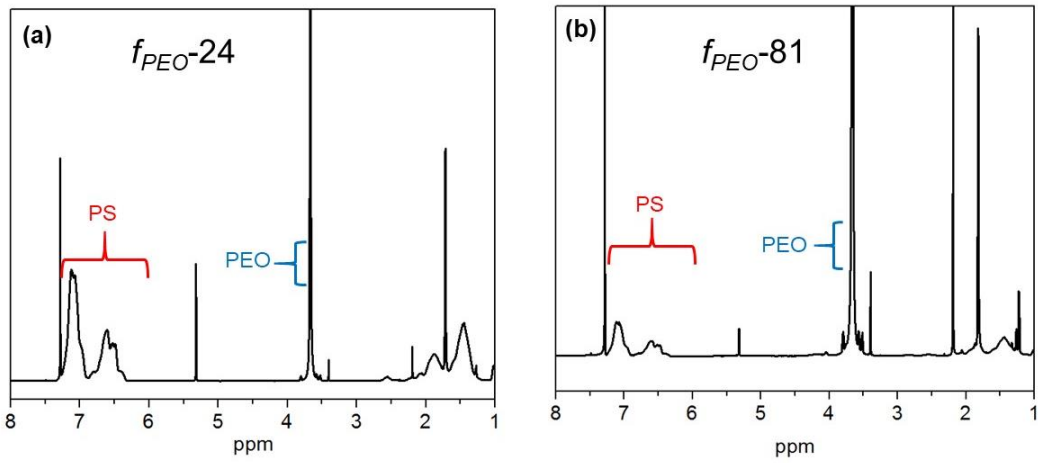

Figure A.3 NMR of PS-*b*-PEO BBCPs at **(a)** f_{PEO} = 0.24 and **(b)** f_{PEO} = 0.81

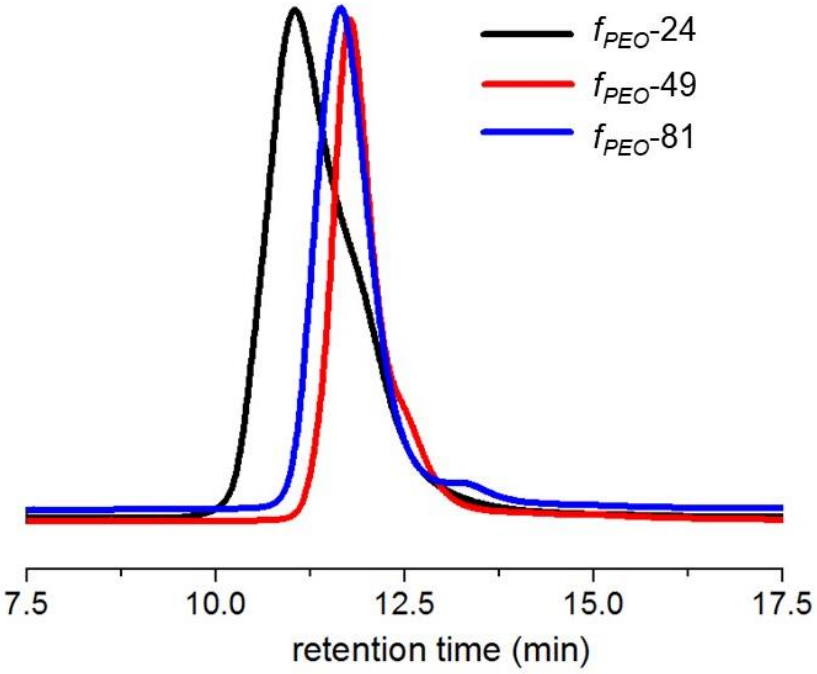

Figure A.4 Select GPC traces of PS-*b*-PEO BBCPs with variable block composition (f_{PEO} = 0.24, 0.49, and 0.81). Spectra modified from Ref. 1. Additional spectra available in Ref. 2.[1,2]

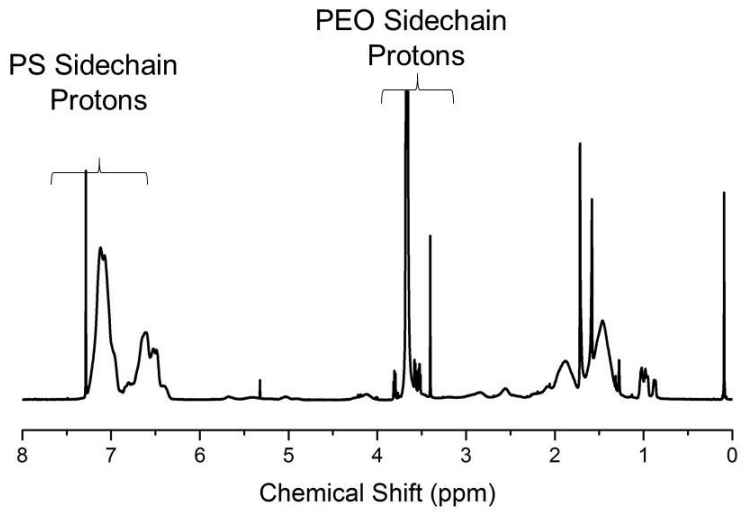

Figure A.5 Select NMR spectra of PS-*b*-PEO BBCPs with equal block composition (f_{PEO} = 0.5)

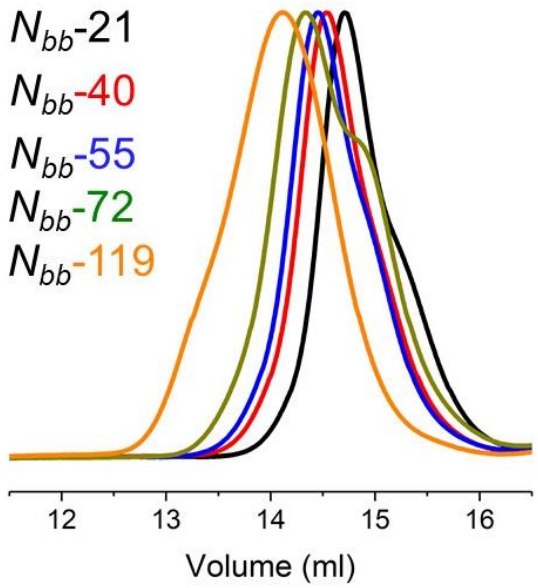

Figure A.6 GPC traces of PS-*b*-PEO BBCPs with variable backbone length and equal block composition (f_{PEO} = 0.5)

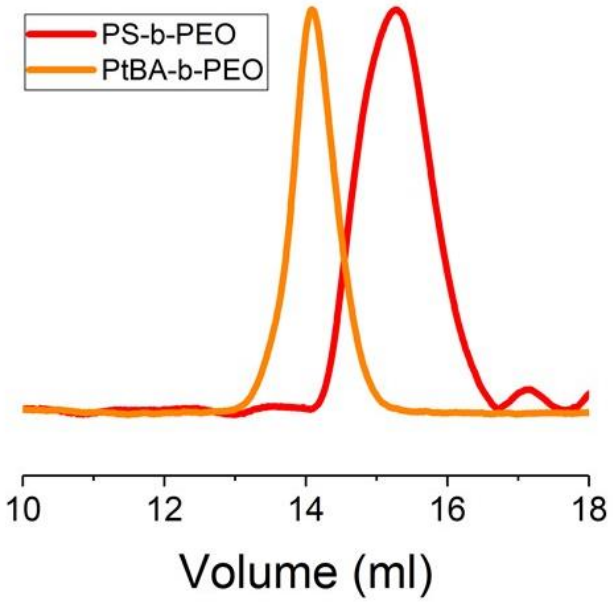

Figure A.7 GPC traces of PS-*b*-PEO and PtBA-*b*-PEO BBCP used in shear alignment investigations

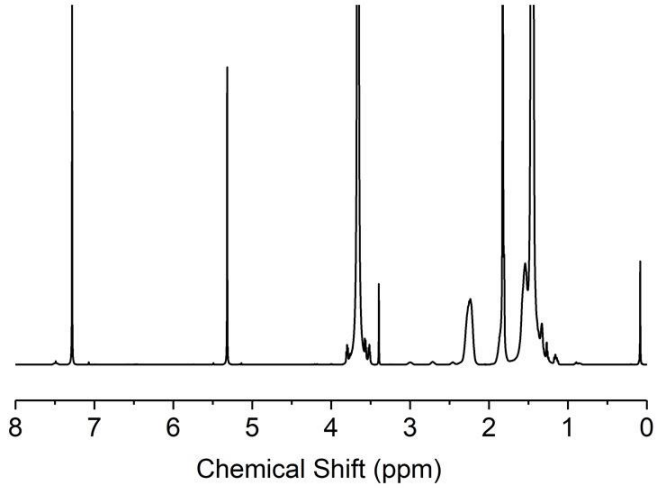

Figure A.8 Characteristic NMR spectra of PtBA-*b*-PEO BBCP (PtBA-*M*)

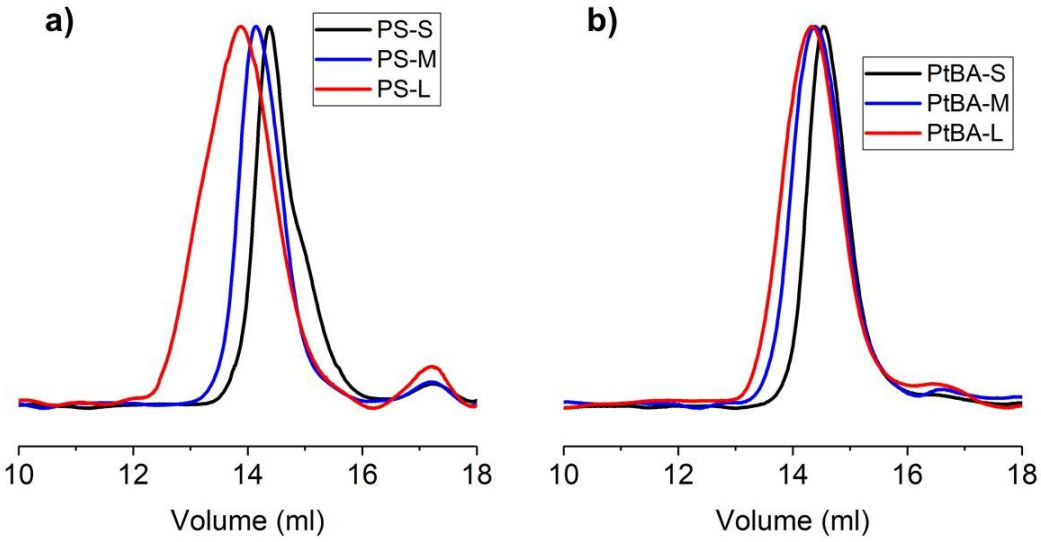

Figure A.9 GPC traces of **(a)** PS-*b*-PEO SML series and **(b)** PtBA-*b*-PEO SML series

REFERENCES

(1) Yavitt, B. M.; Gai, Y.; Song, D.-P.; Winter, H. H.; Watkins, J. J. High Molecular Mobility and Viscoelasticity of Microphase-Separated Bottlebrush Diblock Copolymer Melts. *Macromolecules* **2017**, *50* (1), 396–405.

(2) Gai, Y.; Song, D.-P.; Yavitt, B. M.; Watkins, J. J. Polystyrene- Block -Poly(Ethylene Oxide) Bottlebrush Block Copolymer Morphology Transitions: Influence of Side Chain Length and Volume Fraction. *Macromolecules* **2017**, *50*, 1503–1511.

BIBLIOGRAPHY

Adolf, D.; Martin, J. E. Time-Cure Superposition during Cross-Linking. *Macromolecules* **1990**, *23 (15)*, 3700–3704.

Akcora, P.; Kumar, S. K.; Moll, J. F.; Lewis, S.; Schadler, L. S.; Li, Y.; Benicewicz, B. C.; Sandy, A.; Narayanan, S.; Ilavsky, J.; et al. "Gel-like" Mechanical Reinforcement in Polymer Nanocomposite Melts. *Macromolecules* **2010**, *43* (2), 1003–1010.

Almdal, K.; Koppi, K. A.; Bates, F. S.; Mortensen, K. Multiple Ordered Phases in a Block Copolymer Melt. *Macromolecules* **1992,** *25 (6)*, 1743–1751.

Altay, E.; Nykypanchuk, D.; Rzayev, J. Mesoporous Polymer Frameworks from End-Reactive Bottlebrush Copolymers. *ACS Nano* **2017**, *11 (8)*, 8207–8214.

Balazs, A. C.; Emrick, T.; Russell, T. P. Nanoparticle Polymer Composites: Where Two Small Worlds Meet. *Science*. **2006,** *314 (5802)*, 1107–1110.

Bates, C. M.; Bates, F. S. 50th Anniversary Perspective : Block Polymers—Pure Potential. *Macromolecules* **2017**, *50* (1), 3–22.

Bates, C. M.; Chang, A. B.; Momcilovic, N.; Jones, S. C.; Grubbs, R. H. ABA Triblock Brush Polymers: Synthesis, Self-Assembly, Conductivity, and Rheological Properties. *Macromolecules* **2015**, *48 (14)*, 4967–4973.

Bates, C. M.; Chang, A. B.; Schulze, M. W.; Momcilovic, N.; Jones, S. C.; Grubbs, R. H. Brush Polymer Ion Gels. *J. Polym. Sci. Part B Polym. Phys.* **2015**, *54*, 292–300.

Bates, F. S. Block Copolymers near the Microphase Separation Transition. 2. Linear Dynamic Mechanical Properties. *Macromolecules* **1984**, *17* (12), 2607–2613.

Bates, F. S.; Fredrickson, G. H. Block Copolymer Thermodynamics: Theory and Experiment. *Annu. Rev. Phys. Chem.* **1990**, *41* (1), 525–557.

Bates, F. S.; Fredrickson, G. H. Block Copolymers—Designer Soft Materials. *Phys. Today* **1999**, *52* (2), 32.

Bates, F. S.; Rosedale, J. H.; Fredrickson, G. H. Fluctuation Effects in a Symmetric Diblock Copolymer near the Order – Disorder Transition. *J. Chem. Phys.* **1990,** *92 (1990)*, 6255.

Bates, F. S.; Schulz, M. F.; Khandpur, A. K.; Förster, S.; Rosedale, J. H.; Almdal, K.; Mortensen, K. Fluctuations, Conformational Asymmetry and Block Copolymer Phase Behaviour. *Faraday Discuss.* **1994**, *98*, 7–18.

Baumgaertel, M.; Schausberger, A.; Winter, H. H. The Relaxation of Polymers with Linear Flexible Chains of Uniform Length. *Rheol. Acta* **1990**, *29*, 400–408.

Baumgaertel, M.; Winter, H. H. Determination of Discrete Relaxation and Retardation Time Spectra from Dynamic Mechanical Data. *Rheologica Acta.* **1989**, 511–519.

Beers, K. L.; Gaynor, S. G.; Matyjaszewski, K.; Sheiko, S. S.; Moeller, M. Synthesis of Densely Grafted Copolymers by Atom Transfer Radical Polymerization. *Macromolecules* **1998**, *31 (26)*, 9413–9415.

Berriot, J.; Montes, H.; Lequeux, F.; Long, D.; Sotta, P. Evidence for the Shift of the Glass Transition near the Particles in Silica-Filled Elastomers. *Macromolecules* **2002**, *35 (26)*, 9756–9762.

Bockstaller, M. R.; Lapetnikov, Y.; Margel, S.; Thomas, E. L. Size-Selective Organization of Enthalpic Compatibilized Nanocrystals in Ternary Block Copolymer/Particle Mixtures. *J. Am. Chem. Soc.* **2003**, *125* (18), 5276–5277.

Bockstaller, M. R.; Mickiewicz, R. A.; Thomas, E. L. Block Copolymer Nanocomposites: Perspectives for Tailored Functional Materials. *Adv. Mater.* **2005**, *17* (11), 1331–1349.

Bodycomb, J.; Funaki, Y.; Kimishima, K.; Hashimoto, T. Single-Grain Lamellar Microdomain from a Diblock Copolymer. *Macromolecules* **1999,** *32 (6)*, 2075–2077.

Bolton, J.; Bailey, T. S.; Rzayev, J. Large Pore Size Nanoporous Materials from the Self-Assembly of Asymmetric Bottlebrush Block Copolymers. *Nano Lett.* **2011,** *11 (3)*, 998–1001.

Booij, H. C.; Palmen, J. Some Aspects of Linear and Nonlinear Viscoelastic Behavior of Polymer Melts in Shear. *Rheol. Acta* **1982,** *21 (4)*, 376–387.

Buonsanti, R.; Pick, T. E.; Krins, N.; Richardson, T. J.; Helms, B. A.; Milliron, D. J. Assembly of Ligand-Stripped Nanocrystals into Precisely Controlled Mesoporous Architectures. *Nano Lett.* **2012,** *12 (7)*, 3872–3877.

Caputo, F. E.; Burghardt, W. R. Real-Time 1-2 Plane SAXS Measurements of Molecular Orientation in Sheared Liquid Crystalline Polymers. *Macromolecules* **2001**, *34 (19)*, 6684–6694.

Caputo, F. E.; Burghardt, W. R.; Krishnan, K.; Bates, F. S.; Lodge, T. P. Time-Resolved Small-Angle X-Ray Scattering Measurements of a Polymer Bicontinuous Microemulsion Structure Factor under Shear. *Phys. Rev. E - Stat. Nonlinear, Soft Matter Phys.* **2002**, *66 (4)*, 1–18.

Cavicchi, K. A.; Russell, T. P. Solvent Annealed Thin Films of Asymmetric Polyisoprene - Polylactide Diblock Copolymers. *Macromolecules* **2007,** *40 (4)*, 1181–1186.

Chae, C.; Yu, Y.; Seo, H.; Kim, M.; Grubbs, R. H.; Lee, J. Experimental Formulation of Photonic Crystal Properties for Hierarchically Self-Assembled POSS −

Bottlebrush Block Copolymers. *Macromolecules* **2018**, *51 (9)*, 3458–3466.

Chambon, F.; Winter, H. H. Analysis of Linear Viscoelasticity of a Crosslinking Polymer at the Gel Point. *J. Rheol.* **1986,** *30 (2)*, 367.

Chang, A. B.; Bates, C. M.; Lee, B.; Garland, C. M.; Jones, S. C.; Spencer, R. K. W.; Matsen, M. W.; Grubbs, R. H. Manipulating the ABCs of Self-Assembly via Low-X Block Polymer Design. *Proc. Natl. Acad. Sci.* **2017**, *114 (25)*, 6462–6467.

Chang, A. B.; Lin, T.-P.; Thompson, N. B.; Luo, S.-X.; Liberman-Martin, A. L.; Chen, H.-Y.; Lee, B.; Grubbs, R. H. Design, Synthesis, and Self-Assembly of Polymers with Tailored Graft Distributions. *J. Am. Chem. Soc.* **2017**, *139 (48)*, 17683–17693.

Chen, Z.-R.; Kornfield, J. A. Flow-Induced Alignment of Lamellar Block Copolymer Melts. *Polymer* **1998**, *39 (19)*, 4679–4699.

Chen, Z.-R.; Kornfield, J. A.; Smith, S. D.; Grothaus, J. T.; Satkowski, M. M. Pathways to Macroscale Order in Nanostructured Block Copolymers. *Science*, **1997**, *277 (5330)*, 1248–1253.

Cheng, L.; Gadelrab, K. R.; Kawamoto, K.; Yager, K. G.; Johnson, J. A.; Alexander-Katz, A.; Ross, C. A. Templated Self-Assembly of a PS- Branch -PDMS Bottlebrush Copolymer. *Nano Lett.* **2018**, *18*, 4360–4369.

Chiu, J. J.; Kim, B. J.; Kramer, E. J.; Pine, D. J. Control of Nanoparticle Location in Block Copolymers. *J. Am. Chem. Soc.* **2005**, *127* (14), 5036–5037.

Chiu, J. J.; Kim, B. J.; Yi, G. R.; Bang, J.; Kramer, E. J.; Pine, D. J. Distribution of Nanoparticles in Lamellar Domains of Block Copolymers. *Macromolecules* **2007**, *40* (9), 3361–3365.

Chremos, A.; Theodorakis, P. E. Impact of Intrinsic Backbone Chain Stiffness on the Morphologies of Bottle-Brush Diblock Copolymers. *Polym.* (United Kingdom) **2016**, *97*, 191–195.

Chremos, A.; Theodorakis, P. E. Morphologies of Bottle-Brush Block Copolymers. *ACS Macro Lett.* **2014**, *3 (10)*, 1096–1100.

Ciebien, J. F.; Clay, R. T.; Sohn, B. H.; Cohen, R. E. Brief Review of Metal Nanoclusters in Block Copolymer Đlms S. *New J. Chem.* **1998**, 685–691.

Colby, R. H. Block Copolymer Dynamics. *Curr. Opin. Colloid Interface Sci.* **1996**, *1*, 454–465.

Colby, R. H. Melt Rheology of Block Copolymers. In *Encyclopedia of Materials: Science and Technology*; **2001**; pp 727–730.

Cushen, J. D.; Otsuka, I.; Bates, C. M.; Halila, S.; Fort, S.; Rochas, C.; Easley, J. A.; Rausch, E. L.; Thio, A.; Borsali, R.; et al. Oligosaccharide/Silicon-Containing Block Copolymers with 5 Nm Features for Lithographic Applications. *ACS Nano* **2012**, *6* (4), 3424–3433.

Daga, V. K.; Anderson, E. R.; Gido, S. P.; Watkins, J. J. Hydrogen Bond Assisted Assembly of Well-Ordered Polyhedral Oligomeric Silsesquioxane-Block Copolymer Composites. *Macromolecules* **2011**, *44 (17)*, 6793–6799.

Daga, V. K.; Watkins, J. J. Hydrogen-Bond-Mediated Phase Behavior of Complexes of Small Molecule Additives with Poly(Ethylene Oxide- b -Propylene Oxide- b -Ethylene Oxide) Triblock Copolymer Surfactants. *Macromolecules* **2010**, *43 (23)*, 9990–9997.

Dalsin, S. J.; Hillmyer, M. A.; Bates, F. S. Linear Rheology of Polyolefin-Based Bottlebrush Polymers. *Macromolecules* **2015**, *48*, 4680–4691.

Dalsin, S. J.; Hillmyer, M. A.; Bates, F. S. Molecular Weight Dependence of Zero-Shear Viscosity in Atactic Polypropylene Bottlebrush Polymers. *ACS Macro Lett.* **2014**, *3 (5)*, 423–427.

Dalsin, S. J.; Rions-maehren, T. G.; Beam, M. D.; Bates, F. S.; Hillmyer, M. A.; Matsen, M. W. Bottlebrush Block Polymers : Quantitative Theory and Experiments. *ACS Nano* **2015,** *9 (12)*, 12233–12245.

Daniel, W. F. M.; Xie, G.; Vatankhah Varnoosfaderani, M.; Burdyńska, J.; Li, Q.; Nykypanchuk, D.; Gang, O.; Matyjaszewski, K.; Sheiko, S. S. Bottlebrush-Guided Polymer Crystallization Resulting in Supersoft and Reversibly Moldable Physical Networks. *Macromolecules* **2017**, *50*, 2103–2111.

Darling, S. B. Directing the Self-Assembly of Block Copolymers. *Prog. Polym. Sci.* 2007, *32 (10)*, 1152–1204.

De Jeu, W. H. Basic X-Ray Scattering for Soft Matter, 1st ed.; Oxford University Press: Oxford, **2016.**

De La Fuente, J. L.; Fernandez-Garcia, M.; Cerrada, M. L.; Spiess, H. W.; Wilhelm, M. Small-Angle X-Ray Scattering and Linear Melt Rheology of Poly(Tert-Butyl Acrylate-g-Styrene) Graft Copolymers. *Polymer* **2006**, *47 (5)*, 1487–1495.

De La Fuente, J. L.; Wilhelm, M.; Spiess, H. W.; Madruga, E. L.; Fernandez-Garcia, M.; Cerrada, M. L. Thermal, Morphological and Rheological Characterization of Poly(Acrylic Acid-g-Styrene) Amphiphilic Graft Copolymers. *Polymer* **2005**, *46 (13)*, 4544–4553.

Dealy, J. M.; Plazek, D. Time-Temperature Superposition—a Users Guide. *Rheol. Bull.* **2009**, pp 16–21.

Di Mauro, A. E.; Villone, V.; Ingrosso, C.; Corricelli, M.; Oria, L.; Pérez-Murano, F.; Agostiano, A.; Striccoli, M.; Curri, M. L. H-Bonding Driven Assembly of Colloidal Au Nanoparticles on Nanostructured Poly(Styrene-b-Ethylene Oxide) Block Copolymer Templates. *J. Mater. Sci.* **2014**, *49* (15), 5246–5255.

Fairclough, J. P. A.; Yu, G.-E.; Mai, S.-M.; Crothers, M.; Mortensen, K.; Ryan, A. J.; Booth, C. First Observation of an Ordered Microphase in Melts of Poly(Oxyethylene)-Poly(Oxypropylene) Block Copolymers. *Phys. Chem. Chem. Phys.* **2000,** *2 (7)*, 1503–1507.

Faure, B.; Salazar-Alvarez, G.; Ahniyaz, A.; Villaluenga, I.; Berriozabal, G.; De Miguel, Y. R.; Bergström, L. Dispersion and Surface Functionalization of Oxide Nanoparticles for Transparent Photocatalytic and UV-Protecting Coatings and Sunscreens. *Sci. Technol. Adv. Mater.* **2013**, *14 (2)*, 1–23.

Fox, T. G.; Flory, P. J. The Glass Temperature and Related Properties of Poly-Styrene. Influence of Molecular Weight. *J. Polym. Sci.* **1954**, *14*, 315–319.

Fredrickson, G. H.; Bates, F. S. Dynamics of Block Copolymers: Theory and Experiment. *Annu. Rev. Mater. Sci.* **1996**, *26* (1), 501–550.

Gai, Y.; Lin, Y.; Song, D.-P.; Yavitt, B. M.; Watkins, J. J. Strong Ligand–Block Copolymer Interactions for Incorporation of Relatively Large Nanoparticles in Ordered Composites. *Macromolecules* **2016**, *49* (9), 3352–3360.

Gai, Y.; Song, D.-P.; Yavitt, B. M.; Watkins, J. J. Polystyrene- Block -Poly(Ethylene Oxide) Bottlebrush Block Copolymer Morphology Transitions: Influence of Side Chain Length and Volume Fraction. *Macromolecules* **2017**, *50*, 1503–1511.

Gao, H.; Matyjaszewski, K. Synthesis of Molecular Brushes by "Grafting onto" Method: Combination of ATRP and Click Reactions. *J. Am. Chem. Soc.* **2007**, *129 (20)*, 6633–6639.

Garcia, C. B. W.; Zhang, Y.; Mahajan, S.; DiSalvo, F.; Wiesner, U. B. Self-Assembly Approach toward Magnetic Silica-Type Nanoparticles of Different Shapes from Reverse Block Copolymer Mesophases. *J. Am. Chem. Soc.* **2003**, *125* (44), 13310–13311.

Genix, A.-C.; Oberdisse, J. Nanoparticle Self-Assembly: From Interactions in Suspension to Polymer Nanocomposites. *Soft Matter* **2018**.

Genix, A.-C.; Oberdisse, J. Structure and Dynamics of Polymer Nanocomposites Studied by X-Ray and Neutron Scattering Techniques. *Curr. Opin. Colloid Interface Sci.* **2015**, *20* (4), 293–303.

Gopinadhan, M.; Choo, Y.; Kawabata, K.; Kaufman, G.; Feng, X.; Di, X.; Rokhlenko, Y.; Mahajan, L. H.; Ndaya, D.; Kasi, R. M.; et al. Controlling Orientational Order in Block Copolymers Using Low-Intensity Magnetic Fields. *Proc. Natl. Acad.*

Sci. **2017**, *114 (45)*, E9437–E9444.

Gu, W.; Huh, J.; Hong, S. W.; Sveinbjornsson, B. R.; Park, C.; Grubbs, R. H.; Russell, T. P. Self-Assembly of Symmetric Brush Diblock Copolymers. *ACS Nano* **2013**, 7 (3), 2551–2558.

Guo, A. Z.; Le, A. N.; Feng, X.; Choo, Y.; Liu, B.; Wang, D.; Wan, Z.; Gu, Y.; Li, V.; Osuji, C. O.; et al. Janus Graft Block Copolymers: Design of Polymer Architecture for Independently Tuned Nanostructures and Polymer Properties. *Angew. Chemie Int. Ed.* **2018**.

Gupta, V. K.; Krishnamoorti, R.; Chen, Z.-R.; Kornfield, J. A.; Smith, S. D.; Satkowski, M. M.; Grothaus, J. T. Dynamics of Shear Alignment in a Lamellar Diblock Copolymer: Interplay of Frequency, Strain Amplitude, and Temperature. *Macromolecules* **1996**, 29 (3), 875–884.

Han, C. D.; Kim, J. K. On the Use of Time-Temperature Superposition in Multicomponent/Multiphase Polymer Systems. *Polymer*. 1993, 34 (12), 2533–2539.

Han, C. D.; Kim, J. Rheological Technique for Determining the Order-Disorder Transition of Block Copolymers. *J. Polym. Sci. Part B Polym. Phys.* **1987**, *25* (8), 1741–1764.

Han, C. D.; Kim, J.; Kim, J. K. Determination of the Order-Disorder Transition Temperature of Block Copolymers. *Macromolecules* **1989**, 383–394.

Hashimoto, T.; Koizumi, S.; Hasegawa, H.; Izumitani, T.; Hyde, S. T. Observation of "Mesh" and "Strut" Structures in Block Copolymer/Homopolymer Mixtures. *Macromolecules* **1992**, 25 (5), 1433–1439.

Haugan, I. N.; Maher, M. J.; Chang, A. B.; Lin, T.-P.; Grubbs, R. H.; Hillmyer, M. A.; Bates, F. S. Consequences of Grafting Density on the Linear Viscoelastic Behavior of Graft Polymers. *ACS Macro Lett.* **2018**, 7, 525–530.

Hoheisel, T. N.; Hur, K.; Wiesner, U. B. Block Copolymer-Nanoparticle Hybrid Self-Assembly. *Prog. Polym. Sci.* **2015**, *40*, 3–32.

Hong, S. W.; Gu, W.; Huh, J.; Sveinbjornsson, B. R.; Jeong, G.; Grubbs, R. H.; Russell, T. P. On the Self-Assembly of Brush Block Copolymers in Thin Films. *ACS Nano* **2013**, *7* (11), 9684–9692.

Hu, H.; Gopinadhan, M.; Osuji, C. O. Directed Self-Assembly of Block Copolymers: A Tutorial Review of Strategies for Enabling Nanotechnology with Soft Matter. *Soft Matter* **2014**, *10* (22), 3867–3889.

Hu, M.; Xia, Y.; McKenna, G. B.; Kornfield, J. A.; Grubbs, R. H. Linear Rheological Response of a Series of Densely Branched Brush Polymers. *Macromolecules*

2011, *44* (17), 6935–6943.

Huang, K.; Canterbury, D. P.; Rzayev, J. Synthesis of Segmented Polylactide Molecular Brushes and Their Transformation to Open-End Nanotubes. *Macromolecules* **2010**, *43* (16), 6632–6638.

Huang, K.; Rzayev, J. Well-Defined Organic Nanotubes from Multicomponent Bottlebrush Copolymers. *J. Am. Chem. Soc.* **2009**, *131* (19), 6880–6885.

Huang, P.; Zhu, L.; Guo, Y.; Ge, Q.; Jing, A. J.; Chen, W. Y.; Quirk, R. P.; Cheng, S. Z. D.; Thomas, E. L.; Lotz, B.; et al. Confinement Size Effect on Crystal Orientation Changes of Poly(Ethylene Oxide) Blocks in Poly(Ethylene Oxide)- b -Polystyrene Diblock Copolymers. *Macromolecules* **2004,** *37* (10), 3689–3698.

Huh, J.; Ginzburg, V. V.; Balazs, A. C. Thermodynamic Behavior of Particle/Diblock Copolymer Mixtures: Simulation and Theory. *Macromolecules* **2000,** *33* (21), 8085–8096.

Jang, S. G.; Khan, A.; Hawker, C. J.; Kramer, E. J. Morphology Evolution of PS- b -P2VP Diblock Copolymers via Supramolecular Assembly of Hydroxylated Gold Nanoparticles. *Macromolecules* **2012**, *45*, 1553–1561.

Jang, S. G.; Kramer, E. J.; Hawker, C. J. Controlled Supramolecular Assembly of Micelle-Like Gold Nanoparticles in PS- b -P2VP Diblock Copolymers via Hydrogen Bonding. *J. Am. Chem. Soc.* **2011**, *133*, 16986–16996.

Jiang, L.; Nykypanchuk, D.; Ribbe, A. E.; Rzayev, J. One-Shot Synthesis and Melt Self-Assembly of Bottlebrush Copolymers with a Gradient Compositional Profile. *ACS Macro Lett.* **2018**, 7, 619–623.

Jones, M. R.; Osberg, K. D.; MacFarlane, R. J.; Langille, M. R.; Mirkin, C. A. Templated Techniques for the Synthesis and Assembly of Plasmonic Nanostructures. *Chem. Rev.* **2011**, *111* (6), 3736–3827.

Joshi, Y. M. Dynamics of Colloidal Glasses and Gels. *Annu. Rev. Chem. Biomol. Eng.* **2014**, *5*, 181–202.

Kao, J.; Thorkelsson, K.; Bai, P.; Rancatore, B. J.; Xu, T. Toward Functional Nanocomposites: Taking the Best of Nanoparticles, Polymers, and Small Molecules. *Chem. Soc. Rev.* **2013**, *42* (7), 2654–2678.

Kawamoto, K.; Zhong, M.; Gadelrab, K. R.; Cheng, L. C.; Ross, C. A.; Alexander-Katz, A.; Johnson, J. A. Graft-through Synthesis and Assembly of Janus Bottlebrush Polymers from A-Branch-B Diblock Macromonomers. *J. Am. Chem. Soc.* **2016,** *138* (36), 11501–11504.

Kawasaki, K.; Onuki, A. Dynamics and Rheology of Diblock Copolymers Quenched into Microphase-Separated States. *Phys. Rev. A* **1990**, *42* (6), 3664–3666.

Kelarakis, A.; Giannelis, E. P. Crystallization and Unusual Rheological Behavior in Poly(Ethylene Oxide)-Clay Nanocomposites. *Polymer.* **2011**, *52* (10), 2221–2227.

Keller, A.; Pedemonte, E.; Willmouth, F. M. Macro Lattice from Segregated Amorphous Phases of a Three Block Copolymer. *Kolloid-Z.u.Z.Polymere* **1970,** *238*, 385–389.

Khandpur, A. K.; Förster, S.; Bates, F. S.; Hamley, I. W.; Ryan, A. J.; Bras, W.; Almdal, K.; Mortensen, K. Polyisoprene-Polystyrene Diblock Copolymer Phase Diagram near the Order-Disorder Transition. *Macromolecules* **1995**, *28* (26), 8796–8806.

Kim, B. J.; Bang, J.; Hawker, C. J.; Kramer, E. J. Effect of Areal Chain Density on the Location of Polymer-Modified Gold Nanoparticles in a Block Copolymer Template. *Macromolecules* **2006**, *39* (12), 4108–4114.

Kim, D. H.; Sun, Z.; Russell, T. P.; Knoll, W.; Gutmann, J. S. Organic-Inorganic Nanohybridization by Block Copolymer Thin Films. *Adv. Funct. Mater.* **2005**, *15* (7), 1160–1164.

Kim, D.; Srivastava, S.; Narayanan, S.; Archer, L. A. Polymer Nanocomposites: Polymer and Particle Dynamics. *Soft Matter* **2012**, *8* (42), 10813.

Kim, S.; Hyun, K.; Kim, Y. S.; Struth, B.; Clasen, C.; Ahn, K. H. Drying of a Charge-Stabilized Colloidal Suspension in Situ Monitored by Vertical Small-Angle X-Ray Scattering. *Langmuir* **2013**, *29* (32), 10059–10065.

Kim, S.; Hyun, K.; Struth, B.; Ahn, K. H.; Clasen, C. Structural Development of Nanoparticle Dispersion during Drying in Polymer Nanocomposite Films. *Macromolecules* **2016**, *49* (23), 9068–9079.

Koppi, K. A.; Tirrell, M.; Bates, F. S.; Almdal, K.; Colby, R. H. Lamellae Orientation in Dynamically Sheared Diblock Copolymer Melts. *J. Phys. II* **1992**, *2*, 1941–1959.

Kothari, R.; Winter, H. H.; Watkins, J. J. Rheological Study of Order-to-Disorder Transitions and Phase Behavior of Block Copolymer–Surfactant Complexes Containing Hydrogen-Bonded Small Molecule Additives. *Macromolecules* **2014,** *47* (22), 8048–8055.

Kumar, S. K.; Benicewicz, B. C.; Vaia, R. A.; Winey, K. I. 50th Anniversary Perspective : Are Polymer Nanocomposites Practical for Applications? *Macromolecules* **2017**, *50*, 714–731.

Kumar, S. K.; Krishnamoorti, R. Nanocomposites: Structure, Phase Behavior, and Properties. *Annu. Rev. Chem. Biomol. Eng.* **2010**, *1*, 37–58.

Larson, R. G.; Winey, K. I.; Patel, S. S.; Watanabe, H.; Bruinsma, R. The Rheology of Layered Liquids: Lamellar Block Copolymers and Smectic Liquid Crystals. *Rheol. Acta* **1993,** *32*, 245–253.

Lee, J.-Y.; Thompson, R. B.; Jasnow, D.; Balazs, A. C. Entropically Driven Formation of Hierarchically Ordered Nanocomposites. *Phys. Rev. Lett.* **2002**, *89* (15), 155503.

Leibler, L. Theory of Microphase Separation in Block Copolymers. *Macromolecules* **1980**, *13* (6), 1602–1617.

Liberman-Martin, A. L.; Chu, C. K.; Grubbs, R. H. Application of Bottlebrush Block Copolymers as Photonic Crystals. *Macromol. Rapid Commun.* **2017,** *38*, 1700058.

Lin, T.-P.; Chang, A. B.; Chen, H.-Y.; Liberman-Martin, A. L.; Bates, C. M.; Voegtle, M. J.; Bauer, C. A.; Grubbs, R. H. Control of Grafting Density and Distribution in Graft Polymers by Living Ring-Opening Metathesis Copolymerization. *J. Am. Chem. Soc.* **2017**, *139*, 3896–3903.

Lin, T.-P.; Chang, A. B.; Luo, S.-X.; Chen, H.-Y.; Lee, B.; Grubbs, R. H. Effects of Grafting Density on Block Polymer Self-Assembly: From Linear to Bottlebrush. *ACS Nano* **2017**, *11* (11), 11632–11641.

Lin, Y.; Boker, A.; He, J.; Sill, K.; Xiang, H.; Abetz, C.; Li, X.; Wang, J.; Emrick, T.; Long, S.; et al. Self-Directed Self-Assembly of Nanoparticle / Copolymer Mixtures. *Nature* **2005**, *404*, 55–59.

Lin, Y.; Daga, V. K.; Anderson, E. R.; Gido, S. P.; Watkins, J. J. Nanoparticle-Driven Assembly of Block Copolymers: A Simple Route to Ordered Hybrid Materials. *J. Am. Chem. Soc.* **2011**, *133*, 6513–6516.

Lin, Y.; Gu, Y.; Chen, Z.; Zhang, S.; Zhang, G.; Wang, Y.; Xing, H.; Tang, T. Morphology and Linear Rheology of Comb-like Copolymer Melts with High Grafting Density: I. PVSt- g -(PS- b -PE) Comb-like Block Copolymers. *Polymer* **2017**, *122*, 87–95.

Lin, Y.; Wang, Y.; Zheng, J.; Yao, K.; Tan, H.; Wang, Y.; Tang, T.; Xu, D. Nanostructure and Linear Rheological Response of Comb-like Copolymer PSVS-g -PE Melts: Influences of Branching Densities and Branching Chain Length. *Macromolecules* **2015**, *48* (20), 7640–7648.

Liu, Y.; Momani, B.; Winter, H. H.; Perry, S. L. Rheological Characterization of Liquid-to-Solid Transitions in Bulk Polyelectrolyte Complexes. *Soft Matter* **2017**, *13* (40), 7332–7340.

Loo, Y. L.; Register, R. A.; Ryan, A. J. Modes of Crystallization in Block Copolymer Microdomains: Breakout, Templated, and Confined. *Macromolecules* **2002**, *35* (6), 2365–2374.

López-Barrón, C. R.; Brant, P.; Eberle, A. P. R.; Crowther, D. J. Linear Rheology and Structure of Molecular Bottlebrushes with Short Side Chains. *J. Rheol.* **2015**, *59* (3), 865–883.

Love, J. A.; Morgan, J. P.; Trnka, T. M.; Grubbs, R. H. A Practical and Highly Active Ruthenium-Based Catalyst That Effects the Cross Metathesis of Acrylonitrile. *Angew. Chemie - Int. Ed.* **2002**, *41* (21), 4035–4037.

Macosko, C. W. *Rheology: Principles, Measurements, and Applications*; Wiley VCH: New York, **1994.**

Matsen, M. W.; Bates, F. S. Unifying Weak- and Strong-Segregation Block Copolymer Theories. *Macromolecules* **1996**, *29* (4), 1091–1098.

Mendes, A. C.; Baran, E. T.; Reis, R. L.; Azevedo, H. S. Self-Assembly in Nature: Using the Principles of Nature to Create Complex Nanobiomaterials. *Wiley Interdiscip. Rev. Nanomedicine Nanobiotechnology* **2013**, *5* (6), 582–612.

Mendoza, C.; Gindy, N.; Gutmann, J. S.; Frömsdorf, A.; Förster, S.; Fahmi, A. In Situ Synthesis and Alignment of Au Nanoparticles within Hexagonally Packed Cylindrical Domains of Diblock Copolymers in Bulk. *Langmuir* **2009**, *25* (16), 9571–9578.

Mendoza, C.; Gindy, N.; Wilhelm, M.; Fahmi, A. Linear and Non-Linear Viscoelastic Rheology of Hybrid Nanostructured Materials from Block Copolymers with Gold Nanoparticles. *Rheol. Acta* **2011**, *50* (3), 257–275.

Mendoza, C.; Pietsch, T.; Gindy, N.; Fahmi, A. Fabrication of 3D-Periodic Ordered Metallic Nanoparticles in a Block Copolymer Bulk Matrix via Oscillating Shear Flow. *Adv. Mater.* **2008**, *20* (6), 1179–1184.

Mendoza, C.; Pietsch, T.; Gutmann, J. S.; Jehnichen, D.; Gindy, N.; Fahmi, A. Block Copolymers with Gold Nanoparticles: Correlation between Structural Characteristics and Mechanical Properties. *Macromolecules* **2009**, *42* (4), 1203–1211.

Mittal, K. L. Polymer Science Modification: Relevance to Adhesion Volume 3; **2004.**

Moll, J. F.; Akcora, P.; Rungta, A.; Gong, S.; Colby, R. H.; Benicewicz, B. C.; Kumar, S. K. Mechanical Reinforcement in Polymer Melts Filled with Polymer Grafted Nanoparticles. *Macromolecules* **2011**, *44* (18), 7473–7477.

Morkved, T. L.; Lu, M.; Urbas, a. M.; Ehrichs, E. E.; Jaeger, H. M.; Mansky, P.; Russell, T. P. Local Control of Microdomain Orientation in Diblock Copolymer Thin Films with Electric Fields. *Science* (80-.). **1996**, *273* (5277), 931–933.

Moro, S.; Parneix, C.; Cabane, B.; Sanson, N.; D'Espinose De Lacaillerie, J. B. Hydrophobization of Silica Nanoparticles in Water: Nanostructure and Response to Drying Stress. *Langmuir* **2017**, *33* (19), 4709–4719.

Morrison, F.; Bourvellec, G. LE; Winter, H. H. Flow-Induced Structure and Rheology of a Triblock Copolymer. *J. Appl. Polym. Sci.* **1987,** *33*, 1585–1600.

Morrison, F.; Winter, H. H. The Effect of Unidirectional Shear on the Structure of Triblock Copolymers. I. Polystyrene-Polybutadiene-Polystyrene. *Macromolecules* **1989**, *22*, 3533–3540.

Mortensen, K.; Almdal, K.; Bates, F. S.; Koppi, K. A.; Tirrell, M. V.; Nordén, B. Shear Devices for in Situ Structural Studies of Block-Copolymer Melts and Solutions. *Phys. B Phys. Condens. Matter* **1995**, *213–214* (C), 682–684.

Mortensen, K.; Theunissen, E.; Kleppinger, R.; Almdal, K.; Reynaers, H. Shear-Induced Morphologies of Cubic Ordered Block Copolymer Micellar Networks Studied by in Situ Small-Angle Neutron Scattering and Rheology. *Macromolecules* **2002,** *35* (20), 7773–7781.

Mours, M.; Winter, H. H. Time-Resolved Rheometry. *Rheologica Acta.* **1994**, pp 385–397.

Mykhaylyk, O. O.; Parnell, A. J.; Pryke, A.; Fairclough, J. P. A. Direct Imaging of the Orientational Dynamics of Block Copolymer Lamellar Phase Subjected to Shear Flow. *Macromolecules* **2012**, *45* (12), 5260–5272.

Ninago, M. D.; Satti, A. J.; Ciolino, A. E.; Valles, E. M.; Villar, M. A.; Vega, D. A.; Sanz, A.; Nogales, A.; Rueda, D. R. Synthesis and Morphology of Model PS-b-PDMS Copolymers. *J. Polym. Sci. Part A Polym. Chem.* **2010**, *48*, 3119–3127.

Okamoto, S.; Saijo, K.; Hashimoto, T. Real-Time SAXS Observations of Lamella-Forming Block Copolymers under Large Oscillatory Shear Deformation. *Macromolecules* **1994**, *27* (20), 5547–5555.

Osterwinter, C.; Schubert, C.; Tonhauser, C.; Wilms, D.; Frey, H.; Friedrich, C. Rheological Consequences of Hydrogen Bonding: Linear Viscoelastic Response of Linear Polyglycerol and Its Permethylated Analogues as a General Model for Hydroxyl-Functional Polymers. *Macromolecules* **2015**, *48*, 119–130.

Park, D. Y. Direct Calculation of Inter-Particle Distance in Suspension by Image Processing. *Powder Technol.* **2018**, *330*, 252–258.

Park, M. J.; Balsara, N. P. Anisotropie Proton Conduction in Aligned Block Copolymer Electrolyte Membranes at Equilibrium with Humid Air. *Macromolecules* **2010**, *43* (1), 292–298.

Parnell, A. J.; Tzokova, N.; Pryke, A.; Howse, J. R.; Mykhaylyk, O. O.; Ryan, A. J.; Panine, P.; Fairclough, J. P. A. Shear Ordered Diblock Copolymers with Tuneable Optical Properties. *Phys. Chem. Chem. Phys.* **2011**, *13* (8), 3179–3186.

Paturej, J.; Kreer, T. Hierarchical Excluded Volume Screening in Solutions of Bottlebrush Polymers. *Soft Matter* **2017**, *13* (45), 8534–8541.

Paturej, J.; Sheiko, S. S.; Panyukov, S.; Rubinstein, M. Molecular Structure of

Bottlebrush Polymers in Melts. *Sci. Adv.* **2016,** 2 (11), e1601478.

Pester, C. W.; Schmidt, K.; Ruppel, M.; Schoberth, H. G.; Boker, A. Electric-Field-Induced Order-Order Transition from Hexagonally Perforated Lamellae to Lamellae. *Macromolecules* **2015,** *48* (17), 6206–6213.

Pfleiderer, P.; Baik, S. J.; Zhang, Z.; Vleminckx, G.; Lettinga, M. P.; Grelet, E.; Vermant, J.; Clasen, C. X-Ray Scattering in the Vorticity Direction and Rheometry from Confined Fluids. *Rev. Sci. Instrum.* **2014,** *85* (6).

Phillip, W. A.; O'neill, B.; Rodwogin, M.; Hillmyer, M. A.; Cussler, E. L. Self-Assembled Block Copolymer Thin Films as Water Filtration Membranes. *ACS Appl. Mater. Interfaces* **2010**, *2* (3), 847–853.

Pletsch, H.; Tebbe, M.; Dulle, M.; Forster, B.; Fery, A.; Forster, S.; Greiner, A.; Agarwal, S. Reversible Gold Nanorod Alignment in Mechano-Responsive Elastomers. *Polymer (Guildf).* **2015**, *66*, 167–172.

Quiram, D. J.; Register, R. A.; Marchand, G. R. Crystallization of Asymmetric Diblock Copolymers from Microphase-Separated Melts. *Macromolecules* **1997,** *30* (16), 4551–4558.

Rajan, G. S.; Mauritz, K. A.; Stromeyer, S. L.; Kwee, T.; Mani, P.; Weston, J. L.; Nikles, D. E.; Shamsuzzoha, M. Poly(Styrene-b-Ethylene/Butylene-b-Styrene)/Cobalt Ferrite Magnetic Nanocomposites. *J. Polym. Sci. Part B Polym. Phys.* **2005**, *43* (12), 1475–1485.

Ren, J. M.; McKenzie, T. G.; Fu, Q.; Wong, E. H. H.; Xu, J.; An, Z.; Shanmugam, S.; Davis, T. P.; Boyer, C.; Qiao, G. G. Star Polymers. *Chem. Rev.* **2016**, *116* (12), 6743–6836.

Rendon, S.; Fang, J.; Burghardt, W. R.; Bubeck, R. A. An Apparatus for in Situ X-Ray Scattering Measurements during Polymer Injection Molding. *Rev. Sci. Instrum.* **2009,** *80* (4).

Riise, B. L.; Fredrickson, G. H.; Larson, R. G.; Pearson, D. S. Rheology and Shear-Induced Alignment of Lamellar Diblock and Triblock Copolymers. *Macromolecules* **1995**, *28* (23), 7653–7659.

Rokhlenko, Y.; Gopinadhan, M.; Osuji, C. O.; Zhang, K.; O'Hern, C. S.; Larson, S. R.; Gopalan, P.; Majewski, P. W.; Yager, K. G. Magnetic Alignment of Block Copolymer Microdomains by Intrinsic Chain Anisotropy. *Phys. Rev. Lett.* **2015**, *115* (25), 2–6.

Rokhlenko, Y.; Kawamoto, K.; Johnson, J. A.; Osuji, C. O. Sub-10 Nm Self-Assembly of Mesogen-Containing Grafted Macromonomers and Their Bottlebrush Polymers. *Macromolecules* **2018,** *51*, 3680–3690.

Rosedale, J. H.; Bates, F. S. Rheology of Ordered and Disordered Symmetric Poly(Ethylenepropylene)-Poly(Ethylethylene) Diblock Copolymers. *Macromolecules* **1990**, *23* (8), 2329–2338.

Rubinstein, M.; Obukhov, S. P. Power-Law-Like Stress Relaxation of Block Copolymers: Disentanglement Regimes. *Macromolecules* **1993**, *26* (7), 1740–1750.

Ruppel, M.; Pester, C. W.; Langner, K. M.; Sevink, G. J. A.; Schoberth, H. G.; Schmidt, K.; Urban, V. S.; Mays, J. W.; Böker, A. Electric Field Induced Selective Disordering in Lamellar Block Copolymers. *ACS Nano* **2013**, *7* (5), 3854–3867.

Ryan, A. J.; Hamley, I. W.; Bras, W.; Bates, F. S. Structure Development in Semicrystalline Diblock Copolymers Crystallizing from the Ordered Melt. *Macromolecules* **1995**, *28* (11), 3860–3868.

Rzayev, J. Molecular Bottlebrushes: New Opportunities in Nanomaterials Fabrication. *ACS Macro Lett.* **2012**, *1* (9), 1146–1149.

Rzayev, J. Synthesis of Polystyrene-Polylactide Bottlebrush Block Copolymers and Their Melt Self-Assembly into Large Domain Nanostructures. *Macromolecules* **2009**, *42* (6), 2135–2141.

Sakamoto, N.; Hashimoto, T. Order-Disorder Transition of Low Molecular Weight Polystyrene-Block-Polyisoprene. 1. SAXS Analysis of Two Characteristic Temperatures. *Macromolecules* **1995**, *28* (20), 6825–6834.

Sarkar, B.; Alexandridis, P. Block Copolymer–nanoparticle Composites: Structure, Functional Properties, and Processing. *Prog. Polym. Sci.* **2015**, *40*, 33–62.

Scott, D. B.; Waddon, A. J.; Lin, Y. G.; Karasz, F. E.; Winter, H. H. Shear-Induced Orientation Transitions in Triblock Copolymer Styrene-Butadiene-Styrene with Cylindrical Domain Morphology. *Macromolecules* **1992**, *25* (16), 4175–4181.

Semenov, A. N. Contribution to the Theory of Microphase Layering in Block-Copolymer Melts. *Zh. Eksp. Teor. Fiz* **1985**, *88* (4), 1242–1256.

Sheiko, S. S.; Sumerlin, B. S.; Matyjaszewski, K. Cylindrical Molecular Brushes: Synthesis, Characterization, and Properties. *Prog. Polym. Sci.* **2008**, *33* (7), 759–785.

Shibayama, M.; Hashimoto, T. Small-Angle X-Ray Scattering Analyses of Lamellar Microdomains Based on a Model of One-Dimensional Paracrystal with Uniaxial Orientation. *Macromolecules* **1986**, *19*, 740–749.

Sijbesma, R. P.; Beijer, F. H.; Brunsveld, L.; Folmer, B. J. B.; Hirschberg, J. H. K. K.; Lange, R. F. M.; Lowe, J. K. L.; Meijer, E. W. Reversible Polymers Formed from Self-Complementary Monomers Using Quadruple Hydrogen Bonding. *Science*

(80-.). **1997**, *278* (5343), 1601–1604.

Sollich, P. Rheological Constitutive Equation for a Model of Soft Glassy Materials. *Phys. Rev. E* **1998**, *58* (1), 738–759.

Song, D.-P.; Gai, Y.; Yavitt, B. M.; Ribbe, A.; Gido, S.; Watkins, J. J. Structural Diversity and Phase Behavior of Brush Block Copolymer Nanocomposites. *Macromolecules* **2016**, 49, 6480–6488.

Song, D.-P.; Jacucci, G.; Dundar, F.; Naik, A.; Fei, H.-F.; Vignolini, S.; Watkins, J. J. Photonic Resins: Designing Optical Appearance via Block Copolymer Self-Assembly. *Macromolecules* **2018**, *51* (6), 2395–2400.

Song, D.-P.; Li, C.; Colella, N. S.; Lu, X.; Lee, J.-H.; Watkins, J. J. Thermally Tunable Metallodielectric Photonic Crystals from the Self-Assembly of Brush Block Copolymers and Gold Nanoparticles. *Adv. Opt. Mater.* **2015**, *3* (9), 1169–1175.

Song, D.-P.; Li, C.; Colella, N. S.; Xie, W.; Li, S.; Lu, X.; Gido, S. P.; Lee, J.-H.; Watkins, J. J. Large-Volume Self-Organization of Polymer/Nanoparticle Hybrids with Millimeter-Scale Grain Sizes Using Brush Block Copolymers. *J. Am. Chem. Soc.* **2015**, *137*, 12510–12513.

Song, D.-P.; Li, C.; Li, W.; Watkins, J. J. Block Copolymer Nanocomposites with High Refractive Index Contrast for One-Step Photonics. *ACS Nano* **2016**, *10* (1), 1216–1223.

Song, D.-P.; Lin, Y.; Gai, Y.; Colella, N. S.; Li, C.; Liu, X.-H.; Gido, S. P.; Watkins, J. J. Controlled Supramolecular Self-Assembly of Large Nanoparticles in Amphiphilic Brush Block Copolymers. *J. Am. Chem. Soc.* **2015**, *137* (11), 3771–3774.

Song, D.-P.; Naik, A.; Li, S.; Ribbe, A.; Watkins, J. J. Rapid, Large-Area Synthesis of Hierarchical Nanoporous Silica Hybrid Films on Flexible Substrates. *J. Am. Chem. Soc.* **2016**, *138* (41), 13473–13476.

Song, D.-P.; Shahin, S.; Xie, W.; Mehravar, S.; Liu, X.; Li, C.; Norwood, R. A.; Lee, J.-H.; Watkins, J. J. Directed Assembly of Quantum Dots Using Brush Block Copolymers for Well-Ordered Nonlinear Optical Nanocomposites. *Macromolecules* **2016**, *49* (14), 5068–5075.

Song, Y.; Zheng, Q. Linear Rheology of Nanofilled Polymers. *J. Rheol.* **2015**, *59* (1), 155–191.

Srivastava, S.; Shin, J. H.; Archer, L. A. Structure and Rheology of Nanoparticle–polymer Suspensions. *Soft Matter* **2012**, *8* (15), 4097.

Sveinbjornsson, B. R.; Weitekamp, R. a.; Miyake, G. M.; Xia, Y.; Atwater, H. a.; Grubbs, R. H. Rapid Self-Assembly of Brush Block Copolymers to Photonic Crystals. *Proc. Natl. Acad. Sci.* **2012**, *109* (36), 14332–14336.

Tadmor, Z.; Gogos, C. G. *Principles of Polymer Processing - 2nd Ed.*; 2006.

Tirumala, V. R.; Daga, V. K.; Bosse, A. W.; Romang, A.; Ilavsky, J.; Lin, E. K.; Watkins, J. J. Well-Ordered Polymer Melts with 5 Nm Lamellar Domains from Blends of a Disordered Block Copolymer and a Selectively Associating Homopolymer of Low or High Molar Mass. *Macromolecules* **2008**, *41* (21), 7978–7985.

Tirumala, V. R.; Romang, A.; Agarwal, S.; Lin, E. K.; Watkins, J. J. Well Ordered Polymer Melts from Blends of Disordered Triblock Copolymer Surfactants and Functional Homopolymers. *Adv. Mater.* **2008**, *20* (9), 1603–1608.

Tousley, M. E.; Feng, X.; Elimelech, M.; Osuji, C. O. Aligned Nanostructured Polymers by Magnetic-Field-Directed Self-Assembly of a Polymerizable Lyotropic Mesophase. *ACS Appl. Mater. Interfaces* **2014**, *6* (22), 19710–19717.

Trinkle, S.; Freidrich, C. Van Gurp-Palmen-Plot: A Way to Characterize Polydispersity of Linear Polymers. *Rheol. Acta* **2001**, *40* (4), 322–328.

van Gurp, M.; Palmen, J. Time-Temperature Superposition for Polymeric Blends. *J Rheol Bull* **1998**, *65*, 5–8.

Van Ruymbeke, E. Preface: Special Issue on Associating Polymers. *J. Rheol. (N. Y. N. Y).* **2017**, *61* (6), 1099–1102.

Verduzco, R.; Li, X.; Pesek, S. L.; Stein, G. E. Structure, Function, Self-Assembly, and Applications of Bottlebrush Copolymers. *Chem. Soc. Rev.* **2015**, *44*, 2405–2420.

Wang, L.; Yang, H.; Tan, H.; Yao, K.; Gong, J.; Wan, D.; Qiu, J.; Tang, T. Synthesis and Structure-Property Relationships of Polypropylene-g- Polystyrene and Polypropylene-g-Poly(n-Butyl Acrylate) Graft Copolymers with Well-Defined Molecular Structures. *Polymer* **2013**, *54* (14), 3641–3653.

Warren, S. C.; Messina, L. C.; Slaughter, L. S.; Kamperman, M.; Zhou, Q.; Gruner, S. M.; DiSalvo, F. J.; Wiesner, U. B. Ordered Mesoporous Materials from Metal Nanoparticle-Block Copolymer Self-Assembly. *Science* **2008**, *320* (5884), 1748–1752.

Wiesner, U. B. Lamellar Diblock Copolymers under Large Amplitude Oscillatory Shear Flow: Order and Dynamics. *Macromol. Chem. Phys.* **1997**, *198* (11), 3319–3352.

Williams, M. L.; Landel, R. F.; Ferry, J. D. The Temperature Dependence of Relaxation Mechanisms in Amorphous Polymers and Other Glass-Forming Liquids1. *J. Am. Chem. Soc.* **1955**, *679* (12), 3701–3707.

Winey, K. I.; Sanjay, J.; Larson, R. G.; Watanabe, H. Interdependence of Shear Deformations and Block Copolymer Morphology. *Macromolecules* **1993**, *26*, 2542–2549.

Winter, H. H. Glass Transition as the Rheological Inverse of Gelation. *Macromolecules* **2013**, *46* (6), 2425–2432.

Winter, H. H. The Occurance of Self Similar Relaxation in Polymers. *J. Non. Cryst. Solids* **1994**, *172*, 1158–1167.

Winter, H. H. Three Views of Viscoelasticity for Cox-Merz Materials. *Rheol. Acta* **2009**, *48* (3), 241–243.

Winter, H. H.; Mours, M. Rheology of Polymers near Liquid-Solid Transitions. *Adv. Polym. Sci.* **1997**, *134*, 165–234.

Winter, H. H.; Mours, M. The Cyber Infrastructure Initiative for Rheology. *Rheol. Acta* **2006**, *45* (4), 331–338.

Witten, T. A.; Leibler, L.; Pincus, P. A. Stress Relaxation in the Lamellar Copolymer Mesophase. *Macromolecules* **1990**, *23* (3), 824–829.

Xia, Y.; Kornfield, J. A.; Grubbs, R. H. Efficient Synthesis of Narrowly Dispersed Brush Polymers via Living Ring-Opening Metathesis Polymerization of Macromonomers. *Macromolecules* **2009**, *42* (11), 3761–3766.

Xia, Y.; Olsen, B. D.; Kornfield, J. A.; Grubbs, R. H. Efficient Synthesis of Narrowly Dispersed Brush Copolymers and Study of Their Assemblies: The Importance of Side Chain Arrangement. *J. Am. Chem. Soc.* **2009**, *131* (51), 18525–18532.

Yao, L.; Lin, Y.; Watkins, J. J. Ultrahigh Loading of Nanoparticles into Ordered Block Copolymer Composites. *Macromolecules* **2014**, *47* (5), 1844–1849.

Yavitt, B. M.; Gai, Y.; Song, D.-P.; Winter, H. H.; Watkins, J. J. High Molecular Mobility and Viscoelasticity of Microphase-Separated Bottlebrush Diblock Copolymer Melts. *Macromolecules* **2017**, *50* (1), 396–405.

Yin, D.; Horiuchi, S.; Masuoka, T. Lateral Assembly of Metal Nanoparticles Directed by Nanodomain Control in Block Copolymer Thin Films. *Chem. Mater.* **2005**, *17* (3), 463–469.

Yoo, M.; Kim, S.; Bang, J. Design and Fabrication of Thermally Stable Nanoparticles for Well-Defined Nanocomposites. *J. Polym. Sci. Part B Polym. Phys.* **2013**, *51* (7), 494–507.

Yu, Y.; Chae, C.; Kim, M.; Seo, H.; Grubbs, R. H.; Lee, J. Precise Synthesis of Bottlebrush Block Copolymers from ω - End-Norbornyl Polystyrene and Poly(4-Tert -Butoxystyrene) via Living Anionic Polymerization and Ring-Opening Metathesis Polymerization. *Macromolecules* **2018**, *51* (2), 447–455.

Zalusky, A. S.; Olayo-Valles, R.; Wolf, J. H.; Hillmyer, M. A. Ordered Nanoporous Polymers from Polystyrene-Polylactide Block Copolymers. *J. Am. Chem. Soc.*

2002, *124* (43), 12761–12773.

Zhang, C.; Cavicchi, K. A.; Li, R.; Yager, K. G.; Fukuto, M.; Vogt, B. D. Thickness Limit for Alignment of Block Copolymer Films Using Solvent Vapor Annealing with Shear. *Macromolecules* **2018**.

Zhang, Y.; Wiesner, U. B. Rheology of Lamellar Polystyrene- Block - Polyisoprene Diblock Copolymers. *Macromol. Chem. Phys.* **1998**, *199*, 1771–1784.

Zhao, Y.; Saijo, K.; Hashimoto, T. Order − Disorder Transition of Nanocomposites : Polystyrene- Block - Poly(Methyl Methacrylate) with Palladium Nanoparticles. *Macromolecules* **2013**, *46*, 957–970.

Zhao, Y.; Saijo, K.; Takenaka, M.; Koizumi, S.; Hashimoto, T. Order−Disorder Transition of Nanocomposites: Pd Nanoparticles in Polystyrene- Block - Polyisoprene Microdomain Templates. *Macromolecules* **2009**, *42* (14), 5272–5277.

Zhao, Y.; Thorkelsson, K.; Mastroianni, A. J.; Schilling, T.; Luther, J. M.; Rancatore, B. J.; Matsunaga, K.; Jinnai, H.; Wu, Y.; Poulsen, D.; et al. Small-Molecule-Directed Nanoparticle Assembly towards Stimuli-Responsive Nanocomposites. *Nat. Mater.* **2009**, *8* (October), 979–985.

Zhu, L.; Cheng, S. Z. D.; Calhoun, B. H.; Ge, Q.; Quirk, R. P.; Thomas, E. L.; Hsiao, B. S.; Yeh, F.; Lotz, B. Phase Structures and Morphologies Determined by Self-Organization, Vitrification, and Crystallization: Confined Crystallization in an Ordered Lamellar Phase of PEO-b-PS Diblock Copolymer. *Polymer* **2001**, *42*, 5829–5839.

Zhu, L.; Cheng, S. Z. D.; Calhoun, B. H.; Ge, Q.; Quirk, R. P.; Thomas, E. L.; Hsiao, B. S.; Yeh, F.; Lotz, B. Crystallization Temperature-Dependent Crystal Orientations within Nanoscale Confined Lamellae of a Self-Assembled Crystalline - Amorphous Diblock Copolymer. *J. Am. Chem. Soc.* **2000**, *122* (25), 5957–5967.